Application of UV-radiation and UV-responsive nanocapsules for skin antisepsis

Dissertation

zur

Erlangung des Doktorgrades

der Naturwissenschaften

(Dr. rer. nat.)

dem

Fachbereich Pharmazie der

Philipps-Universität Marburg

vorgelegt von

Loris Busch

aus **Detmold**

Marburg an der Lahn

2023

Erstgutachter: **Prof. Dr. rer. nat. Cornelia M. Keck**

Zweitgutachter: **Prof. Dr. rer. nat. Martina C. Meinke**

Drittgutachter: **Prof. Dr. Dr.-Ing. Jürgen Lademann**

Eingereicht am **05.10.2023**

Tag der mündlichen Prüfung am **22.11.2023**

Hochschulkennziffer: 1180

Eidesstattliche Erklärung

Ich versichere, dass ich meine Dissertation

„**Application of UV-radiation and UV-responsive nanocapsules for skin antisepsis**“

selbständig ohne unerlaubte Hilfe angefertigt und mich dabei keiner anderen als der von mir ausdrücklich bezeichneten Quellen bedient habe. Alle vollständig oder sinngemäß übernommenen Zitate sind als solche gekennzeichnet.

Die Dissertation wurde in der jetzigen oder einer ähnlichen Form noch bei keiner anderen Hochschule eingereicht und hat noch keinen sonstigen Prüfungszwecken gedient.

Berlin, 05.10.2023

Loris Busch

Die vorliegende Dissertation ist zwischen November 2019 und Oktober 2023 extern am Center of Experimental and Applied Cutaneous Physiology (CCP) an der Klinik für Dermatologie, Venerologie und Allergologie der Charité – Universitätsmedizin Berlin unter der Betreuung von **Prof. Dr. Cornelia M. Keck** und **Prof. Dr. Martina C. Meinke** entstanden.

Was für den einfachen Menschen ein Stein ist,
ist für den Wissenden eine Perle.

Rūmī

Abstract

Based on the global health care burden caused by surgical site infections (SSI) as well as the rising prevalence of multi-drug resistant bacteria this dissertation suggests the implementation of two novel and innovative approaches for an advanced skin antisepsis. Hair follicles are known to represent a densely colonized reservoir of pathogens. During prolonged surgical procedures, recolonization of the skin surface can therefore occur from this reservoir transmitting pathogens into the surgical field. It is known that SSI are caused by endogenous germs in 90% of all cases. This leads to two possible approaches for improved skin antisepsis: targeted decontamination of deep sections of hair follicles and repetitive intraoperative decontamination of the skin. The first part of this dissertation addresses the application of a pharmaceutical-based approach for enhanced skin antisepsis. Based on the so-called ratchet effect, nanoparticles penetrate into hair follicles when external forces are applied. Thus, it is known that a significantly deeper follicular penetration of therapeutics can be achieved using nano-delivery systems as compared to the application of free active ingredient solutions. A targeted eradication could therefore be induced by a controlled release of antiseptics in the deeper segments of the hair follicles, whereas these segments are inaccessible to non-particulate substances. For a targeted and rapid release of the antiseptic contained in nanocapsules (NCs), ultraviolet A light (UVA) was utilized due to its accessibility to the dermal portions of the skin. This approach was pursued using UVA light emitting diode (LED) systems as well as biocompatible photo-responsive NCs. The first of two studies focused on principal experiments to evidence the possibility of follicular penetration and intrafollicular UV-triggered drug release using biocompatible polyurethane (PU)-NCs. Using an *ex vivo* porcine skin model, UVA-responsive degradation of the NCs at a mean follicular penetration depth of approximately 500 µm was obtained tracking the model drug sulforhodamine 101 (SR101) in cryohistological slices with confocal laser scanning microscopy (CLSM). In a follow-up approach hydroxyethyl starch (HES)-NCs based on the same technology were utilized. With these, a comparable follicular penetration depth could be achieved. In a final microbiological experiment utilizing HES-NCs with encapsulated ethanol, no significant difference to a particle-free control (80% ethanol) could be observed on *ex vivo* porcine ear skin showing that the choice of nanocarrier materials should always be based on the field of application and compatibility with the continuous phase.

Complementary to this, far-UVC light (UVC < 240 nm) represents the second approach for improved skin surface decontamination as it is very easy to apply consecutively and can therefore quickly disinfect recolonized surfaces to prevent SSI. Based on its high energy, far-UVC radiation has the advantage of inactivating pathogens through the immediate generation of DNA lesions without provoking bacterial resistance. Unlike UVC radiation of 254 nm, which is

mostly applied for the disinfection of water and surfaces, it is absorbed strongly in the non-nucleated stratum corneum limiting the penetration of far-UVC photons into the viable epidermis. In this thesis, a novel LED emitting far-UVC light of 233 nm was comprehensively assessed for its skin compatibility evaluating the formation of DNA damage and free radicals on various skin models. Microbiocidal doses as previously determined by project partners of the University Medicine Greifswald were applied. At an application dose from 40 to 60 mJ/cm^2, a complete eradication of methicillin-resistant *Staphylococcus aureus* (MRSA) on agar plates and germ carriers was observed. Irradiation with microbiocidal 233 nm far-UVC led to a minor development of DNA damage in intact *ex vivo* human skin compared to 10% of a minimal erythema dose (MED) of UVB radiation. Moreover, the formation of free radicals was lower than for visible and near-infrared (VIS–NIR) irradiation equivalent to 20 min solar exposure in reconstructed human epidermal models. To investigate whether 233 nm far-UVC radiation can also be applied to wounds during surgical procedures, an *ex vivo* wound model was assessed in the follow-up study. An increase and relocation of DNA lesions to deeper areas of wounded skin was observed after irradiation with 233 nm far-UVC. Interestingly, applying artificial wound exudate to the exposed viable epidermis before irradiation led to reconstruction of the photoprotective function of an intact stratum corneum. Furthermore, it was found that a certain amount of free radicals is generated in wounded skin, which is an interesting subject for future studies on possible wound healing processes. To determine the influence of the melanin concentration, human skin of different skin types was irradiated *ex vivo* with 222 nm, 233 far-UVC light and with broadband UVB light. In this study it was revealed that the formation of DNA lesions was lower in dark skin types than in fair skin types after irradiation at 233 nm. However, 222 nm radiation caused no skin type-dependent differences due to its limited penetration depth while UVB caused a strong divergence between light and dark skin types when applying 10% of a MED. The melanin concentration differs less between light and dark skin types in the upper epidermal fraction than in the deep layers of the epidermis. This leads to skin type-dependent deviations in tolerability due to the maximum penetration depth of the respective wavelength.

In summary, the nanoparticle-based approach for skin decolonization is usefully complemented by the far-UVC light-based approach, and both bear potential for a preoperative and intraoperative skin antisepsis. Nevertheless, the pharmaceutical side requires significant optimization before it can be finally implemented. The use of far-UVC LEDs for skin surface decontamination has been comprehensively addressed for the first time but still further risk assessment studies need to be performed for the final implementation of this approach.

Zusammenfassung

Angesichts der weltweiten Belastung des Gesundheitswesens durch postoperative Wundinfektionen (SSI) und der steigenden Prävalenz multiresistenter Bakterien, war das Ziel dieser Dissertation die Umsetzung zweier neuartiger und innovativer Ansätze für eine verbesserte Hautantisepsis. Haarfollikel stellen ein dicht kolonisiertes Erregerreservoir dar. Bei langwierigen chirurgischen Eingriffen kann es daher zu einer Rekolonisierung der Hautoberfläche aus diesem Reservoir, und der Verschleppung potenzieller Krankheitserreger in das Operationsgebiet, kommen. Es ist bekannt, dass SSI in 90% aller Fälle durch endogene Keime verursacht werden. Daraus ergeben sich zwei mögliche Ansätze für eine verbesserte Hautantisepsis: die Dekontamination tiefer Bereiche der Haarfollikel und die wiederholte intraoperative Dekontamination der Haut. Der erste Teil dieser Dissertation zielte auf die Anwendung eines pharmazeutisch basierten Ansatzes zur verbesserten Hautantisepsis ab. Basierend auf dem so genannten Ratscheneffekt dringen Nanopartikel in Haarfollikel ein, wenn äußere Kräfte auf sie einwirken. So ist bekannt, dass mit Nano-Delivery-Systemen eine deutlich tiefere follikuläre Penetration von Therapeutika erreicht werden kann als mit der Anwendung von freien Wirkstofflösungen. Eine gezielte Eradikation könnte also durch eine kontrollierte Freisetzung von Antiseptika in den tieferen Segmenten der Haarfollikel erfolgen, während diese Segmente für nicht partikuläre Substanzen unzugänglich sind. Für eine gezielte und schnelle Freisetzung des in den Nanokapseln (NCs) enthaltenen Antiseptikums wurde Ultraviolett A (UVA) Licht verwendet, da es die dermalen Hautbereiche erreichen kann. Dieser Ansatz wurde mit UVA Licht emittierenden Dioden (LED) sowie biokompatiblen photoresponsiven NCs verfolgt. Die erste von zwei Studien konzentrierte sich auf Prinzipexperimente zum Nachweis der Möglichkeit einer follikulären Penetration und intrafollikulären UV-getriggerten Wirkstofffreisetzung unter Verwendung von biokompatiblen Polyurethan (PU)-NCs. Anhand eines *ex vivo* Schweinehautmodells wurde ein UVA-abhängiger Abbau der NCs bei einer mittleren follikulären Eindringtiefe von etwa 500 µm festgestellt, wobei der Modellwirkstoff Sulforhodamin 101 (SR101) in kryohistologischen Schnitten mit konfokaler Laser-Scanning-Mikroskopie (CLSM) verfolgt wurde. In einem weiteren Ansatz wurden Hydroxyethylstärke (HES)-NCs verwendet, die auf der gleichen Technologie basierten. Mit diesen konnte eine vergleichbare follikuläre Eindringtiefe erreicht werden. In einem abschließenden Experiment, bei dem HES-NCs mit eingekapseltem Ethanol verwendet wurden, konnte hinsichtlich der Dekolonisierung kein signifikanter Unterschied zu einer partikelfreien Kontrolle (80% Ethanol) auf der *ex vivo* Schweineohrhaut festgestellt werden, was zeigt, dass die Wahl der Nanoträgermaterialien immer mit dem Anwendungsbereich und der Kompatibilität mit der kontinuierlichen Phase abgestimmt werden sollte.

Ergänzend dazu stellt Fern-UVC-Licht (UVC unter einer Wellenlänge von 240 nm) den zweiten Ansatz zur Dekontamination der Hautoberfläche dar, da es sich sehr leicht sequentiell anwenden lässt und somit rekolonisierte Flächen schnell desinfizieren kann um SSI zu verhindern. Fern-UVC-Strahlung hat aufgrund ihrer hohen Energie den Vorteil, dass sie resistenzfrei Pathogene durch die sofortige Erzeugung von DNA-Läsionen inaktiviert. Im Gegensatz zur UVC-Strahlung von 254 nm, die meist zur Desinfektion von Wasser und Oberflächen eingesetzt wird, wird sie in der obersten, nicht nukleierten Schicht der Haut, dem Stratum corneum, stark absorbiert. Daher ist die Penetration von Fern-UVC-Photonen in die Lebendepidermis nur begrenzt möglich. Im Rahmen dieser Arbeit wurde eine neuartige LED, die Fern-UVC-Licht mit einer Peak-Wellenlänge von 233 nm emittiert, an verschiedenen Hautmodellen hinsichtlich der Bildung von DNA-Schäden und freien Radikalen umfassend auf ihre Hautverträglichkeit geprüft. Dabei wurden zuvor von den Projektpartnern der Universitätsmedizin Greifswald ermittelte mikrobiozide Dosen eingesetzt. Bei einer Anwendungsdosis von 40 bis 60 mJ/cm^2 konnte eine vollständige Eradikation von Methicillin-resistenten *Staphylococcus aureus* (MRSA) auf Agarplatten und Keimträgern beobachtet werden. Die Bestrahlung mit mikrobiozidem 233 nm Fern-UVC führte zu geringeren DNA-Schäden in intakter *ex vivo* Humanhaut im Vergleich zu 10% einer minimalen Erythemdosis (MED) UVB-Strahlung. Darüber hinaus war die Bildung freier Radikale in rekonstruierten humanen Epidermismodellen geringer als bei sichtbarer und nahinfraroter (VIS–NIR) Bestrahlung, die einem 20-minütigen Aufenthalt in der Mittagssonne entspricht. Um der Frage nachzugehen, ob 233 nm Fern-UVC-Strahlung auch während chirurgischer Eingriffe an Wunden angewandt werden kann, wurde in der Folgestudie ein *ex vivo* Wundmodell zur Risikobeurteilung von 233 nm Fern-UVC-Strahlung untersucht. Hier wurde nach Bestrahlung mit 233 nm Fern-UVC eine Zunahme und Verlagerung von DNA-Läsionen in tiefere Bereiche der wunden Haut beobachtet. Interessanterweise führte das Auftragen von künstlichem Wundexsudat auf die exponierte Lebendepidermis vor der Bestrahlung zur Nachahmung der photoprotektiven Funktion eines intakten Stratum corneum. Darüber hinaus wurde festgestellt, dass in der Wunde eine gewisse Menge an freien Radikalen gebildet wird, was die Wundheilung unterstützen könnte. Um den Einfluss der Melaninkonzentration zu ermitteln, wurde menschliche Haut verschiedener Hauttypen *ex vivo* mit 222 nm und 233 far-UVC-Licht sowie mit breitbandigem UVB-Licht bestrahlt. In dieser Studie zeigte sich, dass die Bildung von DNA-Läsionen bei dunklen Hauttypen nach Bestrahlung mit 233 nm geringer war als bei hellen Hauttypen. Die Bestrahlung bei 222 nm verursachte jedoch aufgrund ihrer begrenzten Eindringtiefe keine hauttypabhängigen Unterschiede. Im Gegensatz dazu verursachte UVB eine starke Divergenz zwischen hellen und dunklen Hauttypen bei der Anwendung von 10% einer MED. Die Melaninkonzentration unterscheidet sich zwischen hellen und dunklen Hauttypen in der oberen Epidermis weniger als in den tiefen Schichten der Epidermis. Dies führt,

basierend auf der maximalen Eindringtiefe der jeweiligen Wellenlänge, zu hauttypabhängigen Abweichungen in der Verträglichkeit der Strahlung.

Zusammenfassend lässt sich sagen, dass der in dieser Dissertation untersuchte nanopartikelbasierte Ansatz zur Hautdekolonisierung durch den Fern-UVC-Licht-basierten Ansatz sinnvoll ergänzt wird und beide Ansätze Potenzial für eine präoperative sowie intraoperative Hautantiseptik besitzen. Dennoch müssen für eine endgültige Umsetzung noch deutliche Optimierungen auf pharmazeutischer Seite gesucht werden. Der Einsatz von Fern-UVC-LEDs zur Dekontaminierung der Hautoberfläche wurde in der vorliegenden Arbeit erstmals umfassend behandelt. Auch hier müssen für die endgültige Umsetzung weitere Studien zur Risikobewertung durchgeführt werden.

Table of contents

1. Introduction

The prevalence of surgical site infections (SSI) as well as infections with multi-drug resistant germs in the nosocomial environment represents a severe healthcare problem. Approximately 90% of the SSI recorded are caused by endogenous germs [1]. A total of 25% of the skin microbiome is localized in the depths of the hair follicles [2]. From this reservoir of pathogens, recolonization of the skin surface may occur during surgical procedures [3, 4]. Since conventional antiseptics cannot reach the deep sections of the hair follicles, the use of nanoparticulate systems is well suited for targeting these structures, as they are known for deep penetration into the hair follicles [5]. The pre-surgical application of nanocapsules (NCs) containing antiseptics could thus prevent intraoperative recolonization of the skin surface. Ultraviolet A (UVA) radiation is suitable for the targeted release of antiseptics from NCs, as it can also reach the dermal sections of the skin and thus deeper sections of the hair follicles representing dermal invaginations.

Complementary to this, the use of far-UVC radiation is suitable for skin antisepsis since it can be easily applied in a consecutive manner to disinfect recolonized skin or surgical wounds in different scenarios such as prolonged surgical procedures in order to prevent SSI. In contrast to UVA radiation, the range of UVC radiation below 240 nm, which is also referred to as far-UVC, penetrates at maximum the upper third of the living epidermis, since there is a strong absorption of this radiation in the stratum corneum, which is known for its dense protein network of terminalized and nuclei-free corneocytes [6-8].
Due to the relatively high energy and absorption of this wavelength region by nucleic acids, but low penetration depth into the DNA-containing layers of the skin, far-UVC is potentially suitable for skin surface decolonization as a complement or an alternative to the deep skin decontamination as presented previously. Because of the non-specific characteristics of radiation, it further represents a potential alternative to avoid the formation of antibiotic resistance and as well as cross-resistance, e.g., in the context of wound treatment.

In the present work, two novel and innovative approaches for skin decolonization were explored. First, UVA-responsive NCs were used with the aim of decolonizing deep sections of the hair follicles. In addition, the aim was to investigate the applicability of far-UVC radiation as an alternative or complement for pharmacologically based pre- and intraoperative decolonization of intact and wounded skin, with a focus on safety aspects. For both approaches light

emitting diodes (LEDs) were applied since they can be easily integrated into medical devices due to their compactness.
In the following chapters, the reader will be step by step guided through the fundamentals of the structure of the skin and the hair follicles. Furthermore, the basics of the skin microbiome and skin decontamination utilizing NCs and far-UVC light will be presented. Since the complexity of this subject only allows a brief outline of the respective topic, the interested reader is referred to the corresponding references at the appropriate point.

1.1. Human skin architecture: interactions of anatomical structure with radiation and drug carriers

The skin anatomy is comprised of three layers including the epithelial epidermis (1) with the non-nucleated stratum corneum as its uppermost layer as well as the underlying dermis (2) and subcutis (3). Moreover, the skin has various adnexal organs. These include the hair follicles and their attached sebaceous glands as presented in **Section 1.1.4.**, but also the apocrine and eccrine sweat glands as well as nails [9-11].
In the following chapters, we will work along the penetration path of pharmaceutics and radiation from the superior to the inferior skin fractions covering not only the architecture of the skin but also physiological aspects.

1.1.1. Stratum corneum: a selective gate for radiation and pharmaceutics

As the outermost skin layer, the stratum corneum represents the first (selective) barrier against the penetration of chemical substances, radiation or biological noxes and has the capability of resisting mechanical forces [11, 12]. Between the stratum granulosum of the viable epidermis (**Section 1.1.2.**) and the stratum corneum, an enzyme-driven degradation of the cell organelles takes place [11, 12]. Consequently, the stratum corneum evolves with a thickness of 15–20 µm as a product of an epidermal terminalization process [11-14]. As presented by Elias et al. in 1983 [15], the architecture of this skin layer can be described by the so-called brick and mortar model. Here, the corneocytes, which are non-nucleated, flattened and keratin-rich cells, represent the "bricks" [12]. Those contain densely cross-linked proteins, such as loricrin, involucrin or filaggrin, which substitute the plasma membrane as the so-called cornified envelope deriving from the stratum granulosum [12, 16]. The "mortar" is a hydrophobic matrix surrounding the corneocytes. It consists of the intercellular lipids evolving from the lamellar bodies synthesized in keratinocytes of the stratum spinosum (**Section 1.1.2.**) [12, 13, 16]. The intercellular lipids are composed of ceramides, cholesterol, and free fatty acids [13] and are arranged

as intercellular channels of 19 nm in width [17], which gives a first indication of the penetration ability of different drugs and drug carriers based on the hydrodynamic radius.
The stratum corneum plays a significant role in the regulation of water release to the atmosphere, also known as the transepidermal water loss (TEWL) [12]. On the other hand, the stratum corneum can be seen as an entry point for various therapeutics based on different drug delivery mechanisms making it a selective gate for drugs [18, 19]. The inverse relationship between the thickness of the stratum corneum and the TEWL is an important indicator for the barrier function of the skin [20, 21]. In this context, the stratum corneum represents a Fick's membrane despite its heterogeneous structure [22]. In spite of its considerable barrier function, the intact stratum corneum is not a completely impermeable barrier making the skin accessible to various substances [23]. Low molecular weight substances can penetrate through the intact stratum corneum depending on Fick's diffusion law [11, 14, 24] with an increased drug penetration rate after ablation by tape-stripping procedures [25, 26] based on an intercellular penetration pathway [27]. Based on retrospective observations by Bos and Meinardi, molecules up to a weight of 500 Da are feasible for percutaneous absorption by healthy skin [27].

Depending on the wavelength, radiation is absorbed and scattered in the skin and can penetrate the tissue to different depths. This is particularly remarkable in terms of far-UVC, which, unlike therapeutic substances, is supposed to act only on the surface. Here, a difference of a few nanometers in wavelength can make a dramatic difference in the penetration depth [8]. As compared to UVC radiation between 250 and 280 nm, most of far-UVC radiation ($\lambda < 240$ nm) penetrating the skin is absorbed by the stratum corneum [6-8, 28] (**Figure 1**) (see also: **Section 1.3.3.**). The significant role of the stratum corneum in the absorption of far-UVC light was demonstrated by ablation of these structures to induce superficial wounds in the framework of a risk assessment (**publication IV**).

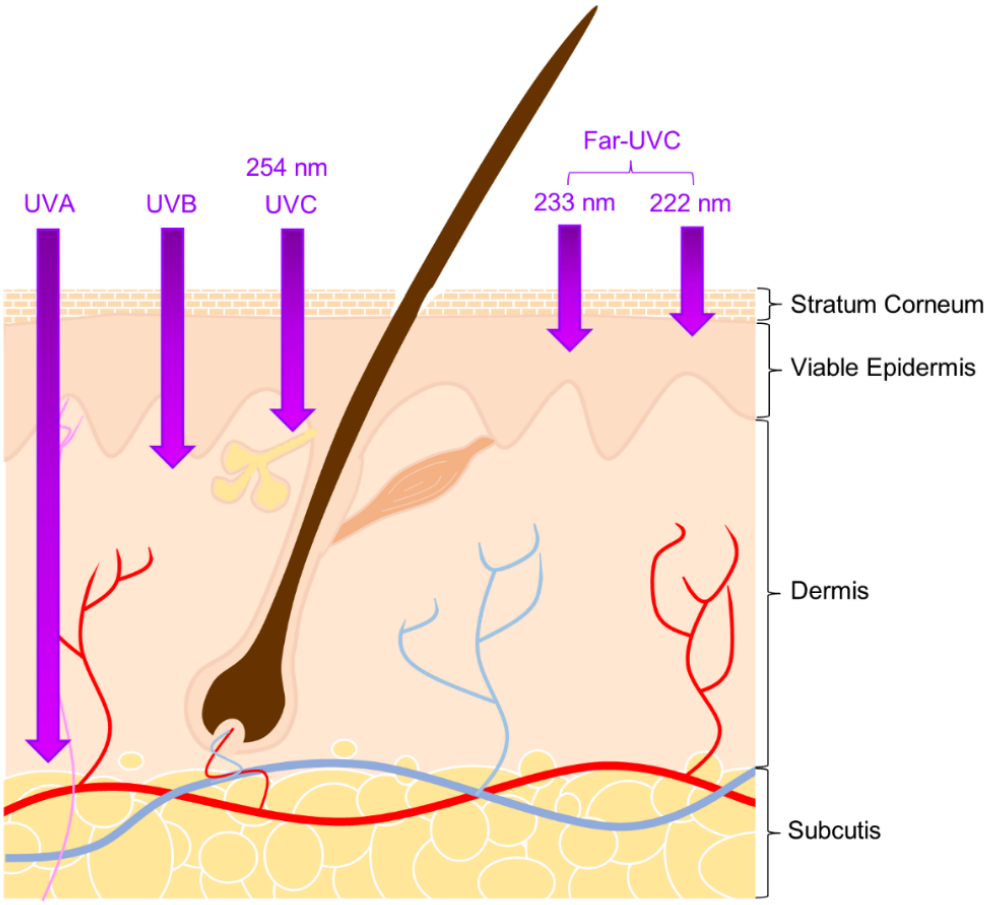

Figure 1: Schematic representation of a skin section including a pilosebaceous unit. Presentation of the skin layers stratum corneum, viable epidermis, dermis and subcutis from top to bottom. Violet arrows schematically represent the penetration depth of far-ultraviolet C (UVC) radiation (222 nm and 233 nm), UVC (254 nm) as well as UVB and UVA radiation.

1.1.2. The viable epidermis: to be targeted and protected

The viable epidermis mainly consists of keratinocytes and is built up as a layered epithelium constantly keratinizing to build the stratum corneum in a terminalization process (**Section 1.1.1.**) [11]. Further cell types are: melanocytes (melanin production, UV barrier), Merkel cells (tactile perception) and Langerhans cells (immune response) [9]. The viable part of the epidermis is composed of three layers. Each of those is characterized by a specific morphology and physiology corresponding to the stages of a mitotically driven irreversible differentiation process, which evolves from the deepest epidermal layer, the stratum basale [11, 29]. This layer harbors the stem cells from which epidermal development as well as homeostasis derive [16]. From there, the suprabasally localized layers stratum spinosum as well as stratum granulosum are formed. In the latter, tight junctions are developed in a complex polygonal network to play

a key role in the prevention of water loss [16]. A terminalization of the keratinocytes into corneocytes occurs in the stratum granulosum to form the uppermost skin layer, the stratum corneum (**Section 1.1.1.**) [11].

UVC radiation of 254 nm, which is mainly used for water and surface disinfection as well as UVB radiation are able to reach the stem cells of the stratum basale inducing DNA damage [7, 8, 30] (**Figure 1**) (see also: **Section 1.3.3.1.**). In contrast to that, 222 nm and 233 nm far-UVC radiation are already strongly absorbed in the overlying stratum corneum as simulated by Zamudio Díaz et al. [8]. Thus, radiation below 240 nm only reaches the upper layers of the epidermis, making the application of far-UVC light possible for skin disinfection purposes. On the other hand, the epidermis constitutes a gate for UVA light [30] to a certain extent ensuring the applicability of UVA light as a trigger for the release of actives from various nano-delivery systems in deeper skin parts. Nevertheless, the dose of the applied UVA light represents a key factor in risk management, since this wavelength region is known to induce irreversible oxidative stress from a certain dose threshold [31] (**Section 1.3.3.1.**).

A special role in the protection against UV radiation is attributed to melanin, a skin chromophore which is produced in the basally localized melanocytes. This skin pigment shows a higher concentration in darker skin types protecting skin cells against UV-induced DNA damage [32-36]. In contrast to that, melanin also bears photosensitizing effects when exposed to UV radiation [36]. As a response to UV exposure and the resulting DNA damage, keratinocytes produce the α-melanocyte-stimulating hormone (α-MSH) which derives from pro-opiomelanocortin (POMC) in a p53-dependent pathway. α-MSH functions as a messenger for the communication with melanocytes via the melanocortin-1 receptor (MC1R) which induces the synthesis of melanin from the amino acid tyrosine. Subsequently, the melanin is transferred via lysosome-like melanosomes to adjacent keratinocytes where it is positioned over the nucleus to form a UV-protecting cap-like structure [36, 37]. Due to its astonishingly high variety of distinctive physicochemical properties, melanin can be detected in the skin using various measurement methods. In addition to the classical histological Fontana-Masson staining [38], non-invasive methods such as the measurement of near-infrared (NIR) fluorescence [39] and Raman scattering [40], absorbance [38], reflectance measurements with confocal laser scanning microscopy [41], fluorescence lifetime measurements with 2-photon excited fluorescence lifetime microscopy [42-44] as well as determinations by electron paramagnetic resonance spectroscopy [45, 46] are feasible. In this thesis, the short fluorescence lifetime of melanin has been harnessed to visualize the distribution of the molecule in skin sections (**publication V**) (**Figure**

2) to better characterize the damage potential of antimicrobial far-UVC light in different skin types.

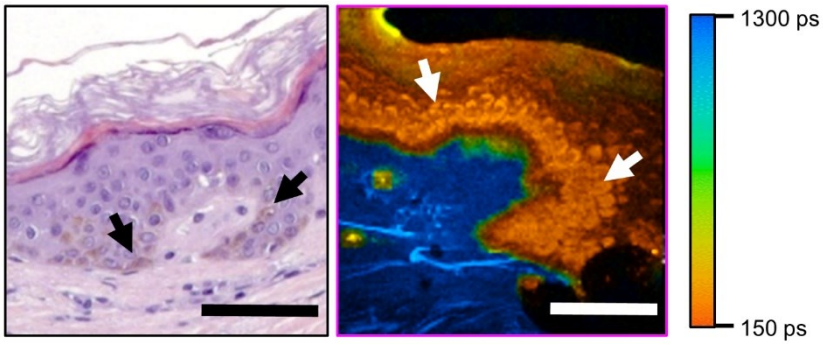

Figure 2: Hematoxylin and eosin (H&E) stain of a skin section with black arrows pointing on the basally located melanin (left) and fluorescence lifetime imaging of a same donor's skin section with white arrows showing basally located melanin (right). The mean fluorescence lifetime τ_m is depicted in false colors from orange (150 ps) to blue (1300 ps) with short lifetimes representing melanin. Scale bar: 50 µm.

1.1.3. Dermis and subcutis: the foundation

The connection between epidermis and dermis is mediated by the dermo-epidermal junction [11]. This connection is made from a structure of the lamina lucida and the underlying lamina densa, which is connected to the dermal fibers by anchoring complexes [47]. Here, the adhesion between the basal keratinocytes and the underlying extracellular matrix of the papillary dermis is mediated by so-called hemidesmosomes and focal adhesions consisting of integrins [16, 48].

The dermis is a fibrous connective tissue composed of two layers: the stratum papillare and the underlying stratum reticulare. In the stratum papillare, a fine architectural structure of nerves and blood vessels can be found (**Figure 3**). The stratum reticulare represents the basic structure of the skin consisting of interconnected collagen fiber bundles and elastic fibers that mediate the skin's tensile strength and elasticity [11, 13]. Fibroblasts (synthesis of most dermal structures), mast cells (immune response) and other tissue cells are located between these fiber structures. The so-called extracellular matrix is formed by glycosaminoglycans and proteoglycans in which the cells and fibers are embedded.

The structures of the dermis are reachable for UVA light, which can induce different effects like oxidative stress or inflammatory responses and the activation of matrix metalloproteinases leading to the degradation of collagen and elastin fibers [49].

As the lowest skin layer, the subcutis is composed of adipocytes which have the function of energy storage, thermal insulation and mechanical protection [9, 11, 13, 50]. Connective tissue septa mechanically support the adipose tissue [11]. Furthermore, the subcutis surrounds the

hair follicles, sweat glands and nerves, as well as lymphatic and blood vessel networks building an anatomical framework for these structures [9, 11, 50].

1.1.4. Hair follicles: pathogen reservoirs and drug delivery gates

1.1.4.1. Anatomy and physiology

The human hair follicle is defined as an epidermal invagination into the dermis formed from numerous mesenchymal and epithelial cell layers from a total of over 20 cell populations. It forms an anatomic unit together with the arrector pili muscle as well as the sebaceous gland [51] (**Figure 3**).

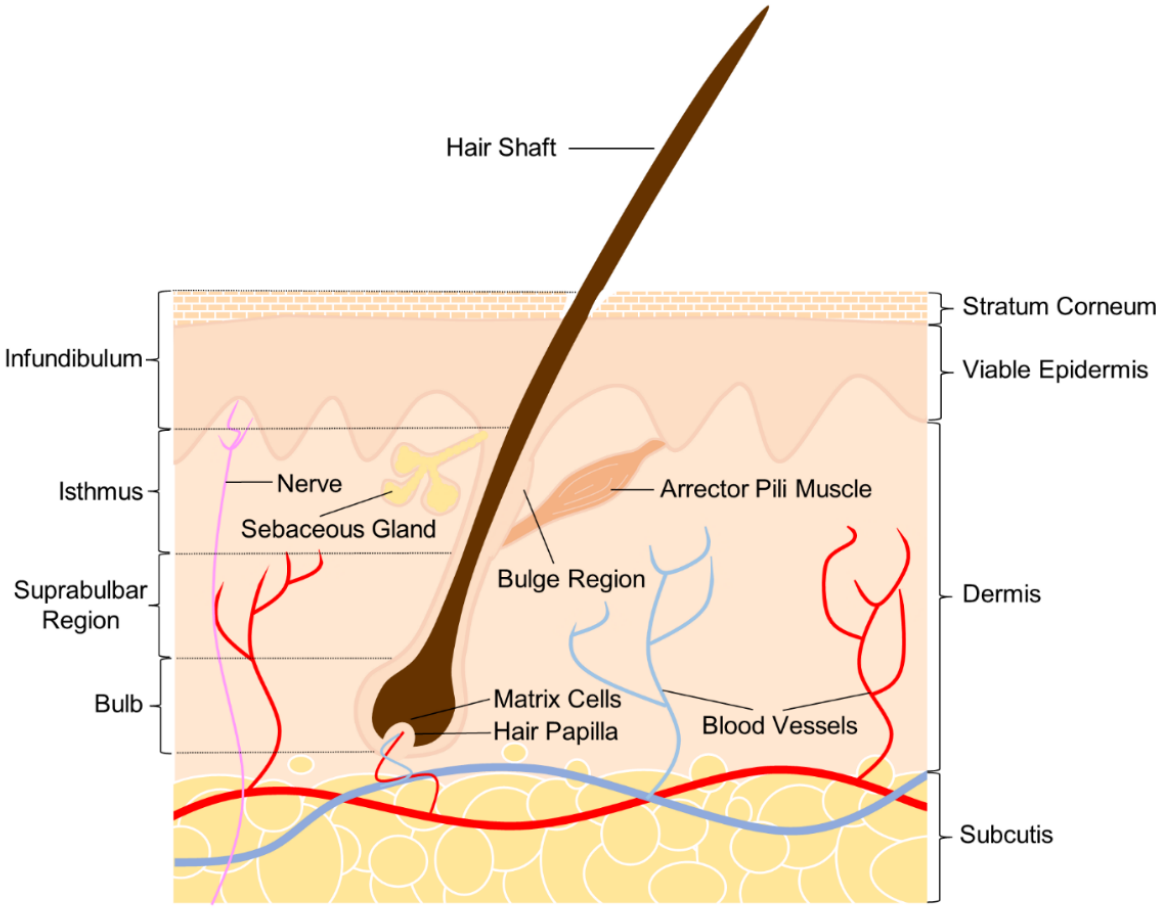

Figure 3: Schematic representation of a skin section with a pilosebaceous unit, blood vessels and nerves including anatomical designations. Partition into infundibulum, isthmus, suprabulbar region and bulb from top to bottom.

Anatomically, the hair follicle can be divided into a continuous superior portion, which does not cycle, as well as a transient portion beginning under the bulge region at the insertion site of

the arrector pili muscle, which underlies the hair cycle physiology continuously being remodelled [51-53]. The lower end of the hair follicle represents the bulb, which is associated with the mesoderm-derived dermal papilla [52, 54].

The uppermost part of the hair follicle is the infundibulum, a funnel-shaped unit between the surface of the stratum corneum and the sebaceous gland excretory duct [51]. The superior part of the infundibulum is framed by an intact epidermis. Contrary to that, epidermal differentiation is incomplete in the inferior part of the infundibulum leading to a barrier impairment and the possibility of transfollicular drug delivery [23, 51, 55]. Besides the possibility of a rapid systemic drug uptake based on the dense perifollicular vascularization, perifollicular immunological cells constitute potential targets for topical vaccination approaches [23, 55]. The sebaceous gland releases sebum into the infundibular part of the hair follicle creating an apolar environment consisting of triglycerides, squalene, sterol and wax esters, free sterols as well as fatty acids [56]. Due to its dense colonization with various microorganisms [2], the sebaceous gland and the upper third of the hair follicle constitute important targets for pre-surgical skin antisepsis [57] or the treatment of acne vulgaris [55] using nano-delivery systems. Between the sebaceous gland excretory duct and the aforementioned bulge region, the isthmus region can be found connecting to the proximal part of the infundibulum [51]. The bulge region, which represents the end of the permanent, non-cycling region, has a remarkably high capacity of epithelial and melanocytic stem cells and thus represents another target region for nano-delivery systems [52, 55]. Below this region, the stretched suprabulbar region as well as the bulb of the hair follicle can be found. The latter harbors the matrix keratinocytes as well as the follicular melanocytes [52]. From the matrix cells of the bulb up to the sebaceous gland excretory ducts the outer root sheath evolves as an epithelial part of the hair follicle expressing a large repertoire of biochemical mediators, hormones and receptors. The rigid inner root sheath consists of three keratinized layers, the Henle layer, Huxley layer, as well as the cuticle and constitutes to the longitudinal shape of a newly developing hair [51]. The only barrier in the region below the infundibulum of the hair follicle is built by tight junctions in the outer root sheath and additionally between the Henle and Huxley layer in the suprabulbar region. In the bulb region of the hair follicle those are missing, which is of importance for the substance supply from the surrounding dermal environment [58].

Hair matrix keratinocytes in the hair follicle bulb, which are attached to the highly vascularized dermal papilla, proliferate in the framework of the hair growth cycle. As a result, the inner root sheath and the hair shaft grow [51]. Evolving from hair-specific epithelial stem cells of the bulge

region and regulated by complex cell interactions of endocrine, paracrine as well as autocrine nature, the lifetime of a hair underlies three different phases [51, 52]. The growth phase (anagen), which is driven by mitosis, an apoptotic phase (catagen) as well as a resting phase (telogen) [56, 59, 60]. Within one cycle the formation of a new hair shaft is completed and the old hair is shed (exogen) [52]. The resulting hair shaft represents a fiber composed of terminally differentiated, dead keratinocytes. The surface of the hair follicle is formed by the cuticle which enwraps the inner part of the hair consisting of cortex and medulla [52]. Based on its characteristic zig-zag structure, the cuticle plays a key role in the intrafollicular transport process of nanoparticles as explained in **Section 1.1.4.2**.

It is well known that the cyclic growth process of hair results in anatomical and physiological changes influencing the follicular penetration of various substances [55]. Lademann et al. suggested a distinction between active and inactive follicles with regard to follicular penetration of externally applied substances [61]. This means that active hair follicles show sebum flow and hair growth, whereas inactive follicles are inaccessible for penetration due to a coverage with sebum and cell debris [23, 62, 63].

1.1.4.2. Targeted follicular drug delivery and skin antisepsis using responsive nano-delivery systems

After learning about the anatomical structure of the hair follicle and the physiological conditions prevailing there, the corresponding drug delivery aspects and the benefits resulting from a specific targeting will be addressed at this point. Because of the anatomical complexity of the hair follicle [52], the dense colonization of pathogens [2], and the wide variety of different hair follicle-associated diseases, it represents an important target for drug delivery [52]. Furthermore, the hair follicle constitutes a parenteral gate for topically applied therapeutics enabling their systemic and dermal availability [19]. Therefore, in addition to the commonly known intercellular and transcellular penetration pathways of therapeutics, the (trans)follicular pathway represents an important route for drug delivery [64-66]. Already in 1967, Feldmann and Maibach found that skin permeability is increased in follicle-dense areas [67] making the hair follicle a remarkable target in the context of skin penetration. The contribution of hair follicles to percutaneous absorption was further demonstrated in works of the early 1990s [68, 69]. More recently, the underlying transfollicular penetration was demonstrated by a decreased and slower absorption of actives after selectively blocking the hair follicles [70-72].

For reaching deeper parts of the hair follicles, nanoparticles are known to be well suited. Nano-delivery systems not only improve the solubility of highly hydrophobic drugs, but also ensure a controlled release of various drugs, increase their stability and lead to an increased concentration and retention at the target area [24] with an intrafollicular remanence of nanoparticles up to 10 days [73]. Generally, it can be assumed that penetration through the intact skin barrier is unlikely with particles ≥40 nm [74, 75]. Considering the molar mass of most nanoparticles, which is in the order of 10^3 kDa, the cut-off of 500 Da for intercellular skin penetration of substances as presented by Bos and Meinardi, is vastly exceeded [66]. In this context, the intercellular lipids of the stratum corneum appear to be the main barrier against nanoparticle penetration [76], with the spatial barrier based on an intercellular lipid channel width of 19 nm in the stratum corneum [17] (**Section 1.1.1.**). As shown by Patzelt et al. in an *ex vivo* porcine skin model, it is possible to selectively target different fractions of hair follicles by varying the particle size [77]. In this context, a maximum penetration depth can be achieved with particle diameters between 400 and 700 nm [77] when applied with a massage frequency of around 4 Hz [19].
It is a well-known fact that nanoparticles penetrate significantly deeper into hair follicles than non-particulate substances [5, 78]. But how actually is this effect achieved mechanistically? Applying skin massage constitutes the main driving force of follicular penetration by inducing a movement of the hair shaft (**Figure 4A**). The deposition of nanoparticles along the longitudinal axis of a hair follicles evolves from the so-called ratchet effect [79]. Based on the intrafollicular radial movement of the hair shaft, the nanoparticles are transported deeply into the hair follicle as assumed by a stochastic model of Radtke et al. [79]. Here, the zig-zag-shaped cuticula [78] of the hair plays a key role for the deposition movement representing the “ratchet”. The effect evolves its maximum efficacy at relatively low radial hair movement frequencies which are reversed by hair movements along the longitudinal axis [79].

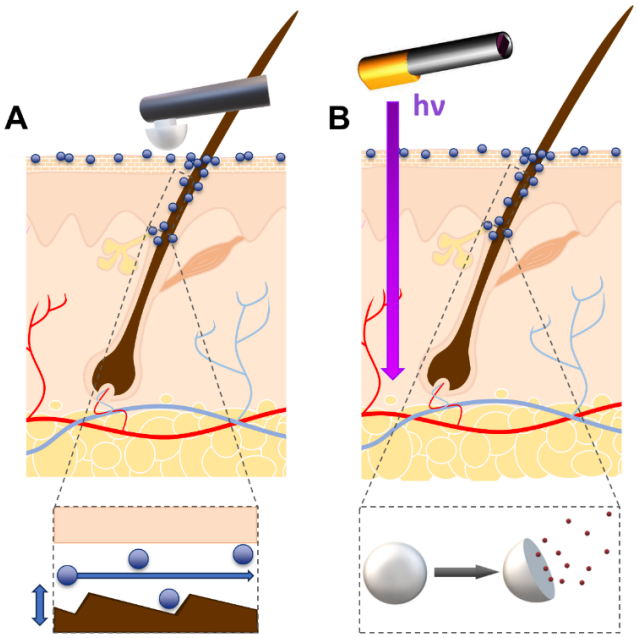

Figure 4: (**A**): Skin massage leads to a radial movement of the hair shaft. This induces an interaction of the cuticle and the nanoparticles in the framework of the ratchet effect leading to a deposition of nanoparticles towards the proximal parts of the hair follicle. (**B**): Penetration of LED-derived UVA light into the skin leads to an intrafollicular release of an active from the nanoparticles.

There is a large variety of studies today showing that active ingrendients can be successfully transported into the hair follicle using nano-delivery systems such as liposomes [56, 80-84], solid lipid nanoparticles [85], nanostars [86], nanocrystals [87, 88], several forms of spheric polymeric nanocarriers [57, 89-93] or even microspheres [60, 94, 95]. Thus, the application of nano-delivery systems for follicular drug delivery is a door opener to various therapeutic approaches [55] like follicular decolonization [96-99] or transcutaneous vaccination [75, 89, 100, 101]. Moreover targeting the stem cell-rich bulge region [81, 83] to tackle genetic disorders like various alopecia subtypes [102], or the sebaceous glands [84, 94], which are relevant in cases of acne [103], are possible areas of application [104]. Additionally, the encapsulation of different therapeutics like spironolactone [93], isotretinoin-delonix [105], minoxidil and latanoprost [106, 107], fibroblast growth factor [108], zinc pyrithione [109], flutamide [85], finasteride [110], tofacitinib [111], dexamethasone [112], retinol [90], adapalene [113], betamethasone [114], or clobetasol [115] into various nano-delivery systems showed to reduce dermal side effects while simultaneously enabling targeted follicular delivery and enhancing local efficacy.

As soon as the nanoparticles have reached the target site in the hair follicle, a controlled release of the drug can be induced by external physical, chemical, and biological stimuli or by internal stimuli such as the environmental pH value. Thus, Mak et al., were able to demonstrate the intrafollicular degradation of nanoparticles in the hair follicle by using a protease [116, 117]. Tran et al. presented an intrafollicular release of a model drug from nanocarriers based on diffusion gradients [118]. In another work, Lademann et al. presented an intrafollicular drug release from gold-loaded BSA nanoparticles via NIR irradiation [119]. Dong et al. demonstrated the possibility of a pH-induced drug release from nanoparticles [92].

UV radiation is a well suited trigger for dermal drug release since it is able to reach the dermal layers of the skin [30] and thus is supposed to reach even the deeper fractions of the hair follicles (**Figure 4B**). Nowadays, there are several options for equipping nano-delivery systems with UV responsivity [120, 121]. An effective way to establish this property is to incorporate photo-cleavable groups like the *o*-nitrobenzyl group [122-124]. These aromatic groups are known for their high photo-responsiveness (**see publications I and II**). Here, the photo-lability is based on a radical mechanism including the intramolecular benzylic hydrogen abstraction by a nitro group oxygen followed by a rearrangement and bond cleavage [125, 126].

1.2. Human skin microbiome

1.2.1. Physiological conditions

The human skin represents a colonization surface for remarkably complex microbial communities [127]. Here, microbiota are mainly located on and in the stratum corneum as well as the pilosebaceous units [2, 4, 11, 127-130]. Interestingly, a proportion of about 20% of the skin microbiome is located at a depth > 300 µm [128].
A high skin colonization can be found in areas with high moisture as well as a high density of sebaceous glands (head, forehead, chest, interdigital and axillary skin areas). In contrast to that, significantly less bacteria can be isolated from dry and sebum-poor areas like the extremities, palms and plants or the abdomen [128, 130].
However, not only quantitative differences are associated with skin area, but also qualitative differences of the local microbiome, resulting from locally varying physiological parameters [127]. Lipophilic *Propionibacterium* species can be isolated from sebaceous skin areas such as the forehead, chest and back. In contrast to that, coagulase-negative staphylococci such as *Staphylococcus epidermidis* and *hominis* but also *Corynebacterium* species show a high abundance in moist skin areas like the armpit, the inguinal and gluteal crease or the sole of the foot [11, 127, 128, 130].

It is known that cutaneous invaginations and appendages like the pilosebaceous units are associated with specific local microbial communities due to the relatively anoxic and lipophilic environment [130]. In a 1970 paper, Montes et al. already described an increased colonization of hair follicles compared to the skin surface [131]. As shown later by Lange-Asschenfeldt et al., the pilosebaceous unit represents a densely populated bacterial reservoir comprising about 25% of all bacteria isolated from skin [2]. Here, microorganisms including bacteria like *Propionibacterium* ssp., *Staphylococcus* ssp., *Corynebacterium* ssp. and micrococci as well as fungi like *Malassezia* ssp. [127, 129] can be found. Furthermore, hair follicles potentially represent a habitat for arthropods such as *Demodex folliculorum* and *Demodex brevis* [130]. The longitudinal intrafollicular distribution of microorganisms depends on local ambient factors in the individual sections. Malassezia furfur and micrococci are primarily localized in the upper infundibular region. Below that, coryneforms can be found [11, 128].

1.2.2. Pathological conditions

1.2.2.1. Surgical site infections (SSI)

SSIs are known to occur within 30 days postoperatively or within one year of implant placement and can be classified into three subtypes: superficial incisional infections (skin level), deep incisional infections (muscular level) and visceral infections (organ level) [132, 133]. After representing the third most common nosocomial infection in German acute care hospitals in 1995 with a 16% incidence, SSI became the most common nosocomial infection in 2011 with over 24% incidence [128, 134, 135]. In the period 2010–2016 the SSI rate in Germany was 4.9% accompanied by median case costs for the SSI group of €19,008 compared to €9,040 for the control group according to a retrospective analysis by Eckmann et al. [136]. The risk of developing SSI is significantly determined by the site of surgery, the endogenous microbiome and its pathogenicity, exogenous pathogen contamination and surgical-technical factors as well as the age of the patient and preexisting infection-promoting factors [132, 137, 138].
Among the latter are lifestyle-related factors and morbidities including preoperative malnutrition, alcohol consumption, smoking, obesity, anemia, diabetes mellitus, HIV-associated immune suppression, and preexisting infections in other body regions [132, 137, 139]. Pathogens causing SSI originate from the patient's endogenous skin and mucosa microbiome with a proportion of 90% of all cases surveyed in a 2-year period in Germany with an incidence of 4.7% [1, 132-134]. Due to the variability of pathogens colonizing the skin surface depending on the local environmental parameters of the skin (**Section 1.2.1.**), the spectrum of pathogens involved in the etiology of SSI varies depending on the location of the surgical site. The most common pathogens isolated from SSI are *Staphylococcus* ssp. such as *Staphylococccus aureus* and coagulase-negative staphylococci as well as *Enterococcus* spp. (gram-negative cocci) [133]. Furthermore, gram-negative bacteria, such as *Escherichia coli*, *Enterobacter* spp., *Klebsiella* spp. and *Pseudomonas aeruginosa* are known to be SSI-associated [135]. In addition, more and more cases are due to typical antibiotic-resistant nosocomial pathogens such as methicillin-resistant *Staphylococcus aureus* (MRSA) or *Candida albicans* [132, 133].

After the incision of the patients skin in the framework of a surgical intervention, the risk of contamination of the surgical site is given [133]. Thus, preoperative skin antisepsis of the region relevant to surgery is a mandatory measure [132] and should be executed within the framework of a moving application of the antiseptic for 30 s with a subsequent wetting time of 1.5 min [140]. The improvement of deep skin disinfection by targeted use of NCs for the antiseptics' transport into and their subsequent controlled release in the hair follicles represents an important part of this thesis which was covered in **publication II**.

1.2.2.2. Wounds and wound infections

According to Lazarus et al., a wound is defined as a disruption of normal anatomic structure and function [141] which can result from internally or externally induced pathologic processes. A distinction can be made between acute and chronic wounds (pressure ulcers, diabetic ulcers, venous ulcers and arterial insufficiency ulcers) [142]. In the first case, there is a reestablishment of the anatomical structures and function over time, while in the latter case this process is incomplete or absent. In the framework of this healing process, a number of biological reactions occur including coagulation and haemostasis, inflammation as well as proliferation, the reestablishment of a connective tissue matrix, and re-epithelialization [141, 143].
In order to initiate an unrestricted wound healing process, not only the antiseptic treatment of critically colonized and infected wounds but also the preventive treatment of wounds at risk of infection is mandatory [144]. Bacteria cultivated from infected and chronic wounds in most cases are *Staphylococcus* ssp. such as MRSA, but also *Pseudomonas aeruginosa* [145, 146]. In addition to bacteria, various fungal strains like *Cladosporidium herbarum, Candida albicans, Trichosporon* and *Rodhosporidum* could also be cultivated from non-healing wounds. [146]. A major economic and health burden associated with a vastly increased mortality rate proceeds from chronic wounds [142, 147]. The prevalence of chronic wounds is up to 2.21 per 1000 population [148] along with the expectation of an internationally increasing incidence [149]. The application of far-UVC light for the treatment of wounds (**publication IV**) is a promising alternative approach because of the vast increase of bacterial resistances caused by antibiotic treatment [150] or treatment with microbiostatic antiseptics like chlorhexidine gluconate quaternary ammonium compounds or silver ions [144, 151].

1.3. State of the art: drug- and radiation-guided skin decolonization

1.3.1. The hair follicle as a target for enhanced skin antisepsis: smart treatment options using nano-delivery systems for deep skin decolonization

Penetration of liquid substances into the deeper parts of the hair follicle is not possible, which makes these parts a protected reservoir for microorganisms. In a study by Selwyn et al. from 1972 up to 20% of the total skin flora remained hidden from conventional antiseptics being located in the hair follicles and skin furrows [4]. Within 5 hours after antiseptic treatment of the skin, a complete recolonization occurred.
From this reservoir microorganisms constantly return to the surface of the skin via the sebum flow. Due to this recontamination process, the risk of developing SSI [1] rises. Targeting hair

follicles and sebaceous glands using nano-delivery systems is therefore a conceivable approach to decolonize hair follicles and prevent intraoperative recontamination of the skin surface [57]. Previously published research has shown that decontamination of the skin at depth, including hair follicles, may be a promising approach for improved skin antisepsis by preventing recolonization of the skin. Lbouttoune et al. demonstrated that NCs loaded with the antiseptic chlorhexidine applied *ex vivo* to porcine skin were detected in hair follicles, resulting in sustained release of the antiseptic. Furthermore, NCs were proven to mediate an increased and prolonged contact to the targeted pathogen *Staphylococcus epidermidis*, the skin surface and the hair follicles [96-98]. In addition, polihexanide in liposomes is known to result in less recolonization of the skin surface after application than in an aqueous control solution. [99]. On the other hand, far-UVC light could be applied repetitively for long-term skin decolonization, which is the subject of the following chapters.

1.3.2. UV radiation and UV LED systems for skin surface skin decolonization

Discovered in 1801 by the German physicist Johann Wilhelm Ritter [152], UV light belongs to the electromagnetic radiation spectrum of 10–400 nm [153]. UV radiation can be further categorized into vacuum UV (10-200 nm), UVC (200-290 nm), UVB (290-320 nm), and UVA (320-400 nm) [153]. On the one hand, UV exposure potentially bears high risks of skin damage and the development of skin cancer [36, 49, 154, 155], but on the other hand UV radiation can also be used for curative purposes (UVA) [156, 157] or skin surface decontamination without reaching the epidermal stem cells (far-UVC) [6] (**Section 1.3.3.**). Due to its broad therapeutic applicability, UV is provided by various lamp systems for clinical use [158]. Furthermore, UVA light is able to reach the dermis and hair follicles [30] (**Section 1.1.2.**), where it can be used to trigger intrafollicular drug release from NCs (**publications I and II**).

LEDs are modern light sources that provide UV light in different wavelengths. LED systems are used for the conversion of electric current into incoherent electromagnetic radiation. They consist of semiconductor materials with a so-called p-n junction, which is formed by doping with chemical elements of the third and fifth main group [153, 159]. III-nitride based semiconductor crystals, such as gallium nitride (GaN) [160], indium gallium nitride (InGaN) [161], aluminum gallium nitride (AlGaN) [162-165], and aluminum gallium indium nitride (AlGaInN) [166], are used for the emission of various wavelengths within the UV radiation region. Depending on the III-nitride heterostructure composition, the wavelength of the LED is tunable [153, 159]. Due to their compact design and stable power characteristics, UV LEDs can be mounted on a wide range of instrument types and are therefore ideal for a variety of medical applications

[158]. Moreover, UV LEDs are known for their narrow emission spectrum [167] and reduced energy consumption [168].

Recently, Glaab et al. presented a 233 nm far-UVC LED system based on AlGaN semiconductor heterostructures [6, 164, 169], which constitutes an interesting alternative to the so far common 207 nm [170, 171] and 222 nm Kr-Cl excimer lamps [171-180] for skin and wound decontamination. This alternative entails a compact design and the avoidance of ozone formation. As applied in **publications I and II**, GaN-based LEDs emit at 365 nm, while AlGaN-based LEDs can be used for the emission in shorter wavelength regions like far-UVC (**publications III, IV, and V**).

1.3.3. The impact of UV radiation on the skin microbiome and epidermal cells

1.3.3.1. UV-induced epidermal DNA damage

With the naked eye, UV-related skin damage can be recognized by the formation of erythema and tanning. The first effect is based on a UVB-induced cascade of cytokines as well as vasoactive and neuroactive mediators which produce inflammation in a complex interplay leading to a “sunburn” [154]. When cell damage in this response exceeds a certain threshold, cells activate apoptotic pathways that lead to controlled cell death characterized by pyknosis of the cell nuclei, also known as sunburn cells. [154]. Tanning results from a UVB-induced p53-associated signaling cascade that leads to the synthesis and transport of melanin from melanocytes to keratinocytes, which is also associated with cell cycle arrest, apoptosis, and DNA repair (**Section 1.1.2.**) [36, 154]. However, damage can occur at the subcellular level even after exposure to small doses of UV radiation before it becomes clinically visible (suberythemal doses). On this level an important acute effect is the formation of DNA lesions [36, 37]. While UVB and UVC are directly absorbed by DNA and thus modify the structure of nucleic bases, UVA generates reactive oxygen species such as superoxide anion, hydrogen peroxide, and singlet oxygen [36, 181]. A well-known oxidation-derived mutagenic photolesion in DNA, predominantly produced by UVA is 8-hydroxy-2′-deoxyguanine [154].

The human body is not exposed to UVC radiation under natural conditions, as it is absorbed by the atmosphere [36]. Nevertheless, there are numerous artificial sources of radiation that emit UVC and are used, for example, for drinking water treatment or surface disinfection, such as 254 nm low-pressure mercury lamps. These, on the other hand, are not suitable for use on the human skin because their high dermal penetration depth leads to DNA damage in the basal

cell layer of the skin [7]. Here, the nucleic acids of the skin cells absorb UVC light resulting in photo-induced dimerization of consecutive pyrimidine bases (**Figure 5**) [7]. This leads to the formation of two prominent types of highly mutagenic DNA lesions which are known as cyclobutane pyrimidine dimers (CPDs) and pyrimidine (6-4) pyrimidone photoproducts (6-4PPs).

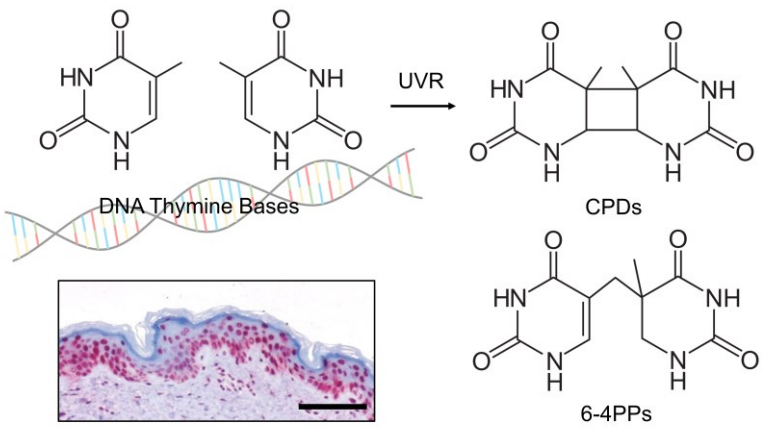

Figure 5: Formation of the photo lesions cyclobutane pyrimidine dimers (CPDs) and pyrimidine (6-4) pyrimidone photoproducts (6-4PPs) from two consecutive thymine bases in DNA by absorption of UV radiation (UVR). An exemplary skin section immunohistochemically stained for CPDs shows CPD-positive cell nuclei in dark red (scale bar: 100 µm).

Both types of photolesions also develop at suberythemal doses of UVB, although the initial abundance of CPDs is generally higher compared to 6-4PPs and is also removed more slowly [7, 36, 182]. UVA, on the other hand, is known to mainly produce CPDs [183]. These are implicated in the process of photocarcinogenesis because they can lead to gene mutations in key genes encoding cell cycle regulators such as the tumor suppressor protein p53 [36].

Interestingly, as compared to UVC radiation between 250 and 280 nm, a large proportion of far-UVC light ($\lambda < 240$ nm) is absorbed by the uppermost layer of the skin, the stratum corneum [8, 170]. This results in a significantly reduced penetration depth of the far-UVC light, leaving the stem cells of the epidermal basal layer unaffected, making it potentially suitable for skin decontamination. In numerous publications the skin safety of 222 nm far-UVC was demonstrated [184]. Thus, studies showed that 222 nm far-UVC radiation was significantly less harmful than 254 nm radiation in an *in vivo* mouse model [172, 173], which can be attributed to the higher absorption of 254 nm radiation by nucleic acids (absorption maximum at 260 nm). Long-term skin damage was neither induced by 222 nm far-UVC radiation in a cancer-prone mouse model, nor after a single radiation dose of 500 mJ/cm^2 in humans [176, 178, 179]. Interestingly, a recent study by Tavares et al. [181] further showed that exposure of 3D skin and mouse models led to fewer alterations on molecular, cellular, and tissue level than 254 nm.
Building on this knowledge, the world's first risk assessment study on 233 nm far-UVC light was carried out in **publication III**.

1.3.3.2. Interaction of far-UVC radiation and pathogens

A highly debated approach for antiseptic treatment of the skin is the application of far-UVC radiation since it might constitute an interesting physical alternative for skin antisepsis. Even though the number of studies on microbial resistance formation is not yet pronounced, it has already been shown that after the exposure of several multidrug-resistant bacteria including MRSA with UVC radiation, no UV resistance after 25 serial exposures *in vitro* could be observed [185]. Contrary to that, it must be considered that MRSA have evolved several antibiotic resistance mechanisms, which include a set of DNA repair mechanisms as well as mechanisms for detoxification of free radicals [7, 186]. These mechanisms could also increase tolerance to UV radiation [7].

However, how does the inactivation of microorganisms by UVC radiation work?
As in the epidermal cells, the inactivation is based on the strong absorption of UVC by the nucleic acids of microorganisms (peak germicidal wavelength of 262 nm) [187] and the resulting induction of DNA- or RNA-lesions [187] deriving from photo-induced dimerization of consecutive pyrimidine bases [7], which include CPDs and 6-4PPs [187] (**Section 1.3.3.1.**). The incorporation of such lesions into the genome of the pathogens leads to the termination of transcription, which results in an inhibition of replication and cell death [187]. Furthermore far-UVC light is strongly absorbed by proteins leading to oxidation and cross-linking [181].
Thus, a significant germicidal effect on bacteria, yeast and viruses of 222 nm far-UVC radiation is known [175]. Bactericidal effects on MRSA were further demonstrated on mouse skin *in vivo* [172, 173], as well as for different bacteria in gluteal pressure-induced ulcera of patients [188]. For 233 nm far-UVC, comparable effects are known from *in vitro* studies. Radiation of this wavelength not only leads to an inactivation of MRSA on blood agar plates as well as germ carriers at a dose of 40 mJ/cm^2 [6, 7], but also eradicates the fungal strains *C. albicans* and *C. parapsilosis* at an efficiency comparable to 222 nm irradiation [189].

References

[1] M. Ulmer, J. Lademann, A. Patzelt, F. Knorr, A. Kramer, T. Koburger, O. Assadian, G. Daeschlein, B. Lange-Asschenfeldt, New strategies for preoperative skin antisepsis, Skin Pharmacol Physiol 27(6) (2014) 283-292.

[2] B. Lange-Asschenfeldt, D. Marenbach, C. Lang, A. Patzelt, M. Ulrich, A. Maltusch, D. Terhorst, E. Stockfleth, W. Sterry, J. Lademann, Distribution of bacteria in the epidermal layers and hair follicles of the human skin, Skin Pharmacol Physiol 24(6) (2011) 305-311.

[3] D. Dörfel, M. Maiwald, G. Daeschlein, G. Müller, R. Hudek, O. Assadian, G. Kampf, T. Kohlmann, J.C. Harnoss, A. Kramer, Comparison of the antimicrobial efficacy of povidone-iodine-alcohol versus chlorhexidine-alcohol for surgical skin preparation on the aerobic and anaerobic skin flora of the shoulder region, Antimicrob Resist Infect Control 10(1) (2021) 17.

[4] S. Selwyn, H. Ellis, Skin Bacteria and Skin Disinfection Reconsidered, Br Med J 1(5793) (1972) 136-140.

[5] J. Lademann, H. Richter, A. Teichmann, N. Otberg, U. Blume-Peytavi, J. Luengo, B. Weiss, U.F. Schaefer, C.M. Lehr, R. Wepf, W. Sterry, Nanoparticles--an efficient carrier for drug delivery into the hair follicles, Eur J Pharm Biopharm 66(2) (2007) 159-164.

[6] J. Glaab, N. Lobo-Ploch, H.K. Cho, T. Filler, H. Gundlach, M. Guttmann, S. Hagedorn, S.B. Lohan, F. Mehnke, J. Schleusener, C. Sicher, L. Sulmoni, T. Wernicke, L. Wittenbecher, U. Woggon, P. Zwicker, A. Kramer, M.C. Meinke, M. Kneissl, M. Weyers, U. Winterwerber, S. Einfeldt, Skin tolerant inactivation of multiresistant pathogens using far-UVC LEDs, Sci Rep 11(1) (2021) 14647.

[7] P. Zwicker, J. Schleusener, S.B. Lohan, L. Busch, C. Sicher, S. Einfeldt, M. Kneissl, A.A. Kuhl, C.M. Keck, C. Witzel, A. Kramer, M.C. Meinke, Application of 233 nm far-UVC LEDs for eradication of MRSA and MSSA and risk assessment on skin models, Sci Rep 12(1) (2022) 2587.

[8] D.F. Zamudio Díaz, A.L. Klein, M. Guttmann, P. Zwicker, L. Busch, M. Kröger, H. Klose, S. Rohn, J. Schleusener, M.C. Meinke, Skin optical properties from 200–300 nm support far-UVC skin safety in vivo, J Photochem Photobiol B 247 (2023) 112784.

[9] M. Gupta, U. Agrawal, S.P. Vyas, Nanocarrier-based topical drug delivery for the treatment of skin diseases, Expert Opin Drug Deliv 9(7) (2012) 783-804.

[10] J.P. Sundberg, L.B. Nanney, P. Fleckman, L.E. King, Skin and Adnexa, in: P.M. Treuting, S.M. Dintzis (Eds.), Comparative Anatomy and Histology, Elsevier, Amsterdam, 2012, pp. 433-455.

[11] P. Fritsch, Dermatologie und Venerologie für das Studium, Springer, Heidelberg, 2009.

[12] E. Proksch, J.M. Brandner, J.M. Jensen, The skin: an indispensable barrier, Exp Dermatol 17(12) (2008) 1063-1072.

[13] G.K. Menon, A.M. Kligman, Barrier functions of human skin: a holistic view, Skin Pharmacol Physiol 22(4) (2009) 178-189.

[14] J. Hadgraft, Modulation of the barrier function of the skin, Skin Pharmacol Appl Skin Physiol 14 Suppl 1 (2001) 72-81.

[15] P.M. Elias, Epidermal lipids, barrier function, and desquamation, J Invest Dermatol 80(1 Suppl) (1983) 44s-49s.

[16] R.S. Moreci, T. Lechler, Epidermal structure and differentiation, Curr Biol 30(4) (2020) R144-R149.

[17] D. van der Merwe, J.D. Brooks, R. Gehring, R.E. Baynes, N.A. Monteiro-Riviere, J.E. Riviere, A physiologically based pharmacokinetic model of organophosphate dermal absorption, Toxicol Sci 89(1) (2006) 188-204.

[18] T.W. Prow, J.E. Grice, L.L. Lin, R. Faye, M. Butler, W. Becker, E.M. Wurm, C. Yoong, T.A. Robertson, H.P. Soyer, M.S. Roberts, Nanoparticles and microparticles for skin drug delivery, Adv Drug Deliv Rev 63(6) (2011) 470-491.

[19] L. Busch, Y. Keziban, L. Dähne, C.M. Keck, M.C. Meinke, J. Lademann, A. Patzelt, The impact of skin massage frequency on the intrafollicular transport of silica nanoparticles: Validation of the ratchet effect on an ex vivo porcine skin model, Eur J Pharm Biopharm 158 (2021) 266-272.

[20] M. Machado, T.M. Salgado, J. Hadgraft, M.E. Lane, The relationship between transepidermal water loss and skin permeability, Int J Pharm 384(1-2) (2010) 73-77.

[21] D.A. Schwindt, K.P. Wilhelm, H.I. Maibach, Water diffusion characteristics of human stratum corneum at different anatomical sites in vivo, J Invest Dermatol 111(3) (1998) 385-389.

[22] Y.N. Kalia, F. Pirot, R.H. Guy, Homogeneous transport in a heterogeneous membrane: water diffusion across human stratum corneum in vivo, Biophys J 71(5) (1996) 2692-2700.

[23] A. Patzelt, J. Lademann, Drug delivery to hair follicles, Expert Opin Drug Deliv 10(6) (2013) 787-797.

[24] R. Goyal, L.K. Macri, H.M. Kaplan, J. Kohn, Nanoparticles and nanofibers for topical drug delivery, J Control Release 240 (2016) 77-92.

[25] J. Lademann, U. Jacobi, C. Surber, H.J. Weigmann, J.W. Fluhr, The tape stripping procedure--evaluation of some critical parameters, Eur J Pharm Biopharm 72(2) (2009) 317-323.

[26] M. Breternitz, M. Flach, J. Prassler, P. Elsner, J.W. Fluhr, Acute barrier disruption by adhesive tapes is influenced by pressure, time and anatomical location: integrity and cohesion assessed by sequential tape stripping. A randomized, controlled study, Br J Dermatol 156(2) (2007) 231-240.

[27] J.D. Bos, M.M. Meinardi, The 500 Dalton rule for the skin penetration of chemical compounds and drugs, Exp Dermatol 9(3) (2000) 165-169.

[28] L. Busch, M. Kröger, J. Schleusener, A.L. Klein, S.B. Lohan, M. Guttmann, C.M. Keck, M.C. Meinke, Evaluation of DNA lesions and radicals generated by a 233 nm far-UVC LED in superficial ex vivo skin wounds, J Photochem Photobiol B 245 (2023) 112757.

[29] B. Liu, F. Zhu, X. Xia, E. Park, Y. Hu, A tale of terminal differentiation: IKKalpha, the master keratinocyte regulator, Cell Cycle 8(4) (2009) 527-531.

[30] M. Meinhardt, R. Krebs, A. Anders, U. Heinrich, H. Tronnier, Wavelength-dependent penetration depths of ultraviolet radiation in human skin, J Biomed Opt 13(4) (2008) 044030.

[31] S.B. Lohan, D. Ivanov, N. Schuler, B. Berger, L. Zastrow, J. Lademann, M.C. Meinke, Switching from healthy to unhealthy oxidative stress - does the radical type can be used as an indicator?, Free Radic Biol Med 162 (2021) 401-411.

[32] S. Del Bino, J. Sok, E. Bessac, F. Bernerd, Relationship between skin response to ultraviolet exposure and skin color type, Pigment Cell Res 19(6) (2006) 606-614.

[33] D. Fajuyigbe, S.M. Lwin, B.L. Diffey, R. Baker, D.J. Tobin, R.P.E. Sarkany, A.R. Young, Melanin distribution in human epidermis affords localized protection against DNA photodamage and concurs with skin cancer incidence difference in extreme phototypes, FASEB J 32(7) (2018) 3700-3706.

[34] Y. Yamaguchi, K. Takahashi, B.Z. Zmudzka, A. Kornhauser, S.A. Miller, T. Tadokoro, W. Berens, J.Z. Beer, V.J. Hearing, Human skin responses to UV radiation: pigment in the upper epidermis protects against DNA damage in the lower epidermis and facilitates apoptosis, FASEB J 20(9) (2006) 1486-1488.

[35] T. Tadokoro, N. Kobayashi, B.Z. Zmudzka, S. Ito, K. Wakamatsu, Y. Yamaguchi, K.S. Korossy, S.A. Miller, J.Z. Beer, V.J. Hearing, UV-induced DNA damage and melanin content in human skin differing in racial/ethnic origin, FASEB J 17(9) (2003) 1177-1179.

[36] M. Brenner, V.J. Hearing, The protective role of melanin against UV damage in human skin, Photochem Photobiol 84(3) (2008) 539-549.

[37] J.Y. Lin, D.E. Fisher, Melanocyte biology and skin pigmentation, Nature 445(7130) (2007) 843-850.

[38] S. Del Bino, S. Ito, J. Sok, Y. Nakanishi, P. Bastien, K. Wakamatsu, F. Bernerd, Chemical analysis of constitutive pigmentation of human epidermis reveals constant eumelanin to pheomelanin ratio, Pigment Cell Melanoma Res 28(6) (2015) 707-717.

[39] S. Kalia, J. Zhao, H. Zeng, D. McLean, N. Kollias, H. Lui, Melanin quantification by in vitro and in vivo analysis of near-infrared fluorescence, Pigment Cell Melanoma Res 31(1) (2018) 31-38.

[40] B.P. Yakimov, E.A. Shirshin, J. Schleusener, A.S. Allenova, V.V. Fadeev, M.E. Darvin, Melanin distribution from the dermal-epidermal junction to the stratum corneum: non-invasive in vivo assessment by fluorescence and Raman microspectroscopy, Sci Rep 10(1) (2020) 14374.

[41] T. Yamashita, T. Kuwahara, S. Gonzalez, M. Takahashi, Non-invasive visualization of melanin and melanocytes by reflectance-mode confocal microscopy, J Invest Dermatol 124(1) (2005) 235-240.

[42] A.M. Pena, E. Decencière, S. Brizion, P. Sextius, S. Koudoro, T. Baldeweck, E. Tancrède-Bohin, In vivo melanin 3D quantification and z-epidermal distribution by multiphoton FLIM, phasor and Pseudo-FLIM analyses, Sci Rep 12(1) (2022) 1642.

[43] A.M. Pena, T. Baldeweck, E. Decenciére, S. Koudoro, S. Victorin, E. Raynaud, B. Ngo, P. Bastien, S. Brizion, E. Tancrède-Bohin, In vivo multiphoton multiparametric 3D quantification of human skin aging on forearm and face, Sci Rep 12(1) (2022) 14863.

[44] Y. Dancik, A. Favre, C.J. Loy, A.V. Zvyagin, M.S. Roberts, Use of multiphoton tomography and fluorescence lifetime imaging to investigate skin pigmentation in vivo, J Biomed Opt 18(2) (2013) 26022.

[45] E. Cesareo, L. Korkina, G. D'Errico, G. Vitiello, M.S. Aguzzi, F. Passarelli, J.Z. Pedersen, A. Facchiano, An Endogenous Electron Spin Resonance (ESR) signal discriminates nevi from melanomas in human specimens: a step forward in its diagnostic application, PLoS One 7(11) (2012) e48849.

[46] L. Mignion, C.M. Desmet, E. Harkemanne, I. Tromme, N. Joudiou, M. Wehbi, J.F. Baurain, B. Gallez, Noninvasive detection of the endogenous free radical melanin in human skin melanomas using electron paramagnetic resonance (EPR), Free Radic Biol Med 190 (2022) 226-233.

[47] E. Roig-Rosello, P. Rousselle, The Human Epidermal Basement Membrane: A Shaped and Cell Instructive Platform That Aging Slowly Alters, Biomolecules 10(12) (2020) 1607.

[48] J.R. McMillan, M. Akiyama, H. Shimizu, Epidermal basement membrane zone components: ultrastructural distribution and molecular interactions, J Dermatol Sci 31(3) (2003) 169-177.

[49] P.W. Wang, Y.C. Hung, T.Y. Lin, J.Y. Fang, P.M. Yang, M.H. Chen, T.L. Pan, Comparison of the Biological Impact of UVA and UVB upon the Skin with Functional Proteomics and Immunohistochemistry, Antioxidants (Basel) 8(12) (2019) 569.

[50] R.K. Zwick, C.F. Guerrero-Juarez, V. Horsley, M.V. Plikus, Anatomical, Physiological, and Functional Diversity of Adipose Tissue, Cell Metab 27(1) (2018) 68-83.

[51] A. Vogt, K.J. McElwee, U. Blume-Peytavi, Biology of the Hair Follicle, in: U. Blume-Peytavi, A. Tosti, D.A. Whiting, R.M. Trüeb (Eds.), Hair Growth and Disorders, Springer, Berlin Heidelberg, 2008, pp. 1-22.

[52] M.R. Schneider, R. Schmidt-Ullrich, R. Paus, The hair follicle as a dynamic miniorgan, Curr Biol 19(3) (2009) R132-142.

[53] A. Patzelt, F. Knorr, U. Blume-Peytavi, W. Sterry, J. Lademann, Hair follicles, their disorders and their opportunities, Drug Discovery Today: Disease Mechanisms 5(2) (2008) e173-e181.

[54] V.A. Randall, The Endocrine Control of the Hair Follicle, in: U. Blume-Peytavi, A. Tosti, D.A. Whiting, R.M. Trüeb (Eds.), Hair Growth and Disorders, Springer, Berlin Heidelberg, 2008, pp. 23-39.

[55] A. Patzelt, J. Lademann, Recent advances in follicular drug delivery of nanoparticles, Expert Opin Drug Deliv 17(1) (2020) 49-60.

[56] A.C. Lauer, C. Ramachandran, L.M. Lieb, S. Niemiec, N.D. Weiner, Targeted delivery to the pilosebaceous unit via liposomes, Adv Drug Deliv Rev 18(3) (1996) 311-324.

[57] L. Busch, A.M. Hanuschik, Y. Avlasevich, K. Darm, E.F. Hochheiser, C. Kohler, E.A. Idelevich, K. Becker, P. Rotsch, K. Landfester, M.E. Darvin, M.C. Meinke, C.M. Keck, A. Kramer, P. Zwicker, Advanced Skin Antisepsis: Application of UVA-Cleavable Hydroxyethyl Starch Nanocapsules for Improved Eradication of Hair Follicle-Associated Microorganisms, Pharmaceutics 15(2) (2023) 602.

[58] C. Mathes, J.M. Brandner, M. Laue, S.S. Raesch, S. Hansen, A.V. Failla, S. Vidal, I. Moll, U.F. Schaefer, C.M. Lehr, Tight junctions form a barrier in porcine hair follicles, Eur J Cell Biol 95(2) (2016) 89-99.

[59] R. Paus, G. Cotsarelis, The biology of hair follicles, N Engl J Med 341(7) (1999) 491-497.

[60] H. Wosicka, K. Cal, Targeting to the hair follicles: current status and potential, J Dermatol Sci 57(2) (2010) 83-89.

[61] J. Lademann, N. Otberg, H. Richter, H.J. Weigmann, U. Lindemann, H. Schaefer, W. Sterry, Investigation of follicular penetration of topically applied substances, Skin Pharmacol Appl Skin Physiol 14 Suppl 1 (2001) 17-22.

[62] F. Knorr, J. Lademann, A. Patzelt, W. Sterry, U. Blume-Peytavi, A. Vogt, Follicular transport route--research progress and future perspectives, Eur J Pharm Biopharm 71(2) (2009) 173-180.

[63] U. Blume-Peytavi, A. Vogt, Human hair follicle: reservoir function and selective targeting, Br J Dermatol 165 Suppl 2 (2011) 13-17.

[64] H. Schaefer, J. Lademann, The role of follicular penetration. A differential view, Skin Pharmacol Appl Skin Physiol 14 Suppl 1 (2001) 23-27.

[65] F. Hueber, H. Schaefer, J. Wepierre, Role of transepidermal and transfollicular routes in percutaneous absorption of steroids: in vitro studies on human skin, Skin Pharmacol 7(5) (1994) 237-244.

[66] M. Schneider, F. Stracke, S. Hansen, U.F. Schaefer, Nanoparticles and their interactions with the dermal barrier, Dermatoendocrinol 1(4) (2009) 197-206.

[67] R.J. Feldmann, H.I. Maibach, Regional variation in percutaneous penetration of 14C cortisol in man, J Invest Dermatol 48(2) (1967) 181-183.

[68] F. Hueber, J. Wepierre, H. Schaefer, Role of transepidermal and transfollicular routes in percutaneous absorption of hydrocortisone and testosterone: in vivo study in the hairless rat, Skin Pharmacol 5(2) (1992) 99-107.

[69] B. Illel, H. Schaefer, J. Wepierre, O. Doucet, Follicles play an important role in percutaneous absorption, J Pharm Sci 80(5) (1991) 424-427.

[70] N. Otberg, A. Teichmann, U. Rasuljev, R. Sinkgraven, W. Sterry, J. Lademann, Follicular penetration of topically applied caffeine via a shampoo formulation, Skin Pharmacol Physiol 20(4) (2007) 195-198.

[71] S. Vandersee, U. Erdmenger, A. Patzelt, M. Beyer, M.C. Meinke, M.E. Darvin, J. Koscielny, J. Lademann, Significance of the follicular pathway for dermal substance penetration quantified by laser Doppler flowmetry, J Biophotonics 9(3) (2016) 276-281.

[72] A.L. Klein, M. Lubda, P.S. Skov, A. Vogt, C.M. Keck, J. Lademann, I. Beckers, J. von Hagen, A. Patzelt, Investigation of transfollicular caffeine penetration using microdialysis on ex vivo porcine ear skin, Eur J Pharm Biopharm 157 (2020) 1-8.

[73] J. Lademann, H. Richter, U.F. Schaefer, U. Blume-Peytavi, A. Teichmann, N. Otberg, W. Sterry, Hair follicles - a long-term reservoir for drug delivery, Skin Pharmacol Physiol 19(4) (2006) 232-236.

[74] J. Lademann, H. Richter, M.C. Meinke, B. Lange-Asschenfeldt, C. Antoniou, W.C. Mak, R. Renneberg, W. Sterry, A. Patzelt, Drug delivery with topically applied nanoparticles: science fiction or reality, Skin Pharmacol Physiol 26(4-6) (2013) 227-233.

[75] A. Vogt, B. Combadiere, S. Hadam, K.M. Stieler, J. Lademann, H. Schaefer, B. Autran, W. Sterry, U. Blume-Peytavi, 40 nm, but not 750 or 1,500 nm, nanoparticles enter epidermal CD1a+ cells after transcutaneous application on human skin, J Invest Dermatol 126(6) (2006) 1316-1322.

[76] H.I. Labouta, L.K. el-Khordagui, T. Kraus, M. Schneider, Mechanism and determinants of nanoparticle penetration through human skin, Nanoscale 3(12) (2011) 4989-4999.

[77] A. Patzelt, H. Richter, F. Knorr, U. Schäfer, C.M. Lehr, L. Dähne, W. Sterry, J. Lademann, Selective follicular targeting by modification of the particle sizes, J Control Release 150(1) (2011) 45-48.

[78] J. Lademann, A. Patzelt, H. Richter, C. Antoniou, W. Sterry, F. Knorr, Determination of the cuticula thickness of human and porcine hairs and their potential influence on the penetration of nanoparticles into the hair follicles, J Biomed Opt 14(2) (2009) 021014.

[79] M. Radtke, A. Patzelt, F. Knorr, J. Lademann, R.R. Netz, Ratchet effect for nanoparticle transport in hair follicles, Eur J Pharm Biopharm 116 (2017) 125-130.

[80] S. Jung, N. Otberg, G. Thiede, H. Richter, W. Sterry, S. Panzner, J. Lademann, Innovative liposomes as a transfollicular drug delivery system: penetration into porcine hair follicles, J Invest Dermatol 126(8) (2006) 1728-1732.

[81] R.M. Hoffman, Topical liposome targeting of dyes, melanins, genes, and proteins selectively to hair follicles, J Drug Target 5(2) (1998) 67-74.

[82] S.N. Ciotti, N. Weiner, Follicular liposomal delivery systems, J Liposome Res 12(1-2) (2002) 143-148.

[83] L. Li, V. Lishko, R.M. Hoffman, Liposome targeting of high molecular weight DNA to the hair follicles of histocultured skin: a model for gene therapy of the hair growth processes, In Vitro Cell Dev Biol Anim 29A(4) (1993) 258-260.

[84] E. Bernard, J.L. Dubois, J. Wepierre, Importance of sebaceous glands in cutaneous penetration of an antiandrogen: target effect of liposomes, J Pharm Sci 86(5) (1997) 573-578.

[85] H. Hamishehkar, S. Ghanbarzadeh, S. Sepehran, Y. Javadzadeh, Z.M. Adib, M. Kouhsoltani, Histological assessment of follicular delivery of flutamide by solid lipid nanoparticles: potential tool for the treatment of androgenic alopecia, Drug Dev Ind Pharm 42(6) (2016) 846-853.

[86] N. Friedman, A. Dagan, J. Elia, S. Merims, O. Benny, Physical properties of gold nanoparticles affect skin penetration via hair follicles, Nanomedicine 36 (2021) 102414.

[87] O. Pelikh, R.W. Eckert, S.R. Pinnapireddy, C.M. Keck, Hair follicle targeting with curcumin nanocrystals: Influence of the formulation properties on the penetration efficacy, J Control Release 329 (2021) 598-613.

[88] O. Pelikh, C.M. Keck, Hair Follicle Targeting and Dermal Drug Delivery with Curcumin Drug Nanocrystals-Essential Influence of Excipients, Nanomaterials (Basel) 10(11) (2020) 2323.

[89] A. Mittal, A.S. Raber, U.F. Schaefer, S. Weissmann, T. Ebensen, K. Schulze, C.A. Guzman, C.M. Lehr, S. Hansen, Non-invasive delivery of nanoparticles to hair follicles: a perspective for transcutaneous immunization, Vaccine 31(34) (2013) 3442-3451.

[90] B. Limcharoen, P. Toprangkobsin, W. Banlunara, S. Wanichwecharungruang, H. Richter, J. Lademann, A. Patzelt, Increasing the percutaneous absorption and follicular penetration of retinal by topical application of proretinal nanoparticles, Eur J Pharm Biopharm 139 (2019) 93-100.

[91] A. Patzelt, W.C. Mak, S. Jung, F. Knorr, M.C. Meinke, H. Richter, E. Rühl, K.Y. Cheung, N. Tran, J. Lademann, Do nanoparticles have a future in dermal drug delivery?, J Control Release 246 (2017) 174-182.

[92] P. Dong, F.F. Sahle, S.B. Lohan, S. Saeidpour, S. Albrecht, C. Teutloff, R. Bodmeier, M. Unbehauen, C. Wolff, R. Haag, J. Lademann, A. Patzelt, M. Schäfer-Korting, M.C. Meinke, pH-sensitive Eudragit(R) L 100 nanoparticles promote cutaneous penetration and drug release on the skin, J Control Release 295 (2019) 214-222.

[93] R. Ferreira-Nunes, M. Cunha-Filho, T. Gratieri, G.M. Gelfuso, Follicular-targeted delivery of spironolactone provided by polymeric nanoparticles, Colloids Surf B Biointerfaces 208 (2021) 112101.

[94] A. Rolland, N. Wagner, A. Chatelus, B. Shroot, H. Schaefer, Site-specific drug delivery to pilosebaceous structures using polymeric microspheres, Pharm Res 10(12) (1993) 1738-1744.

[95] R. Toll, U. Jacobi, H. Richter, J. Lademann, H. Schaefer, U. Blume-Peytavi, Penetration profile of microspheres in follicular targeting of terminal hair follicles, J Invest Dermatol 123(1) (2004) 168-176.

[96] H. Lboutounne, J.F. Chaulet, C. Ploton, F. Falson, F. Pirot, Sustained ex vivo skin antiseptic activity of chlorhexidine in poly(ε-caprolactone) nanocapsule encapsulated form and as a digluconate, J Control Release 82(2-3) (2002) 319-334.

[97] H. Lboutounne, V. Faivre, F. Falson, F. Pirot, Characterization of transport of chlorhexidine-loaded nanocapsules through hairless and wistar rat skin, Skin Pharmacol Physiol 17(4) (2004) 176-182.

[98] D.T. Nhung, A.M. Freydiere, H. Constant, F. Falson, F. Pirot, Sustained antibacterial effect of a hand rub gel incorporating chlorhexdine-loaded nanocapsules (Nanochlorex), Int J Pharm 334(1-2) (2007) 166-172.

[99] M. Ulmer, A. Patzelt, T. Vergou, H. Richter, G. Müller, A. Kramer, W. Sterry, V. Czaika, J. Lademann, In vivo investigation of the efficiency of a nanoparticle-emulsion containing polihexanide on the human skin, Eur J Pharm Biopharm 84(2) (2013) 325-329.

[100] A. Mittal, K. Schulze, T. Ebensen, S. Weissmann, S. Hansen, C.A. Guzman, C.M. Lehr, Inverse micellar sugar glass (IMSG) nanoparticles for transfollicular vaccination, J Control Release 206 (2015) 140-152.

[101] A. Vogt, S. Hadam, I. Deckert, J. Schmidt, A. Stroux, Z. Afraz, F. Rancan, J. Lademann, B. Combadiere, U. Blume-Peytavi, Hair follicle targeting, penetration enhancement and Langerhans cell activation make cyanoacrylate skin surface stripping a promising delivery technique for transcutaneous immunization with large molecules and particle-based vaccines, Exp Dermatol 24(1) (2015) 73-75.

[102] M. Ohyama, J.C. Vogel, Gene delivery to the hair follicle, J Investig Dermatol Symp Proc 8(2) (2003) 204-206.

[103] D. Thiboutot, Regulation of human sebaceous glands, J Invest Dermatol 123(1) (2004) 1-12.

[104] C. Costa, A. Cavaco-Paulo, T. Matama, Mapping hair follicle-targeted delivery by particle systems: What has science accomplished so far?, Int J Pharm 610 (2021) 121273.

[105] A.T. Ogunjimi, F. Chahud, R.F.V. Lopez, Isotretinoin-Delonix polymeric nanoparticles: Potentials for skin follicular targeting in acne treatment, Int J Pharm 610 (2021) 121217.

[106] P.M. Oliveira, T. Alencar-Silva, F.Q. Pires, M. Cunha-Filho, T. Gratieri, J.L. Carvalho, G.M. Gelfuso, Nanostructured lipid carriers loaded with an association of minoxidil and latanoprost for targeted topical therapy of alopecia, Eur J Pharm Biopharm 172 (2022) 78-88.

[107] Y. Oaku, A. Abe, Y. Sasano, F. Sasaki, C. Kubota, N. Yamamoto, T. Nagahama, N. Nagai, Minoxidil Nanoparticles Targeting Hair Follicles Enhance Hair Growth in C57BL/6 Mice, Pharmaceutics 14(5) (2022) 947.

[108] J. Kong, W. Qiang, J. Jiang, X. Hu, Y. Chen, Y. Guo, H. Liu, S. Sun, H. Gao, Y. Zhang, Y. Gao, X. Liu, X. Liu, H. Li, Safflower oil body nanoparticles deliver hFGF10 to hair follicles

and reduce microinflammation to accelerate hair regeneration in androgenetic alopecia, Int J Pharm 616 (2022) 121537.

[109] S.E. Mangion, L. Sandiford, Y. Mohammed, M.S. Roberts, A.M. Holmes, Multi-Modal Imaging to Assess the Follicular Delivery of Zinc Pyrithione, Pharmaceutics 14(5) (2022) 1076.

[110] T. Subongkot, N. Charernsriwilaiwat, R. Chanasongkram, K. Rittem, T. Ngawhirunpat, P. Opanasopit, Development and Skin Penetration Pathway Evaluation Using Confocal Laser Scanning Microscopy of Microemulsions for Dermal Delivery Enhancement of Finasteride, Pharmaceutics 14(12) (2022) 2784.

[111] R. Christmann, D.K. Ho, J. Wilzopolski, S. Lee, M. Koch, B. Loretz, T. Vogt, W. Baumer, U.F. Schaefer, C.M. Lehr, Tofacitinib Loaded Squalenyl Nanoparticles for Targeted Follicular Delivery in Inflammatory Skin Diseases, Pharmaceutics 12(12) (2020) 1131.

[112] E. Pena-Rodriguez, M. Lajarin-Reinares, A. Mata-Ventosa, S. Perez-Torras, F. Fernandez-Campos, Dexamethasone-Loaded Lipomers: Development, Characterization, and Skin Biodistribution Studies, Pharmaceutics 13(4) (2021) 533.

[113] M.A. Sallam, M.T. Marin Bosca, Mechanistic Analysis of Human Skin Distribution and Follicular Targeting of Adapalene-Loaded Biodegradable Nanospheres With an Insight Into Hydrogel Matrix Influence, In Vitro Skin Irritation, and In Vivo Tolerability, J Pharm Sci 106(10) (2017) 3140-3149.

[114] M.M. Abdel-Mottaleb, B. Moulari, A. Beduneau, Y. Pellequer, A. Lamprecht, Nanoparticles enhance therapeutic outcome in inflamed skin therapy, Eur J Pharm Biopharm 82(1) (2012) 151-157.

[115] C. Mathes, A. Melero, P. Conrad, T. Vogt, L. Rigo, D. Selzer, W.A. Prado, C. De Rossi, T.M. Garrigues, S. Hansen, S.S. Guterres, A.R. Pohlmann, R.C.R. Beck, C.M. Lehr, U.F. Schaefer, Nanocarriers for optimizing the balance between interfollicular permeation and follicular uptake of topically applied clobetasol to minimize adverse effects, J Control Release 223 (2016) 207-214.

[116] W.C. Mak, A. Patzelt, H. Richter, R. Renneberg, K.K. Lai, E. Rühl, W. Sterry, J. Lademann, Triggering of drug release of particles in hair follicles, J Control Release 160(3) (2012) 509-514.

[117] W.C. Mak, H. Richter, A. Patzelt, W. Sterry, K.K. Lai, R. Renneberg, J. Lademann, Drug delivery into the skin by degradable particles, Eur J Pharm Biopharm 79(1) (2011) 23-27.

[118] N. Tran, F. Knorr, W.C. Mak, K.Y. Cheung, H. Richter, M. Meinke, J. Lademann, A. Patzelt, Gradient-dependent release of the model drug TRITC-dextran from FITC-labeled BSA hydrogel nanocarriers in the hair follicles of porcine ear skin, Eur J Pharm Biopharm 116 (2017) 12-16.

[119] J. Lademann, H. Richter, F. Knorr, A. Patzelt, M.E. Darvin, E. Rühl, K.Y. Cheung, K.K. Lai, R. Renneberg, W.C. Mak, Triggered release of model drug from AuNP-doped BSA nanocarriers in hair follicles using IRA radiation, Acta Biomater 30 (2016) 388-396.

[120] X. Liu, Y. Yang, M.W. Urban, Stimuli-Responsive Polymeric Nanoparticles, Macromol Rapid Commun 38(13) (2017) 1700030.

[121] M.F. Bedard, B.G. De Geest, A.G. Skirtach, H. Mohwald, G.B. Sukhorukov, Polymeric microcapsules with light responsive properties for encapsulation and release, Adv Colloid Interface Sci 158(1-2) (2010) 2-14.

[122] C. Lv, Z. Wang, P. Wang, X. Tang, Photodegradable polyurethane self-assembled nanoparticles for photocontrollable release, Langmuir 28(25) (2012) 9387-9394.

[123] C. Lv, Z. Wang, P. Wang, X. Tang, Photodegradable polyesters for triggered release, Int J Mol Sci 13(12) (2012) 16387-16399.

[124] D. Klinger, K. Landfester, Polymeric photoresist nanoparticles: light-induced degradation of hydrophobic polymers in aqueous dispersion, Macromol Rapid Commun 32(24) (2011) 1979-1985.

[125] S. Bühler, I. Lagoja, H. Giegrich, K.-P. Stengele, W. Pfleiderer, New Types of Very Efficient Photolabile Protecting Groups Based upon the[2-(2-Nitrophenyl)propoxy]carbonyl (NPPOC) Moiety, Helv Chim Acta 87(3) (2004) 620-659.

[126] C.P. Holmes, D.G. Jones, Reagents for Combinatorial Organic Synthesis: Development of a New o-Nitrobenzyl Photolabile Linker for Solid Phase Synthesis, J Org Chem 60(8) (2002) 2318-2319.

[127] A.L. Byrd, Y. Belkaid, J.A. Segre, The human skin microbiome, Nat Rev Microbiol 16(3) (2018) 143-155.

[128] A. Kramer, C.-D. Heidecke, Präoperative Hautantiseptik und Hautschutz, Trauma und Berufskrankheit 17(S2) (2015) 322-329.

[129] J.P. Leeming, K.T. Holland, W.J. Cunliffe, The microbial ecology of pilosebaceous units isolated from human skin, J Gen Microbiol 130(4) (1984) 803-807.

[130] E.A. Grice, J.A. Segre, The skin microbiome, Nat Rev Microbiol 9(4) (2011) 244-253.

[131] L.F. Montes, Anatomical Location of Normal Skin Flora, Arch Dermatol 101(2) (1970) 145-159.

[132] C.D. Owens, K. Stoessel, Surgical site infections: epidemiology, microbiology and prevention, J Hosp Infect 70 Suppl 2 (2008) 3-10.

[133] A.J. Mangram, T.C. Horan, M.L. Pearson, L.C. Silver, W.R. Jarvis, Guideline for Prevention of Surgical Site Infection, 1999, American Journal of Infection Control 27(2) (1999) 97-134.

[134] [Prevention of postoperative surgical wound infection: recommendations of the Hospital Hygiene and Infection Prevention Committee of the Robert Koch Institute], Bundesgesundheitsblatt Gesundheitsforschung Gesundheitsschutz 50(3) (2007) 377-393.

[135] A. Kramer, J. Pochhammer, P. Walger, U. Seifert, M. Ruhnke, J.C. Harnoss, [Spectrum of pathogens in postoperative complications of visceral surgery : The problem of multidrug resistance], Chirurg 88(5) (2017) 369-376.

[136] C. Eckmann, A. Kramer, O. Assadian, S. Flessa, C. Huebner, K. Michnacs, C. Muehlendyck, K.M. Podolski, M. Wilke, W. Heinlein, D.J. Leaper, Clinical and economic burden of surgical site infections in inpatient care in Germany: A retrospective, cross-sectional analysis from 79 hospitals, PLoS One 17(12) (2022) e0275970.

[137] Prävention postoperativer Wundinfektionen: Empfehlung der Kommission für Krankenhaushygiene und Infektionsprävention (KRINKO) beim Robert Koch-Institut, Bundesgesundheitsblatt Gesundheitsforschung Gesundheitsschutz 61(4) (2018) 448-473.

[138] M.C. Robson, Infection in the Surgical Patient: An Imbalance in the Normal Equilibrium, Clin Plast Surg 6(4) (1979) 493-503.

[139] L.G. Bode, J.A. Kluytmans, H.F. Wertheim, D. Bogaers, C.M. Vandenbroucke-Grauls, R. Roosendaal, A. Troelstra, A.T. Box, A. Voss, I. van der Tweel, A. van Belkum, H.A. Verbrugh, M.C. Vos, Preventing surgical-site infections in nasal carriers of Staphylococcus aureus, N Engl J Med 362(1) (2010) 9-17.

[140] A. Kramer, J.C. Harnoss, P. Walger, C.D. Heidecke, A. Schreiber, S. Maier, J. Pochhammer, Fachspezifische Maßnahmen zur Prävention von Surgical Site Infections (SSI), Zentralbl Chir 141(6) (2016) 591-596.

[141] G.S. Lazarus, D.M. Cooper, D.R. Knighton, R.E. Percoraro, G. Rodeheaver, M.C. Robson, Definitions and guidelines for assessment of wounds and evaluation of healing, Wound Repair Regen 2(3) (1994) 165-170.

[142] K. Järbrink, G. Ni, H. Sönnergren, A. Schmidtchen, C. Pang, R. Bajpai, J. Car, The humanistic and economic burden of chronic wounds: a protocol for a systematic review, Syst Rev 6(1) (2017) 15.

[143] T. Velnar, T. Bailey, V. Smrkolj, The wound healing process: an overview of the cellular and molecular mechanisms, J Int Med Res 37(5) (2009) 1528-1542.

[144] A. Kramer, J. Dissemond, S. Kim, C. Willy, D. Mayer, R. Papke, F. Tuchmann, O. Assadian, Consensus on Wound Antisepsis: Update 2018, Skin Pharmacol Physiol 31(1) (2018) 28-58.

[145] I. Negut, V. Grumezescu, A.M. Grumezescu, Treatment Strategies for Infected Wounds, Molecules 23(9) (2018) 2392.

[146] T.R. Johnson, B.I. Gomez, M.K. McIntyre, M.A. Dubick, R.J. Christy, S.E. Nicholson, D.M. Burmeister, The Cutaneous Microbiome and Wounds: New Molecular Targets to Promote Wound Healing, Int J Mol Sci 19(9) (2018) 2699.

[147] R. Zhao, H. Liang, E. Clarke, C. Jackson, M. Xue, Inflammation in Chronic Wounds, Int J Mol Sci 17(12) (2016) 2085.

[148] L. Martinengo, M. Olsson, R. Bajpai, M. Soljak, Z. Upton, A. Schmidtchen, J. Car, K. Järbrink, Prevalence of chronic wounds in the general population: systematic review and meta-analysis of observational studies, Ann Epidemiol 29 (2019) 8-15.

[149] X. Zhu, M.M. Olsson, R. Bajpai, K. Järbrink, W.E. Tang, J. Car, Health-related quality of life and chronic wound characteristics among patients with chronic wounds treated in primary care: A cross-sectional study in Singapore, Int Wound J 19(5) (2022) 1121-1132.

[150] F. Drago, L. Gariazzo, M. Cioni, I. Trave, A. Parodi, The microbiome and its relevance in complex wounds, Eur J Dermatol 29(1) (2019) 6-13.

[151] G. Kampf, Acquired resistance to chlorhexidine - is it time to establish an 'antiseptic stewardship' initiative?, J Hosp Infect 94(3) (2016) 213-227.

[152] H. Hönigsmann, History of phototherapy in dermatology, Photochem Photobiol Sci 12(1) (2013) 16-21.

[153] A. Khan, K. Balakrishnan, T. Katona, Ultraviolet light-emitting diodes based on group three nitrides, Nat Photonics 2(2) (2008) 77-84.

[154] J. D'Orazio, S. Jarrett, A. Amaro-Ortiz, T. Scott, UV radiation and the skin, Int J Mol Sci 14(6) (2013) 12222-12248.

[155] G. Valacchi, C. Sticozzi, A. Pecorelli, F. Cervellati, C. Cervellati, E. Maioli, Cutaneous responses to environmental stressors, Ann N Y Acad Sci 1271(1) (2012) 75-81.

[156] J. Krutmann, A. Morita, J.H. Chung, Sun exposure: what molecular photodermatology tells us about its good and bad sides, J Invest Dermatol 132(3 Pt 2) (2012) 976-984.

[157] J.A. Parrish, T.B. Fitzpatrick, L. Tanenbaum, M.A. Pathak, Photochemotherapy of psoriasis with oral methoxsalen and longwave ultraviolet light, N Engl J Med 291(23) (1974) 1207-1211.

[158] S.I. Ahmad, L. Christensen, E. Baron, History of UV Lamps, Types, and Their Applications, Adv Exp Med Biol 996 (2017) 3-11.

[159] G. Matafonova, V. Batoev, Recent advances in application of UV light-emitting diodes for degrading organic pollutants in water through advanced oxidation processes: A review, Water Res 132 (2018) 177-189.

[160] F.H. Fan, Z.Y. Syu, C.J. Wu, Z.J. Yang, B.S. Huang, G.J. Wang, Y.S. Lin, H. Chen, C. Hauer Kao, C.F. Lin, Ultraviolet GaN Light-Emitting Diodes with Porous-AlGaN Reflectors, Sci Rep 7(1) (2017) 4968.

[161] K. Tadatomo, H. Okagawa, Y. Ohuchi, T. Tsunekawa, H. Kudo, Y. Sudo, M. Kato, T. Taguchi, High Output Power Near-Ultraviolet and Violet Light-Emitting Diodes Fabricated on Patterned Sapphire Substrates Using Metalorganic Vapor Phase Epitaxy, J Light Vis Environ 27(3) (2003) 140-145.

[162] Z. Li, L. Liu, Y. Huang, Q. Sun, M. Feng, Y. Zhou, H. Zhao, H. Yang, High-power AlGaN-based near-ultraviolet light-emitting diodes grown on Si(111), Appl Phys Express 10(7) (2017) 072101.

[163] H. Tsuzuki, F. Mori, K. Takeda, T. Ichikawa, M. Iwaya, S. Kamiyama, H. Amano, I. Akasaki, H. Yoshida, M. Kuwabara, Y. Yamashita, H. Kan, High-performance UV emitter grown on high-crystalline-quality AlGaN underlying layer, Phys Status Solidi (A) 206(6) (2009) 1199-1204.

[164] N. Lobo-Ploch, F. Mehnke, L. Sulmoni, H.K. Cho, M. Guttmann, J. Glaab, K. Hilbrich, T. Wernicke, S. Einfeldt, M. Kneissl, Milliwatt power 233 nm AlGaN-based deep UV-LEDs on sapphire substrates, Appl Phys Letters 117(11) (2020).

[165] J. Glaab, J. Ruschel, F. Mehnke, M. Lapeyrade, M. Guttmann, T. Wernicke, M. Weyers, S. Einfeldt, M. Kneissl, Degradation behavior of AlGaN-based 233 nm deep-ultraviolet light emitting diodes, Semicond Sci Technol 33(9) (2018) 095017.

[166] S.-R. Jeon, S.-J. Son, S.-H. Park, Growth and characterization of quaternary AlGaInN layers and performance of AlGaInN-based ultraviolet light-emitting diodes, J Korean Phys Soc 63(11) (2013) 2204-2208.

[167] L. Busch, Y. Avlasevich, P. Zwicker, G. Thiede, K. Landfester, C.M. Keck, M.C. Meinke, M.E. Darvin, A. Kramer, G. Müller, M. Kerscher, J. Lademann, A. Patzelt, Release of the model drug SR101 from polyurethane nanocapsules in porcine hair follicles triggered by LED-derived low dose UVA light, Int J Pharm 597 (2021) 120339.

[168] Y. Muramoto, M. Kimura, S. Nouda, Development and future of ultraviolet light-emitting diodes: UV-LED will replace the UV lamp, Semicond Sci Technol 29(8) (2014) 084004.

[169] J. Glaab, J. Ruschel, N. Lobo Ploch, H.K. Cho, F. Mehnke, L. Sulmoni, M. Guttmann, T. Wernicke, M. Weyers, S. Einfeldt, M. Kneissl, Impact of operation parameters on the degradation of 233 nm AlGaN-based far-UVC LEDs, Journal of Applied Physics 131(1) (2022).

[170] M. Buonanno, G. Randers-Pehrson, A.W. Bigelow, S. Trivedi, F.D. Lowy, H.M. Spotnitz, S.M. Hammer, D.J. Brenner, 207-nm UV light - a promising tool for safe low-cost reduction of surgical site infections. I: in vitro studies, PLoS One 8(10) (2013) e76968.

[171] M. Buonanno, B. Ponnaiya, D. Welch, M. Stanislauskas, G. Randers-Pehrson, L. Smilenov, F.D. Lowy, D.M. Owens, D.J. Brenner, Germicidal Efficacy and Mammalian Skin Safety of 222-nm UV Light, Radiat Res 187(4) (2017) 483-491.

[172] B. Ponnaiya, M. Buonanno, D. Welch, I. Shuryak, G. Randers-Pehrson, D.J. Brenner, Far-UVC light prevents MRSA infection of superficial wounds in vivo, PLoS One 13(2) (2018) e0192053.

[173] K. Narita, K. Asano, Y. Morimoto, T. Igarashi, M.R. Hamblin, T. Dai, A. Nakane, Disinfection and healing effects of 222-nm UVC light on methicillin-resistant Staphylococcus aureus infection in mouse wounds, J Photochem Photobiol B 178 (2018) 10-18.

[174] K. Narita, K. Asano, Y. Morimoto, T. Igarashi, A. Nakane, Chronic irradiation with 222-nm UVC light induces neither DNA damage nor epidermal lesions in mouse skin, even at high doses, PLoS One 13(7) (2018) e0201259.

[175] K. Narita, K. Asano, K. Naito, H. Ohashi, M. Sasaki, Y. Morimoto, T. Igarashi, A. Nakane, Ultraviolet C light with wavelength of 222 nm inactivates a wide spectrum of microbial pathogens, J Hosp Infect 105(3) (2020) 459-467.

[176] N. Yamano, M. Kunisada, S. Kaidzu, K. Sugihara, A. Nishiaki-Sawada, H. Ohashi, A. Yoshioka, T. Igarashi, A. Ohira, M. Tanito, C. Nishigori, Long-term Effects of 222-nm ultraviolet radiation C Sterilizing Lamps on Mice Susceptible to Ultraviolet Radiation, Photochem Photobiol 96(4) (2020) 853-862.

[177] T. Fukui, T. Niikura, T. Oda, Y. Kumabe, A. Nishiaki, R. Kaigome, H. Ohashi, M. Sasaki, T. Igarashi, K. Oe, M.R. Hamblin, R. Kuroda, Safety of 222 nm UVC Irradiation to the Surgical Site in a Rabbit Model, Photochem Photobiol 98(6) (2022) 1365-1371.

[178] T. Fukui, T. Niikura, T. Oda, Y. Kumabe, H. Ohashi, M. Sasaki, T. Igarashi, M. Kunisada, N. Yamano, K. Oe, T. Matsumoto, T. Matsushita, S. Hayashi, C. Nishigori, R. Kuroda, Exploratory clinical trial on the safety and bactericidal effect of 222-nm ultraviolet C irradiation in healthy humans, PLoS One 15(8) (2020) e0235948.

[179] D. Welch, N.J. Kleiman, P.C. Arden, C.L. Kuryla, M. Buonanno, B. Ponnaiya, X. Wu, D.J. Brenner, No Evidence of Induced Skin Cancer or Other Skin Abnormalities after Long-Term (66 week) Chronic Exposure to 222-nm Far-UVC Radiation, Photochem Photobiol 99(1) (2023) 168-175.

[180] E. Eadie, W. Hiwar, L. Fletcher, E. Tidswell, P. O'Mahoney, M. Buonanno, D. Welch, C.S. Adamson, D.J. Brenner, C. Noakes, K. Wood, Far-UVC (222 nm) efficiently inactivates an airborne pathogen in a room-sized chamber, Sci Rep 12(1) (2022) 4373.

[181] R.S.N. Tavares, D. Adamoski, A. Girasole, E.N. Lima, A. da Silva Justo-Junior, R. Domingues, A.C.C. Silveira, R.E. Marques, M. de Carvalho, A.L.B. Ambrosio, A.F.P. Leme, S.M.G. Dias, Different biological effects of exposure to far-UVC (222 nm) and near-UVC (254 nm) irradiation, J Photochem Photobiol B 243 (2023) 112713.

[182] A.A. Vink, L. Roza, Biological consequences of cyclobutane pyrimidine dimers, J Photochem Photobiol B 65(2-3) (2001) 101-104.

[183] A. Tewari, M.M. Grage, G.I. Harrison, R. Sarkany, A.R. Young, UVA1 is skin deep: molecular and clinical implications, Photochem Photobiol Sci 12(1) (2013) 95-103.

[184] M. Hessling, R. Haag, N. Sieber, P. Vatter, The impact of far-UVC radiation (200-230 nm) on pathogens, cells, skin, and eyes - a collection and analysis of a hundred years of data, GMS Hyg Infect Control 16 (2021) Doc07.

[185] H. Choi, P. Chatterjee, M. Hwang, E.M. Stock, J.S. Lukey, J.E. Zeber, C. Jinadatha, Can multidrug-resistant organisms become resistant to ultraviolet (UV) light following serial exposures? Characterization of post-UV genomic changes using whole-genome sequencing, Infect Control Hosp Epidemiol 43(1) (2022) 72-78.

[186] J.E. Vasquez, E.S. Walker, B.W. Franzus, B.K. Overbay, D.R. Reagan, F.A. Sarubbi, The epidemiology of mupirocin resistance among methicillin-resistant Staphylococcus aureus at a Veterans' Affairs hospital, Infect Control Hosp Epidemiol 21(7) (2000) 459-464.

[187] T. Dai, M.S. Vrahas, C.K. Murray, M.R. Hamblin, Ultraviolet C irradiation: an alternative antimicrobial approach to localized infections?, Expert Rev Anti Infect Ther 10(2) (2012) 185-195.

[188] J.C. Goh, D. Fisher, E.C.H. Hing, L. Hanjing, Y.Y. Lin, J. Lim, O.W. Chen, L.T. Chye, Disinfection capabilities of a 222 nm wavelength ultraviolet lighting device: a pilot study, J Wound Care 30(2) (2021) 96-104.

[189] J. Schleusener, S.B. Lohan, L. Busch, K. Ghoreschi, N.L. Ploch, S. May, S. Vogel, J. Eberle, M.C. Meinke, Treatment of the Candida subspecies Candida albicans and Candida parapsilosis with two far-UVC sources to minimise mycoses in clinical practice, Mycoses 66(1) (2023) 25-28.

2. Aims of the thesis

This dissertation can be divided into two major parts. The aim of the first part was to test an innovative pharmaceutical approach for improved deep preoperative antisepsis of the integument (**Figure 6, Part I**). Nanocapsules (NCs) were to be used here, which penetrate the hair follicles based on the so-called ratchet effect (see also: **Section 1**). Subsequently, the skin surface was irradiated with ultraviolet A (UVA) light emitting diodes (LEDs) in order to mediate the release of the active ingredient. Thus, in contrast to conventional non-nanoparticulate antiseptic formulations, deeper parts of the hair follicle can be targeted which can potentially avoid recolonization of the skin surface during prolonged surgical interventions.

The first objective was to demonstrate the principle of follicular penetration as well as intrafollicular UVA-triggered drug release on *ex vivo* porcine skin (**Figure 6, Publication I**). For this purpose, photoresponsive polyurethane (PU)-based NCs in combination with a commercially available UVA-LED were initially used. The follicular penetration depth as well as the intrafollicular drug release were to be evaluated by image analysis of confocal laser scanning (CLSM) images of cryohistological thin sections. In this way, it was also possible to determine which irradiation times and power densities are realistic to induce an intrafollicular drug release when utilizing UVA.

Based on this, the second objective was to test a system of hydroxyethyl starch (HES)-based NCs, comparable in terms of physicochemical properties but more biocompatible, on *ex vivo* porcine skin for the properties described above (**Figure 6, Publication II**). Here, a UVA-LED radiation source (peak emission wavelength of 365 nm) developed within the project was used which is suitable for application in preoperative antisepsis. Following the examination of the drug delivery properties, the antiseptic performance was also to be tested on *ex vivo* porcine skin in order to come closer to translating the novel model into the clinical field.

The second major part of the dissertation was to test a complementary or alternative physical approach for application in skin antisepsis (**Figure 6, Part II**). For this purpose, a newly developed far-UVC-LED light source was employed, which emits radiation at a peak wavelength of 233 nm. Far-UVC light is a promising approach for skin surface disinfection because, unlike longer wavelength UV light, it primarily penetrates only the non-nucleated uppermost skin layer, the stratum corneum. Nevertheless, it is important to perform various safety tests on skin

models in this context, as far-UVC radiation involves a comparatively high energy and no safety data have yet been available for the 233 nm wavelength.

To ensure broad applicability of the system in the nosocomial and surgical environment, the main objectives of the second part of the dissertation were:

-Testing microbiocidal doses of 233 nm radiation on intact *ex vivo* skin and *in vitro* epidermal 3D models for DNA damage as well as free radical formation (**Figure 6, Publication III**).

-Testing microbiocidal doses of 233 nm radiation on wound *ex vivo* skin for DNA damage and free radicals and comparing the data with ray tracing simulations for light penetration (**Figure 6, Publication IV**).

-The investigation of the influence of microbiocidal far-UVC radiation on DNA damage in different skin types including the biophysical characterization of melanin distribution (**Figure 6, Publication V**).

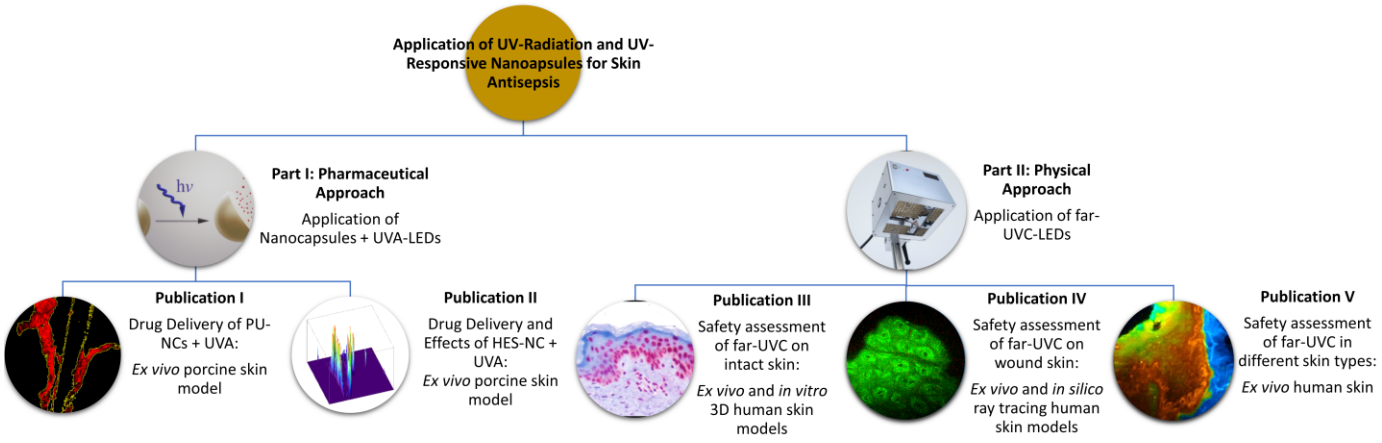

Figure 6: Graphical overview of the two main parts of the dissertation on the application of UV radiation and UV-responsive nanocapsules (NCs) and the resulting publications I-V.


Application of UV-Radiation and UV-Responsive Nanoapsules for Skin Antisepsis
Part I: Pharmaceutical Approach
Application of Nanocapsules + UVA-LEDs
Part II: Physical Approach
Application of far-UVC-LEDs
Publication I
Drug Delivery of PU-NCs + UVA:
Ex vivo porcine skin model
Publication II
Drug Delivery and Effects of HES-NC + UVA:
Ex vivo porcine skin model
Publication III
Safety assessment of far-UVC on intact skin:
Ex vivo and in vitro 3D human skin models
Publication IV
Safety assessment of far-UVC on wound skin:
Ex vivo and in silico ray tracing human skin models
Publication V
Safety assessment of far-UVC in different skin types:
Ex vivo human skin

3. Results

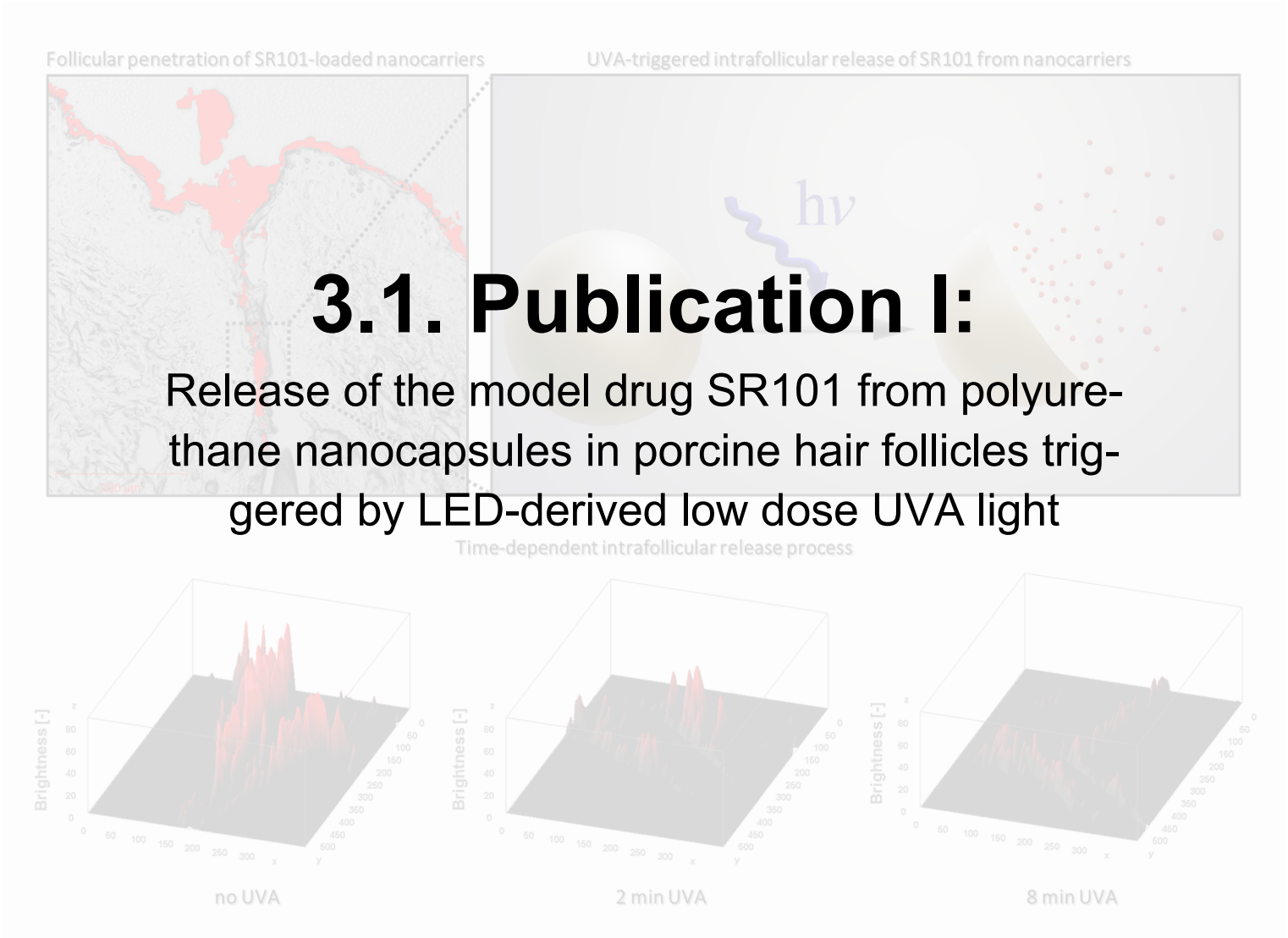

3.1. Publication I:

Release of the model drug SR101 from polyurethane nanocapsules in porcine hair follicles triggered by LED-derived low dose UVA light

3.1. PUBLICATION I:

RELEASE OF THE MODEL DRUG SR101 FROM POLYURETHANE NANOCAPSULES IN PORCINE HAIR FOLLICLES TRIGGERED BY LED-DERIVED LOW DOSE UVA LIGHT

Release of the model drug SR101 from polyurethane nanocapsules in porcine hair follicles triggered by LED-derived low dose UVA light

Loris Busch [1,2], Yuri Avlasevich [3], Paula Zwicker [4], Gisela Thiede [1], Katharina Landfester [3], Cornelia M. Keck [2], Martina C. Meinke [1], Maxim E. Darvin [1], Axel Kramer [4], Gerald Müller [4], Martina Kerscher [5], Jürgen Lademann [1], Alexa Patzelt [1]

[1] *Center of Experimental and Applied Cutaneous Physiology, Department of Dermatology, Venereology and Allergology, Charité - Universitätsmedizin Berlin, Corporate member of Freie Universität Berlin, Humboldt-Universität zu Berlin, and Berlin Institute of Health, Berlin, Germany*

[2] *Department of Pharmaceutics and Biopharmaceutics, Philipps-Universität Marburg, Marburg, Germany*

[3] *Max Planck Institute for Polymer Research, Mainz, Germany*

[4] *Institute of Hygiene and Environmental Medicine, University Medicine Greifswald, Greifswald, Germany*

[5] *Institute of Biochemistry and Molecular Biology, University of Hamburg, Hamburg, Germany*

(adapted from: Int J Pharm 2021;597:120339. doi: 10.1016/j.ijpharm.2021.120339)

Parts of this publication originate from: Loris Busch – Bestimmung bestrahlungsrelevanter Parameter zur Entwicklung einer UVA-LED-Lichtquelle zum Einsatz für die kontrollierte Freisetzung von Antiseptika aus UVA-responsiven Nanocarriern im Haarfollikel zwecks präoperativer Hautantiseptik, Master Thesis, Hamburg, 2019

Abstract

Hair follicles (HFs) are important drug delivery targets for the therapy of miscellaneous skin diseases and for skin antisepsis. Furthermore, HFs significantly contribute to drug delivery of topically applied substances. Nanoparticulate systems are excellently suited for follicular drug delivery as they entail the opportunity of directed drug transport into HFs. Moreover, they involve the possibility of an intrafollicular drug release initiated by extrinsic or intrinsic trigger mechanisms. In this study, we present a novel preclinical model for an anatomically and temporally targeted intrafollicular drug release. *In vitro* release kinetics of the model drug sulforhodamine 101 (SR101) from newly synthesized ultraviolet A (UVA)-responsive polyurethane nanocapsules (NCs) were investigated by fluorescence spectroscopy. Low power density UVA radiation provided by a UVA light emitting diode (LED) induced a drug release of over 50% after 2 min. We further utilized confocal laser scanning microscopy (CLSM) to investigate follicular penetration as well as intrafollicular drug release on an *ex vivo* porcine ear skin model. UVA-responsive degradation of the NCs at a mean follicular penetration depth of 509 ± 104 µm ensured liberation of SR101 in the right place and at the right time. Thus, for the first time a UVA-triggered drug release from NCs within HFs was demonstrated in the present study. Cytotoxicity tests revealed that NCs synthesized with isophorone diisocyanate show sufficient biocompatibility after UVA-induced cleavage. A considerable and controllable release of various water-soluble therapeutics could be reached by means of the presented system without risking any radiation-related tissue damage. Therefore, the implementation of the presented system into clinical routine, e.g. for preoperative antisepsis of HFs, appears very promising.

1. Introduction

The application of nanoparticulate systems (NPs), solid nanoparticles or nanocapsules (NCs), for intrafollicular drug delivery constitutes a well proven approach entailing promising therapeutic opportunities [1]. NPs enable a significantly deeper follicular penetration than non-particulate substances, especially when skin massage is applied [2, 3]. However, above a diameter of 20–40 nm, NPs exclusively penetrate intrafollicularly [1], which makes hair follicles (HFs) key anatomic entities for particle-based drug delivery [4]. In this context, NPs entail a deep and selective follicular penetration [2, 5-7]. Moreover, they offer the opportunity of a controlled intrafollicular drug release [8-10] resulting in an increased drug concentration and drug retention at the desired target site [11, 12]. A deep follicular penetration is supported by the natural movement of the hair shaft. The moving hair shaft causes a mechanical interaction between the spherical particles, intrafollicular cell layers and hair cuticula, which together act as a kind of ratchet. This ratchet effect has been described by Radtke et al. and was simulated in a two-dimensional stochastic model [13]. Once the NPs have transported the drug to the target site within the hair follicle, a controlled liberation of the encapsulated drug can be induced by various physical or chemical trigger mechanisms. Different physical trigger mechanisms, based on diffusion [10] or infrared light [8] as well as chemical trigger mechanisms based on pH [11] or proteolysis [9, 14], are available today to initiate a controlled release within HFs. However, the application of an intrafollicular ultraviolet (UV)-responsive drug release system has not been published until now and represents the aim of the present study. Polyurethanes as materials for drug carrier systems have the advantage of chemical versatility and the option to implement functional modifications [15-17]. Their drug release characteristics as well as their mechanical properties [15] are tailorable while exhibiting a good biocompatibility [17]. Since a variety of stimuli-responsive groups can be incorporated into the polymer by synthesis, UV-responsive polyurethane NCs can be applied to obtain a controlled drug release [18]. Thus, the encapsulation, delivery and release of hydrophilic [19-21] as well as lipophilic [17, 18] cargo drugs can be obtained. Cleavable *o*-nitrobenzyl derivatives are widely investigated because of their good photolytic properties [22] under mild irradiation conditions [23]. The photoreaction is based on a radical mechanism including the intramolecular benzylic hydrogen abstraction by a nitro group oxygen followed by a rearrangement and bond cleavage. Polymers containing such groups in the main chain are known to be easily cleavable under UV irradiation [24], which makes them suitable for the formation of photodegradable NCs. UV light is supplied by different light source systems in modern medicine because of its broad field of application [25]. For the implementation of an ultraviolet A (UVA, 320–400 nm)-triggered intrafollicular release of drugs from NCs into clinical applications, light emitting diodes (LEDs) might

be advantageous since these compact devices can be mounted on various types of instruments. In addition to being compact, III-nitride semiconductor-based UV-LEDs [26], as potential substitutes for mercury vapor lamps [27], provide a reasonably narrow emission spectrum, which can be tailored to the application. They also promise an increase of the lifetime along with reduced voltage requirements, as well as a reduced risk of mercury exposure [28]. Consequently, UV-LEDs are already implemented into various biomedical applications [25]. By means of LED-derived UVA light, an external, anatomically targeted, low energy stimulus would be available for the immediate and controlled release of drugs from photodegradable NCs within the follicular compartment. Subsequently to the process of liberation within the hair follicle, either a drug effect within the follicular compartment or a transfollicular penetration of the drug is desirable, depending on the therapeutic aim. For instance, targeting the intrafollicular microbiome constitutes a promising approach for antiseptic purposes, since approximately 25% of the skin microbiome is localized within HFs [29]. Considering the fact that surgical site infections are caused by endogenous pathogens in 90% of all cases [30], this approach is gaining even more importance.

In the present study, we introduce a novel innovative system for the transport of the model drug sulforhodamine 101 (SR101) into the hair follicle by spherical polyurethane NCs as well as its intrafollicular liberation triggered by low dose UVA which is supplied by an external LED light source. This system represents a promising model for the translation to various dermatological applications or the utilization within preoperative skin antisepsis.

2. Materials and methods

2.1. Materials

Ethylene glycol (EG, ≥99%), isophorone diisocyanate (IPDI, 98%) and cyclohexane (**≥**99%, HPLC-grade) were purchased from Acros Organics (Nidderau, Germany). 2-nitro-*p*-xylylene glycol (NXG, >95%) was purchased from TCI (Eschborn, Germany). 2,4-toluene diisocyanate (TDI, 95%) and SR101 (95%) were purchased from Sigma-Aldrich (Steinheim, Germany). The substances were of commercial grade and used without further purification. Lubrizol U (polyisobutylenesuccinimide pentamine, Mw = 384–875 $g \cdot mol^{-1}$, determined from gel permeation chromatography, HLB (hydrophilic lipophilic balance) < 7, containing 50:50 wt% mineral oil as a diluent, Lubrizol, France) was used as a surfactant. Milli-Q water was used as aqueous phase throughout the experiments.

2.2. Preparation of polyurethane nanocapsules

NXG (100 mg) was dissolved in EG (700 mg) upon stirring and an aqueous solution of SR101 (10^{-3} M, 0.2 ml) was slowly added. Then, a solution of Lubrizol U (100 mg) in cyclohexane (6 g) was added. After stirring for 1 h with a magnetic stirrer for pre-emulsification, the mini-emulsion was prepared by ultrasonication of the mixture for 180 s at 70% amplitude (Branson sonifier W450 Digital, tip size 12.5 mm, pulse 10 s, pause 20 s) under ice cooling. Subsequently, 174 mg of TDI or 220 mg of IPDI dissolved in cyclohexane (4 g) was added slowly to the mini-emulsion within 5 min at room temperature. The reaction was carried out upon stirring at 700 rpm for 24 h at 25 °C resulting in dispersions of toluene diisocyanate polyurethane nanocapsules (TDI-PU-NCs) or isophorone diisocyanate polyurethane nanocapsules (IPDI-PU-NCs). The so-obtained dispersions of NCs in cyclohexane were then used for characterization by dynamic light scattering (DLS) and transmission electron microscopy (TEM). Polyaddition reaction at the interface between diols and isocyanates was confirmed by infrared spectroscopy (disappearance of the isocyanate group peak at 2300 cm^{-1} after the reaction) in previous publications [20, 21].

2.3. Characterization of polyurethane nanocapsules

2.3.1. Dynamic light scattering (DLS)

The size of the NCs and their size distribution (as polydispersity index, PDI) were measured by DLS (Nano-Zetasizer, Malvern Instruments Ltd., Worcestershire, UK) at 20 ◦C under a scattering angle of 173° at a wavelength of λ = 633 nm. DLS measurements evaluated by the standard cumulant analysis (ISO standard document 13321:1996 E) yield a Z-average size based on the intensity mean, and the polydispersity index, PDI, which provides information about the width of the particle size distribution. For the measurement, the cyclohexane dispersion was diluted 100 times and transferred into disposable glass tubes. Particle sizes and PDIs were calculated by the device as the average of 12 runs of one representative aliquot.

2.3.2. Transmission electron microscopy (TEM)

The morphology of NCs was studied using a TEM (JEM 1400, Jeol Ltd, Tokyo, Japan) operating at an accelerating voltage of 80 kV. 10 µl of the original dispersion was diluted with 5 ml of cyclohexane, and then 3.0 µl of the diluted sample was placed on a 400-mesh carbon-coated copper grid and dried at room temperature overnight. To examine the UVA-responsive degradation of the polymeric shell, the original dispersion was diluted 100 times, transferred to a 10 mm quartz cuvette (Hellma GmbH & Co. KG, Müllheim, Germany) and irradiated for

20 min from a distance of 10 cm with a UV low-pressure lamp (neoLab Migge GmbH, Heidelberg, Germany) at a peak wavelength of λ = 366 nm. Subsequently, TEM analysis was repeated as stated above.

2.4. Examination of *in vitro* release kinetics of the model drug SR101

TDI-PU-NC and IPDI-PU-NC dispersions were diluted with cyclohexane (Cyclohexane ROTISOL V® HPLC, Carl Roth GmbH & Co. KG, Karlsruhe, Germany) at a ratio of 1:9 to a volume of 800 µl. The fluorescence intensity *I* of the encapsulated model drug SR101 was detected by fluorescence spectroscopy (LS-55, PerkinElmer Inc., Waltham, USA) at an excitation wavelength of λ_{ex} = 550 nm and at the emission wavelengths λ_{em} = 598 nm (IPDI-PU-NC) and λ_{ex} = 607 nm (TDI-PU-NC), respectively, and corrected by the corresponding intensity of pure cyclohexane. For standardized irradiation of the samples, a gallium nitride-based UVA-LED (Ferdinand-Braun-Institut, Berlin, Germany) emitting at a peak wavelength of λ = 365 nm was mounted at a distance of 1.5 cm towards a micro-cuvette (111.057-QS, Hellma GmbH & Co. KG, Müllheim, Germany). The mean power density of the UVA-LED was determined by a dosimeter (ILT1400, International Light Technologies Inc., Peabody, MA, USA) after an operating time of five minutes with an operating current of 100 mA. Spectroscopic measurements were repeated for shaded controls and related cumulative radiation periods of 1, 2, 3, 4, 5, 6, 8, 10, 12, and 15 min with a mean power density of 11.96 mW/cm^2 by directly measuring the irradiated dispersion in the micro-cuvette. The normalized fluorescence intensity $I/I0$ was generated for each measuring point and mean values for n = 3 independent experiments were calculated. The relative change of fluorescence intensity corresponds to the release kinetics of the model drug SR101 from the relevant NCs. To ensure an exclusion of potential bias based on photobleaching of SR101, an aqueous SR101 solution of 100 nM was irradiated within a separate control experiment under corresponding conditions.

2.5. Examination of *ex vivo* follicular penetration of the nanocapsules and release of the model drug SR101

2.5.1. Preparation of skin samples

Porcine skin is excellently suitable as a preclinical model to investigate follicular penetration of topically applied agents [31] as well as NPs [32-34] due to its comparability to human skin hair follicle morphology and density [35], anatomy [36], barrier function [37], and permeability [38-41]. A proper representation of the penetration process is ensured in the absence of any contraction of *ex vivo* porcine ear skin and its follicles because the skin sample can remain fixed on the underlying cartilage, which is not possible if *ex vivo* human skin is utilized [42]. Porcine

ears were obtained from a local butcher. The donor pigs were six months old at the date of slaughter. The preparation of the porcine ears as well as the experiments took place at the day of slaughter. The experiments were authorized by the Commission of Consumer Protection and Agriculture, District Dahme-Spreewald, Germany. Porcine ears without any visible injuries were selected for further examinations. Preparatory, the head-proximal part of the auricles was separated by means of a scalpel to utilize the planar part of the porcine ear, exclusively. Subsequently, the porcine ears were cleaned under cold tap water and dried with paper towels. After that, every porcine ear was fixed on a polystyrene board covered by aluminum foil. In total, five test areas of 4 cm^2 per ear (preliminary experiment) or four areas of 4 cm^2 (main experiment) were selected and the included hairs were shortened with scissors. The outer edges of the areas were covered by window color (fun & fancy, Marabu GmbH & Co. KG, Tamm, Germany) to avoid a subsequent lateral spreading of the NC dispersions.

2.5.2. *Ex vivo* application of the nanocapsules and sampling

A concentration of 20 µl/cm^2 of the NC-containing cyclohexane dispersion was applied onto each test area, except one area per porcine ear which remained untreated to function as negative control. Subsequently, the test areas were massaged with a sonic wave device (NOVAVON pro, NOVAFON GmbH, Weinstadt, Germany) at a frequency of 50 Hz for 2 min, followed by an incubation period of 30 min. Afterwards, the test areas were irradiated by means of the UVA-LED from a distance of 1.5 cm (power density of 11.96 mW/cm^2, peak wavelength of λ = 365 nm) for 2 min or 8 min, respectively. To obtain an approximately constant power density, the UVA-LED was operated for 5 min before irradiation of the test areas. In the framework of a preliminary experiment with n = 1 porcine ear, both NC dispersions (TDI-PU-NC and IPDI-PU-NC) were utilized. Subsequently, n = 6 porcine ears were treated with IPDI-PU-NCs in the main experiment. The precise application protocol is presented in **Table 1**. After incubation, the respective skin area was hardened by a cryospray (Solidofix®, Carl Roth GmbH + Co. KG, Karlsruhe, Germany). Skin biopsies of 0.5 cm × 0.5 cm were excised by means of a scalpel, transferred to cryotubes, and shock frozen with liquid nitrogen. The samples were stored at 20 °C until further preparation.

2.5.3. Cryohistological preparation

Subsequently to the embedding of the skin biopsies in a cryomedium (Tissue Freezing Medium, Leica Biosystems Richmond Inc., Richmond, IL, USA), vertical sections of a thickness of 10 µm were prepared by means of a cryotome (Microm Cryo-Star HM 560, MICROM International GmbH, Walldorf, Germany) and transferred onto microscope slides. Anatomical conditions were verified with the help of an inverse transmission microscope (Olympus IX 50,

Olympus K.K., Shinjuku, Tokyo, Japan). The so-obtained sections were stored at a temperature of 20 °C until further examination.

2.5.4. Confocal laser scanning microscopy (CLSM)

Examination of the cryohistological sections was carried out via confocal laser scanning microscopy (CLSM) (LSM 700, Carl Zeiss AG, Oberkochen, Germany) with a 10x objective lens (numerical aperture 0.45) in both transmission mode and fluorescence mode. Imaging of the fluorophore-loaded NCs was effected through excitation of SR101 by means of a laser wavelength of λ = 555 nm and detection at an emission maximum of λ_{em} = 593 nm. The acquisition of the digital images and evaluation of the follicular penetration depth of SR101-loaded NCs was conducted via the corresponding software (ZEN 2012, Carl Zeiss AG, Oberkochen, Germany) by measuring the distance from the skin surface to the deepest signal of fluorescence emission. In case of the presence of multiple sections per hair follicle, the global maximum of each follicle was included into the evaluation. For each donor and test region, *n* = 10 HFs were examined. Statistical analysis only included HFs which were cross-sectioned longitudinally and appeared receptive to follicular penetration.

Table 1: Synopsis of the treatment of *ex vivo* porcine skin with NC dispersions in cyclohexane and UVA irradiation in the preliminary experiment as well as in the main experiment.

Experiment	Area	Treatment
Preliminary experiment (*n* = 1)	I	Negative control (untreated)
	II	TDI-PU-NC
	III	TDI-PU-NC + 2 min UVA
	IV	IPDI-PU-NC
	V	IPDI-PU-NC + 2 min UVA
Main experiment (*n* = 6)	I	Negative control (untreated)
	II	IPDI-PU-NC
	III	IPDI-PU-NC + 2 min UVA
	IV	IPDI-PU-NC + 8 min UVA

2.5.5. Graphical processing

For the analysis of the intrafollicular signal intensity of SR101- loaded NCs, CLSM-images recorded in the fluorescence mode were processed by the software ImageJ (Wayne Rasband, National Institutes of Health, Bethesda, MD, USA). After specification of the hair follicle infundibulum as a region of interest (ROI), an image segmentation based on the image brightness was conducted to exclude black pixels from the analysis. Furthermore, the mean brightness value for the residuary pixels was calculated. The mean brightness value corresponds to the signal intensity of the fluorophore SR101 encapsulated by the NCs, thus providing information about its release status.

2.6. Cell viability tests

2.6.1. Cell culture and cell viability assay

Human HaCaT keratinocytes (DKFZ, Heidelberg, Germany) were grown in Dulbecco's modified Eagle's medium (DMEM, high glucose, PAN-Biotech GmbH, Aidenbach, Germany) supplemented with 10% (*v/v*) fetal bovine serum (Life Technologies, Carlsbad, CA, USA) and 2 mM L-glutamine (ccPro, Oberdorla, Germany) in a humidified atmosphere (37 °C, 5% CO_2, HeraCel 150i, Thermo Scientific, Waltham, MA, USA). The cells were subcultured twice a week and cell viability was assessed using trypan blue exclusion. The morphology of the cells was checked regularly. Before starting the experiment, the absence of mycoplasma was tested. The influence of TDI-PU-NCs and IPDI-PU-NCs on cell viability was tested using the MTT assay. The HaCaT keratinocytes were seeded into 96 well cell culture plates with a density of 0.1 × 106 cells/ml and a volume of 100 µl/well. The cells were incubated for 47 h following treatment with the NC dispersion in decreasing concentrations (2-fold dilution in each row) in Hank's balanced salt solution (HBSS, ccPro, Oberdorla, Germany) with 0.1% Tween 20 (Sigma-Aldrich, St. Louis, MO, USA) before and after UV-induced cleavage of the NCs (see **Section 2.6.2.**). The cells were exposed to different concentrations of each dispersion, determined via measuring of the optical density at λ = 600 nm (OD_{600}) (Helios Omega, Thermo Scientific, Waltham, MA, USA). After treatment of the cells for 1 h in humidified atmosphere (37 ◦C, 5% CO_2), cells were washed with 100 µl HBSS once and fresh medium containing 0.5 mg/ml 3-(4,5-dimethylthiazol-2-yl)-2,5-diphenyltetrazolium bromide (MTT, Sigma-Aldrich, St. Louis, MO, USA) was added. The cells were further incubated for 3 h. Subsequently, the supernatant was discarded and the cells were lysed using isopropanol/HCl (0.04 M) (both Carl Roth, Karlsruhe, Germany) for 15 min while shaking. The absorption of solubilized formazan was measured in a microplate reader (PowerWave XS, BIO-TEK, Winooski, VT, USA) at λ = 570 nm and λ = 650 nm. HBSS (with 0.1% Tween 20) served as a negative control while

sodium dodecyl sulfate (SDS, 0.2%) (AppliChem, Darmstadt, Germany) was used as a positive control.

2.6.2. Transfer of the nanocapsules and UV-induced cleavage for cell viability assays

For the cell viability assays, the NCs had to be transferred into a salt solution to prevent cytotoxicity of the solvent. Therefore, 100 µl of each NC dispersion in cyclohexane was transferred into a micro reaction tube and centrifuged for 5 min at 5.500 × g (Biofuge fresco, Heraeus, Hanau, Germany). The supernatant was discarded and the pellet was redispersed in 1 ml HBSS with 0.1% Tween 20 using ultrasound for 30 min. Afterwards, the dispersion was transferred into a glass vial and stirred without lid for at least 30 min (300 rpm) to evaporate residual cyclohexane. 50 µl of the dispersion was mixed with 950 µl HBSS and the OD_{600} was measured. For cleavage of the NCs, each dispersion was transferred into a glass vial and placed directly on a LED (NCSU033b, Nichia, Anan, Japan) emitting at a peak wavelength of λ = 365 nm (interpolated power density of 30.06 mW/cm^2). The irradiation was conducted over a time period of 3 min.

2.7. Statistical analysis

The calculation of mean values and standard deviations of the follicular penetration depth and brightness of the NCs as well as corresponding statistical tests were carried out via IBM SPSS® Statistics 25 (IBM, Armonk, NY, USA). The normal distribution of the data was proven by the Shapiro–Wilk test. If the data were normally distributed, variance homogeneity was checked by means of the Levene's test. Due to variance heterogeneity, a Welch-adapted one-way analysis of variance (one-way ANOVA), followed by Games–Howell post hoc tests, was utilized to compare the penetration depth and brightness. If the data distribution was non-normal, a Kruskal–Wallis ANOVA, followed by Bonferroni post hoc tests, was conducted to compare the penetration depth and brightness. For the statistical analysis of cell viability assays, GraphPad Prism 8 (GraphPad Software, San Diego, CA, USA) was utilized. A Welch-adapted one-way ANOVA followed by Dunnett's T3 multiple comparison tests was conducted if data were normally distributed. Non-normally distributed data were analyzed by a Kruskal- Wallis ANOVA followed by Dunn's multiple comparison tests. All statistical tests were conducted affording a significance of $p < 0.05$.

3. Results and discussion

3.1. Synthesis and characterization of polyurethane nanocapsules

During the preparation of the NCs, photosensitive *o*-nitrobenzyl blocks have been incorporated into the main chain of the shell-forming polyurethane by means of a mixed interfacial polyaddition reaction of EG and NXG (UV-sensitive block) with the two different isocyanates TDI and IPDI (**Figure 1**). The obtained NCs exhibited a spherical shape as examined by TEM (**Figure 2A, B**). After irradiation with a UV low-pressure lamp at a wavelength of 366 nm for 20 min, a significant burst of the NCs was observed (**Figure 2C, D**). Corresponding size characteristics, obtained by DLS, are depicted in **Table 2**. During the sample preparation for the TEM experiment, the NCs collapsed due to drying. This phenomenon has already been described in previous publications [43]. Therefore, TEM images revealed higher NC diameters in comparison to DLS data.

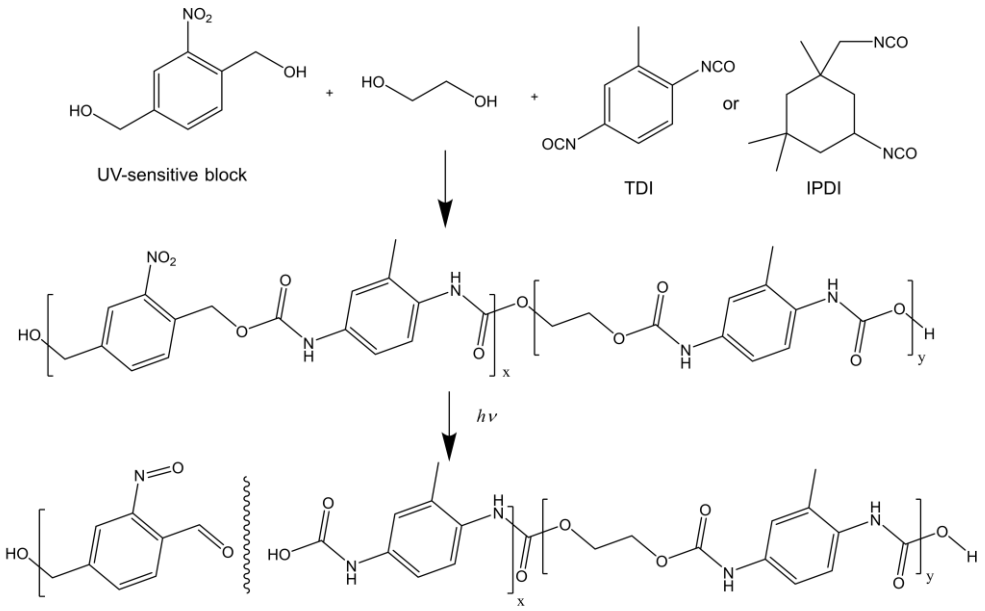

Figure 1: Formation of the polymer for the polyurethane shell of NCs and UV light-induced cleavage of the polymer.

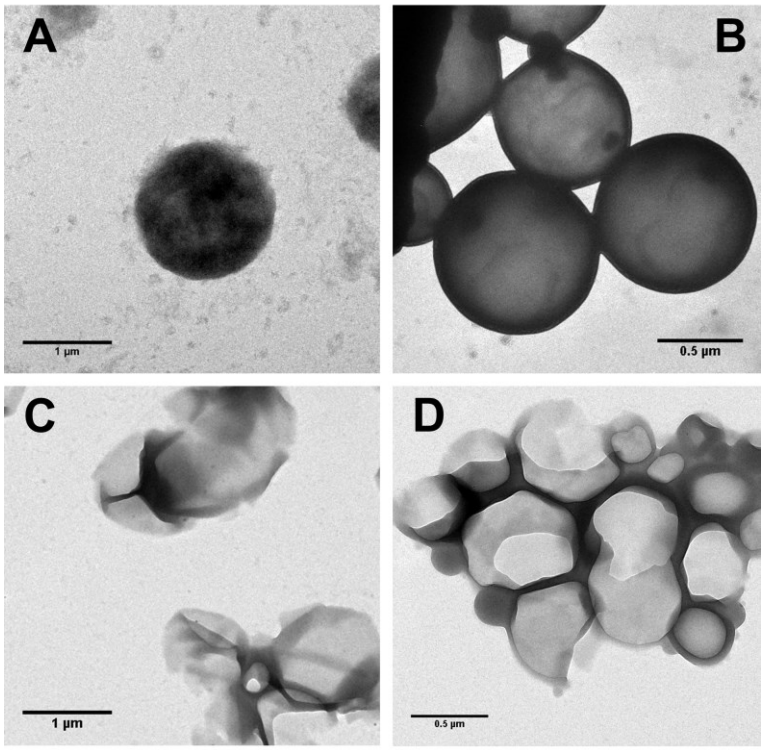

Figure 2: TEM images of the samples TDI-PU-NC (**A**) and IPDI-PU-NC (**B**) as well as TDI-PU-NC after 20 min UVA irradiation (**C**) and IPDI-PU-NC after 20 min UVA irradiation (**D**).

From literature, it is known that NCs with a mean diameter of approximately 600 nm penetrate deeper into porcine hair follicles than smaller or larger particles [6]. With average diameters of 703 nm (TDI-PU-NC) and 741 nm (IPDI-PU-NC), respectively, the NCs provided an appropriate size for an efficient follicular penetration depth. A second peak of 5.37 µm (8% of total intensity) was observed in the size distribution of the TDI-PU-NCs contributing to an increased PDI. The relatively high PDI values, as presented in **Table 2**, may have been caused by crosslinking of two NCs by the reaction of the corresponding diisocyanate and free hydroxyl groups at the surface of every NC.

Table 2: Size characteristics of polyurethane NCs as obtained by DLS.

Sample	Z-average [nm]	PDI	Main size by intensity (±SD) [nm]
TDI-PU-NC	703	0.64	575 (±144)
IPDI-PU-NC	741	0.46	603 (±157)

3.2. *In vitro* release kinetics of the model drug SR101

A biphasic inverted release kinetics of the model drug SR101, including an initial time-dependent and a subsequent time-independent liberation, became apparent after irradiation of the dispersions IPDI-PU-NC and TDI-PU-NC with UVA *in vitro*. Initially measured shaded controls of the dispersions revealed a signal loss of merely 1%, which indicated that a degradation of the NCs occurred only during UVA-irradiation (**Figure 3A**). After two minutes of irradiation at a peak wavelength of 365 nm and a power density of approximately 12 mW/cm^2, a loss of the initial signal by 54% (TDI-PU-NC) and 58% (IPDI-PU-NC) was obtained in accordance with a burst release. These findings are comparable with results of Lv et al., which were achieved with polyurethane NPs [18] or polyester NPs [44] after *in vitro* irradiation at 365 nm, 11 mW/cm^2

and a duration of 2 min. As published by Jiang et al., *in vitro* release kinetics of micellar systems were lower in comparison to the results presented in this work, even with application of the 4-fold power density of UVA, whereas higher release rates were obtained when the power density of UVA was 12- to 167-fold [45]. After six minutes of irradiation, a predominantly linear, time-independent release was observed. Thus, after eight minutes of cumulative irradiation, a signal decrease of 69% (TDI-PU-NC) and 71% (IPDI-PU-NC) was achieved, which corresponded to the macroscopic appearance of the dispersions (**Figure 3C**). A total decrease in fluorescence intensity of 78% appeared after 15 min of irradiation (both dispersions). Thus, the IPDI-PU-NCs exhibited a higher release capability, although the irradiation caused an approximation of the signals of both NC types. The time-dependent change of the IPDI-PU-NC spectrum is depicted in **Figure 3B**. We concluded that the characteristic inverted release kinetics was based on the loss of fluorescence signal of the model drug SR101 during its liberation from the NCs. To exclude a possible source of bias, we conducted a control experiment: by irradiating aqueous SR101 solution, we could not observe any effect of photobleaching of SR101. Furthermore, SR101 did not exhibit any solubility in cyclohexane. Excitation of solid SR101 in cyclohexane via CLSM did not lead to a detectable fluorescence signal. Moreover, resuspending precipitated SR101 after its liberation from the NCs did not effect any change of fluorescence intensity as measured spectroscopically. Consequently, the observed release kinetics is most likely based on the loss of fluorescence signal of the model drug SR101 due to its transfer from the polar intraparticulate (water) to the apolar extraparticulate (cyclohexane) compartment along with recrystallization after liberation.

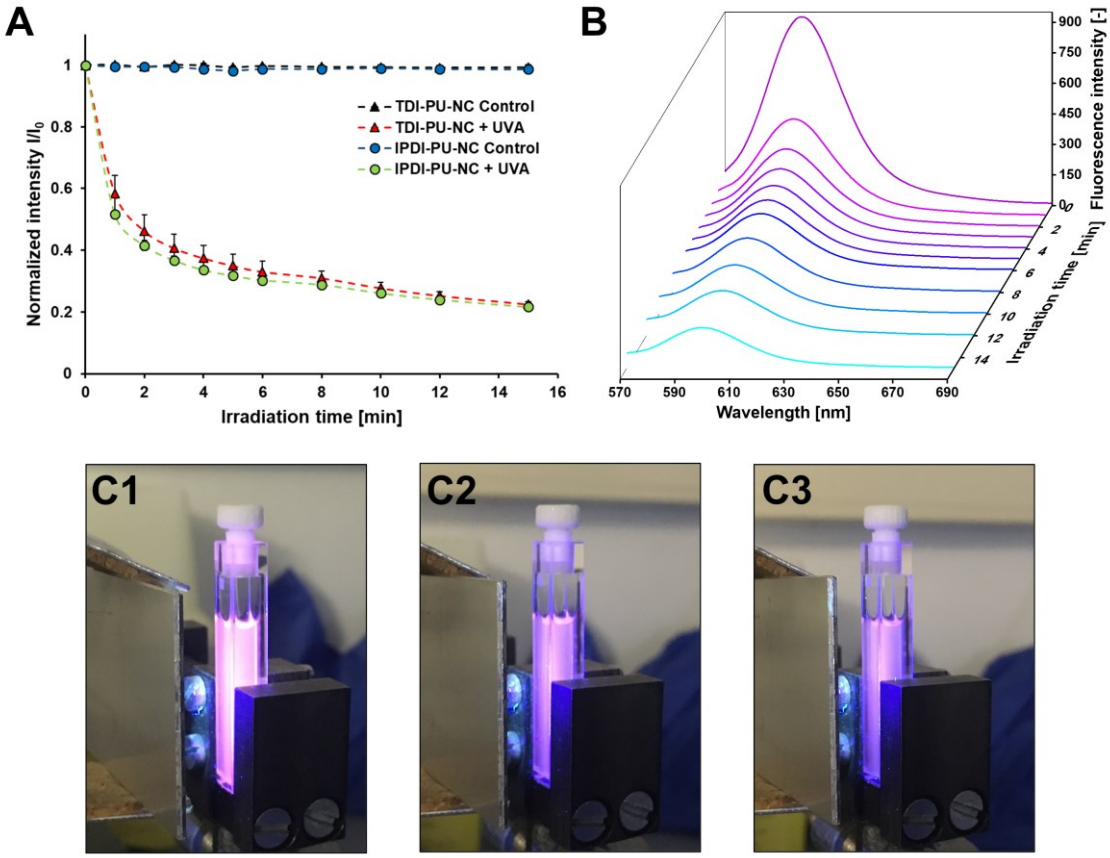

Figure 3: (**A**): Course of the irradiation time-dependent, normalized fluorescence intensity I/I_0 of the dispersions TDI-PU-NC and IPDI-PU-NC and their respective shaded controls, corresponding with the release kinetics of SR101. Excitation at a wavelength of λ_{ex} = 550 nm via fluorescence spectroscopy. Presentation of mean values with the corresponding standard deviations (error bars) of n = 3 independent experiments. (**B**): Averaged irradiation time-dependent fluorescence spectra of the IPDI-PU-NC dispersion. Micro cuvettes with IPDI-PU-NC dispersions at the beginning of irradiation (**C1**); after two minutes of irradiation (**C2**); after eight minutes of irradiation (**C3**).

3.3. *Ex vivo* follicular penetration of the nanocapsules and release of the model drug SR101

3.3.1. Preliminary experiment

A preliminary experiment was conducted on an *ex vivo* porcine skin model to establish the previously detected UVA-responsive properties of the NCs on skin. In this context, TDI-PU-NCs and IPDI-PU-NCs were analyzed for their capacity of liberation (brightness) as well as their penetration depth on n = 10 HFs (n = 1 donor) per group to determine the more efficient NC type.

3.3.1.1. Penetration depth

IPDI-PU-NCs exhibited a mean penetration depth of 491 ± 112 µm. This was significantly enhanced in comparison to the penetration depth of TDI-PU-NCs, which was determined at 342 ± 23 µm ($p < 0.01$) (**Figure 4A**). An influence on the follicular penetration depths due to material or due to size of the NCs has to be taken into consideration [6]. In this context, the lower PDI obtained for IPDI-PU-NCs (see **Section 3.1.**) might be an explanation for the higher follicular penetration depth observed, since polydispersity might affect the transport process of the NCs. After two minutes of irradiation of the respective NCs *ex vivo*, no statistically significant change of penetration depth was ascertainable ($p > 0.05$).

3.3.1.2. Brightness

The characteristics of both NC types with regard to the parameter brightness, initially and after two minutes of irradiation, are presented in **Figure 4B**. This parameter corresponded with the fluorescence intensity and therefore also indicated the localization (release status) of the model drug SR101 (intraparticulate signal > extraparticulate signal). A highly significant difference between the groups IPDI-PU-NC and TDI-PU-NC was ascertained ($p < 0.0001$). In this connection, the mean brightness of the TDI-PU-NCs turned out to be 68% lower than the brightness of the IPDI-PU-NCs. Considering that, as already mentioned, the mean follicular penetration depth of the IPDI-PU-NCs was significantly higher compared to the penetration depth of the TDI-PU-NCs (see **Section 3.1.1.1.**), it is assumable that the observed penetration depth also involved a function of signal intensity, possibly as a result of different loading capacities. After two minutes of irradiation with UVA, a highly significant loss of brightness of 42% ($p < 0.001$) was detectable within the IPDI-PU-NC group. Corresponding with the results of the *in vitro* experiment (**Section 3.2.**), this can be interpreted as an indicator for the release of SR101. Within the TDI-PU-NC group this effect was not observed ($p > 0.05$), probably because the fluorescence intensity had been low from the start. Thus, differences were hard to represent due to approximation to a lower boundary of detection. Consequently, the IPDI-PU-NC dispersion was utilized in the main experiment.

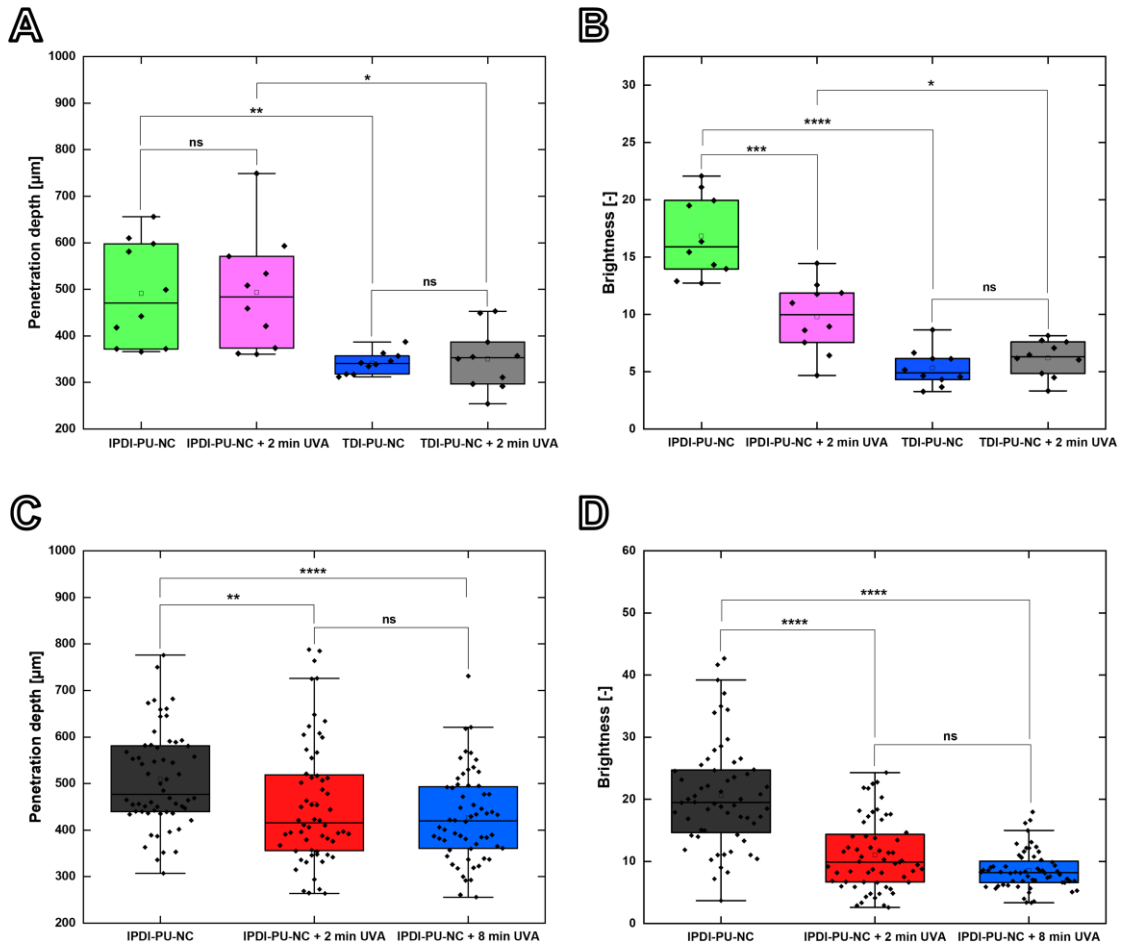

Figure 4: Boxplots of the groups IPDI-PU-NC, IPDI-PU-NC + 2 min UVA, TDI-PU-NC, and TDI-PU-NC + 2 min UVA, investigated in the preliminary experiment for penetration depth (**A**) and brightness (**B**) with n = 10 HFs (n = 1 donor) in each case. Presentation of the statistical significance obtained by the post hoc Games–Howell test (according to Welch-ANOVA) with: ns = $p > 0.05$ (no significance); * = $p < 0.05$; ** = $p < 0.01$; *** = $p < 0.001$; **** = $p < 0.0001$. Boxplots of the groups IPDI-PU-NC, IPDI-PU-NC + 2 min UVA, and IPDI-PU-NC + 8 min UVA, investigated in the main experiment for penetration depth (**C**) and brightness (**D**) with n = 60 HFs (n = 6 donors). Presentation of the statistical significance obtained by the post hoc Bonferroni test (according to Kruskal–Wallis test) with: ns = $p > 0.05$ (no significance); ** = $p < 0.01$; **** = $p < 0.0001$.

3.3.2. Main experiment

3.3.2.1. Penetration depth

Based on the results of the preliminary experiment, IPDI-PU-NCs were selected for the *ex vivo* main experiment. The mean follicular penetration depth initially (without irradiation) amounted to 509 ± 104 µm. Mak et al. achieved penetration depths of > 800 µm by utilizing NCs, made of bovine serum albumine (BSA), with average sizes of 532 nm and 500 nm [9, 14]. Tran et al. obtained penetration depths of over 400 µm with BSA-NCs of 663 nm in diameter [10]. Lademann et al. reached a mean penetration depth of > 700 µm by applying gold-coated BSA-NCs of 545 nm in size [8]. Influential factors on the experiments of the present study could

have been the size and PDI as well as the diverging material of the NCs (polyurethane). The NC material, however, seems to play a subordinate role in influencing the ability of follicular penetration compared to the average diameter, but nevertheless represents a potential influencing factor [6]. A significant influence of the vehicle on the follicular penetration depth of NPs seems to be minor if no gelling agents are used [46]. After two minutes of irradiation with UVA, a decrease in follicular penetration depth to 456 ± 134 µm was observed ($p < 0.01$). The follicular penetration depth further dropped to 427 ± 96 µm after eight minutes of irradiation ($p < 0.0001$) (**Figure 4C**). A statistically significant difference between the two final irradiation times was not detectable regarding the penetration depth ($p > 0.05$). Exemplary images including the entire pilosebaceous unit demonstrate that the fluorescence signal of SR101 is traceable until the excretory ducts of the sebaceous glands before irradiation (**Figure 5**).

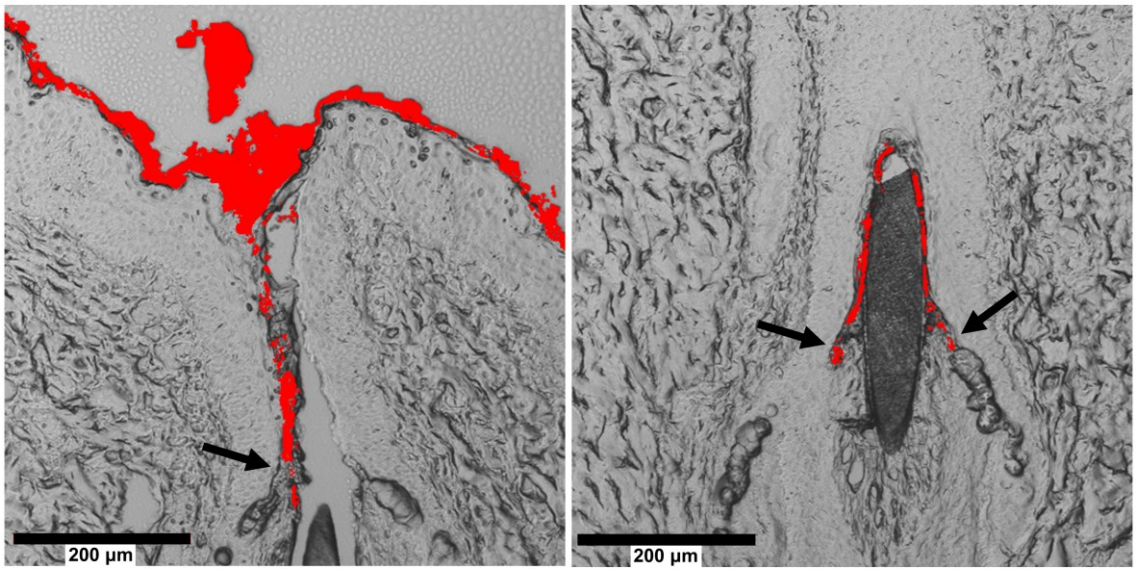

Figure 5: CLSM images of two HFs including NC-associated, SR101-emitted fluorescence. Superimposition of the transmission mode and the fluorescence mode. The exits of sebaceous glands are marked by black arrows. The signal of fluorescence was illustrated with a maximum contrast for the purpose of an improved visualization.

As already described for the preliminary experiment (**Section 3.3.1.2.**), the phenomenon of irradiation-dependent reduction of the penetration depth probably corresponds to a loss of brightness and therefore might be based on a deletion of the fluorescence signal. This leads to the conclusion that the phenomenon involved a pseudo-loss of penetration because biasing effects such as sebum flow are excludable under *ex vivo* conditions.

3.3.2.2. Brightness

The fluorescence of the CLSM images exhibited a gradual decrease of brightness after two minutes and eight minutes of UVA irradiation of IPDI-PU-NC-treated *ex vivo* porcine skin.

Equivalent to the burst release observed in the *in vitro* model (**Section 3.2.**), a highly significant loss of brightness after two minutes of irradiation (46%) was recognized ($p < 0.0001$) (**Figure 4D**). The decrease of brightness after eight minutes of irradiation amounted to 59% relating to the initial value ($p < 0.0001$), but showed minor differences with regard to the two-minute irradiation ($p > 0.05$). This saturation effect is also comparable with the *in vitro* release kinetics. The intrafollicular decrease of fluorescence brightness therefore indicates the liberation of SR101 *ex vivo*. Pseudo- 3D-plots, including the variable “brightness” applied to the z-axis, serve to visualise the phenomenon based on representative CLSM images of the three treatment groups (**Figure 6**). The loss of fluorescence brightness of SR101 might have been caused by insolubility of SR101 in the apolar intrafollicular environment (comparison to **Section 3.2.**), which is mainly represented by the sebum lipids secreted by sebaceous glands of the pilosebaceous units [47]. Until now, an intrafollicular drug release from NCs could be triggered by infrared light [8], enzymatically [9, 14], and by a concentration gradient [10]. In a recent study, Dong et al. presented the possibility of a pH-responsive drug release from NCs, which generated a significantly increased intrafollicular accumulation as well as an increased transfollicular penetration of a model drug in comparison to reference galenics [11]. However, in the present study an intrafollicular UVA-triggered drug release from NCs was shown for the first time to the best of our knowledge.

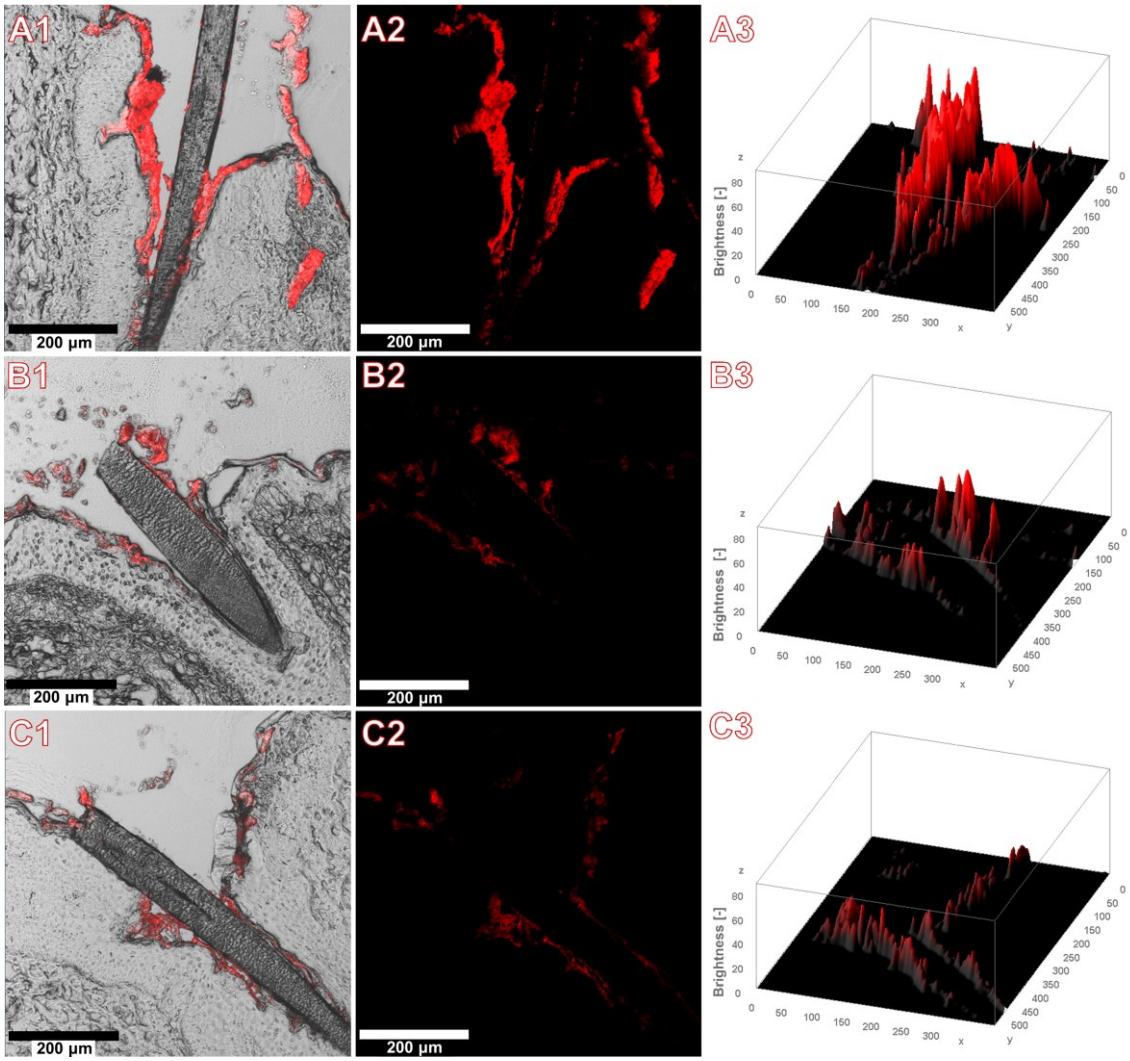

Figure 6: CLSM images of representative HFs including NC-associated, SR101-emitted fluorescence with (**A1/A2/A3**): IPDI-PU-NC (transmission + fluorescence/ fluorescence only/pseudo-3D-plot for the parameter brightness); (**B1/B2/B3**): IPDI-PU-NC + 2 min UVA; (**C1/C2/C3**): IPDI-PU-NC + 8 min UVA.

3.4. Cell viability

After treatment of HaCaT keratinocytes with the highest concentration of intact TDI-PU-NCs tested in this study (OD_{600} = 0.271), cell viability decreased to 77.51% in comparison to untreated cells. With lower PU-NC concentration, cell viability increased up to 84.20% (**Figure 7A**). Similar results were achieved by treating the cells with IPDI-PU-NCs. The treatment with the IPDI-PU-NCs decreased the cell viability to 61.00% for the highest concentration tested (OD_{600} = 0.178). A cell viability > 70% was reached by using a dispersion with OD_{600} = 0.045 (**Figure 7B**). UV-cleaved TDI-PU-NCs had a slightly higher effect on cell viability. A cell viability > 70% was reached by using a dispersion of UVA-cleaved NCs with an OD_{600} = 0.022 (**Figure 7C**). A lower drop of HaCaT viability was observed for IPDI-PU-NCs after UVA-induced cleavage. Here, a cell viability of > 70% was reached with a dispersion of OD_{600} = 0.045 (**Figure 7D**). A concentration of a substance leading to a loss of cell viability of over 30% is assigned

as cytotoxic according to DIN 10993–5. Thus, the 30% cell viability inhibition concentration (IC30) as determined by non-linear regression was used to describe a limit value. Even in the highest concentration of TDI-PU-NCs (OD_{600} = 0.271) used in the current experiment, cell viability was reduced by maximum 22.49% after 1 h of incubation. Hence, the dispersion was not classified as cytotoxic. A dispersion of IPDI-PU-NCs with an $OD_{600} \leq 0.05$ (IC30 = 0.05) was also regarded as non-cytotoxic. The IC30 for UVA-cleaved TDI-PU-NCs corresponded to an OD_{600} = 0.02. UVA-cleaved IPDI-PU-NCs were regarded as non-cytotoxic for concentrations of $OD_{600} \leq 0.06$. The increased drop of cell viability after UVA-induced cleavage of TDI-PU-NCs in comparison to IPDI-PU-NCs might have been caused by the lower biocompatibility known for aromatic diisocyanates in comparison to aliphatic diisocyanates [15, 17, 48, 49].

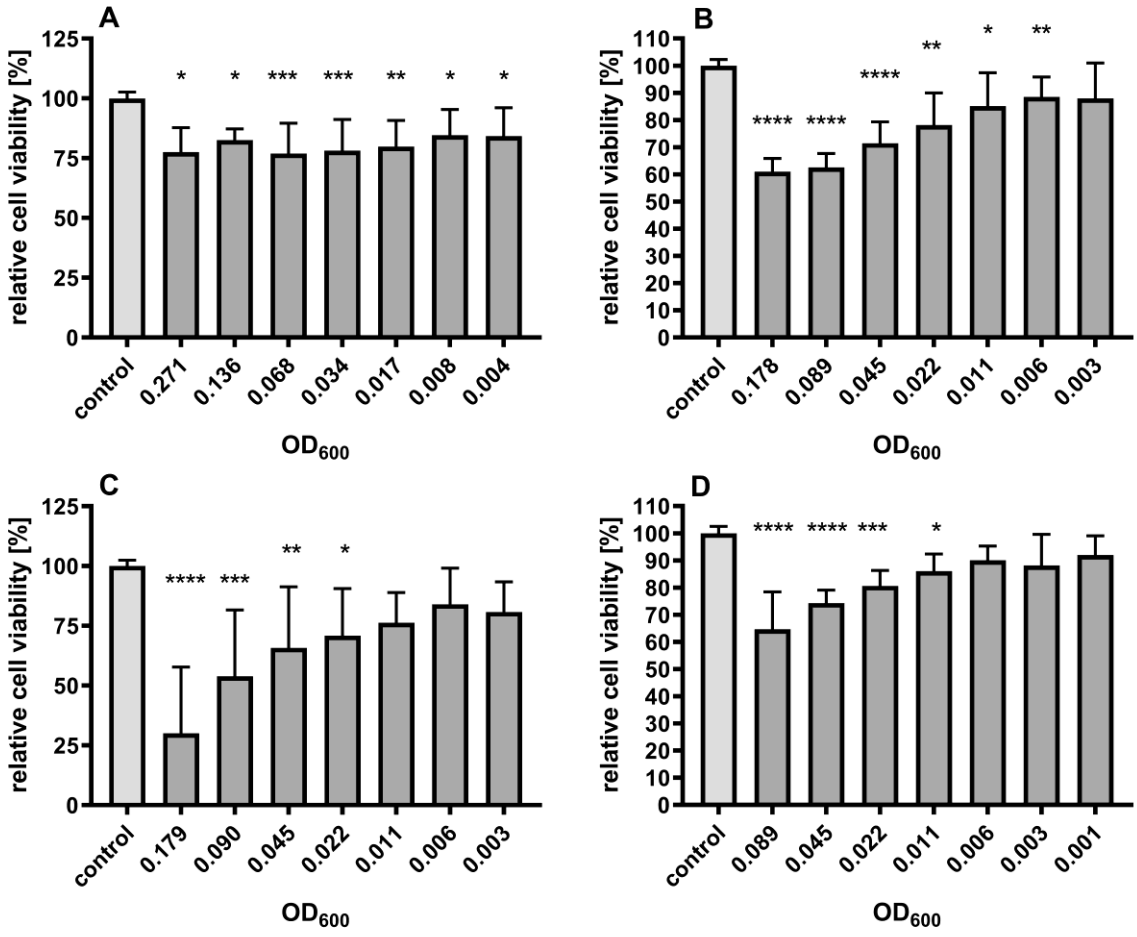

Figure 7: Cell viability of HaCaT keratinocytes after treatment with different concentrations of PU-NCs for 1 h following cell viability assessment via MTT. Treatment with (**A**): Intact TDI-PU-NCs; (**B**): Intact IPDI-PU-NCs; (**C**): UVA-cleaved TDI-PU-NCs; (**D**): UVA-cleaved IPDI-PU-NCs. Presentation of the statistical significance obtained by Dunn's post hoc test according to Kruskal–Wallis ANOVA (**A,C,D**) or Dunnett's T3 post hoc test according to Welch-adapted one-way ANOVA (**B**) with: * = $p < 0.05$, ** = $p < 0.01$, *** = $p < 0.001$, **** = $p < 0.0001$ with n = 3 biological replicates except for (**A**) OD_{600} = 0.271, (**D**)

OD_{600} = 0.001: *n* = 1 and (**A**) OD_{600} = 0.136, (**B**) OD_{600} = 0.178, (**C**) OD_{600} = 0.179 and OD_{600} = 0.003: *n* = 2. 3 technical replicates were conducted in each case.

3.5. Translational outlook

Due to the burst release characteristics and the overall high responsivity of the polyurethane NCs at a relatively low power density of the applied UVA light, the presented system can be excellently implementable in clinical application, like, e.g., preoperative skin antisepsis, where short application times represent a clear benefit. Previous studies revealed that the involvement of antiseptics into NCs promises an enhanced efficiacy of skin antisepsis [50-53]. A considerable proportion of the skin microbiome is localized within both the infundibulum and the excretory ducts of the sebaceous glands. Thus, 80% of the pathogens are detectable to a depth of 300 µm [54]. Based on this fact, a remarkable antisepsis of the hair follicle could be accomplished by the mean follicular penetration depth of 509 ± 104 µm of the IPDI-PU-NCs. Additionally, also the safety of patients has to be taken into consideration. UVA-LEDs for clinical use have the advantage of a high-area illumination, while exhibiting a not too high power density, thus preventing potential tissue damage [25]. The power density applied in the present study (11.96 mW/cm^2 at a wavelength of 365 nm) is classified below the calculated limit value for actinic damage according to the International Commission on Non-Ionizing Radiation Protection (ICNIRP). This corresponds to 5.3% of the limit value (227.27 mW/cm^2) for an irradiation of two minutes, and to 21% of the limit value (56.82 mW/cm^2) for an irradiation of eight minutes, respectively. Consequently, a considerable release of a certain drug at the targeted location is reachable at shorter exposure times without risking radiation-induced tissue damage. Various non-drug-loaded stimuli-responsive polyurethane NPs exhibit a high biocompatibility as well as low cytotoxicity [18, 55-60]. The IPDI-PU-NCs of the present study are preferable to TDI-PU-NCs because of their higher biocompatibility after UVA-induced cleavage, which is in consistency with previous publications [15, 17, 48, 49]. To assess the susceptibility of the system for inducing UVA-mediated reactive oxygen species in the skin, spectroscopic analyses of *ex vivo* skin, e.g. via electron paramagnetic resonance [61-63], should nevertheless be implemented. Advantages of the application of UVA light in comparison to other triggers (see **Section 3.3.2.2.**) are for example the controllability (in comparison to pH or concentration gradients) or the temperature independence (in comparison to IR irradiation). As already mentioned, the follicular penetration process of NCs is strongly depending on the movement of the hair [13]. Recent results demonstrate that a significantly increased penetration depth of NCs is reachable by applying a massage at a relatively low frequency (approximately 4 Hz) compared to the here utilized frequency (50 Hz) [64]. This might represent a major advantage for application of the proposed system within the clinical field. For example, in the

preoperative skin antiseptic procedure such low frequency could be obtained by manual massage, as also recommended by Kramer et al. [54].

4. Conclusions

In the present study, we introduced a novel system for anatomically and temporally targeted intrafollicular drug release, which can be applied for miscellaneous clinical purposes. Low power density UVA radiation emitted by an UVA-LED induced an over 50% release of the model drug SR101 from polyurethane NCs after two minutes in the course of an inverse burst release profile *in vitro*. UVA-responsive degradation of the NCs at a mean follicular penetration depth of 509 ± 104 µm led to a tempo-spatial controlled liberation of SR101. Thus, for the first time, a UVA-triggered intrafollicular drug release from NCs was demonstrated. A considerable and controllable release can be reached by means of this preclinical model without risking any irradiation-related tissue damage. Due to the higher biocompatibility after UVA-induced cleavage and higher drug delivery performance, IPDI-PU-NCs are preferable for further application in comparison to TDI-PU-NCs. As a result, the proposed system is a promising approach for the therapy of different skin diseases or preoperative skin antisepsis and recommendable for future implementation into clinical practice.

References

[1] A. Patzelt, J. Lademann, Recent advances in follicular drug delivery of nanoparticles, Expert Opin Drug Deliv 17 (1) (2020) 49-60.

[2] J. Lademann, H. Richter, A. Teichmann, N. Otberg, U. Blume-Peytavi, J. Luengo, B. Weiss, U.F. Schaefer, C.-M. Lehr, R. Wepf, W. Sterry, Nanoparticles–an efficient carrier for drug delivery into the hair follicles, Eur J Pharm Biopharm 66 (2) (2007) 159-164.

[3] J. Lademann, A. Patzelt, H. Richter, C. Antoniou, W. Sterry, F: Knorr, Determination of the cuticula thickness of human and porcine hairs and their potential influence on the penetration of nanoparticles into the hair follicles, J Biomed Opt 14 (2) (2009) 21014.

[4] Vogt, A., Wischke, C., Neffe, A.T., Ma, N., Alexiev, U., Lendlein, A., Nanocarriers for drug delivery into and through the skin - Do existing technologies match clinical challenges?, J Control Release 242 (2016) 3-15.

[5] R. Alvarez-Roman, A. Naik, Y.N. Kalia, R.H. Guy, H. Fessi, Skin penetration and distribution of polymeric nanoparticles, J Control Release 99(1) (2004) 53-62.

[6] A. Patzelt, H. Richter, F. Knorr, U. Schäfer, C.M. Lehr, L. Dähne, W. Sterry, J. Lademann, Selective follicular targeting by modification of the particle sizes, J Control Release 150(1) (2011) 45-48.

[7] A. Patzelt, W.C. Mak, S. Jung, F. Knorr, M.C. Meinke, H. Richter, E. Rühl, K.Y. Cheung, N. Tran, J. Lademann, Do nanoparticles have a future in dermal drug delivery?, J Control Release 246 (2017) 174-182.

[8] J. Lademann, H. Richter, F. Knorr, A. Patzelt, M.E. Darvin, E. Rühl, K.Y. Cheung, K.K. Lai, R. Renneberg, W.C. Mak, Triggered release of model drug from AuNP-doped BSA nanocarriers in hair follicles using IRA radiation, Acta Biomater 30 (2016) 388-396.

[9] W.C. Mak, A. Patzelt, H. Richter, R. Renneberg, K.K. Lai, E. Rühl, W. Sterry, J. Lademann, Triggering of drug release of particles in hair follicles, J Control Release 160(3) (2012) 509-514.

[10] N. Tran, F. Knorr, W.C. Mak, K.Y. Cheung, H. Richter, M. Meinke, J. Lademann, A. Patzelt, Gradient-dependent release of the model drug TRITC-dextran from FITC-labeled BSA hydrogel nanocarriers in the hair follicles of porcine ear skin, Eur J Pharm Biopharm 116 (2017) 12-16.

[11] P. Dong, F.F. Sahle, S.B. Lohan, S. Saeidpour, S. Albrecht, C. Teutloff, R. Bodmeier, M. Unbehauen, C. Wolff, R. Haag, J. Lademann, A. Patzelt, M. Schafer-Korting, M.C. Meinke,

pH-sensitive Eudragit(R) L 100 nanoparticles promote cutaneous penetration and drug release on the skin, J Control Release 295 (2019) 214-222.

[12] R. Goyal, L.K. Macri, H.M. Kaplan, J. Kohn, Nanoparticles and nanofibers for topical drug delivery, J Control Release 240 (2016) 77-92.

[13] M. Radtke, A. Patzelt, F. Knorr, J. Lademann, R.R. Netz, Ratchet effect for nanoparticle transport in hair follicles, Eur J Pharm Biopharm 116 (2017) 125-130.

[14] W.C. Mak, H. Richter, A. Patzelt, W. Sterry, K.K. Lai, R. Renneberg, J. Lademann, Drug delivery into the skin by degradable particles, Eur J Pharm Biopharm 79(1) (2011) 23-27.

[15] J.Y. Cherng, T.Y. Hou, M.F. Shih, H. Talsma, W.E. Hennink, Polyurethane-based drug delivery systems, Int J Pharm 450 (2013) 145-162.

[16] C. Mattu, R.M. Pabari, M. Boffito, S. Sartori, G. Ciardelli, Z. Ramtoola, Comparative evaluation of novel biodegradable nanoparticles for the drug targeting to breast cancer cells, Eur J Pharm Biopharm 85 (2013) 463-472.

[17] G. Morral-Ruíz, P. Melgar-Lesmes, M.L. García, C. Solans, G.J. García-Celma, Polyurethane and polyurea nanoparticles based on polyoxyethylene castor oil derivative surfactant suitable for endovascular applications, Int J Pharm (2013) 461, 1-13.

[18] C. Lv, Z. Wang, P. Wang, X. Tang, Photodegradable polyurethane self-assembled nanoparticles for photocontrollable release, Langmuir 28(25) (2012) 9387-9394.

[19] R.M. Pabari, C. Mattu, S. Partheeban, A. Almarhoon, M. Boffito, G. Ciardelli, Z. Ramtoolaa, Novel polyurethane-based nanoparticles of infliximab to reduce inflammation in an in-vitro intestinal epithelial barrier model, Int J Pharm 565 (2019) 533-542.

[20] U. Paiphansiri, J. Dausend, A. Musyanovych, V. Mailänder, K. Landfester, Fluorescent polyurethane nanocapsules prepared via inverse miniemulsion: surface functionalization for use as biocarriers, Macromol Biosci 9(6) (2009) 575-584.

[21] F. Tiarks, K. Landfester, M. Antonietti, One-step preparation of polyurethane dispersions by miniemulsion polyaddition, J Polym Sci A Polym Chem 39(14) (2001) 2520-2524.

[22] S. Bühler, I. Lagoja, H. Giegrich, K.-P. Stengele, W. Pfleiderer, New Types of Very Efficient Photolabile Protecting Groups Based upon the[2-(2-Nitrophenyl)propoxy]carbonyl (NPPOC) Moiety, Helv Chim Acta 87(3) (2004) 620-659.

[23] C.P. Holmes, D.G. Jones, Reagents for Combinatorial Organic Synthesis: Development of a New o-Nitrobenzyl Photolabile Linker for Solid Phase Synthesis, J Org Chem 60(8) (2002) 2318-2319.

[24] D. Klinger, K. Landfester, Polymeric photoresist nanoparticles: light-induced degradation of hydrophobic polymers in aqueous dispersion, Macromol Rapid Commun 32(24) (2011) 1979-1985.

[25] S.I. Ahmad, L. Christensen, E. Baron, History of UV Lamps, Types, and Their Applications, Adv Exp Med Biol 996 (2017) 3-11.

[26] A. Khan, K. Balakrishnan, T. Katona, Ultraviolet light-emitting diodes based on group three nitrides, Nat Photonics 2(2) (2008) 77-84.

[27] F.H. Fan, Z.Y. Syu, C.J. Wu, Z.J. Yang, B.S. Huang, G.J. Wang, Y.S. Lin, H. Chen, C. Hauer Kao, C.F. Lin, Ultraviolet GaN Light-Emitting Diodes with Porous-AlGaN Reflectors, Sci Rep 7(1) (2017) 4968.

[28] G. Matafonova, V. Batoev, Recent advances in application of UV light-emitting diodes for degrading organic pollutants in water through advanced oxidation processes: A review, Water Res 132 (2018) 177-189.

[29] B. Lange-Asschenfeldt, D. Marenbach, C. Lang, A. Patzelt, M. Ulrich, A. Maltusch, D. Terhorst, E. Stockfleth, W. Sterry, J. Lademann, Distribution of bacteria in the epidermal layers and hair follicles of the human skin, Skin Pharmacol Physiol 24(6) (2011) 305-311.

[30] M. Ulmer, J. Lademann, A. Patzelt, F. Knorr, A. Kramer, T. Koburger, O. Assadian, G. Daeschlein, B. Lange-Asschenfeldt, New strategies for preoperative skin antisepsis, Skin Pharmacol Physiol 27(6) (2014) 283-292.

[31] Y. Frum, G.M. Eccleston, V.M. Meidan, In-vitro permeation of drugs into porcine hair follicles: is it quantitatively equivalent to permeation into human hair follicles?, J Pharm Pharmacol 60(2) (2008) 145-151.

[32] F. Knorr, A. Patzelt, M.E. Darvin, C.-M. Lehr, U. Schäfer, A.D. Gruber, A. Ostrowski, J. Lademann, Penetration of topically applied nanocarriers into the hair follicles of dog and rat dorsal skin and porcine ear skin, Vet Dermatol 27(4) (2016) 256-e60.

[33] J. Lademann, H. Richter, M. Meinke, W. Sterry, A. Patzelt, Which skin model is the most appropriate for the investigation of topically applied substances into the hair follicles?, Skin Pharmacol Physiol 23(1) (2010) 47-52.

[34] A.S. Raber, A. Mittal, J. Schäfer, U. Bakowsky, J. Reichrath, T. Vogt, U.F. Schaefer, S. Hansen, C.-M. Lehr, Quantification of nanoparticle uptake into hair follicles in pig ear and human forearm, J Control Release 179 (2014) 25-32.

[35] S. Mangelsdorf, T. Vergou, W. Sterry, J. Lademann, A. Patzelt, Comparative study of hair follicle morphology in eight mammalian species and humans, Skin Res Technol 20(2) (2014) 147-154.

[36] B. Starcher, R.L. Aycock, C.H. Hill, Multiple roles for elastic fibers in the skin, J Histochem Cytochem 53(4) (2005) 431-443.

[37] N. Sekkat, Y.N. Kalia, R.H. Guy, Biophysical study of porcine ear skin in vitro and its comparison to human skin in vivo, J Pharm Sci 91(11) (2002) 2376-2381.

[38] F. Benech-Kieffer, P. Wegrich, R. Schwarzenbach, G. Klecak, T. Weber, J. Leclaire, H. Schaefer, Percutaneous absorption of sunscreens in vitro: interspecies comparison, skin models and reproducibility aspects, Skin Pharmacol Appl Skin Physiol 13(6) (2000) 324-335.

[39] W. Meyer, J. Kacza, N.-H. Zschemisch, S. Godynicki, J. Seeger, Observations on the actual structural conditions in the stratum superficiale dermidis of porcine ear skin, with special reference to its use as model for human skin, Ann Anat 189(2) (2007) 143-156.

[40] F.P. Schmook, J.G. Meingassner, A. Billich, Comparison of human skin or epidermis models with human and animal skin in in-vitro percutaneous absorption, Int J Pharm 215(1-2) (2001) 51-56.

[41] G.A. Simon, H.I. Maibach, The pig as an experimental animal model of percutaneous permeation in man: qualitative and quantitative observations–an overview, Skin Pharmacol Appl Skin Physiol 13(5) (2000) 229-234.

[42] A. Patzelt, H. Richter, R. Buettemeyer, H.J.R. Huber, U. Blume-Peytavi, W. Sterry, J. Lademann., Differential stripping demonstrates a significant reduction of the hair follicle reservoir in vitro compared to in vivo, Eur J Pharm Biopharm 70(1) (2008) 234-238.

[43] G. Baier, J.M. Siebert, K. Landfester, A. Musyanovych, Surface Click Reactions on Polymeric Nanocapsules for Versatile Functionalization, Macromolecules 45(8) (2012) 3419-3427.

[44] [123] C. Lv, Z. Wang, P. Wang, X. Tang, Photodegradable polyesters for triggered release, Int J Mol Sci 13(12) (2012) 16387-16399.

[45] J. Jiang, X. Tong, D. Morris, Y. Zhao, Toward Photocontrolled Release Using Light-Dissociable Block Copolymer Micelles, Macromolecules 39(13) (2006) 4633-4640.

[46] A. Patzelt, H. Richter, L. Dähne, P. Walden, K.-H. Wiesmüller, U. Wank, W. Sterry, J. Lademann, Influence of the vehicle on the penetration of particles into hair follicles. Pharmaceutics 3(2) (2011) 307-314.

[47] A.C. Lauer, C. Ramachandran, L.M. Lieb, S. Niemiec, N.D. Weiner, Targeted delivery to the pilosebaceous unit via liposomes, Advanced Drug Delivery Reviews 18(3) (1996) 311-324.

[48] M.B. Lowinger, S.E. Barrett, F. Zhang, R.O. Williams 3rd, Sustained Release Drug Delivery Applications of Polyurethanes, Pharmaceutics 10(2) (2018) 55.

[49] A. Wang, H. Gao, Y. Sun, Y.-L. Sun, Y.-W. Yang, G. Wu, Y. Wang, Y. Fan, J. Ma, Temperature- and pH-responsive nanoparticles of biocompatible polyurethanes for doxorubicin delivery, Int J Pharm 441 (2013) 30-39.

[50] H. Lboutounne, J.F. Chaulet, C. Ploton, F. Falson, F. Pirot, Sustained ex vivo skin antiseptic activity of chlorhexidine in poly(ε-caprolactone) nanocapsule encapsulated form and as a digluconate, J Control Release 82(2-3) (2002) 319-334.

[51] H. Lboutounne, V. Faivre, F. Falson, F. Pirot, Characterization of transport of chlorhexidine-loaded nanocapsules through hairless and wistar rat skin, Skin Pharmacol Physiol 17(4) (2004) 176-182.

[52] D.T. Nhung, A.M. Freydiere, H. Constant, F. Falson, F. Pirot, Sustained antibacterial effect of a hand rub gel incorporating chlorhexdine-loaded nanocapsules (Nanochlorex), Int J Pharm 334(1-2) (2007) 166-172.

[53] M. Ulmer, A. Patzelt, T. Vergou, H. Richter, G. Müller, A. Kramer, W. Sterry, V. Czaika, J. Lademann, In vivo investigation of the efficiency of a nanoparticle-emulsion containing polihexanide on the human skin, Eur J Pharm Biopharm 84(2) (2013) 325-329.

[54] A. Kramer, C.-D. Heidecke, Präoperative Hautantiseptik und Hautschutz, Trauma Berufskrankh 17(S2) (2015) 322-329.

[55] M. Ding, X. Zeng, X. He, J. Li, H. Tan, Q. Fu, Cell internalizable and intracellularly degradable cationic polyurethane micelles as a potential platform for efficient imaging and drug delivery, Biomacromolecules 15(8) (2014) 2896-2906.

[56] Y. Guan, Y. Su, L. Zhao, F. Meng, Q. Wang, Y. Yao, J. Luo, Biodegradable polyurethane micelles with pH and reduction responsive properties for intracellular drug delivery, Mater Sci Eng C 75 (2017) 1221-1230.

[57] A.Y. Khosroushahi, H. Naderi-Manesh, H. Yeganeh, J. Barar, Y. Omidi, Novel water-soluble polyurethane nanomicelles for cancer chemotherapy: physicochemical characterization and cellular activities, J Nanobiotechnology 10 (2012) 2.

[58] M.R. Nabid, I. Omrani, Facile preparation of pH-responsive polyurethane nanocarrier for oral delivery, Mater Sci Eng C 69 (2016) 532-537.

[59] I. Omrani, N. Babanejad, H.K. Shendi, M.R. Nabid, Fully glutathione degradable water-borne polyurethane nanocarriers: Preparation, redox-sensitivity, and triggered intracellular drug release, Mater Sci Eng C 70(Pt 1) (2017) 607-616.

[60] C. Wei, Y. Zhang, Z. Song, Y. Xia, H. Xu, M. Lang, Enhanced bioreduction-responsive biodegradable diselenide-containing poly(ester urethane) nanocarriers, Biomater Sci 5(4) (2017) 669-677.

[61] T. Herrling, J. Fuchs, J. Rehberg, N. Groth, UV-induced free radicals in the skin detected by ESR spectroscopy and imaging using nitroxides, Free Radic Biol Med 35(1) (2013) 59-67.

[62] B.A. Jurkiewicz, G.R. Buettnerf, EPR Detection of Free Radicals in UV-Irradiated Skin: Mouse Versus Human, Photochem Photobiol 64(6) (1996) 918-922.

[63] S.B. Lohan, R. Müller, S. Albrecht, K. Mink, K. Tscherch, F. Ismaeel, J. Lademann, S. Rohn, M.C. Meinke, Free radicals induced by sunlight in different spectral regions - in vivo versus ex vivo study, Exp Dermatol 25(5) (2016) 380-385.

[64] L. Busch, Y. Keziban, L. Dähne, C.M. Keck, M.C. Meinke, J. Lademann, A. Patzelt, The impact of skin massage frequency on the intrafollicular transport of silica nanoparticles: Validation of the ratchet effect on an ex vivo porcine skin model, Eur J Pharm Biopharm 158 (2021) 266-272.

3.1. PUBLICATION I:

RELEASE OF THE MODEL DRUG SR101 FROM POLYURETHANE NANOCAPSULES IN PORCINE HAIR FOLLICLES TRIGGERED BY LED-DERIVED LOW DOSE UVA LIGHT

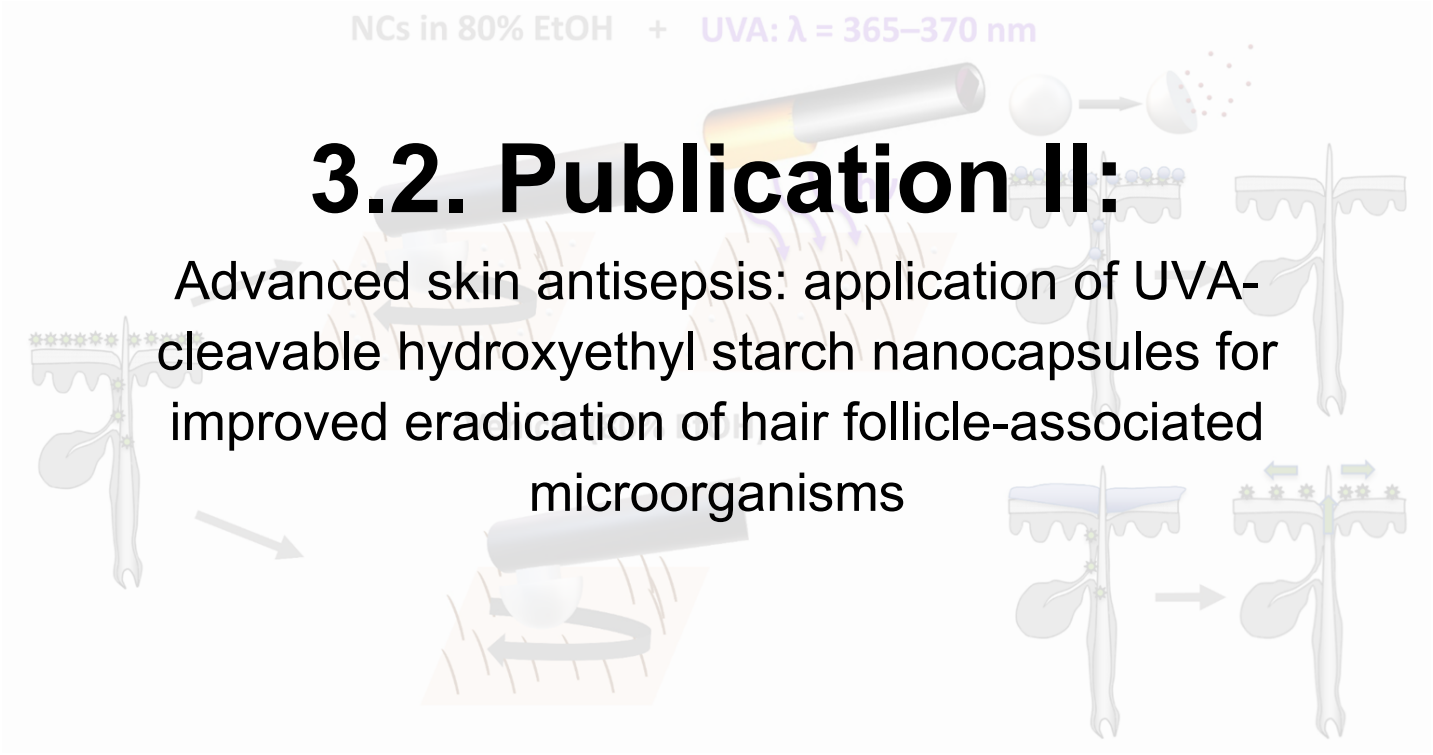

3.2. Publication II:

Advanced skin antisepsis: application of UVA-cleavable hydroxyethyl starch nanocapsules for improved eradication of hair follicle-associated microorganisms

3.2. PUBLICATION II:
ADVANCED SKIN ANTISEPSIS: APPLICATION OF UVA-CLEAVABLE HYDROXYETHYL STARCH NANOCAPSULES FOR IMPROVED ERADICATION OF HAIR FOLLICLE-ASSOCIATED MICROORGANISMS

Advanced skin antisepsis: application of UVA-cleavable hydroxyethyl starch nanocapsules for improved eradication of hair follicle-associated microorganisms

Loris Busch [1,2], Anna Maria Hanuschik [3], Yuri Avlasevich [4], Katrin Darm [5], Elisa F. Hochheiser [5], Christian Kohler [5], Evgeny A. Idelevich [5,6], Karsten Becker [5], Peter Rotsch [7], Katharina Landfester [4], Maxim E. Darvin [1], Martina C. Meinke [1], Cornelia M. Keck [2], Axel Kramer [3], Paula Zwicker [3]

[1] *Center of Experimental and Applied Cutaneous Physiology, Department of Dermatology, Venereology and Allergology, Charité-Universitätsmedizin Berlin, Corporate Member of Freie Universität Berlin and Humboldt-Universität zu Berlin, Berlin, Germany*

[2] *Department of Pharmaceutics and Biopharmaceutics, Philipps University Marburg, Marburg, Germany*

[3] *Institute of Hygiene and Environmental Medicine, University Medicine Greifswald, Greifswald, Germany*

[4] *Max Planck Institute for Polymer Research, Mainz, Germany*

[5] *Friedrich Loeffler-Institute of Medical Microbiology, University Medicine Greifswald, Greifswald, Germany*

[6] *Institute of Medical Microbiology, University Hospital Münster, Münster, Germany*

[7] *OSA Opto Light GmbH, Berlin, Germany*

(adapted from: Pharmaceutics 2023;15(2):609. doi: 10.3390/pharmaceutics15020609)

Abstract

Hair follicles constitute important drug delivery targets for skin antisepsis since they contain ≈25% of the skin microbiome. Nanoparticles are known to penetrate deeply into hair follicles. By massaging the skin, the follicular penetration process is enhanced based on a ratchet effect. Subsequently, an intrafollicular drug release can be initiated by various trigger mechanisms. Here, we present novel ultraviolet A (UVA)-responsive nanocapsules (NCs) with a size between 400 and 600 nm containing hydroxyethyl starch (HES) functionalized by an *o*-nitrobenzyl linker. A phase transfer into phosphate-buffered saline (PBS) and ethanol was carried out, during which an aggregation of the particles was observed by means of dynamic light scattering (DLS). The highest stabilization for the target medium ethanol as well as UVA-dependent release of ethanol from the HES-NCs was achieved by adding 0.1% betaine monohydrate. Furthermore, sufficient cytocompatibility of the HES-NCs was demonstrated. On *ex vivo* porcine ear skin, a strong UVA-induced release of the model drug sulforhodamine 101 (SR101) could be demonstrated after application of the NCs in cyclohexane using laser scanning microscopy. In a final experiment, a microbial reduction comparable to that of an ethanol control was demonstrated on *ex vivo* porcine ear skin using a novel UVA-LED lamp for triggering the release of ethanol from HES-NCs. Our study provides first indications that an advanced skin antisepsis based on the eradication of intrafollicular microorganisms could be achieved by the topical application of UVA-responsive NCs.

1. Introduction

Mammalian body surfaces, including skin, represent a remarkably complex and highly variable microbiological environment [1, 2, 3]. The hair follicle constitutes a special habitat with a considerable bacterial reservoir comprising about 25% of all cultivated bacteria found on the skin [4]. With conventional skin antisepsis, a penetration into the deeper parts of the hair follicle is not possible which makes these parts a protected reservoir for microorganisms [5]. Being in the hair follicles, microorganisms are constantly released to the surface, leading to recontamination of the skin which can result in the development of surgical site infections (SSI). For the prevention of SSI, which are caused by endogenous pathogens in about 90% of all cases [6] and mainly by microorganisms in the depth of the skin surrounding the surgical field, an advanced skin antisepsis is necessary including an efficient targeting of hair follicles to prevent an intraoperative recolonization on the skin surface.

The pathogen spectrum causing SSI varies depending on the location of the surgery field. In general surgery, the etiology of SSI has not significantly changed over the last 30 years. Gram-positive bacteria, e.g., coagulase-negative staphylococci (CoNS), *Staphylococcus aureus* and *Enterococcus* spp. as well as gram-negative bacteria, e.g., *Escherichia coli*, *Enterobacter spp.*, *Klebsiella* spp. and *Pseudomonas aeruginosa*, are the most common findings [7]. In visceral surgery, *E. coli* dominate, followed by *Enterococcus* species [8]. After lower abdominal tract surgery, the most frequent microorganisms isolated were *E. coli*, *Enterococcus* spp., *Streptococcus* spp., *P. aeruginosa*, and *S. aureus*. After upper abdominal tract procedures, the proportion of isolated staphylococci, *Klebsiella pneumoniae*, *Enterobacter* spp., *Acinetobacter* spp. and *Candida albicans* was higher, but that of *E. coli*, *Bacteroides fragilis* and *Clostridium* spp. was less [9]. In contrast, the members of the resident skin flora such as *S. aureus*, CoNS, *Cutibacterium acnes* and streptococci dominate in periprosthetic joint infections [10]. In vascular graft infections, staphylococci remain the most common bacteria [11]. The manifestation of SSI depends on various factors, such as site of surgery, age of the patient, underlying illness, amount and type of the microorganisms in the surrounding surgery field and their pathogenicity [12, 13].

To eliminate the resident skin flora as the major source of SSI, the focus is on the following measures: pre-surgical antiseptic washing, if needed preoperative decolonization of *S. aureus*, deep skin antisepsis [14], antiseptic irrigation of the surgical field before suturing [15], glove change before inserting the sterile implant [16], biofilm reducing wound closure [17], antiseptic suture material [18], and perioperative parenteral antibiotic prophylaxis [19, 20]. Due to the

prevalence of SSI and the resulting high costs, every effort must be made to reduce the SSI rate. For example, the SSI rate in Germany in the period 2010–2016 was 4.9% with median case costs for the SSI group of €19,008 compared to €9,040 for patients without SSI. The median underfunding of SSI was identified at €1534 per patient [21].

Skin antisepsis is a key element for the prevention of SSI. A promising starting point for the prevention of SSI is to improve the depth of preoperative skin antisepsis by reaching the hair follicles. One possibility could be the use of nanocarriers for an optimized delivery of antiseptics into the hair follicle. Thus, the efficacy of skin antisepsis could be increased and the intraoperative carryover of bacteria from the surgical field to the wound could be decreased. Nanoparticulate drug delivery systems show a significantly deeper follicular penetration than non-particulate substances when an external force like massage is applied [22]. Thereby, a movement of the hair shaft is induced which causes a mechanical interaction between the nanoparticles, the intrafollicular stratum corneum and the hair shaft, which together act as a kind of ratchet, also known as the ratchet effect [23]. Following the transport of the nanoparticles to the hair follicle, a release of the encapsulated drug can be induced by various trigger mechanisms [24]. Polymeric nanocapsules (NCs) containing *o*-nitrobenzyl groups are known for their fast photolysis under UV irradiation [25, 26] since these compounds are known to have excellent photolytic properties [27] under mild irradiation conditions [28, 29]. Recently, it was shown that low-dose ultraviolet A (UVA) radiation at about 365 nm is suitable for an intrafollicular release of a model drug from polyurethane NCs containing *o*-nitrobenzyl groups in the shell [26]. In the present study, biocompatible hydroxyl ethyl starch nanocapsules (HES-NCs) prepared by a miniemulsion process were utilized for this approach. HES is well suited for translation into the clinical routine due to its biodegradability and high biocompatibility which is comparable to native starch [30, 31]. Furthermore, it is known for its presence of modifiable chemical groups as well as tailorability [32]. The material was equipped with photolytic characteristics by the incorporation of *o*-nitrobenzyl groups into the capsule shell, which enabled an efficient release of encapsulated ethanol (EtOH) as well as the model drug sulforhodamine 101 (SR101) after UVA irradiation.

Light emitting diodes (LEDs) are advantageous for biomedical applications [33] since they are compact, have stable output characteristics and can be mounted on various types of instruments. Furthermore they represent potential substitutes for mercury vapor lamps [34] and provide a narrow emission spectrum, which can be tailored to the application [26] accompanied by an increase in lifetime and reduced power consumption [35]. Therefore, we decided to use

a novel LED-based device for the emission of UVA radiation at a peak wavelength of 365–370 nm as a trigger for the release of EtOH from the HES-NCs (**Figure 1**). In this context, we hypothesize that the HES-NCs, unlike the non-particulate vehicle, reach the deeper parts of the hair follicles and decontaminate them after UVA-triggered release of EtOH. In contrast, pure EtOH only reaches the skin surface and the upper infundibulum of the hair follicle [6], which is not sufficient for deeper decolonization. Based on this, it can be assumed that, especially in the case of prolonged surgical interventions, recolonization of the skin surface by endogenous microorganisms originating from the hair follicle can occur [5, 14], which increases the risk of developing SSI. To accomplish the utilization of the newly synthesized HES-NCs in preoperative skin antisepsis, the aim of this work was the transfer to an antiseptic continuous phase (EtOH) as well as the physicochemical and toxicological characterization of the system. The physicochemical characterization was carried out using EtOH as well as phosphate-buffered saline (PBS) to assess the applicability of the system in aqueous phases. The toxicological characterization was performed using the outer phase PBS to exclude a bias due to EtOH-related cell toxic effects. We further applied the system on *ex vivo* porcine skin to evaluate follicular penetration as well as drug release characteristics. For the model visualization of the intrafollicular release of the model drug SR101, cyclohexane (CH) turned out to be the ideal outer phase, as its physicochemical properties help to indicate the localization of SR101. We finally elucidated the bactericidal properties of the HES-NCs in EtOH in combination with the novel UVA LED-based lamp using *ex vivo* porcine skin.

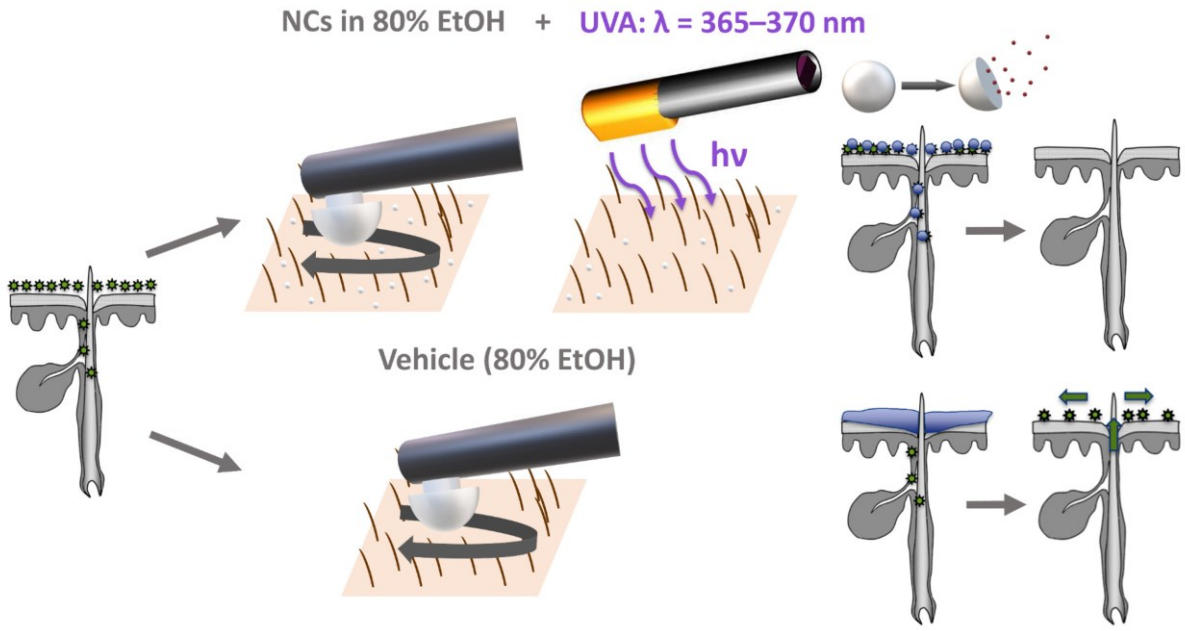

Figure 1: Application of the hydroxyethyl starch nanocapsules (HES-NCs) in 80% ethanol (EtOH) on colonized *ex vivo* porcine skin with a massage device and subsequent irradiation of the skin surface

with a novel LED device emitting at a peak wavelength of 365–370 nm which leads to an intrafollicular release of EtOH from the HES-NCs resulting in a decolonization of the skin surface and the hair follicles. After application of the pure vehicle (80% EtOH) the skin surface is decolonized but the risk of a recolonization of the skin from deeper parts of the hair follicle remains.

2. Materials and methods

2.1. Materials for HES-NC synthesis

NXG (2-nitro-p-xylylene glycol) (TCI, Eschborn, Germany), toluene diisocyanate (TDI) and sulforhodamine 101 (SR101) (both Sigma-Aldrich, Steinheim, Germany), ethanol (EtOH) (GC grade, Merck KGaA, Darmstadt, Germany) and cyclohexane (CH) (HPLC grade, Acros Organics, Nidderau, Germany) were of commercial grade and used without further purification. Hydroxyethyl starch (HES) aqueous infusion solution (10%, Fresenius Kabi, Bad Homburg, Germany) contained 0.9% sodium chloride. Lubrizol (polyisobutylenesuccinimide pentamine, mw = 384–875 $g \cdot mol^{-1}$, determined from GPC, HLB (hydrophilic lipophilic balance) < 7, containing 50:50 wt% mineral oil as a diluent) (Lubrizol, Rouen en Seine Maritime, France) was used as a surfactant. Milli-Q water was used as aqueous phase throughout the experiments. Stock solutions of Lubrizol (1% in CH) and SR101 solutions (10^{-3} M in water and 5×10^{-3} M in EtOH-water, 1:1) were prepared and stored at room temperature protected from light.

2.2. Preparation of HES-NC samples

NXG, HES solution, SR101 solution and EtOH were mixed together and stirred for 5 min to prepare the samples 1144b to g with the corresponding proportions as shown in Table 1. Then, a solution of Lubrizol in CH (7.5 g) was added. After stirring for 1 h with a magnetic stirrer for pre-emulsification, the miniemulsion was prepared by ultrasonication of the mixture for 120 s at 70% amplitude (Branson sonifier W450 Digital, tip size 12.5 mm, pulse 10 s, pause 20 s) under ice cooling. Then 85 mg of TDI dissolved in CH/Lubrizol (2 g) was added slowly to the miniemulsion within 5 min at room temperature. For the synthesis of the HES-NCs 1212, 12 small batches immediately after sonication were combined in one big flask and stirred at 700 rpm to obtain a higher formulation volume but still ensure an appropriate sonication process. To ensure that a reliable miniemulsion was obtained from the sonification, the volume and components of each batch for sample 1212 were identical to those for samples 1144. 1.02 g of TDI in 24 g of Lubrizol solution was added slowly within 10 min. The surface crosslinking was carried out upon stirring at 700 rpm for 24 h at 25 °C. To avoid solar irradiation, vessels were covered with aluminum foil. The obtained dispersions of HES-NCs in CH were used for

characterization by dynamic light scattering (DLS) and transmission emission microscopy (TEM).

Table 1: Composition of the dispersed phase of the HES-NC samples and their DLS characterization (cyclohexane = CH, ethanol = EtOH, hair follicle = HF, hydroxethyl starch = HES, z-average = z-avg, polydispersity index = PDI, phosphate-buffered saline = PBS, 3-(4,5-dimethylthiazolyl-2)-2,5-diphenyl-tetrazolium bromide = MTT, 2-nitro-p-xylylene glycol = NXG, sulforhodamine 101 = SR101).

Sample	Experiment	NXG [mg]	SR101 Aqueous Solution [mg]	EtOH [mg]	H_2O [mg]	HES 10% [mg]	z-Avg [nm] in CH	PDI in CH
1144b	Release in CH (non-cleavable control, **Section 3.3.**)	-	200	300	-	500	366	0.055
1144d	Phase transfer, release in CH and EtOH (**Section 3.2.** and **Section 3.3.**)	50	200	300	-	450	356	0.083
1144e	HF penetration in PBS (**Section 3.5.**)	50	200 *	200	100	450	432	0.127
1144f	HF penetration in CH (**Section 3.5.**)	50	100 *	250	50	450	435	0.187
1144g	Phase transfer (**Section 3.2.**)	50	-	450	-	500	503	0.144
1212	MTT assay, microbial reduction (**Section 3.4.** and **Section 3.6.**)	50	-	450	-	450	613	0.215

* 5×10^{-3} M solution of SR101 in EtOH-water (1:1) was used.

2.3. Characterization of the HES-NC samples by dynamic light scattering (DLS) and transmission electron microscopy (TEM)

The size of the HES-NCs and their size distribution were measured by dynamic light scattering (DLS) (Zetasizer nano ZS, Malvern Instruments Ltd., Worcestershire, UK) at 20 °C under the scattering angle of 173° at a wavelength of 633 nm. DLS measurements give a z-average size (z-avg), which is intensity mean, and the polydispersity index (PDI), which provides information about the width of the particle size distribution. For the measurement, the CH dispersion was diluted 100 times. Particle sizes and PDIs are given as the average of 12 measurements of one representative aliquot. The size of the HES-NCs and their size distribution after transfer in EtOH or PBS with different surfactants were analyzed with four measurements and 12 runs

per measurement. Data were analyzed based on their z-avg and their number as well as the PDI. The particle dispersion was diluted between 20 and 100 times before measurement.

The morphology of the HES-NC samples was studied using a transmission electron microscope (TEM) (JEM 1400, Jeol Ltd., Tokyo, Japan) operating at an accelerating voltage of 80 kV. A total of 10 µL of the original dispersion was diluted with 5 mL of CH, and then 3.0 µL of the diluted sample was placed on a 400-mesh carbon-coated copper grid and dried at room temperature overnight. In case of transfer into water or EtOH, the dispersions were diluted with correspondent solvents.

2.4. Transfer of HES-NCs to EtOH and PBS

The NC dispersion was diluted 1:5 in CH and centrifuged at 1400× *g* for 30 min at room temperature in 60 mL glass vials. The supernatant was removed, and the pellet was resuspended in EtOH (80%) or PBS (PeproTech EC Ltd., London, UK) without or with addition of surfactants in an ultrasonic bath with open cap for 30 min. The dispersion was again centrifuged and resuspended in fresh EtOH or PBS without or with addition of surfactants. Resuspension was again done in an ultrasonic bath. The following surfactants were used in 0.1 % (*w/v*) concentration: Tween® 20 (Sigma Aldrich, St. Louis, MO, USA), betaine monohydrate (Sigma Aldrich, St. Louis, MO, USA), cetyltrimethylammonium chloride (CTMA-Cl, Sigma Aldrich, St. Louis, MO, USA), Nonidet® P40 (NP40, AppliChem GmbH, Darmstadt, Germany).

2.5. Examination of *in vitro* release of the model drug SR101 and EtOH

SR101 was used as a model drug for testing the release after UVA-cleavage in CH and EtOH without and with addition of surfactants. The NC dispersion (1 mL) was diluted in 3 mL of the appropriate solvent. Then, 150 µL were transferred to a glass vial and irradiated with UVA radiation (peak wavelength of λ = 367 nm) for 1–7 min. The dispersion was placed directly onto an LED (NCSU033B, Nichia Corporation, Anan, Japan) (30 mW/cm^2) or with 1.25 cm distance (6.8 mW/cm^2) to the light source resulting in doses of 0.2–12.6 J/cm^2.

Afterwards, 50 µL of the solution in CH was transferred to a black microtiter plate (96 well) and fluorescence was measured at $485_{ex}/590_{em}$ nm after an exposure time of 0.5 s.

HES-NCs in EtOH were centrifuged (1400× *g*, 5 min) after irradiation and before measurement to separate non-cleaved fluorescent HES-NCs. The supernatants were used for fluorescence analysis. In PBS, the release of encapsulated EtOH was analyzed instead of SR101. The

cleaved HES-NCs were removed by centrifugation and the EtOH concentration in the supernatant was determined by a Cer(IV)-based assay.

2.6. EtOH detection

In 100 mL distilled water, 2 mL nitric acid (68%) was dissolved and 2.2 g Cer(IV)ammonium nitrate (Carl Roth GmbH + Co. KG, Karlsruhe, Germany) was added to reach a concentration of 0.04 M. Of this detection reagent, 100 µL were mixed with 100 µL of test solution and absorption was measured immediately at 415 nm. EtOH concentration was calculated by use of a calibration curve.

2.7. Cell culture

The human cell line HaCaT (DKFZ, Heidelberg, Germany) was cultured in Dulbecco's modified Eagle's medium (DMEM, high glucose, PAN-Biotech GmbH, Aidenbach, Germany) supplemented with 10% (*v/v*) heat-inactivated fetal bovine serum (FBS) (Life Technologies, Carlsbad, CA, USA) and 2 mM L-glutamine (ccPro GmbH, Oberdorla, Germany) at 37 °C in a humidified atmosphere (37 °C, 5% CO_2, Heracell™ 150i, Thermo Scientific, Waltham, MA, USA). The cells were subcultured twice a week with additional medium change weekly. For cell detaching, trypsin/EDTA (0.05%/0.02%, PAN-Biotech GmbH, Aidenbach, Germany) was used. Cell morphology was checked regularly. After detaching the cells, viability was assessed via trypan blue exclusion and cells were counted in a counting chamber (Neubauer improved).

2.8. Cytotoxicity analysis

Cell viability was analyzed by a colorimetric assay using the yellow tetrazolium salt 3-(4,5-dimethylthiazolyl-2)-2,5-diphenyltetrazolium bromide (MTT) that is reduced by viable cells to a purple formazan. A HaCaT cell suspension with 0.1×10^6 cells/mL was prepared and 100 µL of the suspension were added per well of a 96 well plate. After incubation for 48 h, the cells were exposed to the test compounds in decreasing concentration for 1 h and 3 h, respectively. Afterwards, cells were washed with PBS/HBSS (ccPro GmbH, Oberdorla, Germany) and 100 µL MTT solution (0.5 mg/mL) (Sigma-Aldrich, St. Louis, MO, USA) per well were added and incubation was continued for 3 h at 37 °C. The supernatant was decanted and for formazan solubilization, 100 µL MTT-elution solution (2-Propanol/HCl) (both Carl Roth GmbH + Co. KG, Karlsruhe, Germany) was added per well. The 96 well plate was incubated protected from light for 15 min while shaking. Absorbance was measured with a microplate reader (BioTek PowerWave XS, Agilent Technologies, Santa Clara, CA, USA) at 550 nm and 620 nm. Sodium

dodecyl sulfate (SDS, 0.08%) (AppliChem GmbH, Darmstadt, Germany) served as a positive control.

2.9. Examination of *ex vivo* follicular penetration of HES-NCs and release of the model drug SR101

2.9.1. Preparation of skin samples

Due to its suitability for investigating follicular penetration *ex vivo*, porcine skin was utilized for the drug delivery experiments [36-39]. The porcine ears were obtained from a local butcher. The age of donor pigs was sixth months at the date of slaughter. Porcine ears without any visible injuries were selected for further examinations and the experiments were executed not later than 48 h after slaughter to exclude possible post-mortem skin changes [40]. The porcine ears were cleaned under cold tap water and dried with paper towels and stored at 4 °C until the experiments [41]. The porcine ears were fixed on a polystyrene board covered by aluminum foil by using cannulas. In total, three test areas of 2 cm × 3 cm per ear (CH-based dispersion) or four areas of 2 cm × 3 cm (PBS-based dispersion) were selected and the included hairs were shortened without damaging the stratum corneum. The outer edges of the areas were covered by window color (fun & fancy, Marabu GmbH & Co. KG, Tamm, Germany) to avoid lateral spreading of the dispersions.

2.9.2. *Ex Vivo* Application of HES-NCs

In total, n = 3 porcine ears were treated with the CH-based dispersion and n = 3 unrelated ears were treated with the PBS-based dispersion. The formulations were applied onto the test areas with a concentration of 20 µL/cm^2 except one area per porcine ear which served as a negative control (untreated area). The porcine ears treated with PBS-based HES-NC dispersions further contained a test area with a solution of 0.001% (*w/v*) SR101 in PBS with 0.1% (*w/v*) betaine monohydrate as a control. After application, the test areas were manually massaged with a circular motion using a sonic wave device (NOVAVON pro, NOVAFON GmbH, Weinstadt, Germany) at a frequency of 4.2 Hz (250 BPM) for 2 min [42] followed by an incubation period of 5 min. Afterwards, one test area per ear containing a NC dispersion was irradiated by means of a UVA-LED module (OLM-018, OSA opto light GmbH, Berlin, Germany) from a distance of 3 cm (irradiance of 214.0 ± 2.3 mW/cm^2, dose of 12.8 J/cm^2, maximum emission wavelength of λ = 368.5 ± 1.5 nm) for 1 min. The corresponding application protocol is presented in Table 2. Subsequently, the skin areas were hardened by a cryospray (Solidofix®, Carl Roth GmbH + Co. KG, Karlsruhe, Germany) and skin biopsies of 0.5 × 0.5 cm were excised by means of a

scalpel, transferred to cryotubes, and shock frozen with liquid nitrogen. The samples were stored at −20 °C until further preparation.

Table 2: Treatment scheme of *ex vivo* porcine skin with HES-NC dispersions in CH and PBS with and without UVA irradiation.

Experiment	Area	Treatment
CH-based HES-NC dispersion (*n* = 3)	A	Negative control (untreated)
	B	HES-NC
	C	HES-NC + UVA
PBS-based HES-NC dispersion (*n* = 3)	A	Negative control (untreated)
	B	SR101 solution
	C	HES-NC
	D	HES-NC + UVA

2.9.3. Cryohistological preparation and confocal laser scanning microscopy (CLSM)

The cryohistological preparation of skin biopsies was performed as described before [26]. Examination of the cryohistological sections was carried out via confocal laser scanning microscopy (CLSM) (LSM 700, Carl Zeiss AG, Oberkochen, Germany) on *n* = 9–10 hair follicles per group on each porcine ear using a laser emitting at 555 nm. The full procedure is likewise described in [26].

2.9.4. Graphical processing of CLSM images

To quantify the intrafollicular UVA-dependent release of the model drug SR101 from the HES-NCs, we utilized an image analysis evaluating the mean brightness value of the fluorescence signal via ImageJ (Wayne Rasband, National Institutes of Health, Bethesda, MD, USA) as already described [26].

2.10. Development and adaption of a UVA-LED lamp for microbial reduction experiments

We developed a handheld, rechargeable battery-operated LED radiation source (LED lamp) for the *ex vivo* microbial reduction experiments to increase the translatability of the system for clinical application. The UVA-LED series OCL-490 applied in the LED lamp are specified with a peak wavelength of 365–370 nm, mean value 368.3 ± 0.5 nm. Further data are a full width at half maximum (FWHM) of 11.1 ± 0.3 nm, radiant intensity 3.1 ± 0.2 W/sr and a viewing angle (full angle) of 20°. The emission spectrum is shown in **Figure 2A**. All LED parameters were measured with a CAS-140 CT spectrometer (Instrument Systems, Munich, Germany) at a measurement current of 500 mA supplied by a National Instruments power source (Austin, TX, USA). The distribution of the irradiance on the skin has been measured by adjusting the LED lamp at a distance of 3 cm between skin and front window of the lamp, which is indicated in **Figure 2B**. We achieved an irradiance above 200 mW/cm² at an area of 12 cm². The UVA lamp contains six LEDs in total, a driver unit, a rechargeable battery pack, a passive heat sink and a sealed aluminum housing. Therefore, the lamp can be disinfected e.g., by wiping the housing surface with EtOH. To support the operator in adjusting the lamp position at 3 ± 1 cm distance above the skin, we integrated an optical distance measurement device and an optical indication of the actual distance at the back side of the LED lamp. We have determined the necessary measures to protect the operator (safety goggles) against UVA radiation. The irradiation dose of 13.1 J/cm² (**Section 2.11.1.**) requested from the experimental set up is below the safety limit of 29 J/cm² according to 2006/25/EG Table 1.1, points a. und o. (safety regulations for non-coherent optical radiation) [43]. UVA irradiation as a trigger for intrafollicular release of antiseptics from NCs bears the advantage of having a potential antiseptic effect itself [44]. Furthermore, UVA light penetrates the dermis, which enables the targeting of hair follicles [45]. It is also able to trigger intrafollicular drug release at very low doses [26] from *o*-nitrobenzyl-based NCs without inducing skin heating, such as infrared A [46].

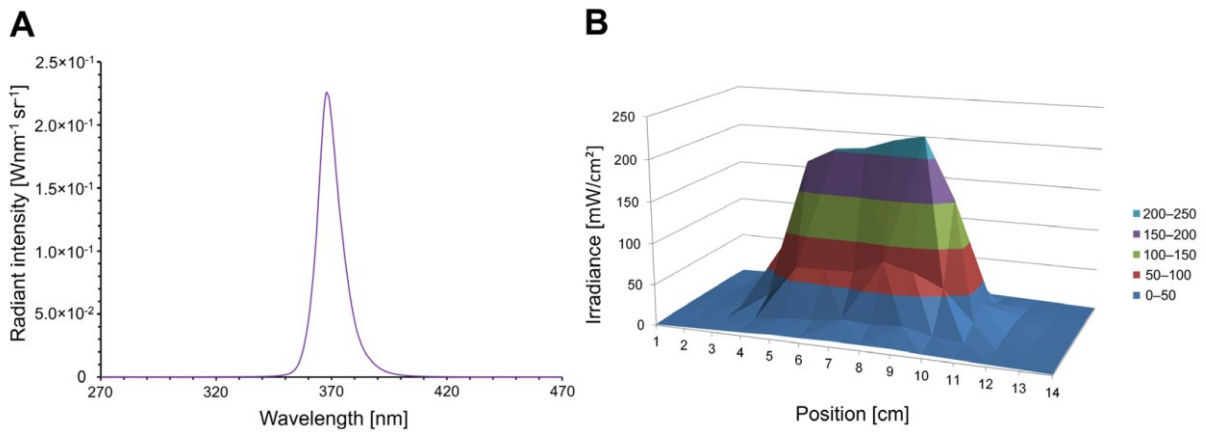

Figure 2: (**A**) Mean emission spectrum of the applied ultraviolet A (UVA)-LED. (**B**) Irradiance in the target range.

2.11. Analysis of microbial reduction

2.11.1. Application of HES-NCs on *ex vivo* porcine skin and sampling via cup scrub technique

Porcine ears (*n* = 10), not refrigerated before the experiments and used at room temperature, were treated as described before (**Section 2.9.1.**). One area served as a negative control and remained untreated. Another negative control was exposed to UVA radiation (irradiation time: 1 min, distance: 4 cm, irradiance: 218.7 ± 2.8 mW/cm^2, dose: 13.1 J/cm^2) using the LED device described in **Section 2.10.** (OSA Opto Light GmbH, Berlin, Germany). The other areas were treated with EtOH (80% including 0.1% betaine monohydrate, positive control), the HES-NC dispersion (in EtOH 80% with 0.1% betaine monohydrate), and with the HES-NC dispersion followed by UVA irradiation.

The antiseptics were applied as follows: 20 µL/cm^2 were administered to a skin area of 3 cm × 3 cm with a pipette and the skin was massaged for 2 min at 4.2 Hz (250 BPM) as described in **Section 2.9.2**. After air curing, an autoclaved steel ring (2 cm in diameter) was put on the skin and filled with 1 mL sterile inactivator solution TSHC (3% Tween® 80 (AppliChem GmbH, Darmstadt, Germany), 3% saponin (Sigma Aldrich, St. Louis, MO, USA), 0.1% L-histidine (Carl Roth GmbH + Co. KG, Karlsruhe, Germany), 0.1% L-cysteine (Sigma Aldrich, St. Louis, MO, USA)). Then, the skin was rubbed with a sterile glass rod for 1 min to flood up the intrafollicular microbiome (cup scrub technique). This procedure was conducted on each area. 500 µL of the received suspension were added to 4.5 mL of inactivator solution and vortexed. Until use, samples were stored at 4–8 °C.

2.11.2. Quantitative determination of the bacterial skin colonization

Samples were diluted, plated on Columbia blood agar (CBA) plates and incubated for 48 h at 37 °C. Afterwards, colony-forming units (CFU) were counted, and lg-reduction was calculated according to the following formula:

$$\lg(reduction) = \lg(CFU\ of\ control) - \lg(CFU\ of\ treatment) \quad (1)$$

2.11.3. Identification of the skin microbiome by MALDI-TOF MS and Sanger sequencing

Colonies differing in their phenotype (color, shape) were sub-cultured on CBA plates and identified using matrix assisted laser desorption ionization—time of flight mass spectrometry (MALDI-TOF MS) from fresh overnight sub-cultures.

Using a toothpick, colony biomass was transferred onto a disposable MALDI target plate (MBT Biotarget 96, Bruker Daltonics GmbH & Co. KG, Bremen, Germany) and 1 µL of 70% formic acid in HPLC grade water (both Honeywell GmbH, Seelze, Germany) was applied. A total of 1 µL bacterial test standard (BTS, Bruker Daltonics, Bremen, Germany) was added on a separate position. On both, the samples and the BTS, 1 µL α-cyano-4-hydroxycinnamic acid matrix (Bruker Daltonics GmbH & Co. KG, Bremen, Germany) was added after drying. The samples were analyzed with the MALDI Biotyper® sirius instrument (Bruker Daltonics GmbH & Co. KG, Bremen, Germany) and the MBT Compass software version 4.1. Microorganisms consistently identified with a score value of ≥1.7 were assumed to be reliably identified. Microorganisms that could not be identified (score < 1.7) were subjected to the protein extraction method and re-analyzed. For this, colony material was resuspended in 300 µL HPLC grade water. Afterwards, 900 µL absolute EtOH (Carl Roth GmbH + Co. KG, Karlsruhe, Germany) was added. After two centrifugations (2 min, 14,800 rpm), the supernatant was discarded, and the pellet was dried for 5 min at room temperature followed by resuspension in 70% formic acid. To this suspension, 20 µL acetonitrile (Honeywell GmbH, Seelze, Germany) were added, the suspension was centrifuged again and 1 µL of the supernatant was applied to the MALDI targets. Afterwards, the procedure was carried out as described previously.

Microorganisms that could not be reliably identified by MALDI-TOF MS were identified using Sanger sequencing. DNA of the bacteria was isolated using the Genomic DNA/Nucleospin® Microbial DNA kit (Macherey-Nagel GmbH, Düren, Germany) according to the manufacturer's instructions. The DNA was stored at −20 °C until use. 16S rRNA were amplified with final concentration of 2 µM primer 27F (5′-AGA GTT TGA TCM TGG CTC AG-3′) and 16S-5 (5′-AAG GAG GTG ATC CAG CCG CA-3′) using Phire hotstart II DNA polymerase (Thermo Fisher

Scientific, Waltham, MA, USA) kit. PCR was performed on a Biometra TRIO 48 thermocycler (Analytik Jena GmbH, Jena, Germany) using the following conditions: initial incubation at 98 °C for 30 s, 35 cycles of 98 °C for 5 s, 60 °C for 5 s, and 72 °C for 2 min, followed by a final incubation at 72 °C for 1 min. The amplicons were purified using a QIAquick Gel Extraction Kit (QIAGEN GmbH, Venlo, The Netherlands). DNA was sequenced according to the SANGER sequencing protocol by Eurofins Genomics Germany GmbH (Ebersberg, Germany) using the PCR primers. Finally, the forward and reverse sequences were aligned, cured and combined to 16S rRNA consensus sequences (Geneious, San Diego, CA, USA). The entire consensus 16S rRNA gene sequences were then subjected to BLAST analysis against the 16S rRNA (bacteria and archaea) of the NCBI nucleotide database [47]. The similarity scores (sc) were regarded as identifications of either the species level, if sc > 99% or at least the genus level sc > 97%. For an additional control, all isolates were subjected to Gram-staining and the microscopic images were compared with the respective results of the 16S rRNA identifications.

2.12. Statistical analysis

Mean value comparisons were carried out via IBM SPSS® Statistics 28 (IBM, Armonk, NY, USA). Normal distribution of the data was proven by the Shapiro–Wilk test. A Mann–Whitney U test (follicular penetration depth and fluorescence intensity) or a one-tailed Student's *t*-test for paired samples (release of EtOH from the HES-NCs) was applied in case of two groups and a Kruskal–Wallis analysis of variance (ANOVA), followed by Bonferroni post hoc tests (DLS after phase transfer, cytotoxicity, follicular penetration depth), was applied in case of more than two groups. A one-way ANOVA with Tukey's multiple comparisons was carried out for the microbial reduction data. All tests were carried out affording a significance of $p < 0.05$.

3. Results and discussion

3.1. Synthesis and physicochemical characterization

In this work, we used biocompatible HES as a shell forming polymer. In contrast to polyurethane, HES is a water-soluble polymer. In order to make it insoluble, crosslinking of hydroxyl groups was used, producing a water-insoluble 3D network. TDI was used as a main crosslinker, whereas photosensitive NXG was used as a co-crosslinker. When TDI acts as a sole crosslinker, non-cleavable bonds are formed (**Figure 3A**). By using both crosslinkers, *o*-nitrobenzyl blocks in the cross bonds make the shell photosensitive. Irradiation with UVA light breaks the cross bonds formed by the NXG crosslinker (**Figure 3B**) which induces disintegration of the capsules accompanied by the release of the content into the surrounding medium.

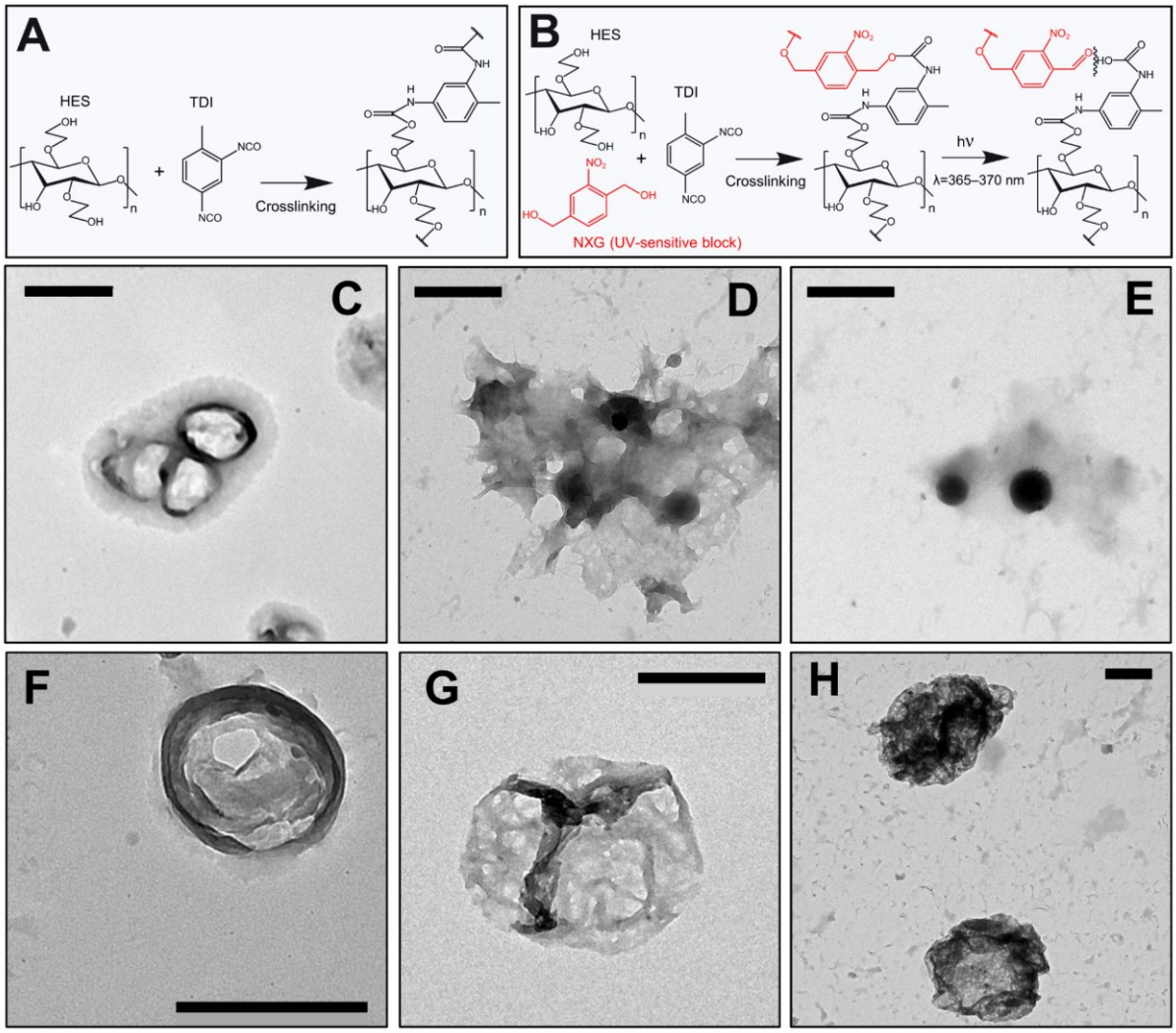

Figure 3: (**A**) Crosslinking of the HES chains with usual crosslinker. (**B**) Crosslinking of the HES chains with photocleavable co-crosslinker, and the UVA light induced cleavage of the cross bonds. Transmission electron microscopy (TEM) images of the formulations 1144d (**C**), 1144d in EtOH/water (**D**), 1144d in EtOH + 1%Tween 20 (**E**), 1144g (**F**), 1144g + UVA (**G**), 1212 (**H**). Scale bars correspond to 500 nm.

In the framework of the synthesis, photoresponsive HES-NCs with a spherical shape were formed (**Figure 3C** and **H**) showing agglomerations as well as morphological alterations after the transfer to 80% EtOH (**Figure 3D**) which vanished after the addition of the surfactant Tween 20 (5%, Figure 3E). UVA radiation induced breakage of the capsule shell (**Figure 3F** and **G**). Since there are two types of cross-links, photocleavable as well as non-photo-cleavable, the capsule shell may not be completely destroyed. However, large openings with a high permeability for the encapsulated drug were formed. This effect of disintegration was already observed in polyurethane-based NCs containing a NXG component in the shell [26].

From the literature various starch-based NCs are known involving the possibility of a controlled drug release triggered by pH [48, 49], GSH [50], glucose or temperature [51]. To our knowledge, the presented NCs are the first UVA-responsive *o*-nitrobenzyl-based HES-NCs.

3.2. Physicochemical HES-NC characteristics after transfer of the HES-NCs to PBS and EtOH

In order to further evaluate the optimal parameters for stabilization, we used DLS to investigate formulations after transfer to PBS and EtOH. Various surfactants were added to the respective phase in cytocompatible concentrations since the formation of adlayers to NC dispersions is a known phenomenon resulting in stabilization [52].

In these experiments the HES-NCs 1144d-g were included. Next to the z-average (**Figure 4A**), the PDI (**Figure 4B**), the number mean (**Figure 4C**), which is the average size based on the number of the particles, and the mean intensity of peak 1 (**Figure 4D**), which is the proportionally largest peak of the particles' intensity distribution, were used for assessing the quality of the transfer. Since a particle size of 600–800 nm is optimal for penetration into the hair follicle [53], z-average and number mean should be in this range. A comparable peak 1 mean (intensity) and small PDI (<0.7) are further criteria. When using PBS without surfactants, z-average, number mean and peak 1 mean were high. Data for HES-NCs in PBS with 0.1% betaine monohydrate are comparable. Nevertheless, number mean and peak 1 mean were in the desired range for follicular penetration using 0.1% betaine monohydrate. Utilization of Tween 20 (0.1%), CTMA-Cl (0.1%), and NP-40 (0.1%) led to a z-average and peak 1 mean intensity in the desired range but very low number peaks, meaning intensity of large particles overlaps the intensity of few small particles which could have been the result of dissolution.

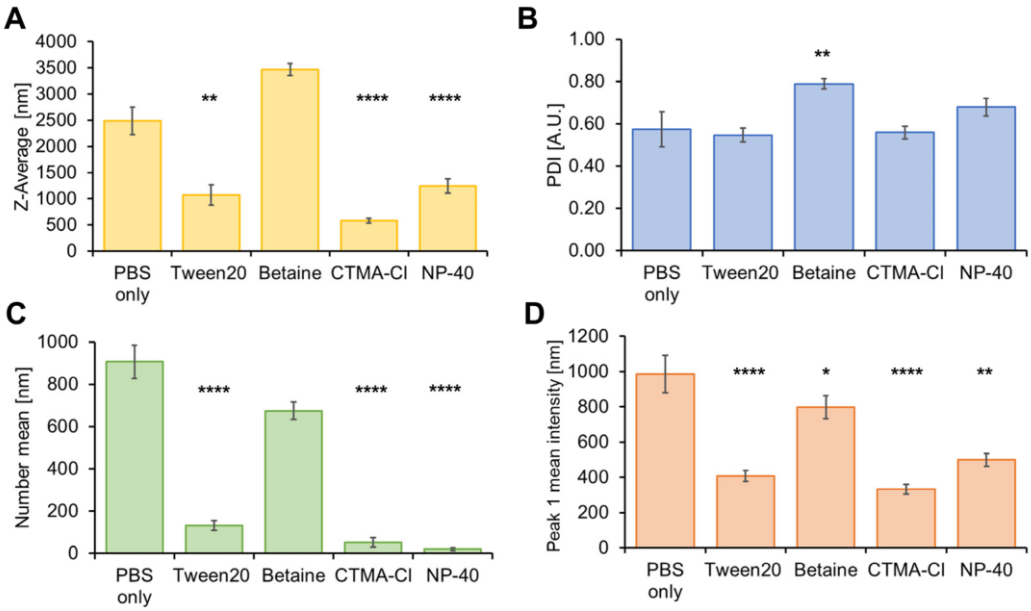

Figure 4: Dynamic light scattering (DLS) parameters (**A**) z-average, (**B**) polydispersity index (PDI), (**C**) number mean, (**D**) peak 1 mean intensity of the HES-NCs 1144d and g after transfer into phosphate-buffered saline (PBS). Different stabilization approaches by adding 0.1% (*w/v*) of the surfactants Tween 20, betaine monohydrate, CTMA-Cl or NP-40 are shown in comparison to PBS only. Significances in comparison to PBS only are indicated by asterisks with * = $p < 0.05$, ** = $p < 0.01$, **** = $p < 0.0001$ as determined by Bonferroni-adjusted post hoc tests after Kruskal–Wallis one-way analysis of variance (ANOVA). Mean values ± standard errors of the means (SEMs) of $n = 4$ to 30 samples with $n = 3$ to 4 measurements and 12 sub-runs each are presented.

When transferring the HES-NCs to EtOH, data are most consistent for solutions containing betaine monohydrate (0.1%) (**Figure 5A–D**). Pure EtOH (80%), EtOH with Tween 20 and CTMA-Cl yielded high z-averages, while NP-40 resulted in a higher amount of small particles.

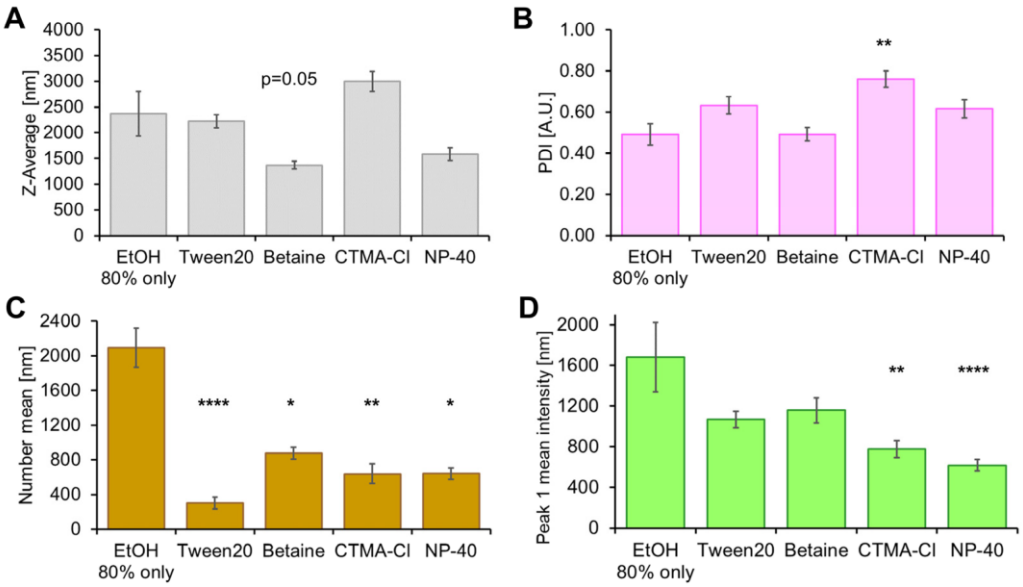

Figure 5: DLS parameters (**A**) z-average, (**B**) PDI, (**C**) number mean, (**D**) peak 1 mean intensity of the HES-NCs 1144d and g after transfer into EtOH (80%). Different stabilization approaches by adding 0.1% (*w/v*) of the surfactants Tween 20, betaine monohydrate, CTMA-Cl or NP-40 are shown in comparison to EtOH 80% only. Significances in comparison to EtOH only are indicated by asterisks with * = $p < 0.05$, ** = $p < 0.01$, **** = $p < 0.0001$ as determined by Bonferroni-adjusted post hoc tests after Kruskal–Wallis ANOVA. Mean values ± SEMs of $n = 5$ to 18 samples with $n = 3$ to 4 measurements and 12 sub-runs each are presented.

3.3. Cleavage of HES-NCs in CH, EtOH (80%) and PBS

When irradiated with 365–370 nm, non-cleavable HES-NCs did not release SR101, which was indicated by a non-depleting fluorescence intensity (**Figure 6A**). When using cleavable HES-NCs, fluorescence intensity decreased as a result of cleavage accompanied with the release of SR101 to CH. The inverted release indication of the model drug SR101 is based on a re-crystallization in apolar CH. A photobleaching effect of SR101 can be excluded in this context as it was shown in a previous study [26]. Cleavage efficiency depends on the distance to the light source and thus on the dose that is applied. Maximum cleavage was reached after 3 min irradiation with 30 mW/cm^2 corresponding to a signal loss of approximately 80%.

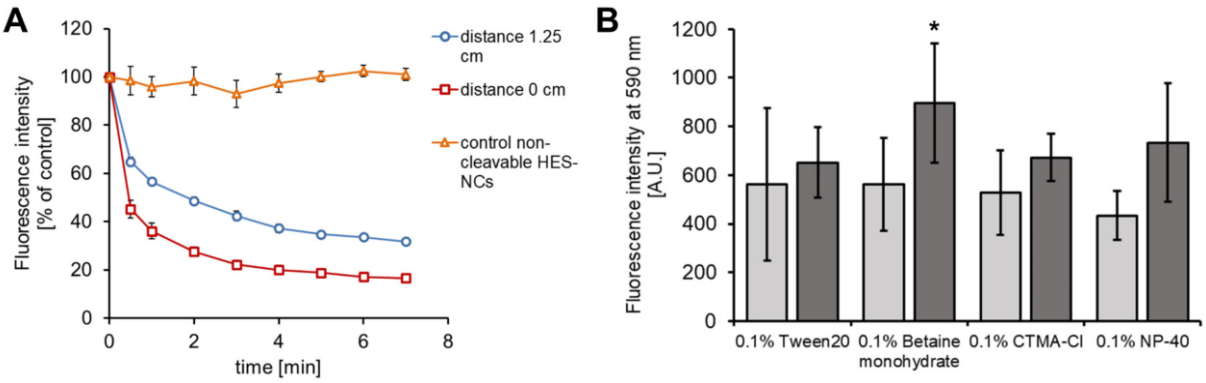

Figure 6: In (**A**) the relative fluorescence intensity of the model drug sulforhodamine 101 (SR101) to a non-irradiated control after irradiation of the HES-NCs 1144d with UVA from a distance of 1.25 cm (6.8 mW/cm^2, blue, n = 6), 0 cm (30 mW/cm^2, red, n = 8) and after irradiation of the non-cleavable HES-NCs 1144b (30 mW/cm^2, orange, n = 4) is presented. (**B**) Release of SR101 as measured by fluorescence intensity of the supernatants (590 nm) after excitation at 485 nm without (light grey) and with cleavage of the HES-NCs (dark grey) showing a significant increase after irradiation of the HES-NC dispersion stabilized by 0.1% betaine monohydrate in EtOH (* = $p < 0.05$) as determined by one-tailed Student's t-test for paired samples (n = 3 to 4 samples). Presentation of mean values ± SEMs in both graphics.

In our previous work involving *o*-nitrobenzyl-based polyurethane NCs we could reach a release of approximately 60% after 2 min by irradiation with 12 mW/cm^2 [26]. Similar values were also obtained in other studies involving *o*-nitrobenzyl-based systems [54, 55] which is in a comparable range to the HES-NCs utilized in this work. Compared to a micellar *o*-nitrobenzyl-based system presented by Jiang et al. [28] the release rate of the HES-NCs is similar when using approximately 20% of the irradiance. Although many UVA-responsive *o*-nitrobenzyl-based NCs have been published in previous papers [25, 26, 54, 55], UVA-responsive *o*-nitrobenzyl-based HES-NCs are not known from the literature. Nevertheless, spyropyrane based UV-responsive starch nanogels were published before [56].

In EtOH, the highest fluorescence intensity was measured in the supernatant when HES-NCs with 0.1% betaine monohydrate were irradiated (**Figure 6B**). Here, a fluorescence increase of 59% ($p < 0.05$) was observed in the supernatant. Therefore, we decided to utilize betaine monohydrate for the HES-NC dispersions in the follow-up experiments.

In PBS, the fluorescence could not be measured, therefore the EtOH concentration was analyzed in the supernatants. The limit of detection (LOD) was calculated to be 0.10% EtOH, whereas the limit of quantification (LOQ) was about 0.37% EtOH. After cleavage of the HES-NCs in PBS, an EtOH concentration of 0.12–0.32% was measured in the supernatant. In comparison, in HES-NC samples without irradiation, no EtOH could be detected.

3.4. Cytotoxicity of HES-NCs

Neither NXG used as the light sensitive linker in HES-NC production (**Figure 7A**), nor betaine monohydrate (**Figure 7B**) used as surfactant when transferring the HES-NCs to EtOH or PBS show any cytotoxicity towards HaCaT cells for contact times of 1 and 3 h in the applied concentrations since cell viability in comparison to the control was never <70%. Referring to the calculated IC_{30}, the concentrations leading to cytotoxicity, are 7.1% and 1.5% for betaine monohydrate and 6.3 mg/mL for NXG within 3 h. Neither non-cleaved HES-NCs (**Figure 7C**), nor UVA-cleaved HES-NCs led to a cytotoxic reaction within 3 h. The high biocompatibility of HES-NCs is associated with previous works on human skin fibroblasts and immune cells [57, 58, 59].

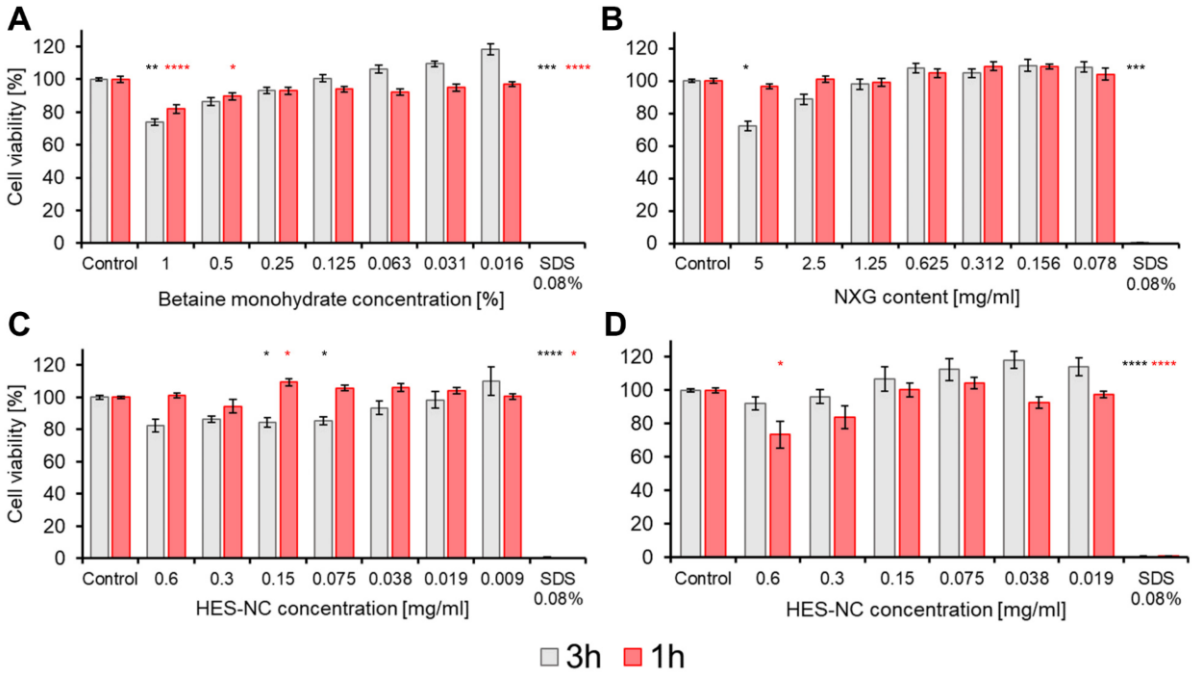

Figure 7: Cell viability as determined by 3-(4,5-dimethylthiazolyl-2)-2,5-diphenyltetrazolium bromide (MTT) assay for (**A**) betaine monohydrate, (**B**) NXG, (**C**) HES-NCs, (**D**) HES-NCs + UVA after 3 h (grey) or 1 h (red) of exposure. Significances in comparison to the control are indicated by asterisks with * = $p < 0.05$, ** = $p < 0.01$, *** = $p < 0.001$, **** = $p < 0.0001$ as determined by Bonferroni-adjusted post hoc tests after Kruskal–Wallis ANOVA. Mean values ± SEMs of $n = 6$ to 21 samples are presented.

3.5. *Ex vivo* follicular penetration and intrafollicular release of SR101

After application of the HES-NCs in CH and subsequent evaluation of cryohistological sections by CLSM, a mean follicular penetration depth of 499 ± 199 µm (mean value ± standard deviation) (without UVA) and 541 ± 230 µm (with UVA) was observed (**Figure 8A**). Indicated by a

40% loss of mean intrafollicular fluorescence intensity after irradiation with UVA, a release of the model drug SR101 from the HES-NC was detected ($p < 0.001$) (**Figure 8B**).

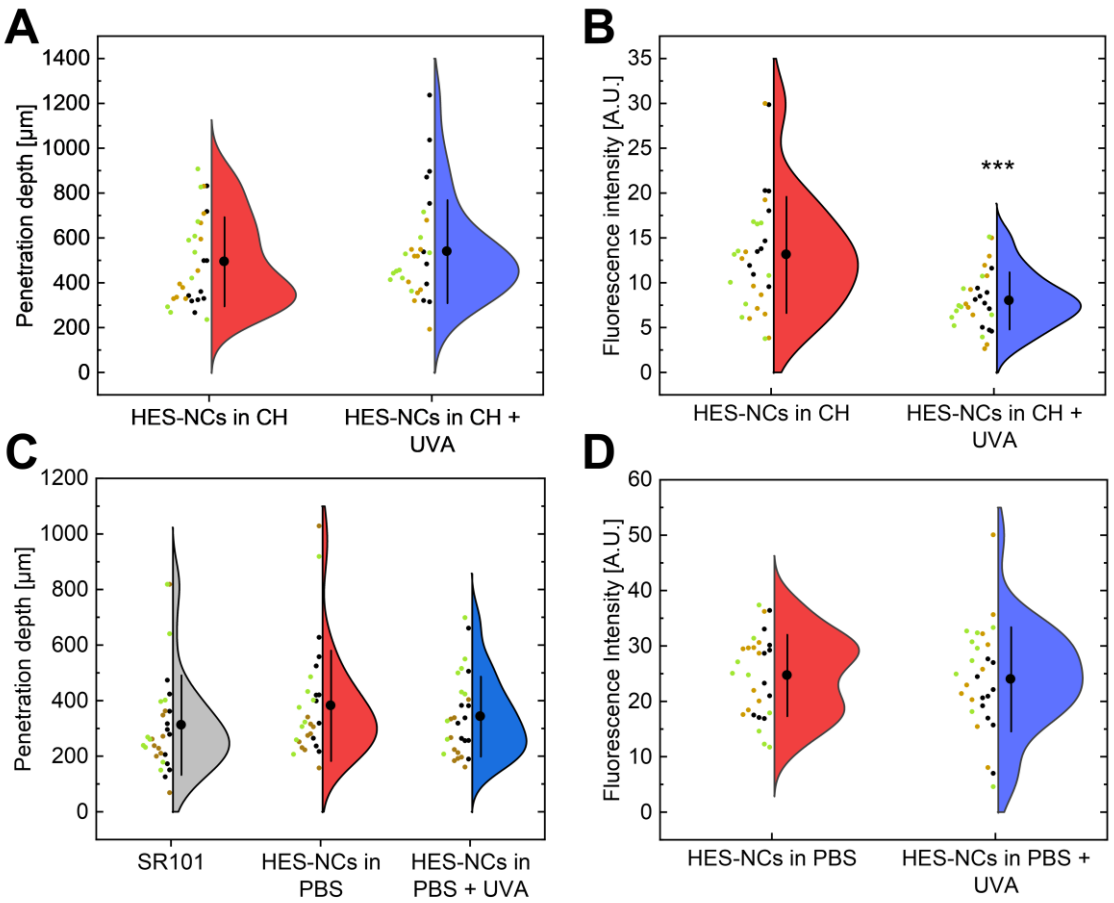

Figure 8: Violin plots, which show the distribution of individual data points including mean values ± standard deviations of $n = 29$ to 30 hair follicles of $n = 3$ donors. The three different colors of the data points serve to assign the hair follicles to the respective donor. An average follicular penetration depth of 499 µm could be reached by HES-NCs in cyclohexane (CH) (1144f) (**A**) as well as an intrafollicular release of the model drug SR101 by 40% as indicated by loss of fluorescence intensity (**B**). After transfer of the HES-NCs into PBS an average follicular penetration depth of 383 µm was observed (**C**) which was not significantly altered after irradiation with UVA but was slightly increased in comparison to a pure solution of the model drug SR101 in PBS (314 µm). No change in fluorescence intensity was detectable using PBS as continuous phase (**D**). Significances are indicated by asterisks with: *** = $p < 0.001$ (Mann–Whitney U test).

Representative CLSM images as well as corresponding false-color plots presenting the fluorescence intensity as an indicator for the release state of SR101 are depicted in **Figure 9A–D**. After transfer of the HES-NC from CH to PBS the size of the HES-NCs increased due to aggregation as already presented in **Figure 4**. Due to the increase in the mean diameter of the particles, a lower penetration depth of 383 ± 199 µm (without UVA) and 344 ± 144 µm (with

UVA) was observed. However, the follicular penetration depth was 22% higher compared to the pure SR101 solution in PBS (314 ± 179 µm) (**Figure 8C**). Furthermore, the measured fluorescence intensity showed no differences before and after irradiation with UVA (**Figure 8D**).

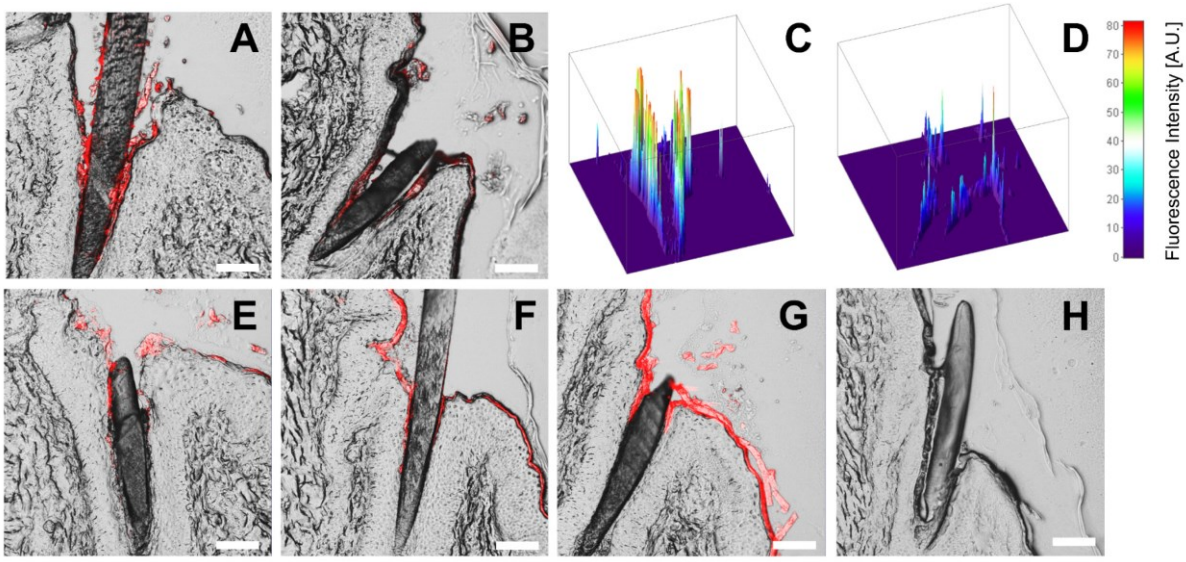

Figure 9: Representative confocal laser scanning microscopy (CLSM) images showed a significant difference of fluorescence intensity (depicted in red) before irradiation of HES-NCs in CH (1144f) (**A**) and after irradiation with UVA light (**B**) which indicated a release of the model drug SR101 from the HES-NCs (by the decrease in fluorescence intensity). The intrafollicular fluorescence intensity is further shown in pseudo-color 3D-plots for HES-NCs in CH before irradiation in (**C**) and after irradiation with UVA light in (**D**). No difference in fluorescence intensity and a slightly reduced penetration depth was noticed after transfer of the HES-NCs to PBS before (**E**) and after (**F**) irradiation with UVA but still higher in comparison to pure SR101 solution (**G**). No fluorescence was observed in untreated follicles (**H**). Scale bars correspond to 100 µm.

Numerous previous studies show the possibility of penetration of spherical nanoparticles into hair follicles inducing an enhanced follicular transport of therapeutics [60-70] and subsequent triggering of release by various external as well as internal trigger mechanisms. Several physical trigger mechanisms, based on diffusion [71] or infrared light [46] as well as chemical trigger mechanisms based on pH [72, 73] or proteolysis [74, 75] were demonstrated in previous studies. In a recent work, we have already demonstrated an intrafollicular release of the model drug SR101 from UVA-responsive NCs [26]. The capsules used were made of polyurethane and contained the photoresponsive group NXG, which was also used in the present study. Using these particles with an approximate size of ≈700 nm, a follicular penetration depth of about 500 µm as well as an intrafollicular release of the model drug were demonstrated. These

data compare well with the penetration depth and release of the HES-NCs in CH used in the present work (**Figure 8A** and **B**).

After transfer of the HES-NCs into PBS, an increase in the z-average and PDI of the particles was observed corresponding to a decrease in follicular penetration depth. It is known that particles with an average diameter of 600 nm are best suited for follicular penetration [42, 53] due to the so-called ratchet effect, which requires the particle size to match the space between the cuticle and the intrafollicular stratum corneum [23]. Because of an increase in the mean particle size (**Figure 4**) this effect did not occur for a certain proportion of the particles, as they were trapped in the described interstitial space. In our previous study, we postulated that the decrease in fluorescence intensity is associated with the release of the model drug SR101 from the polar intraparticulate environment into the apolar extraparticulate environment [26]. Since a polar outer phase was used here, SR101 did not show any measurable alterations in fluorescence intensity. Therefore, the water-based system was not suitable for an indication of release.

3.6. *Ex vivo* microbial reduction

Treating porcine skin with EtOH (80%) reduced the microbial load by 0.75 ± 0.51 lg levels (aerobic conditions) and 1.27 ± 1.46 lg levels (anaerobic conditions) whereas treatment with HES-NCs in EtOH with betaine monohydrate led to a reduction of 1.08 ± 0.55 and 1.36 ± 0.63 lg levels, respectively. Pure EtOH (80%) had minor effects that were not statistically significant. When the HES-NCs were cleaved after application, reduction was about 0.95 ± 0.93 and 1.05 ± 0.83 lg levels meaning that UVA-induced cleavage of the HES-NCs induced no enhanced microbial reduction. The number of CFU of bacteria cultivated under aerobic conditions was statistically significantly reduced by the HES-NC dispersion and the UVA-cleaved HES-NCs in comparison to UVA-treated and the control porcine skin ($p < 0.01$, **Figure 10A**). HES-NCs led to a statistically significant reduction in colonization with bacteria cultivated under anaerobic conditions in comparison to the control and to UVA treated skin ($p < 0.05$, **Figure 10B**). An antiseptic effect caused by irradiation with UVA light as reported in previous studies [44] could not be observed.

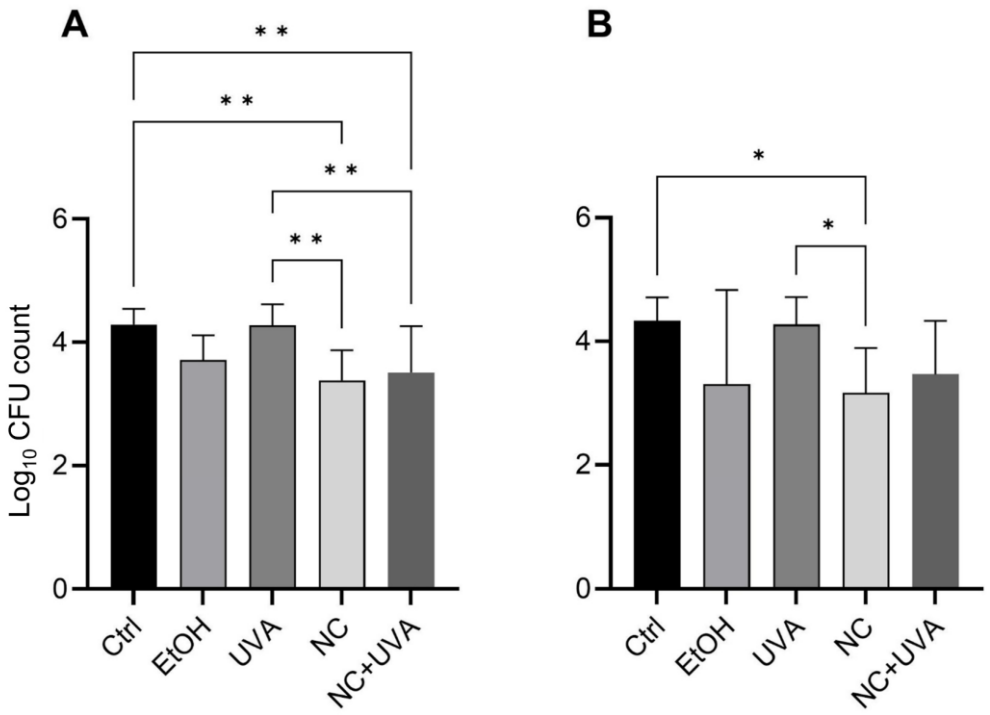

Figure 10: Log_{10} values of *ex vivo* porcine skin colonization for untreated skin (Ctrl) after treatment with 80% EtOH with betaine monohydrate (EtOH), UVA irradiation (UVA), HES-NCs in 80% EtOH with 0.1% betaine monohydrate (NC) and HES-NCs in 80% EtOH with 0.1% betaine monohydrate + irradiation with UVA (NC + UVA) for bacteria cultivated under aerobic conditions (**A**) and bacteria cultivated under anaerobic conditions (**B**). Significances between the treatments are indicated by asterisks with * = $p < 0.05$, ** = $p < 0.01$ as determined by Tukey post hoc tests after one-way ANOVA. Mean values ± standard deviations are presented for $n = 10$ porcine ear skin samples.

Compared to human skin, porcine skin has a concordance of around 97% in the genera found with a higher colonization of 2 log levels [1]. Staphylococci and *Corynebacterium* ssp. were mainly found on porcine skin under aerobic culture conditions on the $n = 10$ porcine ears conducted in this study. Besides the Propionibacteriaceae, these also make up the main part of the colonization of human skin [2, 76]. On control areas they made up the main proportion with 54.1 ± 25.0% and 33.1 ± 22.5%, respectively. On EtOH-treated skin areas, proportions were similar (57.6 ± 36.3% and 30.0 ± 27.5%). The proportion of *Curtobacterium* ssp. was rising (6.9 ± 1.5% to 56.6 ± 9.3%). Interestingly, on skin areas treated with NC and UVA, 72.0 ± 30.8% of the bacteria were staphylococci, whereas 27.5 ± 22.4% were *Corynebacterium* ssp. In contrast, only in one sample, curtobacteria (18.8%) were found. Rising proportions of staphylococci indicate a stronger reduction in further microorganisms with lower abundance as of the genera *Dietzia, Gordonia, Levilactobacillus, Rhodococcus, Micrococcus, Bacillus, Pseudomonas* and others. In most samples, mainly staphylococci and *Corynebacterium* ssp. were found after treatment with EtOH or NC + UVA. Under anaerobic conditions, proportions were similar. Staphylococci accounted for 62.1 ± 22.9% in control samples, 71.1 ± 32.7% on EtOH-

treated samples, and 84.7 ± 15.5% in NC + UVA treated samples. The proportion of *Corynebacterium* ssp. was steady (31.1 ± 27.7%, 30.0 ± 29.5%, 27.2 ± 11.3%).

The results provide a first indication of an influence on the composition of the skin microbiome possibly resulting from differing proportions of species in the samples. Whether the HES formulation actually has a significant effect should nevertheless be evaluated in the context of a larger *in vivo* study.

Besides nanoparticle-free approaches for the hygienic treatment of hair follicles, such as the binding of sebum via triethanolamine [77, 78], it was shown in several previous works that the delivery of antiseptics to hair follicles by using NCs is possible [79] and induces enhanced skin decolonization [80-83]. Since the enhanced antiseptic effect of the HES-NCs was not statistically significant in this experiment, we conclude that the hypothesized reduced recolonization should be elucidated in future experiments under *in vivo* conditions, where sebum flow from the hair follicles is present.

Based on the International Commission on Non-Ionizing Radiation Protection (ICNIRP), the applied dose of 219 mW/cm^2 (**Section 2.11.1.**) corresponds to 48% of the threshold for actinic damage and 36% of the threshold for one minimal erythema dose. According to Lohan et al. [84] this dose is still below the threshold (0.5 MED) causing irreversible lipid oxygen species in skin. Thus, the applied doses of UVA in the microbial reduction experiment can be considered as safe.

4. Conclusions

In the present study we were able to successfully produce photoresponsive HES-NCs in 80% EtOH by incorporating an *o*-nitrobenzyl derivative. Furthermore, we showed that UVA-induced photocleavage as well as efficient release of a model drug EtOH is possible with this system which could be utilized for the delivery and release of numerous hydrophilic drugs. It was found that by using the surfactant betaine monohydrate, the HES-NCs exhibited the highest stability in the target medium water/EtOH. Furthermore, the use of HES as a basic agent for NC manufacture resulted in a cytocompatible product. By using the novel HES-NCs, we achieved deep follicular penetration and intrafollicular release of the model drug EtOH using CH as a continuous phase. Nevertheless, we showed that detection of release of the model drug in the hair follicle is difficult using polar continuous phases. The present work clearly demonstrated the importance of HES-NC stability for follicular penetration. The latter was limited after transfer of the HES-NCs to PBS because agglomeration occurred and the HES-NCs were thus outside

the size range suitable for follicular penetration. For the *ex vivo* microbial reduction experiments we successfully developed a powerful LED device to increase the translatability of the system. Regardless of the reduced penetration depth due to agglomeration, HES-NCs in EtOH led to a significant reduction in bacteria *ex vivo*. EtOH without HES-NCs had minor effects which, however, were not statistically significant. These data provide first indications that the application of the newly developed HES-NCs in combination with UVA light is conceivable for advanced skin antisepsis. Nevertheless, the hypothesis of reduced recolonization when using NCs should be elucidated in future experiments under *in vivo* conditions. In conclusion, when synthesizing the capsules, the targeted application area should be considered in order to avoid possible incompatibilities.

References

[1] S. Wareham-Mathiassen, V. Pinto Glenting, L. Bay, M. Allesen-Holm, H. Bengtsson, T. Bjarnsholt, Characterization of pig skin microbiome and appraisal as an in vivo subcutaneous injection model, Lab Anim (2022) 236772221136173.

[2] A.L. Byrd, Y. Belkaid, J.A. Segre, The human skin microbiome, Nat Rev Microbiol 16(3) (2018) 143-155.

[3] U. Kaspar, A. Kriegeskorte, T. Schubert, G. Peters, C. Rudack, D.H. Pieper, M. Wos-Oxley, K. Becker, The culturome of the human nose habitats reveals individual bacterial fingerprint patterns, Environ Microbiol 18(7) (2016) 2130-2142.

[4] B. Lange-Asschenfeldt, D. Marenbach, C. Lang, A. Patzelt, M. Ulrich, A. Maltusch, D. Ter-horst, E. Stockfleth, W. Sterry, J. Lademann, Distribution of bacteria in the epidermal layers and hair follicles of the human skin, Skin Pharmacol Physiol 24(6) (2011) 305-311.

[5] S. Selwyn, H. Ellis, Skin Bacteria and Skin Disinfection Reconsidered, Br Med J 1(5793) (1972) 136-140.

[6] M. Ulmer, J. Lademann, A. Patzelt, F. Knorr, A. Kramer, T. Koburger, O. Assadian, G. Daeschlein, B. Lange-Asschenfeldt, New strategies for preoperative skin antisepsis, Skin Pharmacol Physiol 27(6) (2014) 283-292.

[7] A. Kramer, J. Pochhammer, P. Walger, U. Seifert, M. Ruhnke, J.C. Harnoss, [Spectrum of pathogens in postoperative complications of visceral surgery : The problem of multidrug re-sistance], Chirurg 88(5) (2017) 369-376.

[8] A. Alkaaki, O.O. Al-Radi, A. Khoja, A. Alnawawi, A. Alnawawi, A. Maghrabi, A. Altaf, M. Aljiffry, Surgical site infection following abdominal surgery: a prospective cohort study, Can J Surg 62(2) (2019) 111-117.

[9] E. Múñez, A. Ramos, T.A. Espejo, J. Vaqué, J. Sánchez-Payá, V. Pastor, A. Asensio, [Mi-crobiology of surgical site infections in abdominal tract surgery patients], Cir Esp 89(9) (2011) 606-612.

[10] A.J. Tande, R. Patel, Prosthetic joint infection, Clin Microbiol Rev 27(2) (2014) 302-345.

[11] A. Gharamti, Z.A. Kanafani, Vascular Graft Infections: An update, Infect Dis Clin North Am 32(4) (2018) 789-809.

[12] M.C. Robson, Infection in the Surgical Patient: An Imbalance in the Normal Equilibrium, Clinics in Plastic Surgery 6(4) (1979) 493-503.

[13] C.D. Owens, K. Stoessel, Surgical site infections: epidemiology, microbiology and prevention, J Hosp Infect 70 Suppl 2 (2008) 3-10.

[14] D. Dörfel, M. Maiwald, G. Daeschlein, G. Müller, R. Hudek, O. Assadian, G. Kampf, T. Kohlmann, J.C. Harnoss, A. Kramer, Comparison of the antimicrobial efficacy of povidone-iodine-alcohol versus chlorhexidine-alcohol for surgical skin preparation on the aerobic and anaerobic skin flora of the shoulder region, Antimicrob Resist Infect Control 10(1) (2021) 17.

[15] G. Norman, R.A. Atkinson, T.A. Smith, C. Rowlands, A.D. Rithalia, E.J. Crosbie, J.C. Dumville, Intracavity lavage and wound irrigation for prevention of surgical site infection, Cochrane Database Syst Rev 10(10) (2017) CD012234.

[16] J. Beldame, B. Lagrave, L. Lievain, B. Lefebvre, N. Frebourg, F. Dujardin, Surgical glove bacterial contamination and perforation during total hip arthroplasty implantation: when gloves should be changed, Orthop Traumatol Surg Res 98(4) (2012) 432-440.

[17] R.H. Fortelny, Abdominal Wall Closure in Elective Midline Laparotomy: The Current Recommendations, Front Surg 5 (2018) 34.

[18] I. Ahmed, A.J. Boulton, S. Rizvi, W. Carlos, E. Dickenson, N.A. Smith, M. Reed, The use of triclosan-coated sutures to prevent surgical site infections: a systematic review and meta-analysis of the literature, BMJ Open 9(9) (2019) e029727.

[19] Prävention postoperativer Wundinfektionen: Empfehlung der Kommission für Krankenhaushygiene und Infektionsprävention (KRINKO) beim Robert Koch-Institut, Bundesgesundheitsblatt Gesundheitsforschung Gesundheitsschutz 61(4) (2018) 448-473.

[20] J. Seifert, D. Gümbel, M. Frank, A. Kramer, A. Ekkernkamp, Wundinfektionen – Infektionsprävention in Unfallchirurgie und Orthopädie, Krankenhaushygiene up2date 12(02) (2017) 127-140.

[21] C. Eckmann, A. Kramer, O. Assadian, S. Flessa, C. Huebner, K. Michnacs, C. Muehlendyck, K.M. Podolski, M. Wilke, W. Heinlein, D.J. Leaper, Clinical and economic burden of surgical site infections in inpatient care in Germany: A retrospective, cross-sectional analysis from 79 hospitals, PLoS One 17(12) (2022) e0275970.

[22] J. Lademann, H. Richter, A. Teichmann, N. Otberg, U. Blume-Peytavi, J. Luengo, B. Weiss, U.F. Schaefer, C.M. Lehr, R. Wepf, W. Sterry, Nanoparticles--an efficient carrier for drug delivery into the hair follicles, Eur J Pharm Biopharm 66(2) (2007) 159-164.

[23] M. Radtke, A. Patzelt, F. Knorr, J. Lademann, R.R. Netz, Ratchet effect for nanoparticle transport in hair follicles, Eur J Pharm Biopharm 116 (2017) 125-130.

[24] A. Patzelt, W.C. Mak, S. Jung, F. Knorr, M.C. Meinke, H. Richter, E. Rühl, K.Y. Cheung, N. Tran, J. Lademann, Do nanoparticles have a future in dermal drug delivery?, J Control Release 246 (2017) 174-182.

[25] D. Klinger, K. Landfester, Polymeric photoresist nanoparticles: light-induced degradation of hydrophobic polymers in aqueous dispersion, Macromol Rapid Commun 32(24) (2011) 1979-1985.

[26] L. Busch, Y. Avlasevich, P. Zwicker, G. Thiede, K. Landfester, C.M. Keck, M.C. Meinke, M.E. Darvin, A. Kramer, G. Müller, M. Kerscher, J. Lademann, A. Patzelt, Release of the model drug SR101 from polyurethane nanocapsules in porcine hair follicles triggered by LED-derived low dose UVA light, Int J Pharm 597 (2021) 120339.

[27] S. Bühler, I. Lagoja, H. Giegrich, K.-P. Stengele, W. Pfleiderer, New Types of Very Efficient Photolabile Protecting Groups Based upon the[2-(2-Nitrophenyl)propoxy]carbonyl (NPPOC) Moiety, Helv Chim Acta 87(3) (2004) 620-659.

[28] J. Jiang, X. Tong, D. Morris, Y. Zhao, Toward Photocontrolled Release Using Light-Dissociable Block Copolymer Micelles, Macromolecules 39(13) (2006) 4633-4640.

[29] C.P. Holmes, D.G. Jones, Reagents for Combinatorial Organic Synthesis: Development of a New o-Nitrobenzyl Photolabile Linker for Solid Phase Synthesis, The Journal of Organic Chemistry 60(8) (2002) 2318-2319.

[30] Y. Li, H. Hu, Q. Zhou, Y. Ao, C. Xiao, J. Wan, Y. Wan, H. Xu, Z. Li, X. Yang, alpha-Amylase- and Redox-Responsive Nanoparticles for Tumor-Targeted Drug Delivery, ACS Appl Mater Interfaces 9(22) (2017) 19215-19230.

[31] B. Kang, P. Okwieka, S. Schottler, O. Seifert, R.E. Kontermann, K. Pfizenmaier, A. Musyanovych, R. Meyer, M. Diken, U. Sahin, V. Mailander, F.R. Wurm, K. Landfester, Tailoring the stealth properties of biocompatible polysaccharide nanocontainers, Biomaterials 49 (2015) 125-134.

[32] H. Wang, H. Hu, H. Yang, Z. Li, Hydroxyethyl starch based smart nanomedicine, RSC Adv 11(6) (2021) 3226-3240.

[33] S.I. Ahmad, L. Christensen, E. Baron, History of UV Lamps, Types, and Their Applications, Adv Exp Med Biol 996 (2017) 3-11.

[34] F.H. Fan, Z.Y. Syu, C.J. Wu, Z.J. Yang, B.S. Huang, G.J. Wang, Y.S. Lin, H. Chen, C. Hauer Kao, C.F. Lin, Ultraviolet GaN Light-Emitting Diodes with Porous-AlGaN Reflectors, Sci Rep 7(1) (2017) 4968.

[35] G. Matafonova, V. Batoev, Recent advances in application of UV light-emitting diodes for degrading organic pollutants in water through advanced oxidation processes: A review, Water Res 132 (2018) 177-189.

[36] A. Patzelt, H. Richter, R. Buettemeyer, H.J. Huber, U. Blume-Peytavi, W. Sterry, J. Lademann, Differential stripping demonstrates a significant reduction of the hair follicle reservoir in vitro compared to in vivo, Eur J Pharm Biopharm 70(1) (2008) 234-238.

[37] F. Knorr, A. Patzelt, M.E. Darvin, C.M. Lehr, U. Schäfer, A.D. Gruber, A. Ostrowski, J. Lademann, Penetration of topically applied nanocarriers into the hair follicles of dog and rat dorsal skin and porcine ear skin, Vet Dermatol 27(4) (2016) 256-e60.

[38] J. Lademann, H. Richter, M. Meinke, W. Sterry, A. Patzelt, Which skin model is the most appropriate for the investigation of topically applied substances into the hair follicles?, Skin Pharmacol Physiol 23(1) (2010) 47-52.

[39] A.S. Raber, A. Mittal, J. Schäfer, U. Bakowsky, J. Reichrath, T. Vogt, U.F. Schaefer, S. Hansen, C.M. Lehr, Quantification of nanoparticle uptake into hair follicles in pig ear and human forearm, J Control Release 179 (2014) 25-32.

[40] C.M. Keck, A. Abdelkader, O. Pelikh, S. Wiemann, V. Kaushik, D. Specht, R.W. Eckert, R.M. Alnemari, H. Dietrich, J. Brussler, Assessing the Dermal Penetration Efficacy of Chemical Compounds with the Ex-Vivo Porcine Ear Model, Pharmaceutics 14(3) (2022) 678.

[41] M. Alhibah, M. Kröger, S. Schanzer, L. Busch, J. Lademann, I. Beckers, M.C. Meinke, M.E. Darvin, Penetration Depth of Propylene Glycol, Sodium Fluorescein and Nile Red into the Skin Using Non-Invasive Two-Photon Excited FLIM, Pharmaceutics 14(9) (2022) 1790.

[42] L. Busch, Y. Keziban, L. Dähne, C.M. Keck, M.C. Meinke, J. Lademann, A. Patzelt, The impact of skin massage frequency on the intrafollicular transport of silica nanoparticles: Validation of the ratchet effect on an ex vivo porcine skin model, Eur J Pharm Biopharm 158 (2021) 266-272.

[43] RICHTLINIE 2006/25/EG DES EUROPÄISCHEN PARLAMENTS UND DES RATES vom 5. April 2006. Available online: https://eur-lex.europa.eu/LexUriServ/LexUriServ.do?uri=OJ:L:2006:114:0038:0059:de:PDF (accessed on 23 December 2022).

[44] A. Rezaie, G.G.S. Leite, G.Y. Melmed, R. Mathur, M.J. Villanueva-Millan, G. Parodi, J. Sin, J.F. Germano, W. Morales, S. Weitsman, S.Y. Kim, J.H. Park, S. Sakhaie, M. Pimentel, Ultraviolet A light effectively reduces bacteria and viruses including coronavirus, PLoS One 15(7) (2020) e0236199.

[45] A. Gupta, P. Avci, T. Dai, Y.Y. Huang, M.R. Hamblin, Ultraviolet Radiation in Wound Care: Sterilization and Stimulation, Adv Wound Care (New Rochelle) 2(8) (2013) 422-437.

[46] J. Lademann, H. Richter, F. Knorr, A. Patzelt, M.E. Darvin, E. Rühl, K.Y. Cheung, K.K. Lai, R. Renneberg, W.C. Mak, Triggered release of model drug from AuNP-doped BSA nanocarriers in hair follicles using IRA radiation, Acta Biomater 30 (2016) 388-396.

[47] BLAST: Basic Local Alignment Search Tool. Available online: https://blast.ncbi.nlm.nih.gov (accessed on 23 December 2022).

[48] H. Yang, Y. Luo, H. Hu, S. Yang, Y. Li, H. Jin, S. Chen, Q. He, C. Hong, J. Wu, Y. Wan, M. Li, Z. Li, X. Yang, Y. Su, Y. Zhou, B. Hu, pH-Sensitive, Cerebral Vasculature-Targeting Hydroxyethyl Starch Functionalized Nanoparticles for Improved Angiogenesis and Neurological Function Recovery in Ischemic Stroke, Adv Healthc Mater 10(12) (2021) e2100028.

[49] R. Tan, D. Tian, J. Liu, C. Wang, Y. Wan, Doxorubicin-Bound Hydroxyethyl Starch Conjugate Nanoparticles with pH/Redox Responsive Linkage for Enhancing Antitumor Therapy, Int J Nanomedicine 16 (2021) 4527-4544.

[50] C. Yu, C. Liu, S. Wang, Z. Li, H. Hu, Y. Wan, X. Yang, Hydroxyethyl Starch-Based Nanoparticles Featured with Redox-Sensitivity and Chemo-Photothermal Therapy for Synergized Tumor Eradication, Cancers (Basel) 11(2) (2019) 207.

[51] M. Yu, N. Ji, Y. Wang, L. Dai, L. Xiong, Q. Sun, Starch-based nanoparticles: Stimuli responsiveness, toxicity, and interactions with food components, Compr Rev Food Sci Food Saf 20(1) (2021) 1075-1100.

[52] A.R. Studart, E. Amstad, L.J. Gauckler, Colloidal stabilization of nanoparticles in concentrated suspensions, Langmuir 23(3) (2007) 1081-1090.

[53] A. Patzelt, H. Richter, F. Knorr, U. Schäfer, C.M. Lehr, L. Dähne, W. Sterry, J. Lademann, Selective follicular targeting by modification of the particle sizes, J Control Release 150(1) (2011) 45-48.

[54] C. Lv, Z. Wang, P. Wang, X. Tang, Photodegradable polyurethane self-assembled nanoparticles for photocontrollable release, Langmuir 28(25) (2012) 9387-9394.

[55] C. Lv, Z. Wang, P. Wang, X. Tang, Photodegradable polyesters for triggered release, Int J Mol Sci 13(12) (2012) 16387-16399.

[56] B. Wang, K. Chen, R.-d. Yang, F. Yang, J. Liu, Photoresponsive nanogels synthesized using spiropyrane-modified pullulan as potential drug carriers, J Appl Polym Sci 131(10) (2014) 40288.

[57] S. Chen, J. Wu, Q. Tang, C. Xu, Y. Huang, D. Huang, F. Luo, Y. Wu, F. Yan, Z. Weng, S. Wang, Nano-micelles based on hydroxyethyl starch-curcumin conjugates for improved stability, antioxidant and anticancer activity of curcumin, Carbohydr Polym 228 (2020) 115398.

[58] D. Narayanan, G.J. Pillai, S.V. Nair, D. Menon, Effect of formulation parameters on pharmacokinetics, pharmacodynamics, and safety of diclofenac nanomedicine, Drug Deliv Transl Res 9(5) (2019) 867-878.

[59] D. Narayanan, S. Nair, D. Menon, A systematic evaluation of hydroxyethyl starch as a potential nanocarrier for parenteral drug delivery, Int J Biol Macromol 74 (2015) 575-584.

[60] R. Ferreira-Nunes, M. Cunha-Filho, T. Gratieri, G.M. Gelfuso, Follicular-targeted delivery of spironolactone provided by polymeric nanoparticles, Colloids Surf B Biointerfaces 208 (2021) 112101.

[61] A.T. Ogunjimi, F. Chahud, R.F.V. Lopez, Isotretinoin-Delonix polymeric nanoparticles: Potentials for skin follicular targeting in acne treatment, Int J Pharm 610 (2021) 121217.

[62] P.M. Oliveira, T. Alencar-Silva, F.Q. Pires, M. Cunha-Filho, T. Gratieri, J.L. Carvalho, G.M. Gelfuso, Nanostructured lipid carriers loaded with an association of minoxidil and latanoprost for targeted topical therapy of alopecia, Eur J Pharm Biopharm 172 (2022) 78-88.

[63] J. Kong, W. Qiang, J. Jiang, X. Hu, Y. Chen, Y. Guo, H. Liu, S. Sun, H. Gao, Y. Zhang, Y. Gao, X. Liu, X. Liu, H. Li, Safflower oil body nanoparticles deliver hFGF10 to hair follicles and

reduce microinflammation to accelerate hair regeneration in androgenetic alopecia, Int J Pharm 616 (2022) 121537.

[64] Y. Oaku, A. Abe, Y. Sasano, F. Sasaki, C. Kubota, N. Yamamoto, T. Nagahama, N. Nagai, Minoxidil Nanoparticles Targeting Hair Follicles Enhance Hair Growth in C57BL/6 Mice, Pharmaceutics 14(5) (2022) 947.

[65] S.E. Mangion, L. Sandiford, Y. Mohammed, M.S. Roberts, A.M. Holmes, Multi-Modal Imaging to Assess the Follicular Delivery of Zinc Pyrithione, Pharmaceutics 14(5) (2022) 1076.

[66] T. Subongkot, N. Charernsriwilaiwat, R. Chanasongkram, K. Rittem, T. Ngawhirunpat, P. Opanasopit, Development and Skin Penetration Pathway Evaluation Using Confocal Laser Scanning Microscopy of Microemulsions for Dermal Delivery Enhancement of Finasteride, Pharmaceutics 14(12) (2022) 2784.

[67] C. Nastiti, T. Ponto, E. Abd, J.E. Grice, H.A.E. Benson, M.S. Roberts, Topical Nano and Microemulsions for Skin Delivery, Pharmaceutics 9(4) (2017) 37.

[68] E. Abd, H.A.E. Benson, M.S. Roberts, J.E. Grice, Minoxidil Skin Delivery from Nanoemulsion Formulations Containing Eucalyptol or Oleic Acid: Enhanced Diffusivity and Follicular Targeting, Pharmaceutics 10(1) (2018) 19.

[69] R. Christmann, D.K. Ho, J. Wilzopolski, S. Lee, M. Koch, B. Loretz, T. Vogt, W. Baumer, U.F. Schaefer, C.M. Lehr, Tofacitinib Loaded Squalenyl Nanoparticles for Targeted Follicular Delivery in Inflammatory Skin Diseases, Pharmaceutics 12(12) (2020) 1131.

[70] E. Pena-Rodriguez, M. Lajarin-Reinares, A. Mata-Ventosa, S. Perez-Torras, F. Fernandez-Campos, Dexamethasone-Loaded Lipomers: Development, Characterization, and Skin Biodistribution Studies, Pharmaceutics 13(4) (2021) 533.

[71] N. Tran, F. Knorr, W.C. Mak, K.Y. Cheung, H. Richter, M. Meinke, J. Lademann, A. Patzelt, Gradient-dependent release of the model drug TRITC-dextran from FITC-labeled BSA hydrogel nanocarriers in the hair follicles of porcine ear skin, Eur J Pharm Biopharm 116 (2017) 12-16.

[72] P. Dong, F.F. Sahle, S.B. Lohan, S. Saeidpour, S. Albrecht, C. Teutloff, R. Bodmeier, M. Unbehauen, C. Wolff, R. Haag, J. Lademann, A. Patzelt, M. Schäfer-Korting, M.C. Meinke, pH-sensitive Eudragit(R) L 100 nanoparticles promote cutaneous penetration and drug release on the skin, J Control Release 295 (2019) 214-222.

[73] D. Kaden, L. Dähne, F. Knorr, H. Richter, J. Lademann, M.C. Meinke, A. Patzelt, M.E. Darvin, S. Jung, Determination of the pH Gradient in Hair Follicles of Human Volunteers Using pH-Sensitive Melamine Formaldehyde-Pyranine Nile Blue Microparticles, Sensors (Basel) 20(18) (2020) 5243.

[74] W.C. Mak, A. Patzelt, H. Richter, R. Renneberg, K.K. Lai, E. Rühl, W. Sterry, J. Lademann, Triggering of drug release of particles in hair follicles, J Control Release 160(3) (2012) 509-514.

[75] W.C. Mak, H. Richter, A. Patzelt, W. Sterry, K.K. Lai, R. Renneberg, J. Lademann, Drug delivery into the skin by degradable particles, Eur J Pharm Biopharm 79(1) (2011) 23-27.

[76] A.A. Ross, A. Rodrigues Hoffmann, J.D. Neufeld, The skin microbiome of vertebrates, Microbiome 7(1) (2019) 79.

[77] W. Musial, A. Kubis, Preliminary assessment of alginic acid as a factor buffering triethanolamine interacting with artificial skin sebum, Eur J Pharm Biopharm 55(2) (2003) 237-240.

[78] A. Kostrzebska, W. Musial, The Influence of Increasing Concentrations of AMPD on the Efficacy of Its Penetration into a Model Skin Sebum Layer, Pharmaceutics 12(12) (2020) 1228.

[79] M. Kirkby, A.B. Sabri, D.J. Scurr, G.P. Moss, Dendrimer-mediated permeation enhancement of chlorhexidine digluconate: Determination of in vitro skin permeability and visualisation of dermal distribution, Eur J Pharm Biopharm 159 (2021) 77-87.

[80] H. Lboutounne, J.F. Chaulet, C. Ploton, F. Falson, F. Pirot, Sustained ex vivo skin antiseptic activity of chlorhexidine in poly(epsilon-caprolactone) nanocapsule encapsulated form and as a digluconate, J Control Release 82(2-3) (2002) 319-334.

[81] D.T. Nhung, A.M. Freydiere, H. Constant, F. Falson, F. Pirot, Sustained antibacterial effect of a hand rub gel incorporating chlorhexdine-loaded nanocapsules (Nanochlorex), Int J Pharm 334(1-2) (2007) 166-172.

[82] M. Ulmer, A. Patzelt, T. Vergou, H. Richter, G. Müller, A. Kramer, W. Sterry, V. Czaika, J. Lademann, In vivo investigation of the efficiency of a nanoparticle-emulsion containing polihexanide on the human skin, Eur J Pharm Biopharm 84(2) (2013) 325-329.

[83] H. Lboutounne, V. Faivre, F. Falson, F. Pirot, Characterization of transport of chlorhexidine-loaded nanocapsules through hairless and wistar rat skin, Skin Pharmacol Physiol 17(4) (2004) 176-182.

[84] S.B. Lohan, D. Ivanov, N. Schuler, B. Berger, L. Zastrow, J. Lademann, M.C. Meinke, Switching from healthy to unhealthy oxidative stress - does the radical type can be used as an indicator?, Free Radic Biol Med 162 (2021) 401-411.

3.2. PUBLICATION II:
ADVANCED SKIN ANTISEPSIS: APPLICATION OF UVA-CLEAVABLE HYDROXYETHYL STARCH NANOCAPSULES FOR IMPROVED ERADICATION OF HAIR FOLLICLE-ASSOCIATED MICROORGANISMS

3.3. Publication III:

Application of 233 nm far-UVC LEDs for eradication of MRSA and MSSA and risk assessment on skin models

3.3. PUBLICATION III:
APPLICATION OF 233 NM FAR-UVC LEDS FOR ERADICATION OF MRSA AND MSSA AND RISK ASSESSMENT ON SKIN MODELS

Application of 233 nm far-UVC LEDs for eradication of MRSA and MSSA and risk assessment on skin models

Paula Zwicker [1,*], Johannes Schleusener [2,*], Silke B. Lohan [2], Loris Busch [2,3], Claudia Sicher [1], Sven Einfeldt [4], Michael Kneissl [4,5], Anja A. Kühl [6], Cornelia M. Keck [3], Christian Witzel [7], Axel Kramer [1], Martina C. Meinke [2]

[1] *Institute of Hygiene and Environmental Medicine, University Medicine Greifswald, Greifswald, Germany*

[2] *Center of Experimental and Applied Cutaneous Physiology, Department of Dermatology, Venerology and Allergology, Charité-Universitätsmedizin Berlin, Corporate Member of Freie Universität Berlin and Humboldt-Universität zu Berlin, Berlin, Germany*

[3] *Department of Pharmaceutics and Biopharmaceutics, Philipps-Universität Marburg, Marburg, Germany*

[4] *Ferdinand-Braun-Institut gGmbH, Leibniz-Institut Für Höchstfrequenztechnik, Berlin, Germany*

[5] *Institute of Solid State Physics, Technische Universität Berlin, Berlin, Germany*

[6] *iPATH.Berlin-Immunopathology for Experimental Models, Core Facility of the Charité-Universitätsmedizin Berlin, Corporate Member of Freie Universität Berlin and Humboldt-Universität zu Berlin, Berlin, Germany*

[7] *Division of Plastic and Reconstructive Surgery, Department of Surgery, Charité-Universitätsmedizin Berlin, Corporate Member of Freie Universität Berlin and Humboldt-Universität zu Berlin, Berlin, Germany*

[*] *contributed equally*

(adapted from: Sci Rep 2022;12(1):2587. doi: 10.1038/s41598-022-06397-z)

Abstract

A newly developed UVC LED source with an emission wavelength of 233 nm was proved on bactericidal efficacy and skin tolerability. The bactericidal efficacy was qualitatively analysed using blood agar test. Subsequently, quantitative analyses were performed on germ carrier tests using the MRSA strain DSM11822, the MSSA strain DSM799, *S. epidermidis* DSM1798 with various soil loads. Additionally, the compatibility of the germicidal radiation doses on excised human skin and reconstructed human epidermis was proved. Cell viability, DNA damage and production of radicals were assessed in comparison to typical UVC radiation from discharge lamps (222 nm, 254 nm) and UVB (280–380 nm) radiation for clinical assessment. At a dose of 40 mJ/cm^2, the 233 nm light source reduced the viable microorganisms by a $\log_{10}$ reduction (LR) of 5 $\log_{10}$ levels if no soil load was present. Mucin and protein containing soil loads diminished the effect to an LR of 1.5–3.3. A salt solution representing artificial sweat (pH 8.4) had only minor effects on the reduction. The viability of the skin models was not reduced and the DNA damage was far below the damage evoked by 0.1 UVB minimal erythema dose, which can be regarded as safe. Furthermore, the induced damage vanished after 24 h. Irradiation on four consecutive days also did not evoke DNA damage. The radical formation was far lower than 20 min outdoor visible light would cause, which is classified as low radical load and can be compensated by the antioxidant defence system.

1. Introduction

Methicillin-resistant *Staphylococcus aureus* (MRSA) belong to the most common multi-resistant pathogens. The primary location of MRSA, as well as methicillin-sensitive *Staphylococcus aureus* (MSSA), is the nasal vestibule that is considered as an initial point for colonization of the body. Both are the main origin of surgical site infections (SSI). If an MRSA carrier is identified preoperatively, an indication for decolonization is given, since the increased risk for SSI resulting in prolonged hospital stays and increased mortality will be reduced [1, 2]. MSSA are an independent risk factor for the colonization of alloplastic implants; nowadays the universal decolonization of MSSA is increasingly gaining importance [3].

The decolonization with the conventional antibiotic Mupirocin leads to resistances [4], followed by decreased efficacy [5]. As an alternative, nasal decolonization is performed with antiseptic agents, such as chlorhexidine digluconate or octenidine dihydrochloride, which are either insufficient [6] or result in formation of resistances with cross-resistance to antibiotics, questioning its use [7]. Thus, a new microbiocidal surgical method that does not evoke formation of resistances is desirable. Therefore, the application of UVC radiation is a suitable and promising alternative [8].

Previous work has shown that MRSA can be eradicated with UVC radiation at a wavelength of 254 nm and more recently also at 222 nm [9, 10].

UV radiation is absorbed by proteins and nucleic acids as DNA, promoting the development of molecular rearrangements and photoproducts, such as the major DNA damage products cyclobutane pyrimidine dimers (CPD) and pyrimidine(6-4) pyrimidone photoproducts (6-4PPs), which are associated with the development of mutations and cancer [11, 12].

After irradiation with 254 nm, about 70% of the basal cells in the skin are negatively affected in their vitality [13], while almost no pre-mutagenous UV-associated DNA lesions were observed with 222 nm, which can be explained by the higher absorption of 254 nm wavelength by proteins and nucleic acids—being associated with the development of mutations leading to skin cancer [11, 12] and eye cataracts [14, 15]. However, high energy UVC radiation ($\lambda < 245$ nm) is strongly absorbed by the stratum corneum (SC), the horny layer that does not contain cell nuclei [16]. In contrast, small microbes (< 1 µm) can be efficiently inactivated on the surface of the skin [17] as already shown on MRSA that could be eradicated by using 222 nm radiation on 3D murine skin [16].

Another key aspect is radical formation which is mainly induced by UVA but also by UVB, visible, and in low amounts also near infrared light [18]. In order to prevent enhanced tumour

development [19, 20] as a consequence of cell and tissue damage [21-23] by increased oxidation of different cell components, radicals need to be tightly controlled. So far, effects on the radical production in skin due to UVC irradiation have not been published.
In this study, the inactivation of different bacterial strains as well as the effect on skin using a recently developed 233 nm far-UVC LED source [24, 25] were evaluated and compared to a 254 nm Hg-vapour lamp and a 222 nm KrCl excimer lamp. In contrast to the mercury and excimer lamps, the emission wavelength peak of semiconductor-based UVC LEDs can be tuned in order to obtain the optimal compromise between limiting penetration depth to avoid DNA damage and providing sufficiently high irradiances for UVC deactivation of MRSA even in the presence of UVC-absorbing soil load. Due to their small form factors UVC LEDs can be easily arranged in larger arrays of any shape and size allowing the controlled irradiation of specific areas of skin without damaging the surroundings. Since the footprint of an UVC LED chip is typically 1 mm^2 or less with a few hundred µm in thickness, compact UVC LED sources could also enable access to narrow body openings, e.g. in the nasal cavity or urinary tract in the future.

2. Results

2.1. Inactivation of MRSA

2.1.1. Persistence

To ensure a minimum number of colony forming units per test specimen, the recovery rates were determined. Recovery rates were obtained for 0.03% albumin sodium chloride solution. For MRSA DSM 11822 it was about (42 ± 6.4)% and for *S. epidermidis* DSM 1798 (30 ± 30)%. Higher rates were found for MSSA DSM 799 (68 ± 20)%. All tests were repeated three times. After drying, a bacterial burden of 1.5×10^5–1.5×10^6 colony forming units/germ carrier was achieved.

2.1.2. Bactericidal efficacy

The bactericidal efficacy of UVC irradiation with three different wavelengths and four doses, each, were proofed in a quantitative germ carrier test following DIN EN 14561 [26] and ASTM E2111-12 [27]. To mimic realistic conditions, a number of soil loads were applied. Using UVC radiation of 222 nm (**Figure 1a**), a $\log_{10}$ reduction (LR) of 4.4 was attained in sodium chloride solution with a dose of 20 mJ/cm^2. Under soil load (artificial sweat pH 8.4, albumin 0.3 g/l, artificial wound exudate, mucin 0.5%), the LRs varied between 0.64 and 1.59. Increasing the

dose from 20 to 40 mJ/cm^2 led to a slight increase in bacterial reduction. Further rising irradiation doses did not result in an additional increase in efficacy.

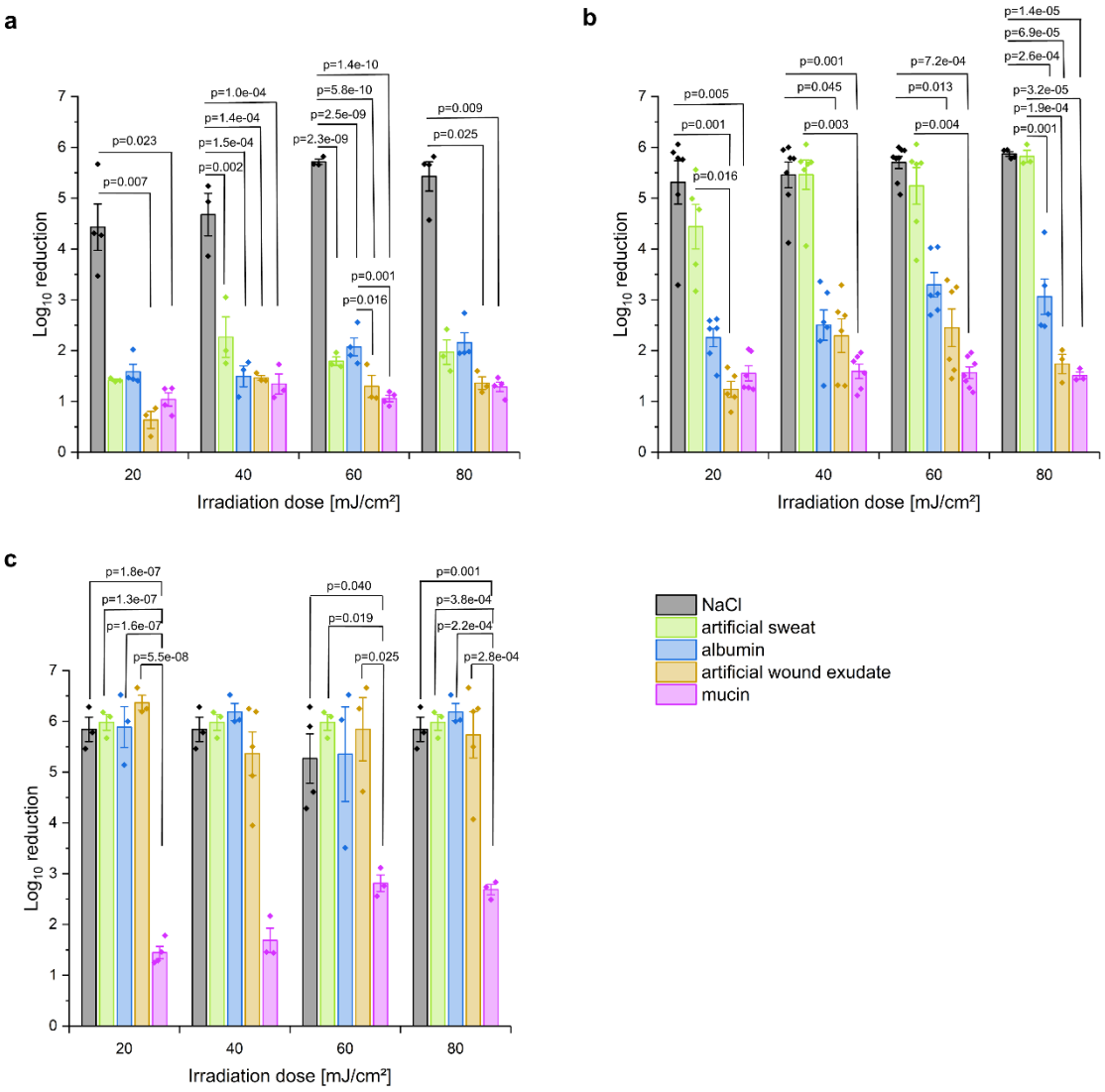

Figure 1: MRSA DSM 11822 $\log_{10}$ reduction of colony forming units (cfu)/germ carrier for irradiation with 222 nm (**a**), 233 nm (**b**) and 254 nm (**c**). Bacteria were suspended in NaCl (black), artificial sweat (green), albumin (blue), artificial wound exudate (orange) and mucin (purple) solutions without and with soil load and dried for 30 min before irradiation. The presented p-values are based on one-way ANOVAs and Kruskal–Wallis tests followed by pairwise post hoc tests with Bonferroni correction. The data show mean ± SEM. n = 3–8.

Radiation with 254 nm wavelength with an irradiance of 0.29 mW/cm^2 resulted in a strong reduction of viable microorganisms in sodium chloride solution, artificial sweat, albumin and artificial wound exudate (LR 5.84–6.37). For mucin, LRs of 1.45 at a dose of 20 mJ/cm^2 up to 2.69 for a dose of 80 mJ/cm^2 could be achieved (**Figure 1c**).

In sodium chloride solution, reduction after irradiation at 233 nm was comparable to 254 nm (LR ≥ 5). With higher doses, the LR is rising slightly from 5.3 (20 mJ/cm^2) to 5.7 (60 mJ/cm^2) (**Figure 1b**). Irradiation of bacteria in artificial sweat with a dose of 20 mJ/cm^2 decreased the LR to 4.44. Doses higher than 20 mJ/cm^2 reduced the applied microorganisms with an LR > 5. The lowest LRs were found with 0.03% sodium chloride albumin mixture (2.26–3.3), artificial wound exudate (1.24–2.45) and 0.5% mucin (1.51–1.59), whereby the LR was nearly constant with rising doses.

Comparing the inactivation efficacy of MRSA DSM 11822, MSSA DSM 799 and *S. epidermidis* DSM 1798 without adding a soil load (sodium chloride solution 0.9%), the irradiation at 233 nm did not result in significant differences (LR = 4.8–5.8), when irradiated with 20 mJ/cm^2, 40 mJ/cm^2 or 60 mJ/cm^2. In artificial wound exudate, MRSA DSM 11822 is significantly less susceptible to irradiation at 233 nm (**Figure 2**) than MSSA DSM 799 and *S. epidermis* DSM 1798 (40 mJ/cm^2, 60 mJ/cm^2). MRSA DSM 11822 was reduced by LRs of 5.5 and 5.7 at 40 and 60 mJ/cm^2 in sodium chloride solution. Suspension in artificial wound exudate decreased the efficacy to LRs of 2.3 and 2.5. For MSSA DSM 799, the LR was 5.8 at an irradiation with 40 and 60 mJ/cm^2. In artificial wound exudate, the LR was 3.5 at 40 mJ/cm^2 and 4.6 at 60 mJ/cm^2. *S. epidermidis* DSM 1798 was reduced by an LR of 5.1 and 5.5, respectively, in sodium chloride solution. In artificial wound exudate, the LR decreased to 3.5 and 4.3.

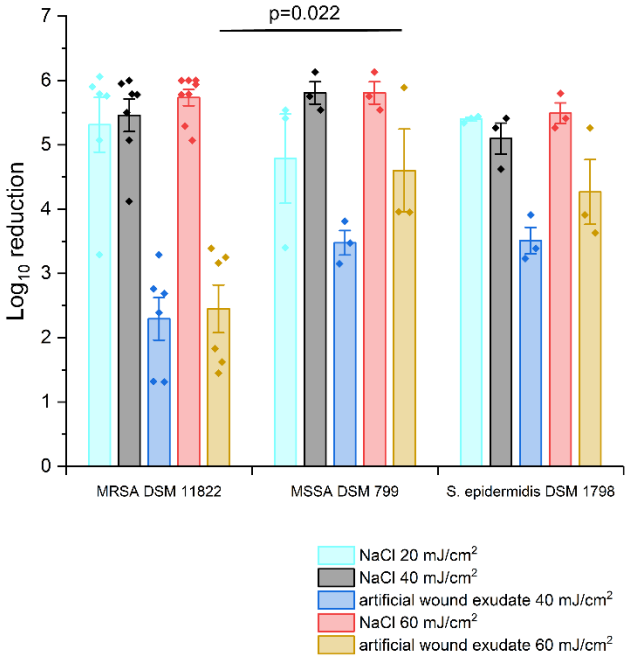

Figure 2: Log_{10} reduction after treating different MRSA DSM 1182 and MSSA DSM 799 strains as well as S. epidermidis DSM 1798 with doses of 40 mJ/cm² and 60 mJ/cm² at 233 nm. Microorganisms were suspended in sodium chloride solution (20 mJ/cm², cyan; 40 mJ/cm², black; 60 mJ/cm², red) or artificial wound exudate (40 mJ/cm², blue; 60 mJ/cm², orange) before drying on germ carriers for 30 min following irradiation. Multiple mean value comparisons were conducted to check for differences between the strains. The presented *p*-value is based on a Kruskal–Wallis test followed by pairwise post hoc tests with Bonferroni correction. The data show mean ± SEM. $n = 3–8$.

Absorption of soil loads differed clearly. At 230 nm, absorption was highest for mucin and the artificial wound exudate. For 222 nm the absorption was even higher. Sodium chloride solution has the lowest observed absorption at the relevant wavelengths (**Supplementary Information, Figure S1**).

2.2. Risk Assessment

2.2.1. Cell Viability

The cell viability was investigated directly after irradiation at different UVC wavelengths using an MTT test on punch biopsies of reconstructed epidermal human skin equivalents (RHEs) based on a fluorescence assay in accordance to [28, 29] (**Supplementary Information, Figure S2**). RHEs incubated for 1 h in sodium dodecyl sulphate (SDS, positive control) showed (2.1 ± 0.5)% viability. None of the applied doses resulted in a decrease of cell viability below 80%. Due to the photosensitivity of the cell culture medium, the RHEs were placed into PBS during irradiation. In order to verify if the minor reduction of cell viability was due to irradiation or the absence of medium, a non-irradiated RHE was kept for 30 min in PBS at room temperature ($n = 1$), which only showed a reduction to 96% cell viability (data not shown).

2.2.2. DNA Damage

For DNA damage, CPDs and 6-4PPs were investigated after irradiation of excised human skin and RHEs, which is well suitable for studies of DNA damage and radical formation in skin during or after UV irradiation [30].

As positive control, irradiation of 40 mJ/cm² at 254 nm resulted in (21.5 ± 1.9)% 6-4PP and (44.2 ± 3.7)% CPD positive epidermal keratinocytes, while untreated RHEs as negative control showed no damage (6-4PP: $p = 3.4e{-}04$, CPD: $p = 0.005$) (**Figures 3a** and **4**).

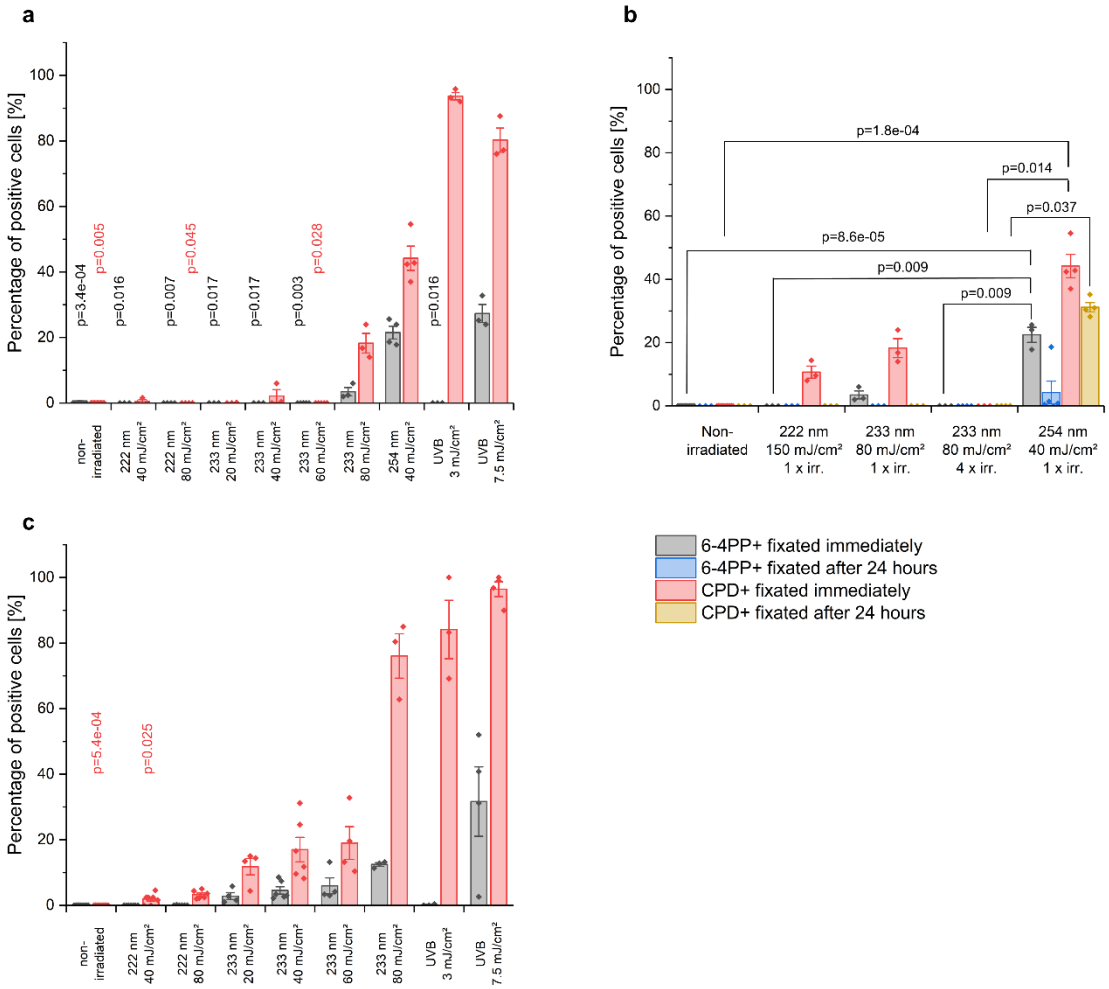

Figure 3: DNA damage of RHEs fixated directly (**a**) and 24 h after UV irradiation (**b**) and excised human skin (**c**). The data show the percentage of positive cells with 6-4PP (grey, blue) and CPD damage (red, orange). For both skin models, non-irradiated skin (negative control) shows no damage. In RHEs 44.2% of epidermal cells irradiated with 40 mJ/cm² at 254 nm (positive control) show CPDs and 21.5% of the epidermal cells show 6-4PPs. In excised human skin, irradiation with 3 mJ/cm² of UVB (positive control) induced 84.1% CPD positive cells. A reduction in DNA damage of RHEs was observed for fixation 24 h after irradiation with 40 mJ/cm² at 254 nm (positive control), indicating a DNA repair mechanism (**b**).

The CPD damage after 150 mJ/cm² irradiation with 222 nm disappeared when fixating 24 h after irradiation. The weak damage after 233 nm irradiation with 80 mJ/cm² when fixated immediately, disappeared when fixating 24 h later. Consecutive irradiation at 80 mJ/cm² of 233 nm every 24 h did not show any DNA damage. The presented p-values derive from multiple comparisons with Bonferroni corrections after a Kruskal–Wallis test. Every group was compared to the positive control (**a**,**c**) and additionally the influence of multiple irradiations and fixation time was checked (**b**). The data show mean ± SEM. $n = 3–12$.

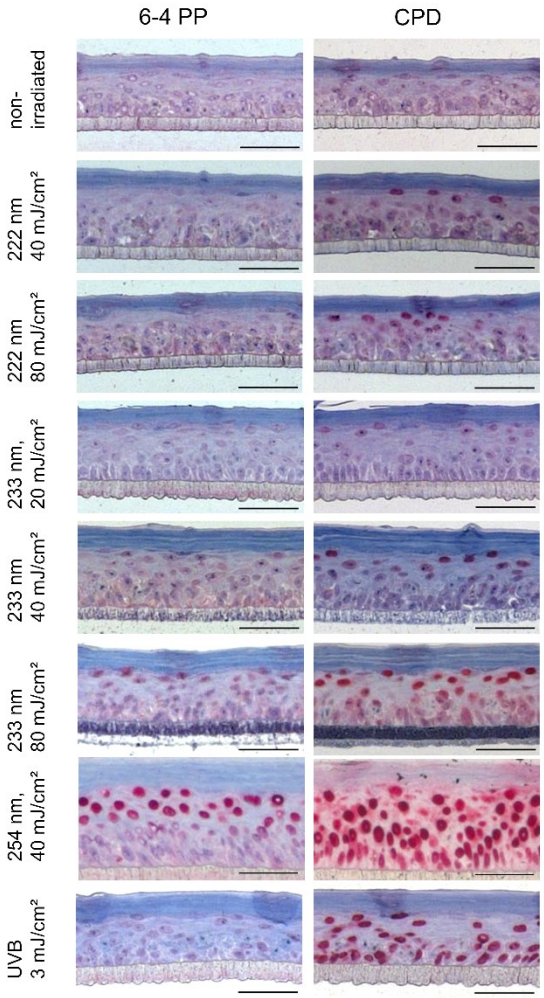

Figure 4: Representative images of histological analysis of DNA damage in RHEs. Paraffin sections are stained for 6-4PP (left column) and CPD damage (right column). Positive cells are stained in dark red. Non-irradiated RHEs (negative control) show no positive cells, while positive epidermal keratinocytes of RHEs irradiated with 40 mJ/cm² at 254 nm (positive control) were found even in the deeper layers of the epidermis. RHEs irradiated with 3 mJ/cm² UVB (0.1 MED) showed > 90% CPD damage throughout the whole epidermis. The CPD damage after 40 mJ/cm² irradiation at 222 nm and 233 nm only occurred at the uppermost layer of the epidermis. Scale bar: 50 µm.

Doses of 20–60 mJ/cm² at 233 nm resulted in only negligible CPD damage which occurred only on the superficial layer of the epidermis (**Figure 4**). When raising the dose to 80 mJ/cm², the CPD damage increased to (18.3 ± 3.0)%. Irradiation of 222 nm at 40 mJ/cm² resulted in (0.5 ± 0.5)% CPD positive keratinocytes; DNA damage after irradiation at 80 mJ/cm² was not observed (6-4PP: $p = 0.007$, CPD: $p = 0.045$). Similar to the irradiation at 233 nm, this damage was limited to the superficial layer of the epidermis (**Figure 4**).

Broad band UVB irradiation (280–400 nm) with a dose of 3 mJ/cm², which amounts to ≈ 10% of a minimal erythema dose (MED) for skin type II, provoked (93.7 ± 1.1)% CPD keratinocytes (**Figure 4**). All damage caused by the high energy UVC is located very superficially directly below the SC (**Figure 4**), whereas 254 nm and UVB-induced damage reaches down to the basal cells.

The maximal depth of DNA damage observed in the epidermis of RHE was measured on 5 positions of the histological images from the skin surface (**Supplementary Information, Figure S3a**). The measured SC thickness was subtracted on every position. For 40 mJ/cm^2 at 254 nm, CPD and 6-4PP damage was observed in the entire epidermis and part of the dermis including the vulnerable basal cells. Similar CPD damage depths were detected after UVB irradiation at ≥ 3 mJ/cm^2; the 6-4PP damage at the higher dose occurred down to (3.2 ± 1.0) µm depth. In contrast, at 222 nm irradiation, CPD damage depths of maximally (10.7 ± 3.7) µm were observed for 150 mJ/cm^2. For irradiation at 233 nm, maximal depths of CPD damage of (16.1 ± 0.7) µm were observed for 80 mJ/cm^2. The epidermal thickness was determined to be 37–50 µm.

The mean SC thickness of RHEs was (17 ± 4.3) µm. An increase after single or multiple irradiation could not be observed. The thickness of the epidermis only increased insignificantly after fourfold irradiation on four consecutive days from (95.6 ± 2.9) µm for non-irradiated, to (97.4 ± 0.9) and (97.8 ± 3.5) µm for RHEs irradiated with 60 and 80 mJ/cm^2 at 233 nm, respectively (each $n = 4$).

As shown in **Figure 3b**, the CPD and 6-4PP damage measured for the RHEs immediately after irradiation with 40 mJ/cm^2 at 254 nm (positive control) partly regenerated after their incubation in medium for 24 h. After irradiation with 150 mJ/cm^2 at 222 nm, the (10.7 ± 1.9)% CPD damage disappeared when the RHEs were fixated 24 h after irradiation.

For 80 mJ/cm^2 irradiation at 233 nm, the immediately determined CPD damage disappeared during 24 h of further incubation. In order to evaluate a possible accumulative effect, the measurements were repeated after multiple irradiations. RHEs were irradiated four times every 24 h with the identical dose and incubated in medium at 37 °C in between. No DNA damage was observed at 80 mJ/cm^2 at 233 nm (**Figure 3b**). Non-irradiated control RHEs were incubated for the entire time with daily breaks for 30 min, showing no DNA damage. Selected investigations using cleaved caspase-3 staining for apoptosis [31] showed no apoptosis positive cells of RHEs fixated after 24 h for 40 mJ/cm^2 at 254 nm ($n = 4$), 150 mJ/cm^2 at 222 nm ($n = 3$), as well as 60 ($n = 4$) and 80 mJ/cm^2 ($n = 4$) at 233 nm, as well as for non-irradiated RHEs ($n = 3$) (data not shown).

Additionally to RHE irradiation, experiments were also performed on excised human skin obtained from plastic reduction surgeries. Here, UVB (280–400 nm) at 3 mJ/cm^2 (≈ 1/10 MED) was applied as a positive control leading to (84.1 ± 8.9)% CPD damage, while non-irradiated skin showed no DNA damage ($p = 5.4e{-}04$) (**Figures 3c** and **5**).

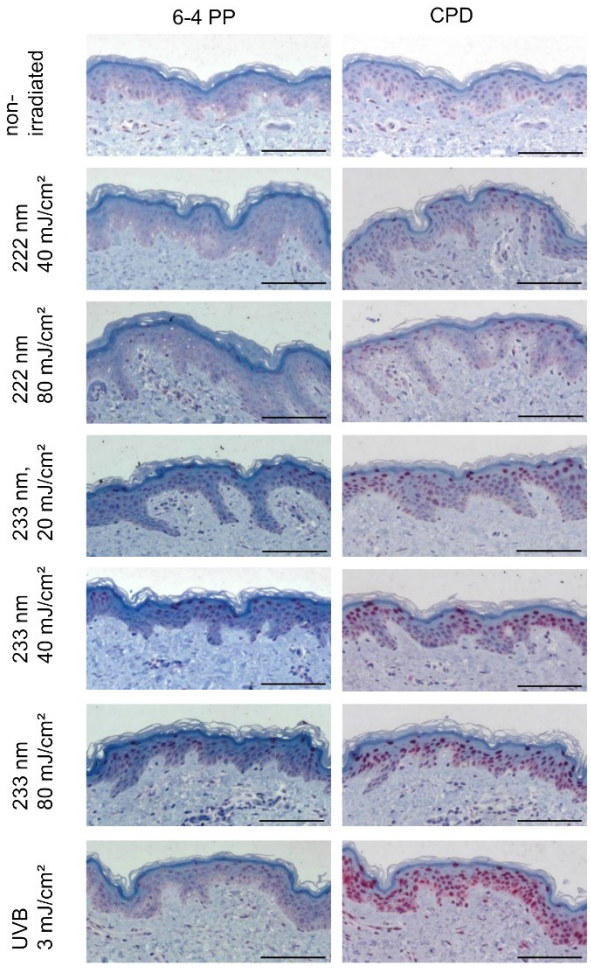

Figure 5: Representative images of histological analysis of DNA damage in excised human skin. Paraffin sections are stained for 6-4PP (left column) and CPD damage (right column). Positive cells are stained in dark red. Non-irradiated human skin (negative control) shows no positive cells. Human skin irradiated with 3 mJ/cm² UVB (0.1 MED) showed > 80% CPD damage throughout the whole epidermis. The CPD damage after 40 mJ/cm² irradiation at 222 nm and 233 nm only occurred on the uppermost layer of the epidermis. Scale bar: 100 µm.

Irradiation with 222 nm led to maximally (3.3 ± 0.5)% CPD damage at 80 mJ/cm² ($p = 0.045$). For irradiation at 233 nm, a gradual increase of CPD damage from (11.8 ± 2.5)% (20 mJ/cm²) to (76.1 ± 5.6)% (80 mJ/cm²) was observed.

The mean SC thickness of excised human skin was (12.5 ± 2.1) µm. The DNA damage depth for ≥ 3 mJ/cm² UVB irradiation, was observed in the entire epidermis down to ≥ 30 µm (**Supplementary Information, Figure S3b**). At 222 nm irradiation, a maximal depth of CPD damage of (4.6 ± 0.3) µm was observed for 150 mJ/cm². For 80 mJ/cm² irradiation at 233 nm, a maximal CPD damage depth of (16.8 ± 1.6) µm was determined.

2.2.3. Radical formation

EPR spectroscopy was used to assess the radical formation after irradiation. For biological assessment of the formed radicals, irradiation in the visible and near-infrared spectral region (λ = 400–2000 nm) was performed for 20 min (Dose: (118.7 ± 0.8) J/cm²), which is considered to be harmless. This dose induced a radical formation of $(3.10 \pm 0.26) \times 10^{14}$ spins/mm³. A lower radical formation of maximally $(1.09 \pm 0.30) \times 10^{14}$ spins/mm³ was detected after irradiation of RHEs with 222 nm of the doses 40 mJ/cm² or 60 mJ/cm² ($p = 1.0e{-}06$ and $p = 6.5e{-}07$). Furthermore, also an irradiation with 254 nm (40 mJ/cm²) induced a lower radical formation of $(0.67 \pm 0.03) \times 10^{14}$ spins/mm³ ($p = 1.2e{-}07$). A dose of 40 mJ/cm² and 60 mJ/cm² of 233 nm induced an average spin concentration of $(1.49 \pm 0.10) \times 10^{14}$ spins/mm³ and

$(2.16 \pm 0.18) \times 10^{14}$ spins/mm^3, which was 52% and 29% lower than the irradiation with 119 J/cm^2 visible-near infrared (VIS–NIR) (**Figure 6a**, $p = 1.2e{-}05$, $p = 0.01$), respectively.

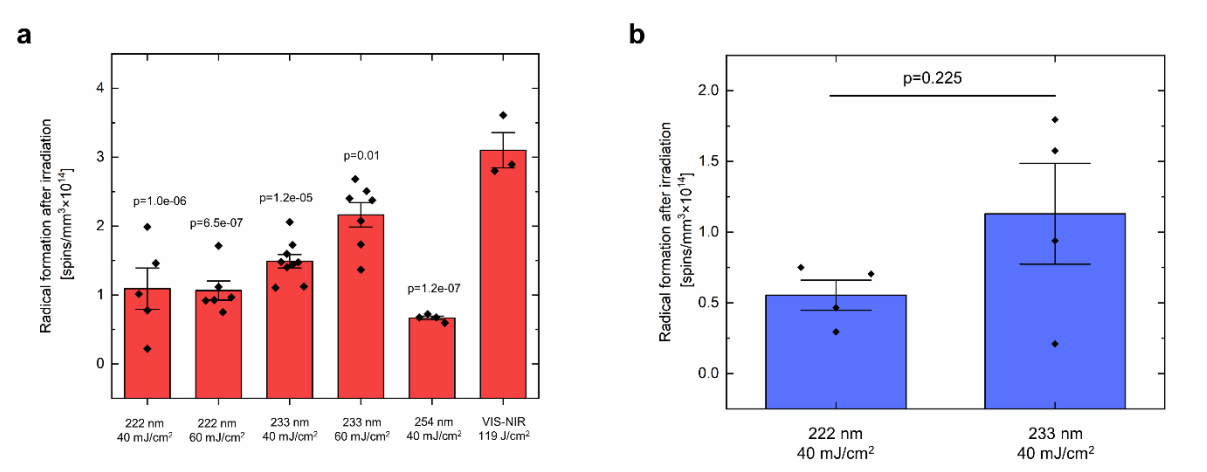

Figure 6: Radical formation of RHEs (**a**) and excised human skin (**b**) after UV irradiation. The data show the spin concentration (spins/mm^3 × 10^{14}) representative for radical formation in RHEs (**a**) and excised human skin (**b**) after irradiation with different wavelengths and irradiation doses. The corresponding *p*-values were obtained by comparing the different UVC wavelengths against VIS–NIR by one-way ANOVA with Dunnett post hoc tests for RHEs (**a**). All groups showed significantly lower radical formation in comparison to VIS–NIR. In excised human skin (**b**), the radical formation after irradiation with 233 nm (40 mJ/cm^2) was twofold higher compared to irradiation with 222 nm (40 mJ/cm^2). Radical formation was compared with the Student's *t*-test for paired samples and showed no significant differences. Data were collected with $n = 3$ to $n = 9$ RHE models and $n = 4$ donors of excised human skin with 2 to 3 technical replicates, each. The data show mean ± SEM.

Radical formation on excised human skin was only investigated for 40 mJ/cm^2. The radical formation in *ex vivo* human skin is presented in **Figure 6b**. A radical formation of $(0.55 \pm 0.11) \times 10^{14}$ spins/mm^3 was observed after irradiation of excised human skin with 222 nm. Irradiation with 233 nm induced a twofold higher average spin concentration of $(1.13 \pm 0.36) \times 10^{14}$ spins/mm^3 ($p = 0.225$).

3. Discussion

3.1. Inactivation of MRSA

Conventionally, UV radiation with 254 nm wavelength is used for surface decontamination [32]. The radiation inactivates bacteria by damaging DNA, RNA and proteins resulting in, e.g. DNA breakage due to the energy received from absorption. Maximum absorption takes place at wavelengths lower than 300 nm with a second minor minimum at 230 nm. Additionally, espe-

cially *S. aureus* strains are susceptible to UV radiation because of their higher content of thymine bases, leading to CPD as well as 6-4PP damage [33]. This suggests a biocidal efficacy of 233 nm radiation against MRSA as well as MSSA.

However, all microorganisms harbour different repair mechanisms as base excision repair, UV damage endonucleases or nucleotide excision repair to treat mutations or even DNA strand breaks. One mechanism is the photo reactivation by photolyases using energy of blue light to repair damage, which primarily results from UV irradiation as CPD and 6-4PP damage [34-36]. Maclean et al. [34] stated a degree of photo reactivation of up to 0.025 for *S. aureus*. Another mechanism of *S. aureus* to repair damage resulting from UV irradiation is a special SOS-response that includes RecA and LexA, two hypothetical proteins. Cirz et al. [37] created a mutant strain lacking LexA that was more sensitive to UV treatment than the wild-type strain. But even if bacteria have various repair mechanisms, since UVC radiation is almost absent in the environment, bacteria do not have any direct protection against it. That is why no differences in efficacy between different species or strains were expected. On the other hand, MRSA have evolved different mechanisms to resist treatment with antibiotics [4]. These resistance mechanisms comprise a set of DNA repair mechanisms as well as mechanisms for detoxification of, e.g. reactive oxygen species, additionally to those evolved in MSSA. These mechanisms might increase the tolerance to UV radiation as well. Indeed, in the presented study, a lower sensitivity of the MRSA strain DSM 11822 in comparison to the MSSA strain DSM 799 and *S. epidermidis* DSM 1798 was observed for irradiation at 40 mJ/cm^2 and 60 mJ/cm^2 in artificial wound exudate. But, in sodium chloride solution, no significant differences were observed, even when irradiated with lower doses. This might be due to the nearly full inactivation of bacteria. Similar results were obtained by Kerr et al. [38], who treated MRSA and MSSA plated on blood agar plates with various high doses of UV light (254 nm) and observed no differences in reduction between the strains.

Without the addition of a soil load, e.g. albumin or inorganic compounds, the newly developed 233 nm UVC LED source was able to reduce the viable microorganisms by more than an LR of 5, thus reaching the required reduction as stated in various EN standards for disinfection and antisepsis [26, 27, 39]. The soil loads added are substances naturally occurring in saliva as mucin or proteins (albumin) or sweat (different salts) or wound exudate (proteins) to mimic realistic conditions.

However, the existence of organic and inorganic loads in the natural habitat of the microorganisms, as it exists on the skin or the mucosa, decrease the biocidal efficacy of radiation by absorption of photons. Nevertheless, the used doses in the presented study to investigate the biocidal activity of radiation at 233 nm were limited to a maximum of 80 mJ/cm^2 with regard to

skin compatibility. Indeed, decreasing biocidal effects were clearly observed for all tested wavelengths when adding a soil load. Especially mucin, a biopolymer as part of the mucus, which is present also on the surfaces of the mucosa in the human body, had protective effects. At 233 nm, the protection by albumin was comparable to that of mucin. In contrast, inorganic salts as found in human sweat certainly had a protective effect, but this effect was overcome by doses of > 40 mJ/cm^2. Interesting, that the reduction factors at 233 nm when using mucin or proteins are not increasing with increasing doses. A reason might be the strong absorbance of proteins and mucin at the given wavelengths resulting in a protection of the bacteria below. At 254 nm, reduction factors when using mucin are slightly increasing with increasing doses, possibly resulting from the higher penetration depth of the radiation. However, the differences are small.

Interestingly, the addition of soil loads led to a reduction of viable microorganisms with nearly equal LR, independent of the applied dose. Similar effects were observed for radiation with 222 nm. A reason might be the reduced penetration depth of radiation with lower wavelength. Soil loads might act as a shield, protecting the bacteria. This corresponds to the protection effect of living cells of the skin. The slightly higher LR of 233 nm compared to 222 nm supports this assumption. In the **Supplementary Information, Figure S1**, the absorption spectra of selected soil loads are shown. Sweat, which almost does not reduce the LR for 233 nm, provides very low absorption at this wavelength but the absorption is increased at 222 nm and thus, decreases the LR here. Mucin also shows an absorption at all wavelengths but it is less pronounced at 254 nm, which could explain the reduced LR at 254 nm but the increase with dose.

As stated in various EN standards, an LR ≥ 5 is necessary for disinfection/antisepsis [26, 27, 39]. However, even lower biocidal effects with an LR between 1 and 3, which means a reduction of 90.0–99.9% of viable microorganisms, are able to reduce the risk of infection.

Similar to absorption processes by proteins added as soil load, also extracellular substances, produced by biofilm-forming bacteria as well as clusters of microorganisms, can absorb the radiation leading to reduced biocidal effects [40]. Next to liquid layers as saliva or sweat, in clinical practice also biofilms with a certain thickness may occur. Even if these biofilms will be removed before treatment by rinsing with, e.g. sodium chloride solution, the bacterial load will be high resulting in multi-layered bacterial burden that possibly shields bacteria in the lower layers. To consider these factors, the bacterial load in the laboratory experiments was high (10^7 cfu/ml) and further soil loads as mucin and salts were added. However, to what extent the treatment of biofilms, e.g. as found in wounds, with radiation of 233 nm is efficient for antisepsis has to be clarified in further studies.

Another point is the higher bactericidal effect when the irradiance of the 254 nm lamp was raised. Higher irradiances at 233 nm might also lead to higher reduction of viable microorganisms in solutions containing organic or inorganic soil loads. For better understanding of the relationship between dose, irradiance and bacterial eradication, and also to determine the optimal treatment procedure for antimicrobial efficacy, further investigations are necessary.

3.2. Risk assessment

3.2.1. Cell viability

Due to the strong variability, it is generally accepted that only a decrease of cell viability < 80% is considered meaningful [41, 42]. In our experiments, this threshold was not reached. Thus, in the investigated time frame the viability was not significantly reduced, indicating that the cell viability was not affected directly by irradiation. It cannot be excluded that cell viability would decrease at later time points. During irradiation, the RHEs were kept in PBS instead of medium as UV interacts with the medium, entailing death of keratinocytes due to the formation of ROS via riboflavin photosensitization [43].

3.2.2. DNA damage

The applied doses of far-UVC irradiation (222 and 233 nm) provoke only a small fraction of the CPD damage generated by 10% MED of UVB radiation. This dose is at a level likely unavoidable in daily life.

Although there is no threshold of UV exposure, under which it is considered to be harmless [44, 45], it must be argued that a low amount of UV exposure is necessary for vitamin D generation [46]. The pre-vitamin D concentration reaches a maximum at a dose far below 1 MED. The low amount of DNA damaged by far-UVC irradiation is located directly below the SC. No damage is found in the vicinity of the basal cells, which are most vulnerable, whereas the applied doses of UVB and 254 nm irradiation induce DNA damage throughout the entire epidermis and reach the fibroblasts in the dermis. The results indicate that 233 nm penetrate deeper than 222 nm, which is comparable for RHEs and excised human skin. Thus, the DNA damage at the required dose to reduce the pathogens (40–60 mJ/cm^2) by an LR of 5 using high energy UVC can be neglected.

Compared to irradiation with 233 nm at 80 mJ/cm^2, the CPD formation was only 2.5-fold higher after irradiation with 254 nm (40 mJ/cm^2), while 0.1 MED of UVB induced a fivefold higher damage. It has to be mentioned that the irradiation with 254 nm had to be repeated in the framework of the experiments. Since the RHEs used for 254 nm showed a higher SC thickness

(28.1 ± 0.8 µm) compared to the samples used for 222 nm, 233 nm and UVB, the observed DNA damage after irradiation with 254 nm might be underestimated.

3.2.3. Repair mechanisms

The DNA damage induced by UV exposure is not persistent and can quickly be reversed by the enzymatic repair system [47] or apoptosis [48].

Experiments with increased regeneration times were performed on RHEs. As for the previous experiments, half of the RHEs were fixated directly after irradiation, the other half were set in medium and incubated for further 24 h at 37 °C, 5% CO_2. Here, a complete repair of DNA damage was observed within 24 h after high energy UVC irradiation at 233 nm. Previous studies using 222 nm suggested a repair mechanism for CPD damage after 7 days [9]. While the molecular dynamics for CPD and 6-4PP damage have been described to occur as fast as in the femtosecond range [49], the repair mechanisms in irradiated skin became effective within days. Using broad band UV irradiation (43% UVA, 54% UVB and 3% UVC), a significant reduction of CPD damage was observed 3 days after irradiation in human skin *in vivo*, which further reduced to zero after 10 days [45]. In another study, most initial CPD damage was repaired within 48 h after UV irradiation (95% UVA, 5% UVB) with 80% MED [44]. In another study using hairless mice (Hos:HR-1) and 222 nm irradiation, the CPD damage was gradually reduced from 37 to 13% within 24 h [50].

Apoptosis was not observed 24 h after RHE irradiation at the selected doses. Nevertheless, we cannot exclude the formation of other photoproducts which are described for example for hydrolysed keratin in the UVB spectral range [51], or other degradation processes such as epidermal CXCL5 mRNA and protein expression [52, 53]. Up regulation of epidermal CXCL5 was independent of keratinocyte differentiation and keratinocyte-keratinocyte interactions in epidermal layers.

Upon multiple irradiations, our results suggest that the process of DNA damage formation restarts after every irradiation, if the RHEs can fully recover. The (18.5 ± 3.9)% CPD and (1.1 ± 1.0)% 6-4PP damage for RHEs fixated 24 h after single irradiation (80 mJ/cm^2 at 233 nm) vanished after irradiating four times every 24 h with identical fixation. Therefore, it can be concluded that the repair mechanism becomes more effective after the first 24 h. Otherwise, no decrease in DNA damage would be expected. In other studies, the occurrence of sunburn and desquamation was observed in dorsal skin of mice irradiated at 254 nm, but not at 222 nm after 4 days [50]. We did not observe this effect in RHEs. Neither was an increase of the epidermal thickness observed. CPDs are considered to be primarily related to the formation of skin tumours due to the quicker repair of 6-4PPs [54, 55]. In this study, we only observed 6-

4PP damage > 20% if the CPD damage was > 90%. This can be explained by a relatively higher formation of CPD damage, but also a quicker repair is possible, which occurs already in the timeframe between irradiation and fixation (≈ 3 min).

3.2.4. Excised human skin

Our experiments using excised human skin followed the same trend, but resulted in considerably more DNA damage and variation compared to RHE models after irradiation with 233 nm. At 40 mJ/cm^2 233 nm irradiation, excised human skin showed tenfold increased CPD damage compared to RHEs.

The larger variations for excised human skin can be explained by increased biological variability. The higher DNA damage could be related to the lower enzymatic activity of repair enzymes, such as photolyase. Human skin must be transported from the surgery to the laboratory and was stored for max. 24 h at 4 °C without culture medium supply. A comparison with a previous investigation [24] showed that the DNA damage of porcine ear skin was in between that of RHEs and excised human skin. Similar storing conditions to excised human skin were conducted in this case. The different SC thickness could also contribute to this effect. The irradiated RHEs had 30% lower SC thickness than the obtained human skin. The SC thickness determined by histological sections is influenced by the procedure of staining, but this influence should be identical for both models. As shown by the non-irradiated control, pre-existing DNA damage or effects of surgical disinfection can be ruled out.

3.2.5. Radical formation

It could be shown that radical formation was measurable but significantly lower at 233 nm irradiation than after irradiation with VIS–NIR on RHE. In human skin no significant difference between 233 nm irradiation and 222 nm irradiation could be found, which is correlated to the relatively high data spread within the 233 nm group. This might be based on the diversity in human skin type, respectively melanin and antioxidant content. To elucidate this phenomenon in more detail, further studies with higher number of samples are required.

The assessment criteria of how many and which radicals are physiological and where the detrimental turning point is, are more uncertain than for DNA damage but 20 min VIS and NIR irradiation could be considered to be safe and thus the radical formation during this exposure as well. Furthermore, we could show a higher radical formation in RHEs for 233 nm as well as for 222 nm (40 mJ/cm^2) as compared to *ex vivo* human skin (32% and 98%). These findings correspond with the statement of Albrecht et al. [30] that the radical formation in reconstructed

human skin is higher compared to *ex vivo* skin when irradiated by a simulated sun spectrum (305–2200 nm). The observed effect can be explained by a lasting metabolic rate within RHEs [30] during irradiation as the RHEs are more metabolically active than excised human skin and contain less antioxidants because no exogenous antioxidants are available. In the latter study, the radical load of reconstructed human skin was comparable to the *in vivo* situation. However, all these investigations have to be confirmed *in vivo* for UVC irradiation.

4. Conclusion

The results of our investigations pave the way for future therapies to decolonise patients with MSSA and MDR bacteria such as MRSA in various areas (nasal cavity, throat, wounds) in order to prevent infections as well as the spread of MDR in hospitals. Therefore, further *in vitro* and *in vivo* studies are planned to assess the impact of 233 nm UVC irradiation on various bacteria, biofilms, on human mucosa, skin and corneal biopsies. Furthermore, the use of 233 nm UVC in everyday clinical practice is conceivable to treat all patients after admission and thus significantly reduce the MRSA problem. It should also be examined whether other MDR besides MRSA can be effectively eradicated by this UVC radiation.

At the biocidal doses for multi-resistant pathogens at 40 to 60 mJ/cm^2 irradiation of 222 and 233 nm irradiation, achieving an LR of 5, no relevant DNA damage and radical formation occurred in the skin.

The bacterial eradication efficacy demonstrated for the recently developed 233 nm LED may also suggest its application/suitability to inactivate SARS-Cov-2 [56, 57]; like it has been already shown for 254 nm [58] and 222 nm [59].

5. Methods

5.1. Microorganisms, media, and bacterial multiplication

As test organisms, the Gram-positive bacteria *S. aureus* DSM 799 (ATCC 6538) and DSM 11822 as well as *S. epidermidis* DSM 1798 were used. *S. aureus* DSM 11822 is a MRSA strain, whereas DSM 799 is a MSSA strain.

Cryopreserved bacteria were inoculated onto Columbia blood agar plates and incubated for 24 h at 37 °C as a first subculture. After verifying the purity of the strains by examination of visible criteria as colour and colony shape, these subcultures were used as starting cultures for the following experiments. One colony was picked, plated on fresh TSA agar plates (Carl

Roth, Karlsruhe, Germany), and incubated again at 37 °C for 24 h. The bacteria were harvested by rinsing the plate with 2 ml sodium chloride solution (0.9%) and the suspension was centrifuged three times at 10,000× *g* for 1 min and once at 7,150× *g*. The supernatant was discarded each time and the pellet resuspended in fresh sodium chloride solution. Afterwards, the pellet was resuspended in the relevant solutions used for further experiments. To ensure appropriate number of colony forming units (cfu) of 1–3 × 10^8/ml, the optical density at 620 nm (OD_{620}) was adjusted to 0.10–0.14 for *S. aureus* strains, to 0.30–0.35 for *S. epidermidis* and to 0.12–0.15 for *P. aeruginosa*. The bacterial suspensions were used within 2 h after adjusting the initial suspension to the appropriate density.

5.2. Soil loads

In addition to bacteria suspensions in sodium chloride solution, different soil loads in sodium chloride solution were used. For protein load 0.03% albumin solution was used (Carl Roth, Karlsruhe, Germany) as minor load given by EN 14561 and EN 13727. For soil load of mucosa 0.5% mucin was used (Carl Roth, Karlsruhe, Germany). Artificial sweat pH 8.4 was composed of 0.5% NaCl solution with 0.05% l-histidine (Merck KGaA, Darmstadt, Germany), 0.5% Na_2HPO_4 (Carl Roth, Karlsruhe, Germany) [60, 61]. Artificial wound fluid was composed of Eagle's minimal essential medium with Earle's salts with 2 mM l-glutamine (both PAN-Biotech GmbH, Aidenbach, Germany) and 10% fetal bovine serum (gibco Life Technologies, Carlsbad, CA, USA) [62, 63]. Experiments for comparison of LRs by using different irradiances (254 nm) were carried out in cell culture medium (DMEM/F12, PAN Biotech GmbH, Aidenach, Germany) with addition of 10% fetal bovine serum (gibco Life Technologies, Carlsbad, CA, USA) and 2 mM l-glutamine.

5.3. Drying on germ carrier and recovery rate

The initial suspensions with 1–3 × 10^8 cfu/ml were further diluted from 1 × 10^7 cfu/ml up to 10 cfu/ml. To confirm the correct number of cfu/ml, 100 µl of the suspensions likely containing 10^3–10 cfu/ml were plated in duplicate on TSA plates; the colonies were counted after incubation at 37 °C for 24 h and the amount of cfu/ml at the starting solution was calculated. For further experiments, 100 µl of the suspensions containing likely 10^7 cfu/ml were pipetted on the germ carrier (stainless steel, 20 mm diameter, polished to grade 2), spread with an inoculating loop, and dried for 30 min in a laminar flow cabinet inspired by EN 14561:2006 and ASTM E2197-11.

To ensure a number of minimum 1×10^5 cfu/test specimen after drying, the recovery rate in sodium chloride solution after 30 min of drying was determined for 0.03% albumin sodium chloride solution. Specimens with dried bacterial suspension were placed in a 6-well-plate containing 3 ml of tryptone sodium chloride solution and Ø = (2.9–3.5 ± 0.3) mm glass beads per well. The specimens were incubated while shaking for 2 min (400 rpm) on an orbital shaker to detach the bacteria, and the resulting suspensions were diluted and plated on TSA plates in duplicate followed by incubation for 24 h at 37 °C to determine the number of viable bacteria. Simultaneously, 100 µl of the initial solution (1×10^7 cfu/ml) were diluted in the same way and plated on agar plates without spreading on germ carriers before.

5.4. UV irradiation

Irradiation of bacteria as well as excised human skin and RHEs was conducted with different UVC irradiation modules. UVC radiation of the wavelengths 254 nm (0.29 mW/cm^2 for bacteria and 0.54 mW/cm^2 for excised human skin and RHEs, LPL-R-01, Hg gas discharge lamp, sglux GmbH, Berlin, Germany, as positive control), 233 nm (0.041 mW/cm^2, UVC LED irradiation source with a short pass optical filter suppressing wavelengths > 240 nm, Ferdinand-Braun-Institut, Berlin, Germany) [24] and 222 nm (3.34 mW/cm^2, ExciJet222 30–130 Kit (111073) Kr-Cl Excimer lamp with a short pass filter suppressing wavelengths > 230 nm, USHIO Deutschland GmbH, Steinhöring, Germany) were examined for their eradicating effect on different pathogens, and their effect on skin (cell viability, DNA damage, radical formation). Doses of 20, 40, 60 and 80 mJ/cm^2 were investigated. The UVC LED irradiation system is comprised of an array of 120 LEDs with a narrow band emission peaking at a wavelength of 233 nm and a full-width at half maximum (FWHM) of 12 nm [25]. In order to remove unwanted emission at wavelengths > 240 nm, a short pass filter was added consisting of HfO_2 and SiO_2 quarter wavelength stacks that form a distributed Bragg reflector (DBR) with a photonic stopband between 240 and 300 nm. The spectrally pure 233 nm LED irradiation system delivered a uniform optical power density of 0.041 mW/cm^2 over a target area of 70 mm × 70 mm at a distance of 25 mm from the system.

For detecting the microbicidal efficacy, all experiments were conducted with MRSA DSM 11822. Comparability of the effects with irradiation at 233 nm was investigated using MRSA DSM 11822, MSSA DSM 799 and *S. epidermidis* DSM 1798. Additionally, for the 254 nm UVC irradiation module, the efficacy of different doses by varying irradiance (0.45 mW/cm^2, 0.9 mW/cm^2) was proofed.

To assess skin DNA damage, a UVB lamp, containing also a small UVA fraction (280–400 nm, 0.041 mW/cm^2; TH-1E; Cosmedico Medizintechnik, Stuttgart, Germany) was applied to induce

1/10 MED. For assessment of the radical formation, irradiation was additionally performed using a solar simulator (Low Cost Solar Simulator LS0104, with Lamp Type Xenon short arc 150W, LOT-Quantum Design GmbH, Darmstadt, Germany) with an optical fibre (liquid-filled, transmission: VIS/NIR (420–2000 nm) and a long pass filter (cut-on wavelength of 400 nm, 400FH90-50S, LOT-Quantum Design GmbH) as well as AMO Filter LSZ185 (air mass 0, outer space) to simulate solar irradiation within the VIS–NIR range on earth.
Irradiance of radiation and doses for 254 nm, 233 nm and 222 nm, were measured with the UV radiometer SXL55 with a SiC UVC sensor (sglux GmbH, Berlin, Germany), and an ILT 1400 Radiometer Photometer (International Light Technologies, Peabody, MA, USA) for UVA (SEL033) and UVB (SEL240) lamps. The irradiation dose for VIS–NIR was measured with an 843-R optical power meter and a 919-003-10 detector (Newport Spectra-Physics GmbH, Darmstadt, Germany).

5.5. Irradiation of microorganisms on germ carriers/antibacterial efficacy of irradiation

After spreading and drying of the bacterial suspension on the germ carrier, the microorganisms were irradiated with varying doses of 222 nm, 233 nm and 254 nm (positive control) wavelength. Towards exposure, the specimens were treated as described above. A specimen without irradiation was used as negative control.
The bactericidal LR for each irradiation dose is given in $\log_{10}$ levels and was calculated according to Eq. (1), where n_c is the number of cfu on control specimen without irradiation and n_p is the number of cfu on irradiated test specimen.

$$LR = log_{10}\,(n_c) - log_{10}(n_p) \quad (1)$$

5.6. Skin models

OS-Rep-1 RHEs (Henkel AG & Co. KGaA, Düsseldorf, Germany) were used to study cell viability, radical formation and DNA damage immediately, 24 h after irradiation, and after multiple irradiation. Excised human female stomach and breast skin (Fitzpatrick skin types II–III) without any skin diseases originating from plastic surgeries were used for the determination of immediate DNA damage and radical formation. All experimental protocols were approved by the Ethics Committee of the Charité-Universitätsmedizin Berlin (EA1/324/19). Informed written consent was obtained from the seven participants and all procedures complied with the Declaration of Helsinki.

The removed skin reached the laboratory on the day of surgery and had been disinfected with a solution of 2-propanol 70% before starting surgery. In the laboratory it was cleaned with PBS, excess fatty tissue was removed. Then, the skin was stored at 4 °C on moistened paper until use. All investigations were done within 24 h of receipt.
The RHE models were cultivated in six well plates at 37 °C, 5% CO_2 and 100% humidity in OS Rep-Air–liquid interface medium (OS-Rep-ALI, CM-125, Henkel AG & Co. KGaA, Düsseldorf, Germany). The medium was changed every 2 days. Due to photosensitivity of the medium, the RHEs were placed into PBS during irradiation.

5.7. Cell viability

The influence of UV irradiation on the skin cell metabolism was controlled by an MTT [3-(4,5-dimethylthiazol-2-yl)-2,5-diphenyltetrazolium bromide] assay [28, 29]. Therefore, Ø = 4 mm punch biopsies of excised human skin or RHE were investigated directly after irradiation as previously described [64].

5.8. Analysis of DNA damage

To assess the effect of UV irradiation on skin cells, 6-4PP and CPD were examined immunohistochemically on 1–2 µm paraffin sections as previously described [24]. The sections were incubated with either anti-6-4PP (clone 64M-2, Cosmo Bio) or anti-CPD (clone TDM-2, Cosmo Bio). Alkaline Phosphatase/RED, Rabbit/Mouse (Agilent Technologies) was employed for the detection of 6-4PP$^+$ and CPD$^+$. Nuclei staining was performed with hematoxylin (Merck Millipore) and slides were coverslipped with Kaiser's glycerol gelatine (Merck Millipore). Analysis of apoptosis in irradiated cells was performed by cleaved caspase-3 staining (clone 5A1E, Cell Signaling Technologies) on selected sections [31]. Negative controls were performed by omitting the primary antibody. An AxioImager Z1 microscope (Carl Zeiss MicroImaging, Inc.) was used for histologic documentation in a blinded manner.

5.9. Quantitative radical measurements

Quantitative analysis of free radicals induced by UVC irradiation in excised human skin was performed and epidermal skin equivalents were measured by electron paramagnetic resonance (EPR) spectroscopy, using the spin marker PCA (3-(carboxy)-2,2,5,5-tetramethylpyrrolidin-1-oxyl) (Sigma Aldrich, Steinheim, Germany).

Excised human skin was horizontally dermatomed (Aesculap® Acculan 3Ti, Aesculap, Tuttlingen, Germany) to a thickness of 300 µm, the RHE were around 100 µm thick and were not processed further.
Ø = 3 mm skin punch biopsies were incubated from both sides with 21.6 µl of the spin marker PCA [1.5 mM] by using Ø = 6 mm filters (SmartPractice Europe GmbH, Greven, Germany) for 10 min at 37 °C. The EPR measurements were performed on an X-band EPR spectrometer (Bruker Elexsys E500, BioSpin GmbH, Karlsruhe, Germany) at room temperature. A TMHS resonator (E2044500TMHS, Bruker BioSpin GmbH, Karlsruhe, Germany) was used with the following parameter settings: frequency = 9.5 GHz, central magnetic field = 350.5 mT, magnetic field sweep width = 40 mT, modulation frequency = 100 kHz, modulation amplitude = 0.5 mT, attenuation = 22 dB, sweep time = 45 s.

5.10. Statistical Analysis

All antibacterial efficacy tests were conducted at least in triplicate on distinct samples. DNA damage and cell viability measurements were performed on $n \geq 3$ distinct samples. Radical formation experiments were conducted with $n = 3$ to $n = 9$ RHE models and $n = 4$ human skin donors with 2 to 3 technical replicates each. Either a Kruskal–Wallis test or a one-way analysis of variance (ANOVA) was conducted to compare antibacterial efficacy. Mean value comparisons were performed with the Kruskal–Wallis test for DNA damage data. Bonferroni correction was applied to account for multiple testing in all cases. An ANOVA with Dunnett post hoc tests was conducted for mean value comparison of radical formation and cell viability in RHEs. Mean value comparison of radical formation in excised human skin was performed by using the Student's *t*-test for paired samples. The statistical analysis was executed using IBM SPSS® Statistics 27 (IBM, Armonk, NY, USA) affording a significance level of $\alpha = 0.05$. Display of data was performed in OriginPro 2020 (Origin, OriginLab Corporation, Northampton, MA, USA). All data are expressed as mean ± standard error (SEM).

References

[1] D. Sadigursky, H.S. Pires, S.A.C. Rios, F.L.B. Rodrigues Filho, G.C. Queiroz, M.L. Azi, Prophylaxis with nasal decolonization in patients submitted to total knee and hip arthroplasty: systematic review and meta-analysis, Rev Bras Ortop 52(6) (2017) 631-637.

[2] E.C. Rodriguez-Merchan, Screening and decolonization of MRSA among joint arthroplasty patients: efficacy, cost-effectiveness and durability, J Acute Dis 3(3) (2014) 218-220.

[3] S.E. Kline, J.D. Neaton, R. Lynfield, P. Ferrieri, S. Kulasingam, K. Dittes, A. Glennen, S. Jawahir, A. Kaizer, J. Menk, J.R. Johnson, Randomized controlled trial of a self-administered five-day antiseptic bundle versus usual disinfectant soap showers for preoperative eradication of Staphylococcus aureus colonization, Infect Control Hosp Epidemiol 39(9) (2018) 1049-1057.

[4] J.E. Vasquez, E.S. Walker, B.W. Franzus, B.K. Overbay, D.R. Reagan, F.A. Sarubbi, The epidemiology of mupirocin resistance among methicillin-resistant Staphylococcus aureus at a Veterans' Affairs hospital, Infect Control Hosp Epidemiol 21(7) (2000) 459-464.

[5] S. Harbarth, N. Liassine, S. Dharan, P. Herrault, R. Auckenthaler, D. Pittet, Risk factors for persistent carriage of methicillin-resistant Staphylococcus aureus, Clin Infect Dis 31(6) (2000) 1380-1385.

[6] B. Jahn, T.M. Wassenaar, A. Stroh, Integrated MRSA-Management (IMM) with prolonged decolonization treatment after hospital discharge is effective: a single centre, non-randomised open-label trial, Antimicrob Resist Infect Control 5 (2016) 25.

[7] G. Kampf, Acquired resistance to chlorhexidine - is it time to establish an 'antiseptic stewardship' initiative?, J Hosp Infect 94(3) (2016) 213-227.

[8] Y. Maeda, C.E. Goldsmith, W.A. Coulter, B.C. Millar, J.S. Dooley, C.J. Lowery, A. Loughrey, P.J. Rooney, D.A. McDowell, M. Matsuda, J.E. Moore, UVc-irradiation sublethal stress does not alter antibiotic susceptibility of staphylococci (MRSA, MSSA, and coagulase-negative staphylococci) to β-lactam, macrolide, and fluoroquinolone antibiotic agents, J Cosmet Sci 63(2) (2012) 133-137.

[9] B. Ponnaiya, M. Buonanno, D. Welch, I. Shuryak, G. Randers-Pehrson, D.J. Brenner, Far-UVC light prevents MRSA infection of superficial wounds in vivo, PLoS One 13(2) (2018) e0192053.

[10] K. Narita, K. Asano, K. Naito, H. Ohashi, M. Sasaki, Y. Morimoto, T. Igarashi, A. Nakane, Ultraviolet C light with wavelength of 222 nm inactivates a wide spectrum of microbial pathogens, J Hosp Infect 105(3) (2020) 459-467.

[11] J. D'Orazio, S. Jarrett, A. Amaro-Ortiz, T. Scott, UV radiation and the skin, Int J Mol Sci 14(6) (2013) 12222-12248.

[12] G.P. Pfeifer, A. Besaratinia, UV wavelength-dependent DNA damage and human non-melanoma and melanoma skin cancer, Photochem Photobiol Sci 11(1) (2012) 90-97.

[13] S. Saadati, Study of Ultraviolet C Light Penetration and Damage in Skin. Medical Physicist Programme, Sahlgrenska Academy Department of Radiation Physics, University of Gothenburg, 2017.

[14] J.E. Roberts, Ultraviolet Radiation as a Risk Factor for Cataract and Macular Degeneration, Eye Contact Lens 37(4) (2011) 246-249.

[15] S. Sharma, C. Lang, J. Khadka, M.C. Inacio, Association of Age-Related Cataract With Skin Cancer in an Australian Population, Invest Ophthalmol Vis Sci 61(5) (2020) 48.

[16] K. Narita, K. Asano, Y. Morimoto, T. Igarashi, M.R. Hamblin, T. Dai, A. Nakane, Disinfection and healing effects of 222-nm UVC light on methicillin-resistant Staphylococcus aureus infection in mouse wounds, J Photochem Photobiol B 178 (2018) 10-18.

[17] M. Buonanno, B. Ponnaiya, D. Welch, M. Stanislauskas, G. Randers-Pehrson, L. Smilenov, F.D. Lowy, D.M. Owens, D.J. Brenner, Germicidal Efficacy and Mammalian Skin Safety of 222-nm UV Light, Radiat Res 187(4) (2017) 483-491.

[18] S.B. Lohan, D. Ivanov, N. Schüler, B. Berger, L. Zastrow, J. Lademann, M.C. Meinke, Switching from healthy to unhealthy oxidative stress – does the radical type can be used as an indicator?, Free Radic Biol Med 162 (2021) 401-411.

[19] J. Campisi, Aging and cancer: the double-edged sword of replicative senescence, J Am Geriatr Soc 45(4) (1997) 482-488.

[20] J. Campisi, Cancer, aging and cellular senescence, In vivo (Athens, Greece) 14(1) (2000) 183-188.

[21] C. Nishigori, Y. Hattori, S. Toyokuni, Role of reactive oxygen species in skin carcinogenesis, Antioxid Redox Signal 6(3) (2004) 561-570.

[22] S. Pillai, C. Oresajo, J. Hayward, Ultraviolet radiation and skin aging: roles of reactive oxygen species, inflammation and protease activation, and strategies for prevention of inflammation-induced matrix degradation - a review, Int J Cosmet Sci 27(1) (2005) 17-34.

[23] S. Dunaway, R. Odin, L. Zhou, L. Ji, Y. Zhang, A.L. Kadekaro, Natural Antioxidants: Multiple Mechanisms to Protect Skin From Solar Radiation, Front Pharmacol 9 (2018) 392.

[24] J. Glaab, N. Lobo-Ploch, H.K. Cho, T. Filler, H. Gundlach, M. Guttmann, S. Hagedorn, S.B. Lohan, F. Mehnke, J. Schleusener, C. Sicher, L. Sulmoni, T. Wernicke, L. Wittenbecher, U. Woggon, P. Zwicker, A. Kramer, M.C. Meinke, M. Kneissl, M. Weyers, U. Winterwerber, S. Einfeldt, Skin tolerant inactivation of multiresistant pathogens using far-UVC LEDs, Sci Rep 11(1) (2021) 14647.

[25] N. Lobo-Ploch, F. Mehnke, L. Sulmoni, H.K. Cho, M. Guttmann, J. Glaab, K. Hilbrich, T. Wernicke, S. Einfeldt, M. Kneissl, Milliwatt power 233 nm AlGaN-based deep UV-LEDs on sapphire substrates, Appl Phys Lett 117(11) (2020) 111102.

[26] DIN EN 14561:2006-08, Chemical disinfectants and antiseptics - Quantitative carrier test for the evaluation of bactericidal activity for instruments used in the medical area - Test method and requirements (phase 2, step 2), 2006.

[27] ASTM E2111-12, Standard Quantitative Carrier Test Method to Evaluate the Bactericidal, Fungicidal, Mycobactericidal, and Sporicidal Potencies of Liquid Chemicals, 2018.

[28] T. Mosmann, Rapid colorimetric assay for cellular growth and survival: application to proliferation and cytotoxicity assays, J Immunol Methods 65(1-2) (1983) 55-63.

[29] J.C. Stockert, A. Blázquez-Castro, M. Cañete, R.W. Horobin, A. Villanueva, MTT assay for cell viability: Intracellular localization of the formazan product is in lipid droplets, Acta Histochem 114(8) (2012) 785-796.

[30] S. Albrecht, A. Elpelt, C. Kasim, C. Reble, L. Mundhenk, H. Pischon, S. Hedtrich, C. Witzel, J. Lademann, L. Zastrow, I. Beckers, M.C. Meinke, Quantification and characterization of radical production in human, animal and 3D skin models during sun irradiation measured by EPR spectroscopy, Free Radic Biol Med 131 (2019) 299-308.

[31] A.W. Abu-Qare, M.B. Abou-Donia, Biomarkers of apoptosis: release of cytochrome c, activation of caspase-3, induction of 8-hydroxy-2'-deoxyguanosine, increased 3-nitrotyrosine, and alteration of p53 gene, J Toxicol Environ Health B Crit Rev 4(3) (2001) 313-332.

[32] T.P. Coohill, J.L. Sagripanti, Overview of the inactivation by 254 nm ultraviolet radiation of bacteria with particular relevance to biodefense, Photochem Photobiol 84(5) (2008) 1084-1090.

[33] B.J. Adkins, W.E. Allen, Photoreactivation of Ultraviolet-Irradiation Damage in Staphylococcus Aureus, J Gen Appl Microbiol 28(2) (1982) 101-110.

[34] M. Maclean, L.E. Murdoch, M.N. Lani, S.J. MacGregor, J.G. Anderson, G.A. Woolsey, Photoinactivation and Photoreactivation Responses by Bacterial Pathogens after Exposure to Pulsed UV-Light, 2008 IEEE International Power Modulators and High-Voltage Conference, 2008, pp. 326-329.

[35] N. Goosen, G.F. Moolenaar, Repair of UV damage in bacteria, DNA Repair (Amst) 7(3) (2008) 353-379.

[36] R.P. Rastogi, Richa, A. Kumar, M.B. Tyagi, R.P. Sinha, Molecular mechanisms of ultraviolet radiation-induced DNA damage and repair, J Nucleic Acids 2010 (2010) 592980.

[37] R.T. Cirz, M.B. Jones, N.A. Gingles, T.D. Minogue, B. Jarrahi, S.N. Peterson, F.E. Romesberg, Complete and SOS-mediated response of Staphylococcus aureus to the antibiotic ciprofloxacin, J Bacteriol 189(2) (2007) 531-539.

[38] T.A. Conner-Kerr, P.K. Sullivan, J. Gaillard, M.E. Franklin, R.M. Jones, The effects of ultraviolet radiation on antibiotic-resistant bacteria in vitro, Ostomy Wound Manage 44(10) (1998) 50-56.

[39] DIN EN 13697:2019-10, Chemical disinfectants and antiseptics - Quantitative non-porous surface test for the evaluation of bactericidal and/or fungicidal activity of chemical disinfectants used in food, industrial, domestic and institutional areas - Test method and requirements without mechanical action (phase 2, step 2), 2015.

[40] R.M. Chapple, B. Inglis, P.R. Stewart, Lethal and mutational effects of solar and UV radiation on Staphylococcus aureus, Arch Microbiol 157(3) (1992) 242-248.

[41] J. López-García, M. Lehocký, P. Humpolíček, P. Sáha, HaCaT Keratinocytes Response on Antimicrobial Atelocollagen Substrates: Extent of Cytotoxicity, Cell Viability and Proliferation, J Funct Biomater 5(2) (2014) 43-57.

[42] DIN EN ISO 10993-5:2009-10, Biological evaluation of medical devices - Part 5: Tests for in vitro cytotoxicity, 2009.

[43] A. Maguire, B. Morrissey, J.E. Walsh, F.M. Lyng, Medium-mediated effects increase cell killing in a human keratinocyte cell line exposed to solar-simulated radiation, Int J Radiat Biol 87(1) (2011) 98-111.

[44] B.B. Shih, M.D. Farrar, M.S. Cooke, J. Osman, A.K. Langton, R. Kift, A.R. Webb, J.L. Berry, R.E.B. Watson, A. Vail, F.R. de Gruijl, L.E. Rhodes, Fractional Sunburn Threshold UVR Doses Generate Equivalent Vitamin D and DNA Damage in Skin Types I–VI but with Epidermal DNA Damage Gradient Correlated to Skin Darkness, J Invest Dermatol 138(10) (2018) 2244-2252.

[45] S.K. Katiyar, M.S. Matsui, H. Mukhtar, Kinetics of UV light-induced cyclobutane pyrimidine dimers in human skin in vivo: an immunohistochemical analysis of both epidermis and dermis, Photochem Photobiol 72(6) (2000) 788-793.

[46] B.A. Gilchrest, Sun exposure and vitamin D sufficiency, Am J Clin Nutr 88(2) (2008) 570s-577s.

[47] J.D. Mallet, M.M. Dorr, M.C. Drigeard Desgarnier, N. Bastien, S.P. Gendron, P.J. Rochette, Faster DNA Repair of Ultraviolet-Induced Cyclobutane Pyrimidine Dimers and Lower Sensitivity to Apoptosis in Human Corneal Epithelial Cells than in Epidermal Keratinocytes, PLoS One 11(9) (2016) e0162212.

[48] C.H. Lee, S.B. Wu, C.H. Hong, H.S. Yu, Y.H. Wei, Molecular Mechanisms of UV-Induced Apoptosis and Its Effects on Skin Residential Cells: The Implication in UV-Based Phototherapy, Int J Mol Sci 14(3) (2013) 6414-6435.

[49] Z. Liu, L. Wang, D. Zhong, Dynamics and mechanisms of DNA repair by photolyase, Phys Chem Chem Phys 17(18) (2015) 11933-11949.

[50] K. Narita, K. Asano, Y. Morimoto, T. Igarashi, A. Nakane, Chronic irradiation with 222-nm UVC light induces neither DNA damage nor epidermal lesions in mouse skin, even at high doses, PLoS One 13(7) (2018) e0201259.

[51] A. Sionkowska, J. Skopinska-Wiśniewska, J. Kozłowska, A. Płanecka, M. Kurzawa, Photochemical behaviour of hydrolysed keratin, Int J Cosmet Sci 33(6) (2011) 503-508.

[52] O. Reichert, L. Kolbe, L. Terstegen, F. Staeb, H. Wenck, M. Schmelz, H. Genth, V. Kaever, D. Roggenkamp, G. Neufang, UV radiation induces CXCL5 expression in human skin, Exp Dermatol 24(4) (2015) 309-312.

[53] C. López-Camarillo, E.A. Ocampo, M.L. Casamichana, C. Pérez-Plasencia, E. Alvarez-Sánchez, L.A. Marchat, Protein kinases and transcription factors activation in response to UV-radiation of skin: implications for carcinogenesis, Int J Mol Sci 13(1) (2012) 142-172.

[54] S. Tornaletti, G.P. Pfeifer, UV damage and repair mechanisms in mammalian cells, Bioessays 18(3) (1996) 221-228.

[55] J.H. Yoon, C.S. Lee, T.R. O'Connor, A. Yasui, G.P. Pfeifer, The DNA damage spectrum produced by simulated sunlight, J Mol Biol 299(3) (2000) 681-693.

[56] M.G. Strakhovskaya, G.A. Meerovich, A.N. Kuskov, S.A. Gonchukov, V.B. Loschenov, Photoinactivation of coronaviruses: going along the optical spectrum, Laser Phys Lett 17(9) (2020) 093001.

[57] M. Heßling, K. Hönes, P. Vatter, C. Lingenfelder, Ultraviolet irradiation doses for coronavirus inactivation - review and analysis of coronavirus photoinactivation studies, GMS Hyg Infect Control 15 (2020) Doc08.

[58] M.E. Darnell, K. Subbarao, S.M. Feinstone, D.R. Taylor, Inactivation of the coronavirus that induces severe acute respiratory syndrome, SARS-CoV, J Virol Methods 121(1) (2004) 85-91.

[59] M. Buonanno, D. Welch, I. Shuryak, D.J. Brenner, Far-UVC light (222 nm) efficiently and safely inactivates airborne human coronaviruses, Sci Rep 10(1) (2020) 10285.

[60] H.M. Emrich, H. Oelert, [pH value and total ammonia in human sweat], Pflugers Arch Gesamte Physiol Menschen Tiere 290(4) (1966) 311-314.

[61] C. Callewaert, B. Buysschaert, E. Vossen, V. Fievez, T. Van de Wiele, N. Boon, Artificial sweat composition to grow and sustain a mixed human axillary microbiome, J Microbiol Methods 103 (2014) 6-8.

[62] K. Campbell, D. Keast, M.G. Woodbury, P. Houghton, Wear time in two hydrocolloid dressings using a novel in-vivo model, Wounds 15 (2003) 40-48.

[63] G. Müller, A. Kramer, Biocompatibility index of antiseptic agents by parallel assessment of antimicrobial activity and cellular cytotoxicity, J Antimicrob Chemother 61(6) (2008) 1281-1287.

[64] S.B. Lohan, D. Ivanov, N. Schüler, B. Berger, L. Zastrow, J. Lademann, M.C. Meinke, Switching from healthy to unhealthy oxidative stress – does the radical type can be used as an indicator?, Free Radic Biol Med 162 (2021) 401-411.

Supplementary Information

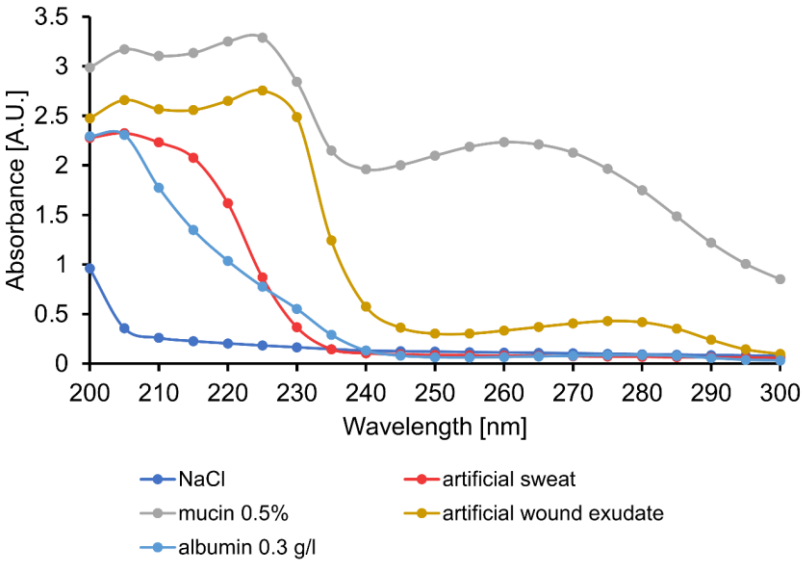

Figure S1: Absorption spectra of soil loads. At 230 nm, absorption was highest for mucin and the artificial wound exudate. For 222 nm the absorption was even higher. Sodium chloride solution has the lowest observed absorption at the relevant wavelengths.

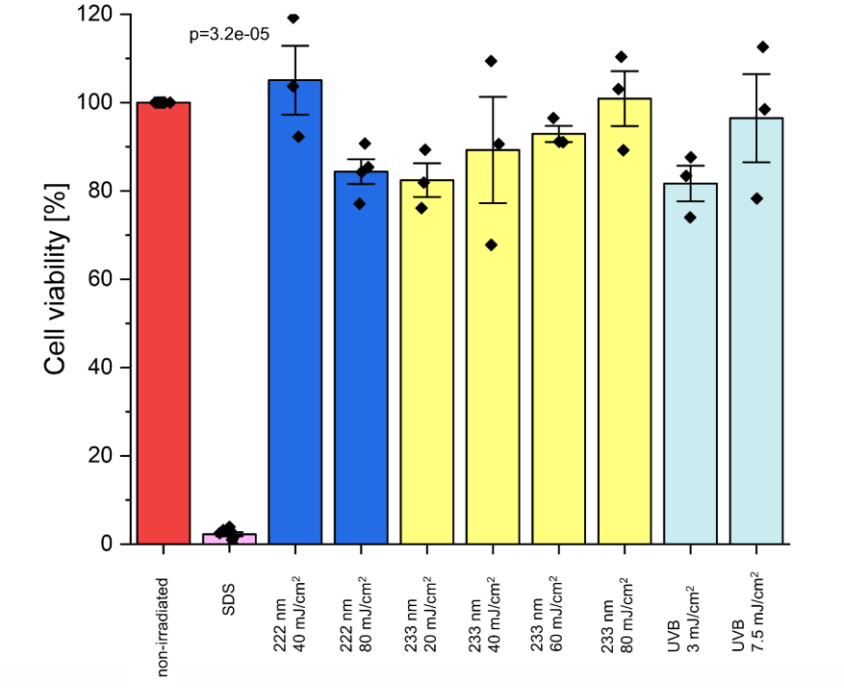

Figure S2: Cell viability of RHEs after UV irradiation. The data show the percentage of cell viability after UV irradiation of RHEs in relation to non-irradiated RHEs (negative control, 100% viability, red) determined by an MTT test. As a positive control, RHEs were incubated for 1 h in sodium dodecyl sulphate (SDS, rosé), entailing (2.1 ± 0.5)% cell viability. Reduction below 80% was not observed. The statistical significance was tested by Dunnett's post hoc tests after one-way ANOVA by testing each group against the negative control. The data show mean ± SEM. *n* = 3–9.

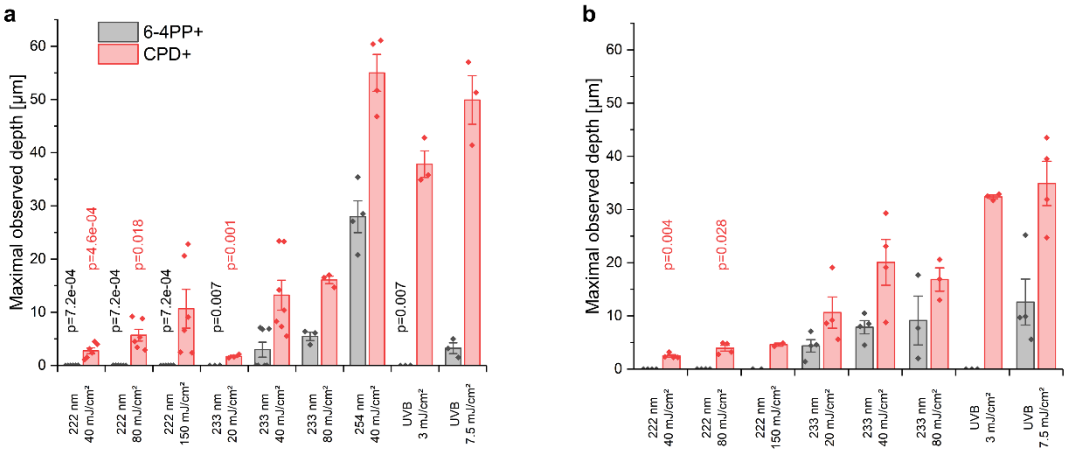

Figure S3: Depth of DNA damage in the viable epidermis for RHEs (**a**) and excised human skin (**b**). The maximal observed depth is measured from the skin surface to the deepest occurrence of 6–4PP⁺ (grey) and CPD⁺ cells (red) cells on five positions in the histology images; the SC thickness is subtracted for comparability. The *p*-values are based on Bonferroni-adjusted post hoc tests executed after Kruskal–Wallis ANOVA. For RHEs (**a**) each group was tested against 254 nm 40 mJ/cm² and for excised human skin (**b**) each group was tested against UVB 3 mJ/cm². In (**b**) the maximal observed depth of DNA damage after irradiation with 222 nm at 150 mJ/cm² is not included in the ANOVA since the sample size was only $n = 2$. The data show mean ± SEM. $n = 2–7$.

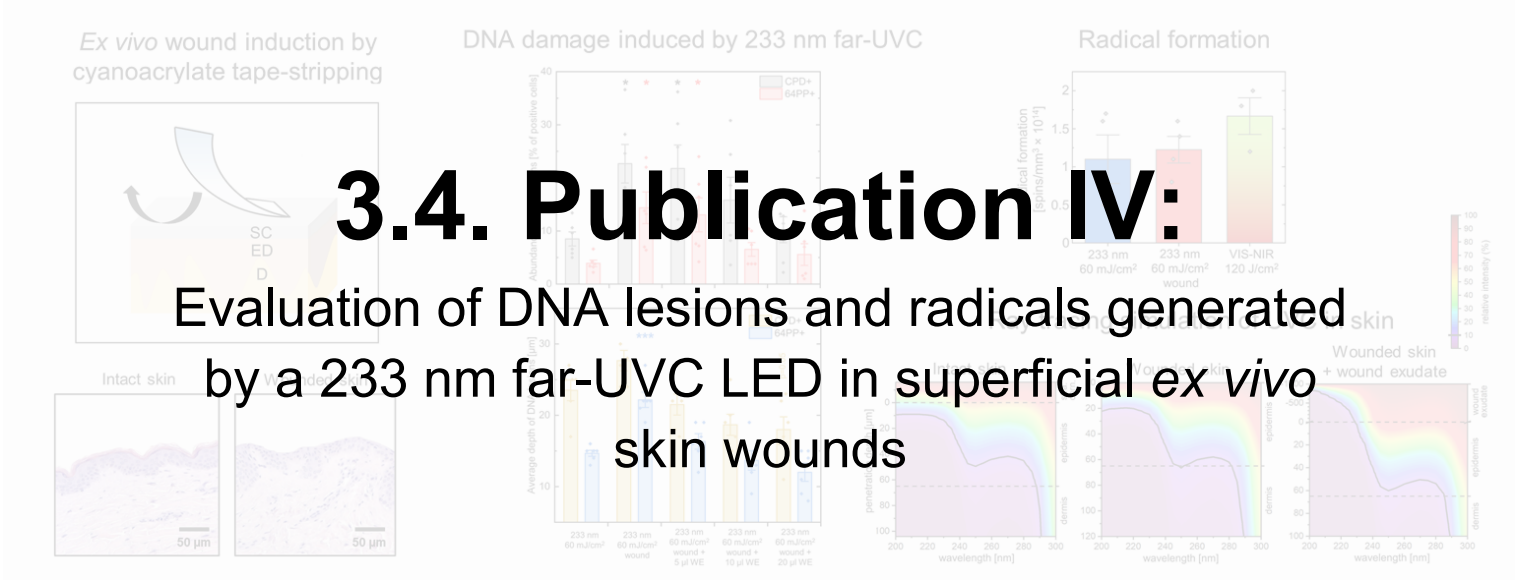

3.4. Publication IV:

Evaluation of DNA lesions and radicals generated by a 233 nm far-UVC LED in superficial *ex vivo* skin wounds

Evaluation of DNA lesions and radicals generated by a 233 nm far-UVC LED in superficial *ex vivo* skin wounds

Loris Busch [1,2], Marius Kröger [1], Johannes Schleusener [1], Anna Lena Klein [1], Silke B. Lohan [1], Martin Guttmann [3], Cornelia M. Keck [2], Martina C. Meinke [1]

[1] *Charité – Universitätsmedizin Berlin, Corporate Member of Freie Universität Berlin and Humboldt-Universität zu Berlin, Department of Dermatology, Venereology and Allergology, Center of Experimental and Applied Cutaneous Physiology, Berlin, Germany*
[2] *Department of Pharmaceutics and Biopharmaceutics, Philipps-Universität Marburg, Marburg, Germany*
[3] *Ferdinand-Braun-Institut (FBH), Berlin, Germany*

(adapted from: J Photochem Photobiol B 2023;245:112757. doi: 10.1016/j.jphotobiol.2023.112757)

Abstract

The application of a far-ultraviolet C (UVC) light emitting diode (LED) of 233 nm showed significant bactericidal efficacy at an applied dose between 20 and 80 mJ cm^{-2} as reported recently. In addition, only minor epidermal DNA lesions were observed in *ex vivo* human skin and *in vitro* epidermal models <10% of the minimal erythema dose of UVB radiation.

To broaden the potential range of applications of such systems, *e.g.* to include postoperative application on wounds for the purpose of decontamination, we assessed how a disruption of normal anatomic skin structure and function influences the skin damage induced by light from 233 nm far-UVC LEDs. Thus, we induced superficial skin wounds by mechanical detachment of the stratum corneum in *ex vivo* human skin. Barrier-disruption of the skin could be successfully determined by measuring an increase in the transepidermal water loss (TEWL) and the stratum corneum loss could be determined morphologically by 2-photon microscopy (2-PM). After far-UVC irradiation of the skin, we screened the tissue for the development of cyclobutane pyrimidine dimers (CPDs) and 6–4 photoproducts (6-4PPs). The abundance of DNA lesions was elevated in wound skin in comparison to intact skin after irradiation with far-UVC. However, no increase in DNA lesions was detected when artificial wound exudate consisting of cell culture medium and serum was applied to the disrupted skin surface prior to irradiation. This effect agrees with the results of ray tracing simulations of the absorption of far-UVC light incident on a superficial skin wound. Interestingly, no significant deviations in radical formation between intact skin and superficially wounded skin were detected after far-UVC irradiation as analyzed by electron paramagnetic resonance (EPR) spectroscopy. In conclusion, 233 nm LED light at a dose of 60 mJ/cm^2 could be applied safely on superficial wounds for the purpose of skin antisepsis as long as the wounds are covered with wound fluid.

1. Introduction

It is of great importance to treat critically colonized and infected wounds antiseptically in order to initiate an unobstructed wound healing process. Furthermore, the preventive treatment of wounds at risk of infection is an essential measure [1]. The most abundant bacteria in infected and chronic wounds are *Staphylococcus* ssp. including methicillin-resistant *S. aureus* (MRSA) and *Pseudomonas aeruginosa* [2, 3] which are next to *Enterobacter* spp., *Klebsiella* spp., *Enterococcus* spp. and *Escherichia coli* also the bacteria predominantly isolated from surgical site infections [4-12]. Interestingly, also several fungal strains like *Cladosporidium herbarum, Candida albicans, Trichosporon* and *Rodhosporidum* have been identified to play a key role in non-healing wounds [3]. Chronic wounds represent a major economic and health burden potentially resulting in the necessity of amputation when all therapeutic options have been exhausted. This is associated with a vastly increased mortality rate [13, 14]. Due to the potential cause of bacterial resistances, antibiotics should be avoided for the treatment of chronic wounds [15]. Over-the-counter sales of the wound antibiotic mupirocin are considered to be a main factor behind the rapid increase of bacterial resistance development [1] resulting in decreased efficacy [16]. On the other hand, antiseptics with unspecific effects like octenidine dihydrochloride, polyhexanide, PVP-Iodine, hypochlorous acid or hydrogen peroxide do not exhibit any resistance formation [1], while microbiostatic antiseptics like chlorhexidine gluconate, quaternary ammonium compounds or silver ions are known to exhibit transferable resistances leading to cross-resistances with distinct antibiotics [1, 17]. Antimicrobial photodynamic inactivation [15], laser therapy and cold plasma therapy [18] are examples for physical approaches for wound treatment, which, however, have only been used rarely in clinical practice or experimentally up to now. Another fairly recent physical approach for the decolonization of intact and wounded skin is the application of far-ultraviolet C (UVC) light. It could be shown that exposure of several multidrug-resistant bacteria including MRSA to UVC light did not induce UV resistance after 25 serial exposures *in vitro* [19]. The inactivating effect of UVC light on microorganisms by inducing DNA- or RNA-lesions as a result of UV absorption is a well-studied phenomenon [20]. Nucleic acids absorb UVC light which leads to a photo-induced dimerization of consecutive pyrimidine bases [21]. The resulting DNA lesions include cyclobutane pyrimidine dimers (CPDs) and pyrimidine (6–4) pyrimidone photoproducts (6-4PPs) which are abundant in microorganisms [20] as well as epidermal cells [22]. Due to the following impaired transcription, the replication of microorganisms is inhibited resulting in a decreased pathogenicity [20]. In comparison to UVC light between 250 and 280 nm, a large proportion of far-UVC light ($\lambda < 240$ nm) is absorbed by the stratum corneum (SC) [23], which is the non-nucleated upper layer of the epidermis. However, it is known that far-UVC light

significantly inactivates microorganisms colonizing the skin surface as well as wounds. On intact and wounded skin of mice it could be demonstrated that far-UVC light of 222 nm is significantly safer than UVC light of 254 nm, which was accompanied by significant bactericidal effects in MRSA [24, 25]. Furthermore, Narita et al. observed the induction of wound healing effects in mice by far-UVC light [25]. Aside from that, harmful long-term effects of 222 nm far-UVC light were neither observed in a cancer-prone mouse model, nor after a single radiation dose of 500 mJ/cm^2 in humans [26-28]. Recently, Goh et al. were able to demonstrate a significant pathogen reduction by applying 222 nm far-UVC light in sacral and gluteal pressure-induced ulcera in patients [29]. The application of light at a wavelength around 233 nm using systems based on light emitting diodes (LEDs) is a novel possibility for the decolonization of wounds with the technical advantages of compact design, low voltage operation and choice of wavelength [30]. It was shown that an inactivation of MRSA is possible on blood agar plates as well as germ carriers by utilizing far-UVC light of 233 nm at a dose of 40 mJ/cm^2 [21,30]. Only superficially located and low-abundant DNA lesions were induced in excised human skin and reconstructed human epidermis models up to 60 mJ/cm^2 in comparison to 10% of the minimal erythema dose of UVB light for Fitzpatrick skin type II. Furthermore, the amount of free radicals was significantly reduced compared to the amount produced by visible and near-infrared light of a dose equivalent to a 20 min solar exposure [21]. In a recent study, the far-UVC LED system was further applied for the successful eradication of the fungal strains *C. albicans* and *C. parapsilosis* [31]. Therefore, 233 nm far-UVC light from LEDs constitutes an interesting alternative for the inactivation of microorganisms in wounds. Although the efficacy of this system against various microorganisms abundant in wound exudate has been tested [21], no data are known about the safety of applying it on wounds or on barrier-damaged skin. This could make it possible to use 233 nm far-UVC systems for pre-, intra- or postoperative antisepsis of the skin as well as indoor air decontamination. To get one step closer to this approach, we induced superficial skin wounds by mechanical detachment of the SC from the viable epidermis in *ex vivo* human skin and screened the tissue for the formation of CPDs, 6-4PPs as well as free radicals after 233 nm far-UVC irradiation of the skin. Furthermore, the effect of artificial wound exudate consisting of cell culture medium and serum on the formation of these DNA lesions was evaluated and compared to ray tracing simulations of the absorption of far-UVC light incident on a superficial skin wound. By this, the biophysical impact of 233 nm far-UVC light on skin in wounded conditions could be characterized for the first time.

2. Materials and methods

The nitroxide spin probe 3-(carboxy)-2,2,5,5-tetramethylpyrrolidin- 1-oxyl (PCA, 98%) was purchased from Sigma-Aldrich (Steinheim, Germany). Gibco™ phosphate-buffered saline (PBS) was purchased from Life Technologies Limited (Paisley, UK). Artificial wound exudate consisted of Eagle's minimal essential medium with Earle's salts containing 2 mM L-glutamine (both PAN-Biotech GmbH, Aidenbach, Germany) and 10% (*v*/*v*) fetal bovine serum (gibco® by life technologies™, Carlsbad, CA, USA) [21, 32]. Tesa® tapes No. 5529 were purchased from Beiersdorf AG (Hamburg, Germany), and UHU® cyanoacrylate glue was purchased from UHU GmbH & Co. KG (Bühl, Germany). Excised human skin samples (average donor age of 45.2 ± 10.8 years (mean value ± standard deviation)) were provided by artMED Berlin, Private Practice for Plastic and Aesthetic Surgery. The experimental protocols were approved by the Ethics Committee of the Charité – Universitätsmedizin Berlin (EA1/324/19). Informed written consent was obtained from the skin donors and all procedures complied with the Declaration of Helsinki.

2.1. Irradiation sources

Ex vivo human skin was irradiated with a 254 nm mercury-vapor lamp (40 mJ/cm^2, 0.54 mW/cm^2, LPL-R-01, sglux GmbH, Berlin, Germany), which served as a positive control due to its high potential to generate DNA lesions throughout the epidermis [21]. A 233 nm far-UVC LED (40–60 mJ/cm^2, 0.13 mW/cm^2, Ferdinand-Braun-Institut, Berlin, Germany) was used for the risk assessment of the target wavelength. To further compare the radical formation induced by 233 nm far-UVC light to visible-near infrared (VIS–NIR) light, we utilized a solar simulator (20 min irradiation time, 119.7 ± 0.3 J/cm^2 (mean value ± standard error of the mean of n = 3 independent experiments), Low Cost Solar Simulator LS0104, LOT-Quantum Design GmbH, Darmstadt, Germany). Further technical information on the irradiation systems and the measurement of irradiance and dose can be found in [21, 30, 33].

2.2. Preparation of excised human skin and cyanoacrylate tape- stripping procedure

The exact preparation procedure of the skin resectates is described in [21]. To induce a superficial skin wound, a small amount of UHU® cyanoacrylate glue was distributed evenly on the skin surface (50 mm × 19 mm). An adhesive tape was then immediately applied onto the glue and a rubber roller weighing about 700 g was moved back and forth ten times. After 5

min, the tape was stripped from the skin with a swift movement [34]. This procedure was carried out 6 times in total. To evaluate the protective effect of the artificial wound exudate, 5, 10 or 20 µl were applied to the taped skin before irradiation, resulting in different layer thicknesses as presented in **Section 3.4**.

2.3. Measurement of transepidermal water loss (TEWL)

The TEWL of intact and wounded skin was measured using a Tewameter® TM 300 (Courage + Khazaka electronic GmbH, Cologne, Germany) in triplicates on *n* = 19 *ex vivo* human skin samples in order to characterize the skin barrier damage induced by cyanoacrylate tape-stripping.

2.4. Determination of SC thickness by 2-photon microscopy (2-PM)

2.4.1. 2-PM measurements

The SC thickness of *ex vivo* human skin of *n* = 5 donors was investigated using 2-PM (DermaInspect, JenLab, Jena, Germany) equipped with a tunable femtosecond Ti:sapphire laser (Mai Tai XF, Spectra Physics, USA) to characterize anatomical alterations of the skin after the tape-stripping procedure. The excitation wavelength was set to 760 nm. Further technical parameters for the image acquisition can be found in [34]. Autofluorescence images were recorded as z-stacks in steps of 2 µm over a field of 152 × 152 μm^2.

2.4.2. Determination of SC thickness

In order to define the SC thickness of the skin samples, the count of nucleated cells in the single layers of the 2-PM z-stacks was determined manually on *n* = 3 spots for each donor until the depth of the stratum granulosum (SG). In this context, the image showing a homogenous structure of corneocytes was defined as the SC surface (depth of 0 µm). The ratio of the count of nucleated cells of a certain depth and the count of the entirely nucleated SG was calculated for each image of the z-stack obtaining the relative proportion of nucleated cells. This value was linearly interpolated as a function of depth to obtain a value of 50% representing the transition area between the SC and the SG according to Dong et al. [34].

2.5. Immunohistological stainings of human skin sections for CPD+ and 6-4PP+ cells

After UVC irradiation, the skin was analyzed for DNA lesions (6-4PPs and CPDs) immunohistochemically on 1–2 µm paraffin sections of *n* = 3 to 9 excised human skin samples as previously described [21, 30]. The maximum depth of damage was determined by measuring the distance from the uppermost point of the viable epidermis to the point of the deepest nucleus showing damage on *n* = 10 spots per skin using the software ImageJ (Wayne Rasband, National Institutes of Health, Bethesda, MD, USA). Hematoxylin and eosin (HE) stains were further obtained to verify the loss of the SC.

2.6. Quantitative evaluation of radical formation by electron paramagnetic resonance (EPR) spectroscopy

UVC irradiation-induced free radical formation was quantitatively analyzed in *n* = 4 excised human skin samples by EPR spectroscopy using the spin probe PCA as this method allows precise quantification of UV-induced extracellular radicals in skin [21, 35-37]. The detailed experimental setup as well as the parameter settings of the EPR measurements are published in [21].

2.7. UV–VIS spectroscopy measurements of artificial wound exudate

Absorption of artificial wound exudate was measured between 200 nm and 300 nm using a UV–VIS spectrophotometer (Lambda 650, PerkinElmer, Rodgau-Jügesheim, Germany) using 1 mm quartz cuvettes. The information obtained by this was further processed in the framework of Monte Carlo ray tracing simulations (**Section 2.8.**).

2.8. Ray tracing simulations

A forward Monte Carlo ray tracing simulation was used to simulate the penetration depth of light between 200 nm and 300 nm for the different skin conditions. This model consisted of 16 µm SC, 65 µm epidermis, and an infinite dermis (intact skin); 65 µm epidermis, and an infinite dermis (superficially wounded skin) or 1 mm artificial wound exudate, 65 µm epidermis, and an infinite dermis (superficially wounded skin with artificial wound exudate) assuming the wavelength-dependent absorption coefficient *µa* and effective scattering coefficient *µs'* from an inverse Monte Carlo simulation by Zamudio Díaz et al. [38], a wavelength-dependent Henyey-Greenstein scattering factor g [39], and a wavelength-dependent refractive index of

skin [40]. Here, the simulation involves the absorption of artificial wound exudate as measured by UV–VIS spectroscopy (**Section 2.7.**), assuming no scattering, and the refractive index of water. During simulation, 2 × 105 rays per wavelength were emitted into the skin model and the intensity was determined as a function of the penetration depth.

2.9. Statistical analysis

All data are expressed as mean ± standard error of the mean (SEM). Statistical tests were performed with IBM SPSS® Statistics 28 (IBM, Armonk, NY, USA). The Shapiro–Wilk test was applied for testing the normal distribution of the data. Variance homogeneity was further proven by the F-test. Wilcoxon signed-rank tests or *t*-tests for paired samples were conducted in case of 2 groups and a Friedman test or a one way analysis of variance (ANOVA) followed by Bonferroni-adjusted *post hoc* tests or Dunnetts's *post hoc* tests were conducted in case of > 2 groups. The tests were performed affording a significance of $p < 0.05$. The visualization of the data was carried out using OriginPro 2020 (Origin, OriginLab Corporation, Northampton, MA, USA).

3. Results and discussion

3.1. Indication of barrier disruption by TEWL and 2-PM

To induce a disruption of normal anatomic structure as well as function [41] of *ex vivo* human skin, cyanoacrylate tape-stripping (CA-TS) was performed (**Figure 1A**). For this purpose, the protocol according to Dong et al. [34] was used, in which complete detachment of the SC was achieved after 4 CA-TS. We increased the number to 6 CA-TS in this study. For the indication of SC detachment, we performed autofluorescence imaging of the skin by 2-PM, in which we gradually scanned the skin along the z-axis in 2 µm steps. A 50% cell nucleation was set as the boundary between the SC and the SG. Thus, the SC thickness of intact skin was 15.8 ± 1.4 µm on average, while that of superficially wounded skin was only 6.5 ± 0.5 µm, corresponding to a loss of approximately 60% ($p < 0.05$) (**Figure 1B** and **C**). The loss of the SC was further verified by HE sections of untreated skin samples (**Figure 1D** and **E**). Furthermore, we indicated the wounded state of the *ex vivo* human skin after the CA-TS procedure by measuring the TEWL which represents a proper parameter for barrier characterization [42] inversely correlating with the SC thickness [43] based on Fick's law of diffusion [44]. Here, we recorded an increase from 6.8 ± 0.5 g/m2/h to 35.6 ± 2.2 g/m2/h which corresponds to a factor > 5 ($p < 0.001$) (**Figure 1F**) clearly indicating barrier impairment. The increase of TEWL is comparable with values obtained in a work by Döge et al. using 50 × TS for mechanical detachment [45],

which was evaluated to be sufficient for removing the entire SC [34]. While the HE sections showed a sufficient detachment of the SC, the results of the 2-PM analysis diverged in the present study. Dong et al. were able to remove the entire SC after only 4 CA-TS [34] using a cubic block for applying pressure, whereas in the present study residual SC was still present after 6 CA-TS applied with a roller despite the fact that the TEWL indicated a particularly high barrier impairment. According to Breternitz et al. the cumulative protein removed from skin is influenced by the factor of pressure [46] which further could explain the discrepancy in the results obtained. On the other hand, the execution of a weighted rolling movement as conducted in the present study was found to be the optimal way for application [47]. Another factor causing inter-experimental variability is the velocity of tape-stripping [47].

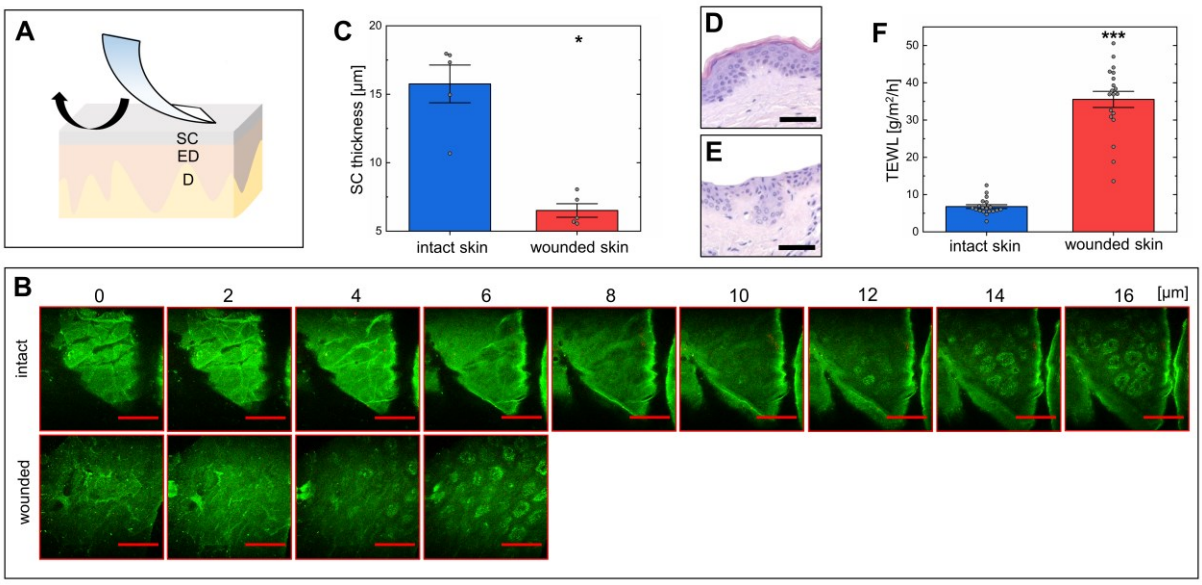

Figure 1: After applying cyanoacrylate tape-stripping (CA-TS) on *ex vivo* human skin for 6 times (**A**), a loss of stratum corneum (SC) thickness by approximately 60% was indicated by autofluorescence images of 2-photon microscopy (2-PM) (**B, C**). Hematoxylin and eosin (HE) sections of intact (**D**) and superficially wounded skin (**E**) confirmed the loss of SC. Furthermore, transepidermal water loss (TEWL) indicated an increase of a factor > 5 in superficially wounded skin (**F**). Indication of mean values ± SEMs of $n = 5$ (**C**) and $n = 19$ (**D**) skin samples and statistical significance with * = $p < 0.05$ and *** = $p < 0.001$ determined by Wilcoxon signed-rank test. Scale bars indicating 50 µm. SC = Stratum corneum, ED = Epidermis, D = Dermis.

3.2. Formation of DNA lesions

3.2.1. Abundance and maximum depth of CPD+ and 6-4PP+ cells

To access the influence of the skin condition on the formation of DNA lesions (CPDs and 6-4PPs) we irradiated intact and superficially wounded skin with 233 nm at a dose of 40 and 60 mJ/cm^2. Furthermore, we considered the reference wavelength 254 nm at a dose of 40

mJ/cm^2, which is known for its deeper penetration depth into the skin as well as its increased damage potential [21, 30, 48-50]. An increase in the general abundance of DNA lesions was visible for both, CPDs and 6-4PPs, after wounding the skin as well as with increasing dose and wavelength (**Figure 2A**). Our controls showed that DNA damage was not observed in non-irradiated skin, neither intact, nor wounded (**Figure 3A–D**). After irradiation with 233 nm at 40 mJ/cm^2 the amount of CPDs increased from 4.7 ± 0.5% to 14.1 ± 1.7% ($p < 0.05$) in superficially wounded skin (**Figure 3I** and **K**). 6-4PPs increased from 1.0 ± 0.2% to 8.6 ± 1.9% ($p = 0.05$) (**Figure 3J** and **L**). After irradiation with 60 mJ/cm^2 there was an increase from 12.2 ± 2.1% to 34.4 ± 6.4% for the CPDs ($p < 0.01$) (**Figure 3M** and **O**), while 6-4PPs increased from 4.4 ± 1.3% to 19.8 ± 6.5% ($p < 0.01$) (**Figure 3N** and **P**). Irradiation with 254 nm, consistent with previous publications [21, 30], induced higher abundance of CPDs by approximately a factor of 6 and approximately 19-fold higher abundance of 6-4PPs at an equivalent dose in intact skin. The abundance in superficially wounded skin was 3-fold (CPDs) or 4-fold (6- 4PPs) higher for superficially wounded skin in comparison to far-UVC of the identical dose. Here, CPDs increased from 27.1 ± 2.1% to 44.7 ± 4.3% ($p < 0.05$) (**Figure 3E** and **G**), while 6-4PPs showed an increase from 18.7 ± 1.2% to 37.1 ± 5.4% ($p < 0.05$) (**Figure 3F** and **H**) after irradiation of superficially wounded skin. The relatively small increase in photo-lesions in the tissue after irradiation with 254 nm could be related to the fact that the radiation of this wavelength is less absorbed by the SC [23] and can therefore already penetrate the intact skin. Thus, a saturation of the abundance of photo-lesions is already reached in intact skin. A limitation of this method is that it does not quantify the number of lesions per nucleus. With regard to the maximum depth of the damage, a comparable pattern became evident. Irradiating the skin with 233 nm at 40 mJ/cm^2, the depth of CPDs increased from 17.9 ± 0.6 µm to 23.6 ± 1.4 µm ($p = 0.05$) and of 6-4PPs from 13.7 ± 0.9 µm to 19.6 ± 1.2 µm ($p = 0.05$) after a wound was induced (**Figure 2B**). After irradiation with a dose of 60 mJ/cm^2, there was an increase from 22.7 ± 1.2 µm to 34.9 ± 2.0 µm for the CPDs ($p < 0.001$), while the increase was from 15.6 ± 0.9 µm to 23.8 ± 1.4 µm for the 6-4PPs ($p < 0.001$). CPDs raised from 47.8 ± 0.9 µm to 62.0 ± 0.9 µm after irradiation of superficially wounded skin with 254 nm at a dose of 40 mJ/cm^2. Here, we observed an increase of 6-4PPs from 37.4 ± 3.3 µm to 51.6 ± 7.2 µm. The average skin thickness as determined on HE sections on *ex vivo* skin of $n = 11$ donors was 64.9 ± 1.9 µm in this study. Thus, it can be concluded that 254 nm irradiation at 40 mJ/cm^2 induced DNA damage in 95% of the epidermis of superficially wounded skin, while 233 nm covered approximately one third of the depth at the same dose which is comparable to previously published data [21].

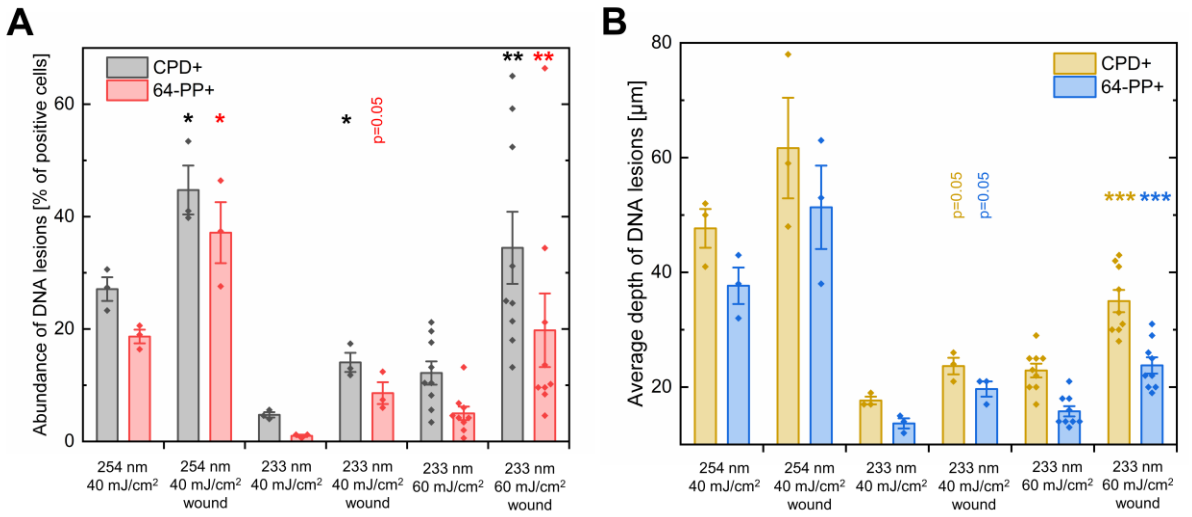

Figure 2: Presentation of the overall immunohistochemical abundance (**A**) and average depth (**B**) of DNA lesions after irradiation with 254 nm 40 mJ/cm², 233 nm 40 mJ/cm² and 60 mJ/cm² of intact and superficially wounded skin shows a dose- and wavelength-dependent increase as well as a higher abundance and depth after wound induction. Indication of mean values ± SEMs of n = 3 to 9 skin samples and statistical significance with * = $p < 0.05$, ** = $p < 0.01$ and *** = $p < 0.001$ determined by one-tailed paired samples t-test in case of normal distributed data or one-tailed Wilcoxon signed-rank test in case of non-normal distributed data and/ or variance heterogeneity (intact *vs.* wound for each category). *P*-values indicating tendencies (p = 0.05) are written out.

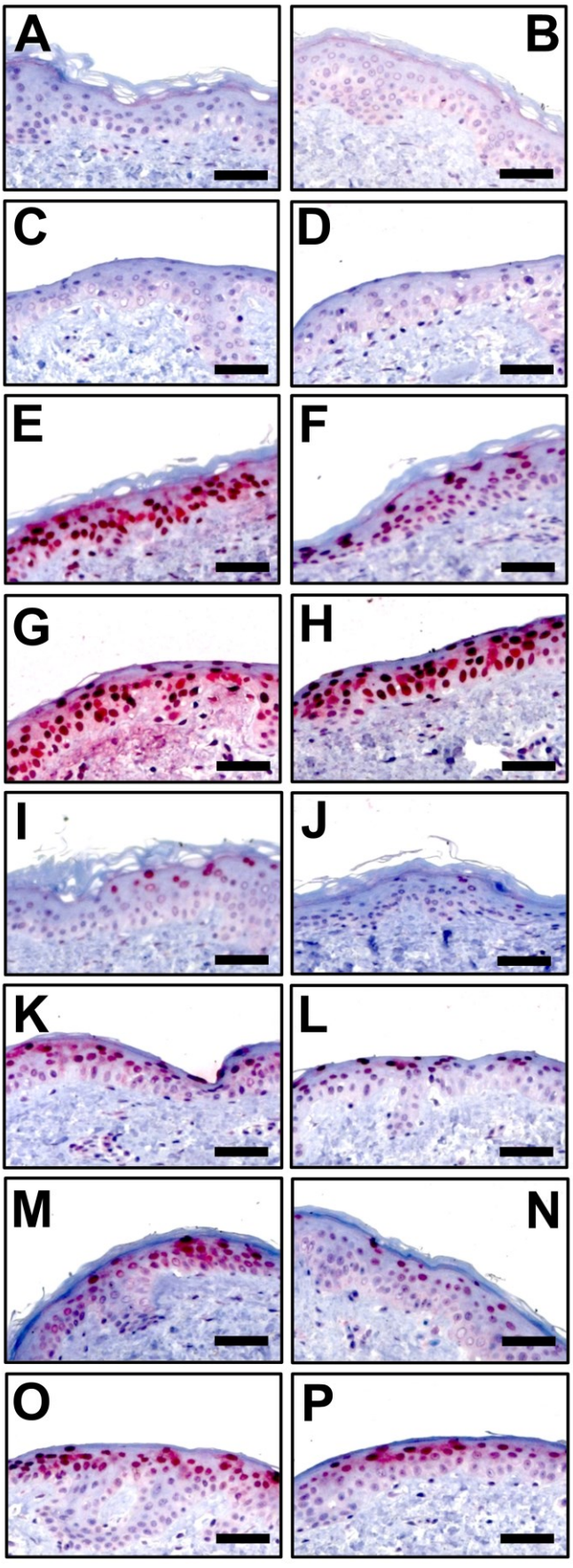

Figure 3: Presentation of immunohistochemical images with immunostainings for UVC-induced cyclobutane pyrimidine dimer positive (CPD+) and pyrimidine (6–4) pyrimidone photoproduct positive (6-4PP+) cells with non-irradiated control skin (**A, B**), superficially wounded non-irradiated control skin (**C, D**) and skin irradiated with 254 nm 40 mJ/cm^2 before (**E, F**) and after wound induction (**G, H**), 233 nm 40 mJ/cm^2 before (**I, J**) and after wound induction (**K, L**) as well as 233 nm 60 mJ/cm^2 before (**M, N**) and after wound induction (**O, P**). Scale bar indicating 50 µm.

3.2.2. Abundance and maximum depth of CPD+ and 6-4PP+ cells under the influence of artificial wound exudate

In a further experiment, our aim was to investigate the influence of different amounts of artificial wound exudate on the formation of epidermal photo-lesions and to test whether there is a protective effect emanating from the artificial wound exudate since increased skin damage was observed in superficially wounded skin as presented in **Section 3.2.1**. In this experiment, any photo-lesions in non-irradiated skin were absent before and after wounding (**Figure 5 A–D**). We observed a CPD abundance of 8.5 ± 1.3% and a proportion of 6-4PPs of 3.9 ± 0.6% in the epidermis after irradiation with 233 nm and a dose of 60 mJ/cm^2 (**Figure 4A, 5E** and **F**). In superficially wounded skin, this increased to 22.7 ± 3.6% (CPDs, $p < 0.05$) and 14.4 ± 3.0% (6-4PPs, $p < 0.05$) (**Figure 5G** and **H**). After the application of 5 µl of artificial wound exudate, the damage was largely maintained (CPDs: 21.8 ± 4.4%, $p < 0.05$, 6-4PPs: 13.0 ± 3.2%, $p < 0.05$) (**Figure 5I** and **J**). After adding 10 µl of artificial wound exudate to the superficial wound (**Figure 5K** and **L**), a decrease could be observed which resulted in a non-significant difference to the control group (CPDs: 15.8 ± 4.3%, 6-4PPs: 6.5 ± 1.3%). An abundance of photo-lesions comparable to that of the control group (233 nm, 60 mJ/cm^2) was achieved with the application of 20 µl of artificial wound exudate (**Figure 5M** and **N**). Here, an amount of 10.2 ± 2.4% CPD-positive cells and 5.6 ± 2.0% 6-4PP-positive cells was observed. A comparable effect was also seen for the maximum depth of DNA damage. After superficial wounding of the skin, the maximum depth of photo-lesions increased from 23.5 ± 1.4 µm to 27.5 ± 1.5 µm (CPDs) as well as 14.7 ± 0.4 µm to 22.2 ± 1.1 µm (6-4PPs, $p < 0.001$) (**Figure 4B**). Application of 5 µl artificial wound exudate reduced the depth of the DNA damage (CPDs: 21.4 ± 1.4 µm, 6-4PPs 16.2 ± 1.1 µm) again, so that significant differences to the control group did not exist any longer. After application of 10 µl artificial wound exudate, the maximum depth of damage decreased to 18.5 ± 1.5 µm and 13.6 ± 1.4 µm and further dropped to 18.0 ± 1.8 µm and 11.0 ± 1.4 µm after application of 20 µl artificial wound exudate. Thus, the depth of the 6-4PPs was significantly reduced compared to an intact skin ($p < 0.05$). Depending on their condition, wounds are covered with a wound exudate [51-53]. The experiment clearly shows that far-UVC absorbent media [21], such as the artificial wound exudate used here, can attenuate the damage caused to barrier-damaged skin and thus replace the protective function of the SC with regard to radiation-induced damage even without containing cellular components or further protein components like fibrin. Nevertheless, it should be taken into account that identical conditions do not always exist in the clinical situation. To the best of our knowledge, the present study is the first to demonstrate 233 nm far-UVC-induced skin damage on wounds under laboratory conditions for the purpose of risk assessment. In order to elucidate the underlying

biophysical effects, we have addressed an *in silico* study in **Section 3.4.** simulating the penetration depth of light between 200 and 300 nm into the skin.

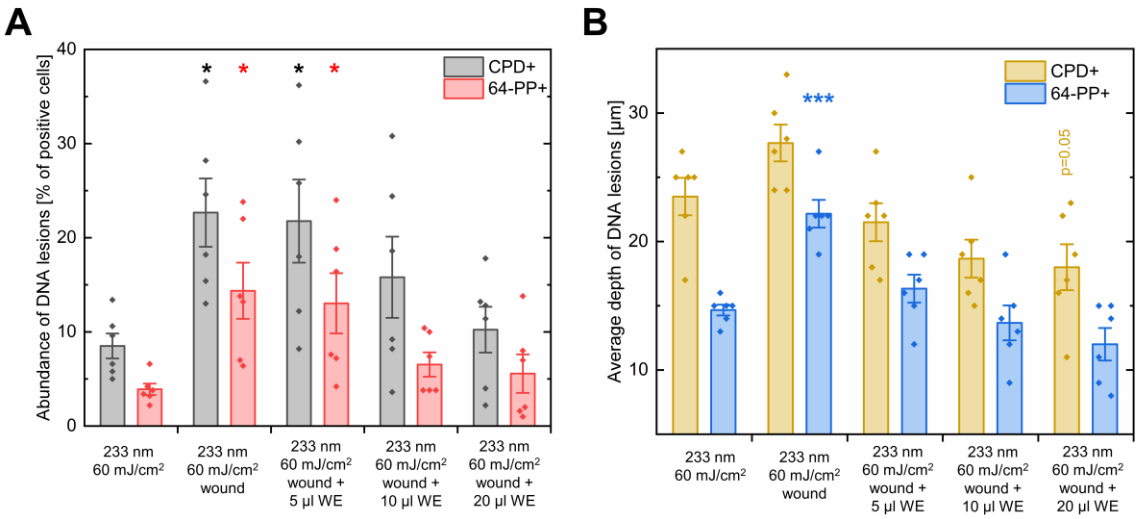

Figure 4: Presentation of the overall immunohistochemical abundance (**A**) and average depth of (**B**) of DNA lesions for 233 nm 60 mJ/cm² (control), 233 nm 60 mJ/ cm2 after superficial wound induction as well as 233 nm 60 mJ/cm² after superficial wound induction and addition of 5, 10 or 20 µl artificial wound exudate (WE). An increase in the abundance and depth of DNA lesions after superficial wound induction was observed, gradually decreasing with increasing application amount of artificial wound exudate. Indication of mean values ± SEMs of n = 6 skin samples and statistical significance with * = $p < 0.05$ and *** = $p < 0.001$ determined by the Friedman test with Bonferroni-adjusted multiple comparisons (A) or one-way analysis of variance (ANOVA) with Dunnett's multiple comparisons (B) testing against the control of 233 nm 60 mJ/cm². *P*-values indicating tendencies ($p = 0.05$) are written out.

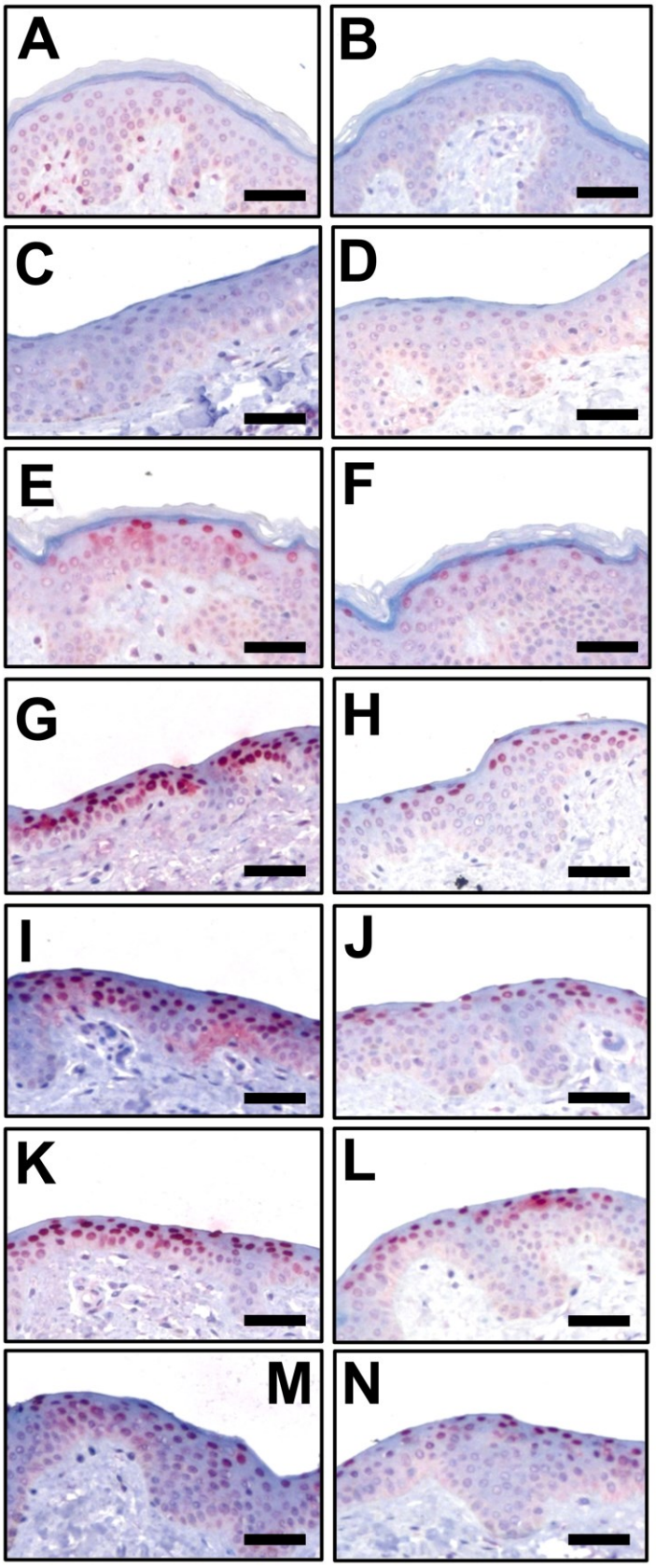

Figure 5: Presentation of immunohistochemical images with immunostainings for UVC-induced CPD+ and 6-4PP+ cells with non-irradiated control skin (**A, B**), superficially wounded non-irradiated control skin (**C, D**) and skin irradiated with 233 nm 60 mJ/cm^2 before (**E, F**) and after superficial wound induction (**G, H**) as well as 233 nm 60 mJ/cm^2 + 5 µl artificial wound exudate (**I, J**), +10 µl artificial wound exudate (**K, L**), +20 µl artificial wound exudate (**M, N**). Scale bar indicating 50 µm.

3.3. Radical formation

Using EPR spectroscopy, we quantitatively evaluated the radical formation further. Here, we wanted to elucidate if there is a difference between intact and superficially wounded skin in respect of the radical formation at a microbiocidal dose of 60 mJ/cm^2 [21, 31]. As a reference, we further utilized VIS–NIR light on intact skin at a dose of 120 J/cm^2, which corresponds to a 20-min stay in the sun [21]. Interestingly, no significant differences were found between intact and superficially wounded skin after irradiation with 233 nm at a dose of 60 mJ/cm^2 (intact: 1.1 ± 0.3 spins/mm^3 × 10^{13}, wounded: 1.2 ± 0.2 spins/mm^3 × 10^{13}) (**Figure 6**). However, radical formation was slightly reduced compared to the VIS–NIR 120 J/cm^2 group (1.7 ± 0.2 spins/mm3 × 10^{13}), which corresponds to a 20 min stay in the sun and is controllable by the antioxidative system [21]. Compared to the SG, the SC has a much higher lipophilicity [54]. In addition, the SC lacks DNA bases [55] if parakeratosis [56] can be excluded. DNA bases are important UV-absorbing chromophores [57] and thus, contribute to radical formation [58]. Even though the biochemical and chemical composition of the SC and the SG differ, interestingly, there were no quantitative differences in radical formation in the skin. However, it should be noted that in superficially wounded skin, DNA is directly exposed to radicals, which could promote the time-dependent formation of DNA lesions in form of dark CPDs when reacting with melanin degradation products producing excited triplet carbonyls [59-61]. On the other hand, due to the formation of radicals the promotion of wound healing could be expected in wounded skin as already known for the application of cold plasma [62].

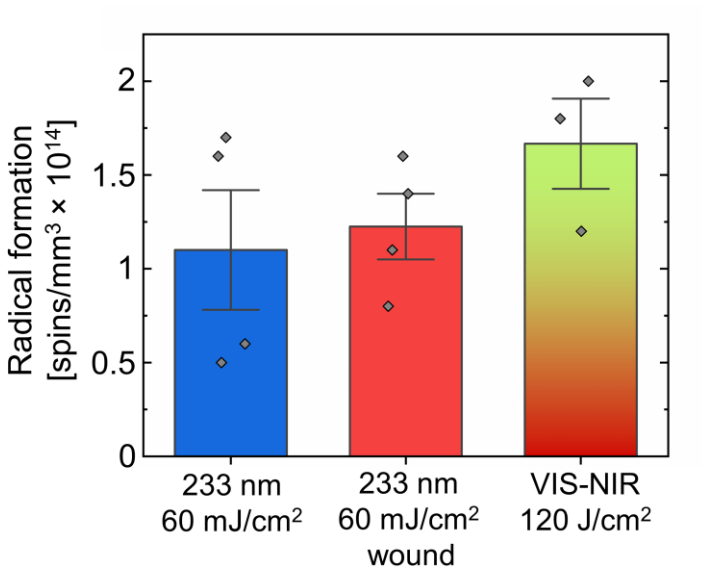

Figure 6: No differences in radical formation were observed between intact and superficially wounded skin (233 nm 60 mJ/cm^2) according to electron paramagnetic resonance (EPR) spectroscopy. A slightly reduced radical formation was found in comparison to visible-near infrared (VIS–NIR) irradiation with a dose of 120 J/cm^2. Indication of mean values ± SEMs of n = 3 to 4 skin samples.

3.4. Ray tracing simulations

In a final experiment, we conducted a model for a forward Monte Carlo ray tracing simulation. We used this model to match the *ex vivo* abundance and localization of photo-lesions with the simulated penetration depth of light between 200 nm and 300 nm. For this purpose, the bio-physical properties of the skin (absorption, scattering) were first mapped in an inverse Monte Carlo simulation [63] by Zamudio Díaz et al. [38]. The variables obtained in this way could then be used for modelling the forward ray tracing simulation. Furthermore, the absorption properties of the artificial wound exudate used were determined by UV spectrometry. Here, an ideal layer thickness of 1 mm (**Figure 7A**) was simulated, which lies exactly between the layer thicknesses for 10 µl artificial wound exudate (approx. 0.8 mm according to **Figure 7C**) and 20 µl artificial wound exudate (approx. 1.3 mm according to **Figure 7D**). For the application amount of 5 µl, the film thickness was only 0.3 mm (**Figure 7B**).

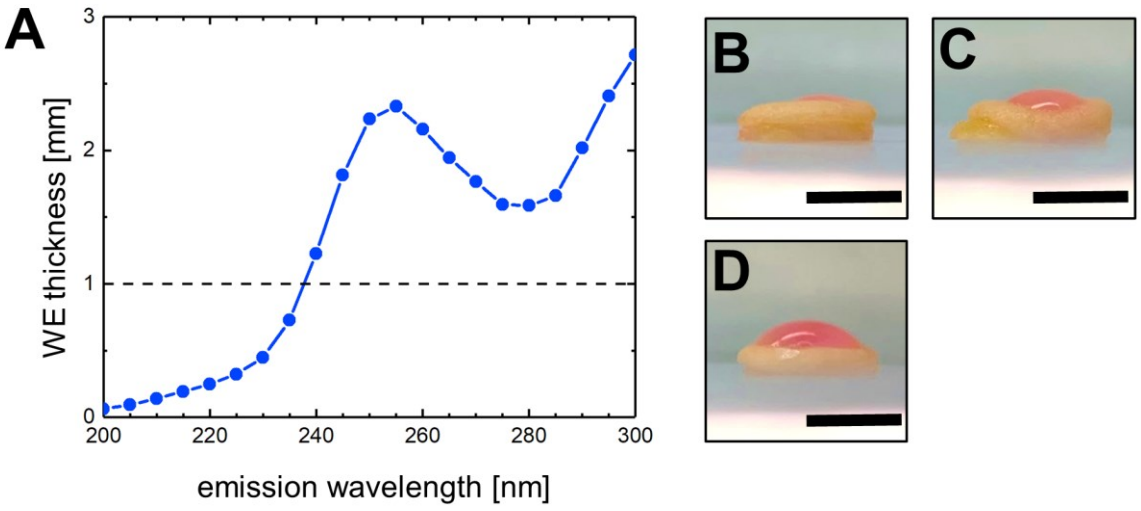

Figure 7: (**A**) shows the optimal artificial wound exudate (WE) thickness to recover the absorption of an intact SC for wavelengths between 200 and 300 nm indicating a required artificial wound exudate thickness of 1 mm for 233 nm. Images of skin biopsies to which artificial wound exudate was applied are shown in (**B**) with droplets of 5 µl artificial wound exudate (0.3 mm), (**C**) 10 µl artificial wound exudate (0.8 mm) and (**D**) 20 µl artificial wound exudate (1.3 mm) with the scale bar indicating 0.5 cm.

This agrees well with the data described in **Section 3.2.2**. The penetration depth of light into the epidermis is shown in **Figure 8A** for intact skin, **Figure 8B** for superficially wounded skin and **Figure 8C** for superficially wounded skin plus artificial wound exudate of 1 mm film thickness. The corresponding 3D beam paths are shown in **Figure 8D** to **8F**, penetration depth of the photons increases to longer wavelengths. For the target wavelength 233 nm, the light penetrated approximately 20 µm into the epidermis reaching a relative intensity of 10% in

intact skin, while the penetration depth within the viable epidermis was extended to ≈ 45 µm at 254 nm correlating well with the results of CPD+ depth presented in **Section 3.2.1**. After removal of the SC, the penetration depth increased to approx. 30 µm at 233 nm and > 60 µm at 254 nm. A penetration depth of 30 µm does not reach the basal layer of the epidermis (**Figure 8H**), which means that the stem cells of the skin remained unaffected. After application of the artificial wound exudate, the situation for 233 nm was similar to that with an intact SC, which can be compared very well with the data obtained *ex vivo* with CPD+ stainings after irradiation with 233 nm and 60 mJ/cm^2 as depicted in **Figure 8G to 8I**. This shows that the penetration depth calculated in the *in silico* model is in accordance with the radiation-related skin damage making it suitable as part of a predictional risk assessment. Nevertheless, it has to be taken into account that the reproduction of the physical properties of actual wound exudate via the artificial wound exudate used in this study is limited because not all cellular and protein contents were included. Thus, a stronger attenuation of UVC light in the clinical situation can be expected. Interestingly, the penetration depth of 233 nm light into the artificial wound exudate was higher as compared to 222 nm as shown in **Figure 8C**. In our previous publication, we could show that far-UVC light of both wavelengths can be considered safe [21]. However, the deeper penetration of 233 nm light into the wound (exudate) might be an advantage for the eradication of microorganisms which should be tested in further studies.

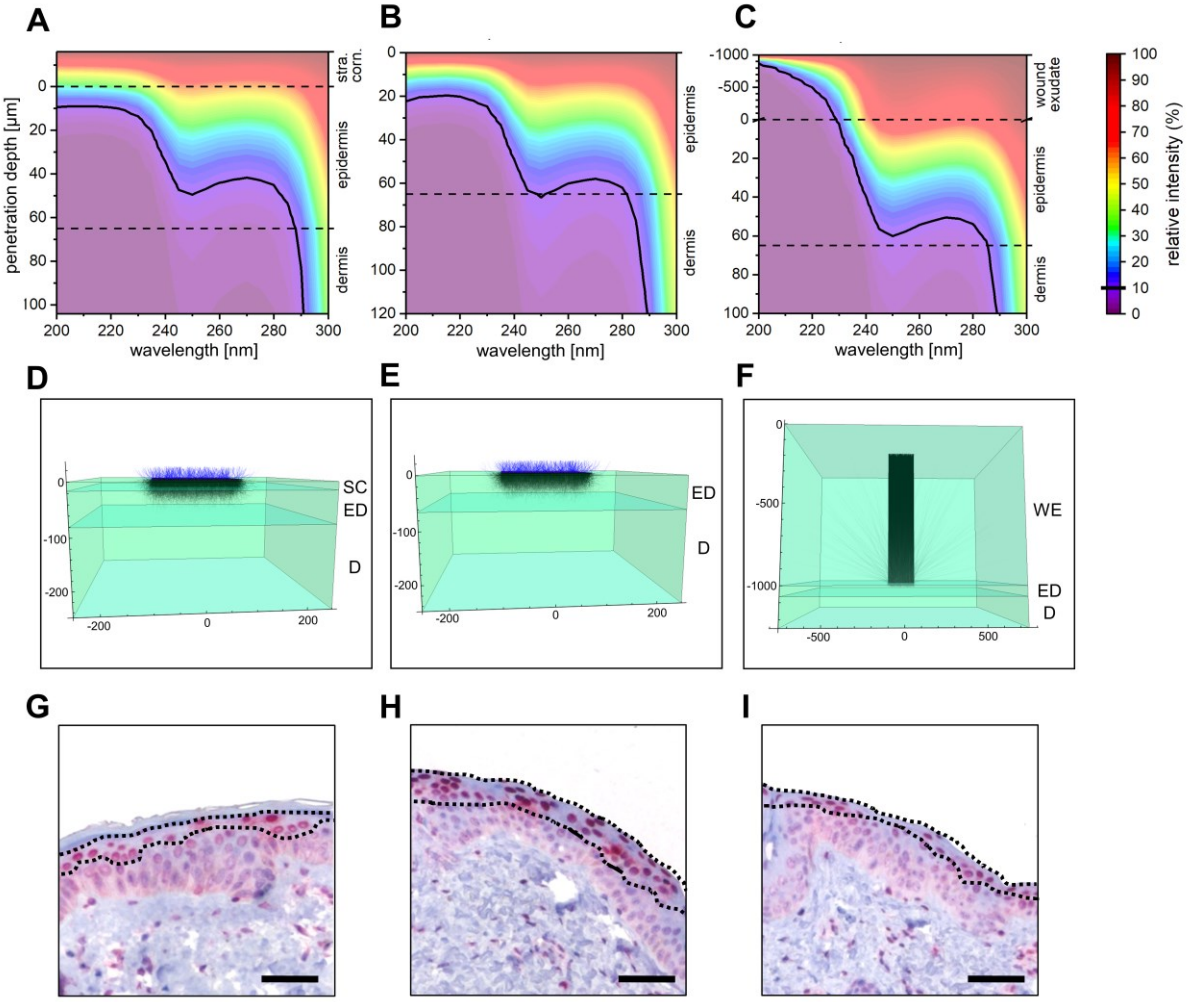

Figure 8: Presentation of the simulated wavelength-dependent penetration depth of light from 200 nm – 300 nm into skin for (**A**): intact skin, (**B**): superficially wounded skin and (**C**): superficially wounded skin plus artificial wound exudate with a thickness of 1 mm. The relative radiation intensity in % is indicated by false colors as shown in the color code bar and a relative intensity of 10% is indicated by a black line. The corresponding simulated beam paths for 233 nm light are shown in (**D**), (**E**) and (**F**) (axis unit of A – F: µm; SC = Stratum corneum, ED = Epidermis, D = Dermis, WE = Artificial wound exudate). The related immunohistological skin sections of human skin irradiated with 233 nm and 60 mJ/cm^2 *ex vivo* showing CPD+ cells in red are presented in (**G**), (**H**) and (**I**) (areas rich in CPD+ cells are marked with a black line; scale bar: 50 µm).

4. Conclusions

The present study successfully simulated the influence of superficial wounds on skin damage induced by light from a 233 nm far-UVC LED lamp using *ex vivo* and *in silico* methods. Utilizing immunohistochemistry, we detected an increased formation of DNA lesions in superficially wounded skin compared with intact skin after irradiation with far-UVC of 233 nm peak wavelength. However, this effect could not be observed if artificial wound exudate was applied on the wounded skin surface before irradiation. The observed effect agrees with the results of

ray tracing simulations of the absorption of far-UVC light incident on a superficial skin wound. Interestingly, intact skin and barrier-disrupted skin showed no significant quantitative deviations in radical formation as investigated by electron paramagnetic resonance (EPR) spectroscopy. In conclusion, 233 nm LED light of 60 mJ/cm^2 could be applied safely on superficial wounds for the purpose of skin antisepsis as long as the wounds are covered with wound fluid. Since the wound fluid in the real situation may contain blood and immune cellular components, a stronger attenuation of the UVC light can be assumed. In future studies the wound healing potential of 233 nm LEDs as well as bactericidal property in wounds should be investigated *in vivo* or in *in vitro* models. Furthermore, the influence of 233 nm UVC light on tissue components in deeper wounds should be evaluated.

References

[1] A. Kramer, J. Dissemond, S. Kim, C. Willy, D. Mayer, R. Papke, F. Tuchmann, O. Assadian, Consensus on wound antisepsis: update 2018, Skin Pharmacol Physiol 31 (1) (2018) 28-58.

[2] I. Negut, V. Grumezescu, A.M. Grumezescu, Treatment strategies for infected wounds, Molecules 23 (9) (2018) 2392.

[3] T.R. Johnson, B.I. Gomez, M.K. McIntyre, M.A. Dubick, R.J. Christy, S. E. Nicholson, D.M. Burmeister, The cutaneous microbiome and wounds: new molecular targets to promote wound healing, Int J Mol Sci 19 (9) (2018) 2699.

[4] H. Misteli, A.F. Widmer, R. Rosenthal, D. Oertli, W.R. Marti, W.P. Weber, Spectrum of pathogens in surgical site infections at a Swiss university hospital, Swiss Med Wkly 140 (2011), w13146.

[5] Y. Takesue, A. Watanabe, H. Hanaki, S. Kusachi, T. Matsumoto, A. Iwamoto, K. Totsuka, K. Sunakawa, M. Yagisawa, J. Sato, T. Oguri, K. Nakanishi, Y. Sumiyama, Y. Kitagawa, G. Wakabayashi, I. Koyama, K. Yanaga, T. Konishi, R. Fukushima, S. Seki, S. Imai, T. Shintani, H. Tsukada, K. Tsukada, K. Omura, H. Mikamo, H. Takeyama, M. Kusunoki, S. Kubo, J. Shimizu, T. Hirai, H. Ohge, A. Kadowaki, K. Okamoto, K. Yanagihara, Nationwide surveillance of antimicrobial susceptibility patterns of pathogens isolated from surgical site infections (SSI) in Japan, J Infect Chemother 18 (6) (2012) 816-826.

[6] A.J. Tande, R. Patel, Prosthetic joint infection, Clin Microbiol Rev 27 (2) (2014) 302-345.

[7] P.D. Fey, M.E. Olson, Current concepts in biofilm formation of Staphylococcus epidermidis, Future Microbiol 5 (6) (2010) 917-933.

[8] E. Moran, S. Masters, A.R. Berendt, P. McLardy-Smith, I. Byren, B.L. Atkins, Guiding empirical antibiotic therapy in orthopaedics: the microbiology of prosthetic joint infection managed by debridement, irrigation and prosthesis retention, J Inf Secur 55 (1) (2007) 1-7.

[9] C.D. Owens, K. Stoessel, Surgical site infections: epidemiology, microbiology and prevention, J Hosp Infect 70 (Suppl. 2) (2008) 3-10.

[10] A.J. Mangram, T.C. Horan, M.L. Pearson, L.C. Silver, W.R. Jarvis, Guideline for prevention of surgical site infection, 1999, Am J Infect Control 27 (2) (1999) 97-134.

[11] T. Takizawa, T. Tsutsumimoto, M. Yui, H. Misawa, Surgical site infections caused by methicillin-resistant *Staphylococcus epidermidis* after spinal instrumentation surgery, Spine (Phila Pa 1976) 42 (7) (2017) 525-530.

[12] A. Kramer, J. Pochhammer, P. Walger, U. Seifert, M. Ruhnke, J.C. Harnoss, Spectrum of pathogens in postoperative complications of visceral surgery : the problem of multidrug resistance, Chirurg 88 (5) (2017) 369-376.

[13] K. Järbrink, G. Ni, H. Sönnergren, A. Schmidtchen, C. Pang, R. Bajpai, J. Car, The humanistic and economic burden of chronic wounds: a protocol for a systematic review, Syst Rev 6 (1) (2017) 15.

[14] R. Zhao, H. Liang, E. Clarke, C. Jackson, M. Xue, Inflammation in chronic wounds, Int J Mol Sci 17 (12) (2016) 2085.

[15] F. Drago, L. Gariazzo, M. Cioni, I. Trave, A. Parodi, The microbiome and its relevance in complex wounds, Eur J Dermatol 29 (1) (2019) 6-13.

[16] S. Harbarth, N. Liassine, S. Dharan, P. Herrault, R. Auckenthaler, D. Pittet, Risk factors for persistent carriage of methicillin-resistant Staphylococcus aureus, Clin Infect Dis 31 (6) (2000) 1380-1385.

[17] G. Kampf, Acquired resistance to chlorhexidine - is it time to establish an 'antiseptic stewardship' initiative? J Hosp Infect 94 (3) (2016) 213-227.

[18] G. Daeschlein, Antimicrobial and antiseptic strategies in wound management, Int Wound J 10 Suppl 1 (Suppl. 1) (2013) 9-14.

[19] H. Choi, P. Chatterjee, M. Hwang, E.M. Stock, J.S. Lukey, J.E. Zeber, C. Jinadatha, Can multidrug-resistant organisms become resistant to ultraviolet (UV) light following serial exposures? Characterization of post-UV genomic changes using whole-genome sequencing, Infect Control Hosp Epidemiol 43 (1) (2022) 72-78.

[20] T. Dai, M.S. Vrahas, C.K. Murray, M.R. Hamblin, Ultraviolet C irradiation: an alternative antimicrobial approach to localized infections? Expert Rev Anti-Infect Ther 10 (2) (2012) 185-195.

[21] P. Zwicker, J. Schleusener, S.B. Lohan, L. Busch, C. Sicher, S. Einfeldt, M. Kneissl, A.A. Kuhl, C.M. Keck, C. Witzel, A. Kramer, M.C. Meinke, Application of 233 nm far-UVC LEDs for eradication of MRSA and MSSA and risk assessment on skin models, Sci Rep 12 (1) (2022) 2587.

[22] J. D'Orazio, S. Jarrett, A. Amaro-Ortiz, T. Scott, UV radiation and the skin, Int J Mol Sci 14 (6) (2013) 12222-12248.

[23] M. Buonanno, G. Randers-Pehrson, A.W. Bigelow, S. Trivedi, F.D. Lowy, H. M. Spotnitz, S.M. Hammer, D.J. Brenner, 207-nm UV light - a promising tool for safe low-cost reduction of surgical site infections. I: in vitro studies, PLoS One 8 (10) (2013), e76968.

[24] B. Ponnaiya, M. Buonanno, D. Welch, I. Shuryak, G. Randers-Pehrson, D. J. Brenner, Far-UVC light prevents MRSA infection of superficial wounds in vivo, PLoS One 13 (2) (2018), e0192053.

[25] K. Narita, K. Asano, Y. Morimoto, T. Igarashi, M.R. Hamblin, T. Dai, A. Nakane, Disinfection and healing effects of 222-nm UVC light on methicillin-resistant Staphylococcus aureus infection in mouse wounds, J Photochem Photobiol B 178 (2018) 10-18.

[26] N. Yamano, M. Kunisada, S. Kaidzu, K. Sugihara, A. Nishiaki-Sawada, H. Ohashi, A. Yoshioka, T. Igarashi, A. Ohira, M. Tanito, C. Nishigori, Long-term effects of 222-nm ultraviolet radiation C sterilizing lamps on mice susceptible to ultraviolet radiation, Photochem Photobiol 96 (4) (2020) 853-862.

[27] T. Fukui, T. Niikura, T. Oda, Y. Kumabe, H. Ohashi, M. Sasaki, T. Igarashi, M. Kunisada, N. Yamano, K. Oe, T. Matsumoto, T. Matsushita, S. Hayashi, C. Nishigori, R. Kuroda, Exploratory clinical trial on the safety and bactericidal effect of 222-nm ultraviolet C irradiation in healthy humans, PLoS One 15 (8) (2020), e0235948.

[28] D. Welch, N.J. Kleiman, P.C. Arden, C.L. Kuryla, M. Buonanno, B. Ponnaiya, X. Wu, D.J. Brenner, No evidence of induced skin Cancer or other skin abnormalities after long-term (66 week) chronic exposure to 222-nm far-UVC radiation, Photochem Photobiol 99 (1) (2023) 168-175.

[29] J.C. Goh, D. Fisher, E.C.H. Hing, L. Hanjing, Y.Y. Lin, J. Lim, O.W. Chen, L.T. Chye, Disinfection capabilities of a 222 nm wavelength ultraviolet lighting device: a pilot study, J Wound Care 30 (2) (2021) 96-104.

[30] J. Glaab, N. Lobo-Ploch, H.K. Cho, T. Filler, H. Gundlach, M. Guttmann, S. Hagedorn, S.B. Lohan, F. Mehnke, J. Schleusener, C. Sicher, L. Sulmoni, T. Wernicke, L. Wittenbecher, U. Woggon, P. Zwicker, A. Kramer, M.C. Meinke, M. Kneissl, M. Weyers, U. Winterwerber, S. Einfeldt, Skin tolerant inactivation of multiresistant pathogens using far-UVC LEDs, Sci Rep 11 (1) (2021) 14647.

[31] J. Schleusener, S.B. Lohan, L. Busch, K. Ghoreschi, N.L. Ploch, S. May, S. Vogel, J. Eberle, M.C. Meinke, Treatment of the Candida subspecies Candida albicans and Candida

parapsilosis with two far-UVC sources to minimise mycoses in clinical practice, Mycoses 66 (1) (2023) 25-28.

[32] G. Müller, A. Kramer, Biocompatibility index of antiseptic agents by parallel assessment of antimicrobial activity and cellular cytotoxicity, J Antimicrob Chemother 61 (6) (2008) 1281-1287.

[33] N. Lobo-Ploch, F. Mehnke, L. Sulmoni, H.K. Cho, M. Guttmann, J. Glaab, K. Hilbrich, T. Wernicke, S. Einfeldt, M. Kneissl, Milliwatt power 233nm AlGaN-based deep UV-LEDs on sapphire substrates, Appl Phys Lett 117 (11) (2020).

[34] P. Dong, V. Nikolaev, M. Kröger, C. Zoschke, M.E. Darvin, C. Witzel, J. Lademann, A. Patzelt, M. Schäfer-Korting, M.C. Meinke, Barrier-disrupted skin: quantitative analysis of tape and cyanoacrylate stripping efficiency by multiphoton tomography, Int J Pharm 574 (2020), 118843.

[35] S.B. Lohan, D. Ivanov, N. Schuler, B. Berger, L. Zastrow, J. Lademann, M. C. Meinke, Switching from healthy to unhealthy oxidative stress - does the radical type can be used as an indicator? Free Radic Biol Med 162 (2021) 401-411.

[36] S.B. Lohan, R. Müller, S. Albrecht, K. Mink, K. Tscherch, F. Ismaeel, J. Lademann, S. Rohn, M.C. Meinke, Free radicals induced by sunlight in different spectral regions - in vivo versus ex vivo study, Exp Dermatol 25 (5) (2016) 380-385.

[37] M.C. Meinke, L. Busch, S.B. Lohan, Wavelength, dose, skin type and skin model related radical formation in skin, Biophys Rev 13 (6) (2021) 1091-1100.

[38] D.F. Zamudio Díaz, A.L. Klein, M. Guttmann, P. Zwicker, L. Busch, M. Kröger, H. Klose, S. Rohn, J. Schleusener, M.C. Meinke, Skin optical properties from 200–300 nm support far-UVC skin safety in vivo, J Photochem Photobiol B 247 (2023) 112784.

[39] M.J. van Gemert, S.L. Jacques, H.J. Sterenborg, W.M. Star, Skin optics, IEEE Trans Biomed Eng 36 (12) (1989) 1146-1154.

[40] A.N. Bashkatov, E.A. Genina, V.V. Tuchin, Optical properties of skin, subcutaneous, and muscle tissues: a review, J Innov Opt Health Sci 04 (01) (2011) 9-38.

[41] G.S. Lazarus, D.M. Cooper, D.R. Knighton, R.E. Percoraro, G. Rodeheaver, M. C. Robson, Definitions and guidelines for assessment of wounds and evaluation of healing, Wound Repair Regen 2 (3) (1994) 165-170.

[42] M. Machado, T.M. Salgado, J. Hadgraft, M.E. Lane, The relationship between transepidermal water loss and skin permeability, Int J Pharm 384 (1-2) (2010) 73-77.

[43] D.A. Schwindt, K.P. Wilhelm, H.I. Maibach, Water diffusion characteristics of human stratum corneum at different anatomical sites in vivo, J Invest Dermatol 111 (3) (1998) 385-389.

[44] Y.N. Kalia, F. Pirot, R.H. Guy, Homogeneous transport in a heterogeneous membrane: water diffusion across human stratum corneum in vivo, Biophys J 71 (5) (1996) 2692-2700.

[45] N. Döge, A. Avetisyan, S. Hadam, E.K.B. Pfannes, F. Rancan, U. Blume-Peytavi, A. Vogt, Assessment of skin barrier function and biochemical changes of ex vivo human skin in response to physical and chemical barrier disruption, Eur J Pharm Biopharm 116 (2017) 138-148.

[46] M. Breternitz, M. Flach, J. Prassler, P. Elsner, J.W. Fluhr, Acute barrier disruption by adhesive tapes is influenced by pressure, time and anatomical location: integrity and cohesion assessed by sequential tape stripping. A randomized, controlled study, Br J Dermatol 156 (2) (2007) 231-240.

[47] J. Lademann, U. Jacobi, C. Surber, H.J. Weigmann, J.W. Fluhr, The tape stripping procedure–evaluation of some critical parameters, Eur J Pharm Biopharm 72 (2) (2009) 317-323.

[48] M. Buonanno, B. Ponnaiya, D. Welch, M. Stanislauskas, G. Randers-Pehrson, L. Smilenov, F.D. Lowy, D.M. Owens, D.J. Brenner, Germicidal efficacy and mammalian skin safety of 222-nm UV light, Radiat Res 187 (4) (2017) 483-491.

[49] K. Narita, K. Asano, Y. Morimoto, T. Igarashi, A. Nakane, Chronic irradiation with 222-nm UVC light induces neither DNA damage nor epidermal lesions in mouse skin, even at high doses, PLoS One 13 (7) (2018), e0201259.

[50] D. Welch, M. Aquino de Muro, M. Buonanno, D.J. Brenner, Wavelength-dependent DNA Photodamage in a 3-D human skin model over the far-UVC and germicidal UVC wavelength ranges from 215 to 255 nm, Photochem Photobiol 98 (5) (2022) 1167-1171.

[51] M. Spear, Wound exudate—the good, the bad, and the ugly, Plast Surg Nurs 32 (2) (2012) 77-79.

[52] T. Chambers, P. Bradley, Wound exudate, Br J Nurs 27 (20) (2018) S28-S32.

[53] K.F. Cutting, Wound exudate: composition and functions, Br J Community Nurs 8 (9 Suppl.) (2003) suppl 4-9.

[54] S.E. Cross, B.M. Magnusson, G. Winckle, Y. Anissimov, M.S. Roberts, Determination of the effect of lipophilicity on the in vitro permeability and tissue reservoir characteristics of topically applied solutes in human skin layers, J Invest Dermatol 120 (5) (2003) 759-764.

[55] Z. Nemes, P.M. Steinert, Bricks and mortar of the epidermal barrier, Exp Mol Med 31 (1) (1999) 5-19.

[56] J. Song, C.R. Shea, Benign versus malignant parakeratosis: a nuclear morphometry study, Mod Pathol 23 (6) (2010) 799-803.

[57] S.L. Walker, A.R. Young, An action spectrum (290-320 nm) for TNFalpha protein in human skin in vivo suggests that basal-layer epidermal DNA is the chromophore, Proc Natl Acad Sci USA 104 (48) (2007) 19051-19054.

[58] A. Tewari, M.M. Grage, G.I. Harrison, R. Sarkany, A.R. Young, UVA1 is skin deep: molecular and clinical implications, Photochem Photobiol Sci 12 (1) (2013) 95-103.

[59] K.P. Lawrence, G.J. Delinasios, S. Premi, A.R. Young, M.S. Cooke, Perspectives on Cyclobutane pyrimidine dimers-rise of the dark dimers, Photochem Photobiol 98 (3) (2022) 609-616.

[60] D.E. Brash, UV-induced melanin Chemiexcitation: a new mode of melanoma pathogenesis, Toxicol Pathol 44 (4) (2016) 552-554.

[61] S. Premi, S. Wallisch, C.M. Mano, A.B. Weiner, A. Bacchiocchi, K. Wakamatsu, E. J. Bechara, R. Halaban, T. Douki, D.E. Brash, Photochemistry. Chemiexcitation of melanin derivatives induces DNA photoproducts long after UV exposure, Science 347 (6224) (2015) 842-847.

[62] S. Mirpour, S. Fathollah, P. Mansouri, B. Larijani, M. Ghoranneviss, M. Mohajeri Tehrani, M.R. Amini, Cold atmospheric plasma as an effective method to treat diabetic foot ulcers: a randomized clinical trial, Sci Rep 10 (1) (2020) 10440.

[63] A. Roggan, M. Friebel, K. Doerschel, A. Hahn, G. Mueller, Optical properties of circulating human blood in the wavelength range 400-2500 nm, J Biomed Opt 4 (1) (1999) 36-46.

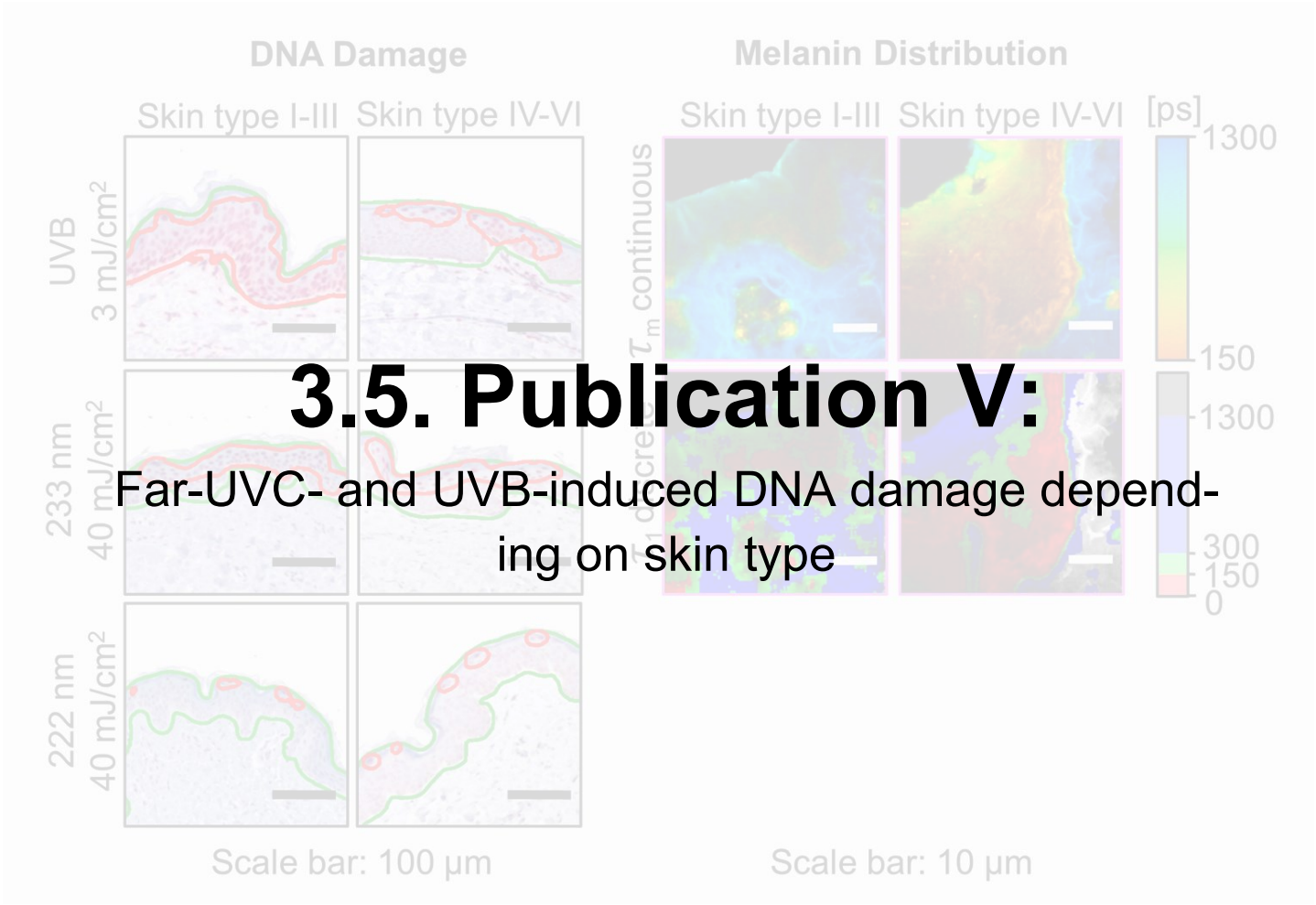

3.5. Publication V:

Far-UVC- and UVB-induced DNA damage depending on skin type

3.5. PUBLICATION V:
FAR-UVC- AND UVB-INDUCED DNA DAMAGE DEPENDING ON SKIN TYPE

Far-UVC- and UVB-induced DNA damage depending on skin type

Loris Busch [1,2,*], Marius Kröger [1,*], Daniela F. Zamudio Díaz [1,3], Johannes Schleusener [1], Silke B. Lohan [1], Jackie Ma [4], Christian Witzel [5], Cornelia M. Keck [2], Martina C. Meinke [1]

[1] *Department of Dermatology, Venereology and Allergology, Center of Experimental and Applied Cutaneous Physiology, Charité - Universitätsmedizin Berlin, Corporate Member of Freie Universität Berlin and Humboldt-Universität zu Berlin, Berlin, Germany*

[2] *Department of Pharmaceutics and Biopharmaceutics, Philipps-Universität Marburg, Marburg, Germany*

[3] *Technische Universität Berlin, Institute of Food Technology and Food Chemistry, Berlin, Germany*

[4] *Department of Artificial Intelligence, Fraunhofer Heinrich Hertz Institute, Berlin, Germany*

[5] *Division of Plastic and Reconstructive Surgery, Department of Surgery, Charité - Universitätsmedizin Berlin, Corporate Member of Freie Universität Berlin and Humboldt-Universität zu Berlin, Berlin, Germany*

[*] *contributed equally*

(adapted from: Exp Dermatol 2023;32(9):1582-1587. doi: 10.1111/exd.14902)

Abstract

Far-UVC radiation sources of wavelengths 222 nm and 233 nm represent an interesting potential alternative for the antiseptic treatment of the skin due to their high skin compatibility. Nevertheless, no studies on far-UVC-induced DNA damage in different skin types have been published to date, which this study aims for. After irradiating the skin with far-UVC of the wavelengths 222 and 233 nm as well as broadband UVB, the tissue was screened for cyclobutane pyrimidine dimer-positive (CPD^+) cells using immunohistochemistry. The epidermal DNA damage was lower in dark skin types than in fair skin types after irradiation at 233 nm. Contrary to this, irradiation at 222 nm caused no skin type-dependent differences, which can be attributed to the decreased penetration depth of radiation. UVB showed the relatively strongest differences between light and dark skin types when using a suberythemal dose of 3 mJ/cm^2. As melanin is known for its photoprotective effect, we evaluated the ratio of melanin content in the stratum basale and stratum granulosum in samples of different skin types using two-photon excited fluorescence lifetime imaging (TPE-FLIM) finding a higher ratio up to skin type IV–V. As far-UVC is known to penetrate only into the upper layers of the viable skin, the aforementioned melanin ratio could explain the less pronounced differences between skin types after irradiation with far-UVC compared to UVB.

1. Background

Following the increased interests in room disinfection and skin antisepsis during the COVID-19 pandemic, studies have been conducted to prove the bactericidal [1-6] and virucidal [7-9] potential of far-UVC radiation (100–240 nm). UVC radiation (100–280 nm) is known to be absorbed by nucleic acids and proteins. As a result of photo-induced pyrimidine dimerisation, DNA lesions including cyclobutane pyrimidine dimers (CPDs) and pyrimidine (6-4) pyrimidone photoproducts (6-4PPs) are formed in microorganisms [10] and epidermal cells [11] with a generally higher abundance of CPDs [2, 12]. Thus, far-UVC radiation can potentially be used for disinfection purposes, for example, in hospitals, but also has to be assessed regarding its potential risks for human health. Interestingly, it was shown that far-UVC radiation of 222 and 233 nm produces less DNA damage in skin than UVC radiation of 254 nm, which is often used for the disinfection of surfaces or water, but still shows bactericidal effects [2, 3, 6]. However, to date, only studies on skin type-dependent protection against DNA damage after irradiation with simulated solar UV radiation have been performed on skin [13, 17], but no investigations have yet been conducted on skin type-dependent protection against far-UVC.
In the present study, we correlated measurements of the absorptiometrically measured melanin index (MI) and histological assessments of irradiated skin thin sections with the two-photon excited fluorescence lifetime imaging (TPE-FLIM) visualisation of the distribution of melanin in the epidermis of non-irradiated skin thin sections and a semantic machine learning model revealing the distribution of DNA damage in the epidermis.

1.1. Questions addressed

Does the radiation-related formation and localisation of DNA damage in different skin types depend on the applied wavelength of UV light?

1.2. Experimental design

See: Supplemental information.

2. Results

For the visualisation of melanin distribution in human skin, cryohistological thin sections of $n = 13$ resected skin samples of Fitzpatrick's skin type I–VI were evaluated. Sections were imaged using TPE-FLIM [18, 19]. The melanin distribution in the epidermis can be assessed using TPE-FLIM via the mean lifetime τ_m, where melanin is a significant contributor of very

short fluorescence lifetimes. The mean fluorescence lifetime τ_m is defined as the weighted average of the lifetime components τ_1 (short lifetime component) and τ_2 (long lifetime component) in each pixel of the image and their respective amplitudes a_1 and a_2 described as,

$$\tau_m = \frac{a_1 \tau_1 + a_2 \tau_2}{a_1 + a_2} \quad (1)$$

τ_m was measured along the stratum basale (SB) and along the upper stratum granulosum (SG). From this, the ratio of τ_m of SG/τ_m of SB was calculated to represent the epidermal melanin gradient.

The mean lifetime τ_m measured in the skin is significantly influenced by the strikingly short lifetime of melanin [20, 21]. As a result, short lifetimes in the skin sections correlate with a high melanin concentration in the skin. As a first step, the MI of the skin samples was determined in order to obtain a quantifiable indication of the general melanin content of the respective skin type. The mean lifetime of the SB was then correlated with the previously measured MI of the skin. **Figure 1A** shows a corresponding exponentially decreasing fluorescence lifetime with increasing amount of melanin. The dependence of fluorescence lifetime and MI could be fitted using an exponential decay function with $a = 183{,}11$; $b = 33.54$ and an adjusted $R^2 = 0.71$ described as,

$$FIT_{\tau_{mSB}} = e^{\frac{a}{MI+b}} \quad (2)$$

Interestingly, the distinction between relatively dark skin types is more difficult, as the short lifetime of melanin approximates the detection limit of time-correlated single-photon counting (instrument response function) between 80 and 100 ps [22]. Thus, the curve flattens out towards higher MI values because of the high sensitivity of TPE-FLIM to the high fluorescence of melanin. As presented in **Figure 1B**, the mean lifetime in the SG of light skin types decreases comparatively less as compared to the SB with an inverse linear correlation with an adjusted $R^2 = 0.93$, intercept $n = 1111.11 \pm 10.04$ and slope $m = -0.89 \pm 0.02$ described as,

$$FIT_{\tau_{mSG}} = n + (m\ MI) \quad (3)$$

Resulting from this, the ratio of the mean lifetime in the SG and SB, representing the melanin gradient of the skin from basal to corneal, increases with the MI, indicating a stronger melanin gradient in darker skins (**Figure 1C**). Interestingly, the skin with a MI of 998 has a lower ratio of the mean lifetime in the SG and SB, presumably due to a saturation of basal melanin, where

only the increase of melanin in SG can be detected. However, this effect should be further investigated in future studies to provide an improved representation of the relationship between the two variables.

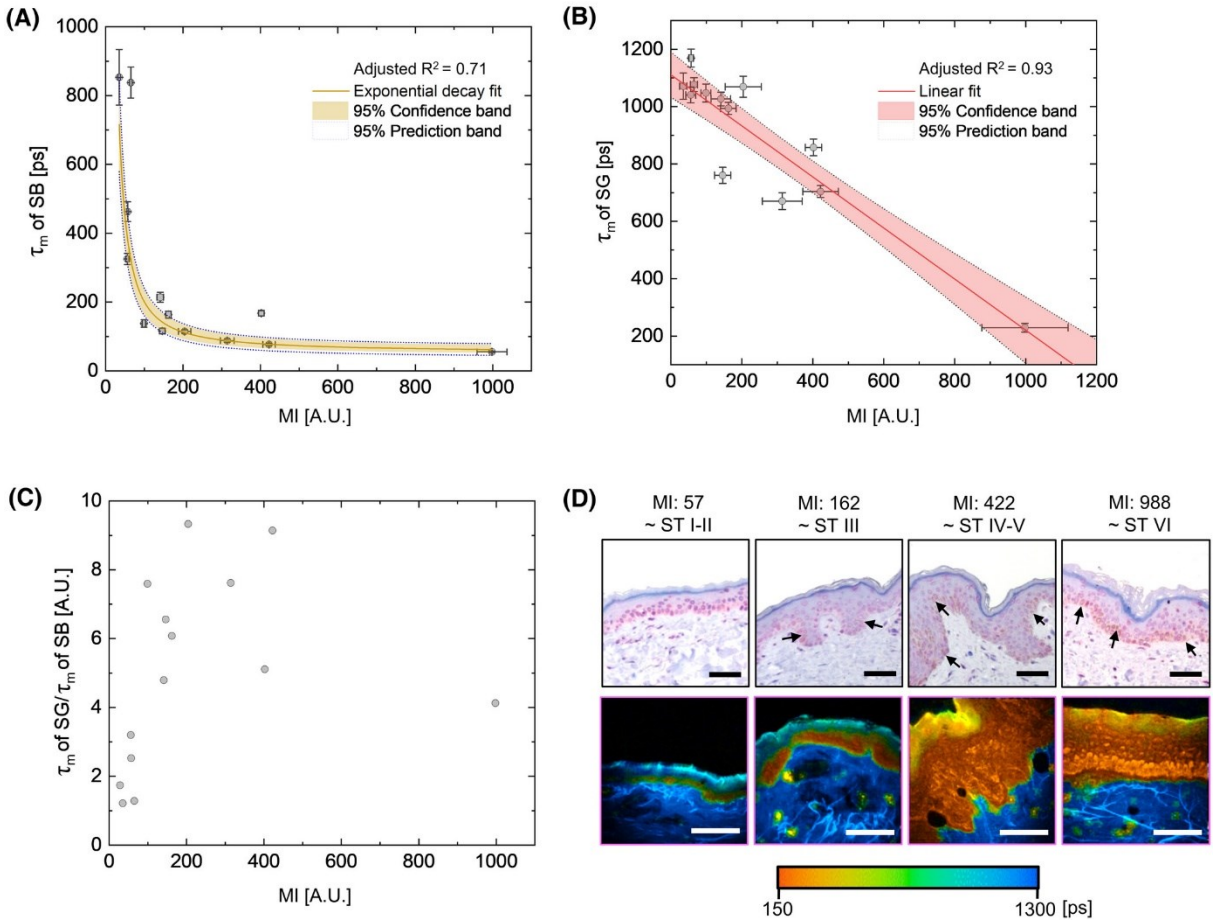

Figure 1: (**A**): Inverse correlation of the mean fluorescence lifetime τ_m of the stratum basale (SB) and melanin index (MI) fitted by an exponential decay function (golden line) with an adjusted R^2 of 0.71 including the 95% confidence band (golden area) as well as 95% prediction band (dotted line). (**B**): Correlation of the mean fluorescence lifetime τ_m of the stratum granulosum (SG) and MI fitted by an inverse linear function (red line) with an adjusted R^2 of 0.93 including the 95% confidence band (red area) as well as 95% prediction band (dotted line). (**C**): Representation of the ratio of mean fluorescence lifetime τ_m of the SG and SB in dependence of the MI. Data of $n = 13$ *ex vivo* skin samples. (**D**): Illustration of histological sections with immunohistological CPD^+ staining representative for the different skin types (upper row, arrows were used to mark the basal melanin) as well as unstained cryohistological TPE-FLIM images with representation of the mean fluorescence lifetime τ_m visualised in false colours for lifetimes between 150 ps (orange) and 1300 ps (blue) (lower row). Scale bars are corresponding to 50 µm.

Representative histological sections (CPD^+ staining and unstained TPE-FLIM images) are depicted in **Figure 1D** to show the melanin content and distribution in the different skin types.

In parallel, we irradiated the human skin resected at least 24 h after surgery with 10% of a minimum erythema dose (MED) (3 mJ/cm^2) with a broadband UVB lamp, with a 233 nm LED and a 222 nm excimer lamp with a microbiocidal dose (40 mJ/cm^2) [2, 23] and evaluated the

abundance of CPD-positive (CPD^+) cells immunohistologically [13, 17]. The individual doses were chosen based on a publication by Zwicker et al. [2], who demonstrated that after irradiation with UVB at 10% of a MED (Fitzpatrick skin type II), CPD^+ cells are highly abundant in light skin types. To avoid a possible saturation effect on CPD^+ abundance after irradiation with UVB in light skin types and to ensure comparability between light and dark skin types, we decided not to increase the dose and to compare it with microbiocidal doses of far-UVC. The far-UVC doses applied (40 mJ/cm^2) were also within the sub-erythemal range, as shown in recent publications by Eadie et al. [24] and Zamudio Díaz et al. [12].

Furthermore, the area score of CPD^+ cells representative for the distribution of DNA damage in the epidermis was calculated using a semantic machine learning model as previously described elsewhere [25]. The area score S_{area} was calculated as the ratio of the area of the epidermis and the area of semantic segmentation maps of damaged cells in the epidermis.

It is noticeable that after irradiation with 10% MED UVB, skin type I–III showed an increased abundance of CPD^+ cells by a factor of two as compared to skin type IV–VI (**Figure 2A**, $p < 0.05$). This difference is also evident for 233 nm 40 mJ/cm^2, while no differences were observed for 222 nm 40 mJ/cm^2. This could be related to the fact that the penetration depth of UVB is known to be higher than that of far-UVC [2, 12, 26]. Furthermore, it is known that the penetration depth of 233 nm is slightly increased compared to 222 nm [2]. Dark skin types have a higher melanin content than light skin types, especially in the SB, while the differences in the SG between skin types are smaller as already presented. As UVB penetrates the entire epidermis, skin types IV–VI show increased protection. Due to the fact that 222 nm penetrates the skin only superficially and the difference in melanin content between light and dark skin types is comparatively smaller in this area, the abundance of CPD^+ cells in the skin showed no significant differences between the skin types.

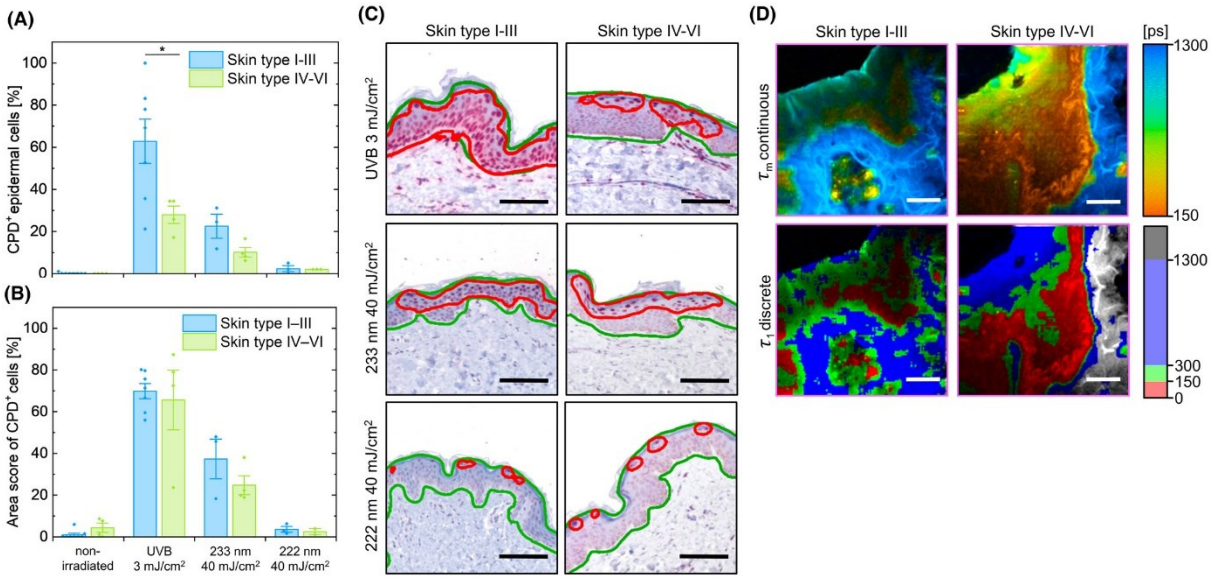

Figure 2: Representation of the abundance (**A**) as well as area score (**B**) of CPD⁺ epidermal cells for Fitzpatrick's skin types I–III (blue columns) and IV–VI (green columns) for irradiation with UVB 3 mJ/cm², 233 nm 40 mJ/cm² and 222 nm 40 mJ/cm² with corresponding representative images showing the damaged area labelled with a red line relative to the total epidermal area labelled with a green line (**C**). (**D**) shows TPE-FLIM images with the epidermal distribution of the mean fluorescence lifetime τ_m visualised continuously in false colours for lifetimes between 150 ps (orange) and 1300 ps (blue) as well as the fluorescence lifetime τ_1 shown for discrete sections in false colours with 0–150 ps (red), 150–300 ps (green) and 300–1300 ps (blue). The images show that the calculated ratio of τ_m of SG/τ_m of SB is representative for a melanin gradient in the skin. Asterisks showing statistical significance with * = $p < 0.05$ based on a two-tailed Mann–Whitney U test. Data of $n = 3–7$ *ex vivo* skin samples. Scale bars are corresponding to 100 µm (**C**) and 10 µm (**D**).

Using the area score, which is suitable for mapping the depth of damage, the differences in damage for UVB and 233 nm were less pronounced between light and dark skin types (**Figure 2B**). However, we found (partially) intact basal layers in two of the four dark skin sections evaluated after irradiation with UVB (Example **Figure 2C**), while the other two skin sections showed evenly distributed lesional areas. On the other hand, the light skin counter parts showed CPD⁺ cells in the whole epidermis. This might be an indication for a photoprotective effect of melanin in the basal layer. The insignificant difference could be due to the fact that the machine learning model is not yet trained for dark skin sections and that melanin darkens the skin in the area of the basal layer even in the absence of special stains for labelling melanin, such as the Fontana-Masson stain, and can thus cause false-positive results in the machine learning model. Additionally, the depth of the epidermis is locally different in the skin, resulting in varying SG/SB thicknesses and heterogeneous photoprotective effects (Example **Figure 2C**). Furthermore, the intradonor distribution of melanin along the basal layer can be heterogeneous and thus lead to varying amounts of CPD⁺ cells which requires the analysis of entire thin sections.

Fayujigbe et al. succeeded in visualising the differences in the degree of damage in different sections of the skin in different skin types [13, 15] showing a protection of the stem cells in dark skin types, which is attributable to the photoprotective effect of melanin [27, 28]. Here, fluorescence staining was used, which allows a broader range of detection of CPD^+ cells. Furthermore, it should be considered that this is a pilot study with a relatively small sample size, which was conducted *ex vivo*.

In the far-UVC range, differences in area were still evident for 233 nm as the damage extended to approximately the middle of the epidermis (**Figure 2C**), where the difference between light and dark skin types in terms of melanin content is greater than in the upper region of the epidermis (exemplary graphics of FLIM parameters τ_m and τ_1 are presented in **Figure 2D**). Here, the depth of DNA lesions is slightly shallower for dark skin, as compared to light skin (**Figure 2C**).

After irradiation with 222 nm, differences between skin types were no longer evident, although an evaluation basis was still present with 15–20 positive nuclei directly below the stratum corneum per donor evaluated.

3. Conclusions and perspectives

The effects of far-UVC radiation on different skin types were evaluated for the first time in the presented pilot study. The findings give an indication that far-UVC radiation has a different effect than UVB light on different skin types. Far-UVC radiation produced less pronounced differences in DNA damage in light and dark skin types compared to UVB radiation which can be attributed to the localisation and concentration of melanin in the skin. Furthermore, it was demonstrated that differences in DNA damage between light and dark skin types might result from the different penetration depths of 222 and 233 nm far-UVC radiation. However, to confirm the hypotheses, future studies will need to look more closely at larger samples and also conduct *in vivo* studies. The results are important for the future application of far-UVC systems for skin decolonisation.

References

[1] J. Glaab, N. Lobo-Ploch, H.K. Cho, T. Filler, H. Gundlach, M. Guttmann, S. Hagedorn, S.B. Lohan, F. Mehnke, J. Schleusener, C. Sicher, L. Sulmoni, T. Wernicke, L. Wittenbecher, U. Woggon, P. Zwicker, A. Kramer, M.C. Meinke, M. Kneissl, M. Weyers, U. Winterwerber, S. Einfeldt, Skin tolerant inactivation of multiresistant pathogens using far-UVC LEDs, Sci Rep 11(1) (2021) 14647.

[2] P. Zwicker, J. Schleusener, S.B. Lohan, L. Busch, C. Sicher, S. Einfeldt, M. Kneissl, A.A. Kuhl, C.M. Keck, C. Witzel, A. Kramer, M.C. Meinke, Application of 233 nm far-UVC LEDs for eradication of MRSA and MSSA and risk assessment on skin models, Sci Rep 12(1) (2022) 2587.

[3] K. Narita, K. Asano, Y. Morimoto, T. Igarashi, M.R. Hamblin, T. Dai, A. Nakane, Disinfection and healing effects of 222-nm UVC light on methicillin-resistant Staphylococcus aureus infection in mouse wounds, J Photochem Photobiol B 178 (2018) 10-18.

[4] J.C. Goh, D. Fisher, E.C.H. Hing, L. Hanjing, Y.Y. Lin, J. Lim, O.W. Chen, L.T. Chye, Disinfection capabilities of a 222 nm wavelength ultraviolet lighting device: a pilot study, J Wound Care 30(2) (2021) 96-104.

[5] M. Buonanno, B. Ponnaiya, D. Welch, M. Stanislauskas, G. Randers-Pehrson, L. Smilenov, F.D. Lowy, D.M. Owens, D.J. Brenner, Germicidal Efficacy and Mammalian Skin Safety of 222-nm UV Light, Radiat Res 187(4) (2017) 483-491.

[6] B. Ponnaiya, M. Buonanno, D. Welch, I. Shuryak, G. Randers-Pehrson, D.J. Brenner, Far-UVC light prevents MRSA infection of superficial wounds in vivo, PLoS One 13(2) (2018) e0192053.

[7] D.J. Brenner, Far-UVC Light at 222 nm is Showing Significant Potential to Safely and Efficiently Inactivate Airborne Pathogens in Occupied Indoor Locations, Photochem Photobiol 99(3) (2022) 1047-1050.

[8] E. Eadie, W. Hiwar, L. Fletcher, E. Tidswell, P. O'Mahoney, M. Buonanno, D. Welch, C.S. Adamson, D.J. Brenner, C. Noakes, K. Wood, Far-UVC (222 nm) efficiently inactivates an airborne pathogen in a room-sized chamber, Sci Rep 12(1) (2022) 4373.

[9] M. Buonanno, D. Welch, I. Shuryak, D.J. Brenner, Far-UVC light (222 nm) efficiently and safely inactivates airborne human coronaviruses, Sci Rep 10(1) (2020) 10285.

[10] T. Dai, M.S. Vrahas, C.K. Murray, M.R. Hamblin, Ultraviolet C irradiation: an alternative antimicrobial approach to localized infections?, Expert Rev Anti Infect Ther 10(2) (2012) 185-95.

[11] J. D'Orazio, S. Jarrett, A. Amaro-Ortiz, T. Scott, UV radiation and the skin, Int J Mol Sci 14(6) (2013) 12222-12248.

[12] D.F. Zamudio Díaz, A.L. Klein, M. Guttmann, P. Zwicker, L. Busch, M. Kröger, H. Klose, S. Rohn, J. Schleusener, M.C. Meinke, Skin optical properties from 200–300 nm support far-UVC skin safety in vivo, J Photochem Photobiol B 247 (2023) 112784.

[13] D. Fajuyigbe, S.M. Lwin, B.L. Diffey, R. Baker, D.J. Tobin, R.P.E. Sarkany, A.R. Young, Melanin distribution in human epidermis affords localized protection against DNA photodamage and concurs with skin cancer incidence difference in extreme phototypes, FASEB J 32(7) (2018) 3700-3706.

[14] D. Fajuyigbe, A.R. Young, The impact of skin colour on human photobiological responses, Pigment Cell Melanoma Res 29(6) (2016) 607-618.

[15] D. Fajuyigbe, T. Douki, A. van Dijk, R.P.E. Sarkany, A.R. Young, Dark cyclobutane pyrimidine dimers are formed in the epidermis of Fitzpatrick skin types I/II and VI in vivo after exposure to solar-simulated radiation, Pigment Cell Melanoma Res 34(3) (2021) 575-584.

[16] Y. Yamaguchi, K. Takahashi, B.Z. Zmudzka, A. Kornhauser, S.A. Miller, T. Tadokoro, W. Berens, J.Z. Beer, V.J. Hearing, Human skin responses to UV radiation: pigment in the upper epidermis protects against DNA damage in the lower epidermis and facilitates apoptosis, FASEB J 20(9) (2006) 1486-1488.

[17] S. Del Bino, J. Sok, E. Bessac, F. Bernerd, Relationship between skin response to ultraviolet exposure and skin color type, Pigment Cell Res 19(6) (2006) 606-614.

[18] M. Kröger, J. Scheffel, V.V. Nikolaev, E.A. Shirshin, F. Siebenhaar, J. Schleusener, J. Lademann, M. Maurer, M.E. Darvin, In vivo non-invasive staining-free visualization of dermal mast cells in healthy, allergy and mastocytosis humans using two-photon fluorescence lifetime imaging, Sci Rep 10(1) (2020) 14930.

[19] M. Kröger, J. Scheffel, E.A. Shirshin, J. Schleusener, M.C. Meinke, J. Lademann, M. Maurer, M.E. Darvin, Label-free imaging of M1 and M2 macrophage phenotypes in the human dermis in vivo using two-photon excited FLIM, Elife 11 (2022) e72819.

[20] A.-M. Pena, E. Decencière, S. Brizion, P. Sextius, S. Koudoro, T. Baldeweck, E. Tancrède-Bohin, In vivo melanin 3D quantification and z-epidermal distribution by multiphoton FLIM, phasor and Pseudo-FLIM analyses, Sci Rep 12(1) (2022) 1642.

[21] Y. Dancik, A. Favre, C.J. Loy, A.V. Zvyagin, M.S. Roberts, Use of multiphoton tomography and fluorescence lifetime imaging to investigate skin pigmentation in vivo, J Biomed Opt 18(2) (2013) 26022.

[22] M. Kröger, J. Schleusener, J. Lademann, M.C. Meinke, S. Jung, M.E. Darvin, Tattoo pigments are localized intracellularly in the epidermis and dermis of fresh and old tattoos - in vivo study using two-photon excited FLIM, Dermatology 239(3) (2023) 478-493.

[23] J. Schleusener, S.B. Lohan, L. Busch, K. Ghoreschi, N.L. Ploch, S. May, S. Vogel, J. Eberle, M.C. Meinke, Treatment of the Candida subspecies Candida albicans and Candida parapsilosis with two far-UVC sources to minimise mycoses in clinical practice, Mycoses 66(1) (2023) 25-28.

[24] E. Eadie, I.M.R. Barnard, S.H. Ibbotson, K. Wood, Extreme Exposure to Filtered Far-UVC: A Case Study, Photochem Photobiol 97(3) (2021) 527-531.

[25] P. Wagner, M. Springenberg, M. Kröger, R.K.C. Moritz, J. Schleusener, M.C. Meinke, J. Ma, Semantic modeling of cell damage prediction: a machine learning approach at human-level performance in dermatology, Sci Rep 13(1) (2023) 8336.

[26] L. Busch, M. Kröger, J. Schleusener, A.L. Klein, S.B. Lohan, M. Guttmann, C.M. Keck, M.C. Meinke, Evaluation of DNA lesions and radicals generated by a 233 nm far-UVC LED in ex vivo skin wounds J Photochem Photobiol B 245 (2023) 112757.

[27] S. Del Bino, J. Sok, F. Bernerd, Assessment of ultraviolet-radiation-induced DNA damage within melanocytes in skin of different constitutive pigmentation, Br J Dermatol 168(5) (2013) 1120-1123.

[28] M. Brenner, V.J. Hearing, The protective role of melanin against UV damage in human skin, Photochem Photobiol 84(3) (2008) 539-549.

Supplemental Information: Experimental Design

Excised human skin samples

Excised human abdominal and mammal skin samples of *n* = 13 donors (Fitzpatrick skin types I–VI) were obtained from the Division of Plastic and Reconstructive Surgery, Department of Surgery, Charité – Universitätsmedizin Berlin. The experimental protocols were approved by the Ethics Committee of the Charité – Universitätsmedizin Berlin (EA1/324/19). Informed written consent was obtained from the skin donors and all procedures complied with the Declaration of Helsinki. The preparation procedure of the skin samples was described elsewhere [1].

Measurements of melanin index

The melanin index (MI) was measured absorptiometrically using a Mexameter® MX 18 (absorption wavelengths: 660 nm and 880 nm, Courage + Khazaka electronic GmbH, Cologne, Germany) with *n* = 10 measurement points per sample on *n* = 13 resected skin samples resulting in a value range from MI=35 ± 3.2 to 998 ± 38.5 (mean value±standard error of the mean).

Fluorescence life time measurements on cryohistological skin sections

8 mm punch biopsies of the skin samples were stored at -20 °C and vertical cryohistological sections of 30 µm thickness were obtained using a cryotome (Microm Cryo-Star HM 560, MICROM International GmbH, Walldorf, Germany) after embedding the skin biopsies in a cryomedium (Tissue Freezing Medium, Leica Biosystems Richmond Inc., Richmond, IL, USA).
A cryohistological section from the center of the biopsy was prepared for each skin sample. The mean fluorescence life time τ_m of each section (*n* = 13) was then investigated using two-photon excited fluorescence lifetime imaging (TPE-FLIM) [2, 3]. Images (*n* = 7–10 per sample) were acquired with a two-photon microscope (DermaInspect, JenLab, Jena, Germany) equipped with a tunable femtosecond Ti:sapphire laser (Mai Tai XF, Spectra Physics, USA). The laser was operated at a power of 3 mW and the excitation wavelength was set to 760 nm. FLIM images were evaluated for τ_m on *n* = 50 spots per donor using SPCImage software version 8.4 (Becker & Hickl, Berlin, Germany) assuming a bi-exponential decay and a binning value of 3 (averaged lifetime value for 48 adjacent pixels).

Irradiation procedure

Ex vivo human skin samples of *n* = 11 donors (Skin types I–III: *n* = 7 with a MI ranging from 35 ± 3.2 to 162 ± 6.9; skin types IV–VI: *n* = 4, MI from 314 ± 17.7 to 998 ± 38.5) were irradiated with a UVB hand lamp containing a small proportion of UVA (3 mJ/cm^2, 0.04 mW/cm^2, 280–400 nm, TH-1E, Cosmedico Medizintechnik, Stuttgart, Germany), a 233 nm far-UVC LED (40 mJ/cm^2, 0.13 mW/cm^2, Ferdinand-Braun-Institut, Berlin, Germany) and a 222 nm Kr-Cl excimer lamp (40 mJ/cm^2, 0.31 mW/cm^2, ExciJet222 30–130 Kit (111073), USHIO Deutschland GmbH, Steinhöring, Germany). Additional technical information can be found in [1].

Immunohistological stainings of human skin sections and evaluation for CPD$^+$ cells

4 mm punch biopsies were taken after the irradiation procedure and the skin samples were analyzed for the abundance of cyclobutane pyrimidine dimer-positive (CPD$^+$) cells immunohistologically on 1–2 µm paraffin sections as previously described by Zwicker et al. [1]. Only skin samples showing a homogeneous horizontal distribution of CPD$^+$ cells were included in the evaluation.

Machine learning-based determination of the area score of CPD$^+$ cells

A semantic model for the prediction of CPD$^+$ cells in the epidermis of immunohistological sections was used, as previously described elsewhere [4]. For data augmentation the epidermis was additionally masked with a separate segmentation model based on the U-Net/64 convolutional network typically used in biomedical image segmentation. This ensures that only information from the epidermis was considered. For all models a fourfold cross validation was performed.

The area score S_{area} was calculated as the ratio of the area of the epidermis and the area of semantic segmentation maps of damaged cells in the epidermis. For the segmentation U-Net was used, where the filter size was not changed and a sliding window approach was chosen. All images are down sampled by a factor of two. U-Net/64 with a base feature dimension of 64 yielded the best results for the application. U-Net was trained for 50 epochs with 100 steps per epoch. Only skin samples showing a homogeneous horizontal distribution of CPD$^+$ cells on the upper viable epidermis were included in the evaluation.

Statistical analysis, data visualization and curve fitting

For all data sets the mean value ± standard error of the mean (SEM) was calculated. Statistical tests were performed with IBM SPSS® Statistics 28 (IBM, Armonk, NY, USA). The normal distribution of the data sets was checked with the Shapiro–Wilk test. Two-tailed Mann–Whitney–U tests were executed for mean value comparison affording a significance of $p < 0.05$. Data visualization as well as curve fittings using exponential and linear decay functions were carried out using OriginPro 2020 (Origin, OriginLab Corporation, Northampton, MA, USA).

Additional References

[1] P. Zwicker, J. Schleusener, S.B. Lohan, L. Busch, C. Sicher, S. Einfeldt, M. Kneissl, A.A. Kuhl, C.M. Keck, C. Witzel, A. Kramer, M.C. Meinke, Application of 233 nm far-UVC LEDs for eradication of MRSA and MSSA and risk assessment on skin models, Sci Rep 12(1) (2022) 2587.

[2] M. Kröger, J. Scheffel, V.V. Nikolaev, E.A. Shirshin, F. Siebenhaar, J. Schleusener, J. Lademann, M. Maurer, M.E. Darvin, In vivo non-invasive staining-free visualization of dermal mast cells in healthy, allergy and mastocytosis humans using two-photon fluorescence lifetime imaging, Sci Rep 10(1) (2020) 14930.

[3] M. Kröger, J. Scheffel, E.A. Shirshin, J. Schleusener, M.C. Meinke, J. Lademann, M. Maurer, M.E. Darvin, Label-free imaging of M1 and M2 macrophage phenotypes in the human dermis in vivo using two-photon excited FLIM, Elife 11 (2022) e72819.

[4] P. Wagner, M. Springenberg, M. Kröger, R.K.C. Moritz, J. Schleusener, M.C. Meinke, J. Ma, Semantic modeling of cell damage prediction: a machine learning approach at human-level performance in dermatology, Sci Rep 13(1) (2023) 8336.

4. Discussion

Based on the health care burden caused by surgical site infections (SSI) [1] as well as the rising prevalence of multi-drug resistant bacteria [2] this cumulative work aimed at the implementation of two novel and innovative approaches for an advanced skin antisepsis.
Hair follicles are known to represent a densely colonized reservoir of pathogens with a total contribution of 25% of the skin microbiome [3]. During prolonged surgical procedures, recolonization of the skin surface can therefore occur from this reservoir [4, 5]. From there, potential pathogens can be transmitted into the surgical field. It is known that SSI are caused by endogenous germs in 90% of all cases [6]. Building on this knowledge, the first part of this dissertation aimed at the application of a pharmaceutical-based approach for advanced skin decontamination.

It is known that nanoparticles of a specific size range penetrate deeply into the hair follicles [7]. This effect is absent when free substances are used, which means that colonization of the deep areas of the hair follicles persists after the application of conventional antiseptics and an intraoperative recolonization of the skin, and thus the surgical site, may occur [4]. Therefore, delivery of antiseptics to deeper areas of hair follicles for targeted eradication of the local skin microbiome could be achieved by using nanocapsules (NCs).
For targeted and rapid release of the antiseptic contained in the NCs, UVA was an obvious choice due to its accessibility to the dermal portions of the skin. This approach was pursued using ultraviolet A (UVA)-emitting light emitting diode (LED) systems as well as polyurethane (PU)- and hydroxy ethyl starch (HES)-NCs in **publications I and II**. While in **publication I** mainly the principles of follicular drug delivery were pursued, **publication II** also included an efficacy study.

Complementary or alternatively to this, far-UVC light (UVC below 240 nm wavelength) is a promising approach for skin surface decontamination. Far-UVC radiation has the advantage of inactivating pathogens through the immediate generation of DNA lesions due to its relatively high energy [8]. Considering the nonspecific nature of radiation, it may be possible to circumvent the potential formation of resistance or cross-resistance and still achieve significant decontamination of the skin surface, surgical wounds or complex chronic wounds [9]. In addition, it can be easily and quickly used repetitively in various scenarios, such as prolonged surgical procedures, to decontaminate recolonized skin areas and prevent the development of SSI. The penetration of far-UVC photons into the viable epidermis is limited due to strong absorption

in the stratum corneum. However, since the far-UVC radiation emitted by innovative LED systems with a wavelength of 233 nm is a novelty, a risk assessment of these systems is essential to ensure the safety of the operating personnel as well as the patient.
In **publications III, IV and V**, a comprehensive risk assessment of 233 nm far-UVC radiation was carried out on intact *ex vivo* human skin of different skin types, on artificially wounded *ex vivo* skin, and on 3D epidermal skin models regarding the formation of DNA lesions. Microbiocidal doses were applied as previously determined by the project partners of the University Medicine Greifswald (first part of **publication III**).

4.1. Deep antisepsis of the skin by NC-based hair follicle targeting

4.1.1. Hair follicle targeting with PU-NCs: drug delivery principles

In the first publication of this thesis, the principle of follicular penetration as well as intrafollicular UVA-triggered drug release was demonstrated using an *ex vivo* porcine skin model. In this principal study, PU-NCs (approximately 700 nm in size) containing the photo-responsive *o*-nitrobenzyl derivative nitro xylylene glycol (NXG) were used in combination with a commercially available UVA-LED emitting at a peak wavelength of 365 nm. The main part of this study focused on the drug delivery principles to gain insight of the doses that are required to induce intrafollicular drug release when applying UVA radiation on skin.
Prior to this publication, several nanoparticulate systems for intrafollicular drug release were already known. These included, for example, systems that were responsive to infrared (IR) light [10], pH [11, 12] and proteases [13, 14] or showed drug release based on concentration gradients [15, 16] achieving follicular penetration depths between 400 µm and > 800 µm. An advantage of the application of UVA light is not only the external controllability (as compared to pH or concentration gradients) but also temperature independence (as compared to IR).

The release kinetics of PU-NCs in response to the UVA dose were recorded in a first step. With an average irradiance of 12 mW/cm^2 at a wavelength of 365 nm, a drug release of over 50% after 2 min could be reached *in vitro* as indicated by a loss of fluorescence intensity. In a second step, this system was translated to an *ex vivo* porcine skin model. Here, the follicular penetration depth and the intrafollicular drug release of the model drug sulforhodamine 101 (SR101) was evaluated on cryohistological sections using confocal laser scanning microscopy (CLSM). Based on the results of a preliminary experiment, isophorone diisocyante based polyurethane NCs (IPDI-PU-NCs) were selected for the *ex vivo* main experiment. According to

Kramer et al. a considerable proportion of skin pathogens are localized within both the infundibulum and the excretory ducts of the sebaceous glands with a proportion of 80% colonizing the upper 300 µm [17]. UVA-responsive degradation of the NCs at a mean follicular penetration depth of 509 ± 104 µm led to a tempo-spatial controlled release of SR101. This was indicated by a loss of fluorescence intensity of approximately 50% after 8 min of irradiation with 12 mW/cm^2 which corresponded to the previously recorded *in vitro* release kinetics.

Various stimuli-responsive polyurethane NPs are known for their high biocompatibility and low cytotoxicity [18-23]. An advantage of the crosslinker toluene diisocyanate (TDI) used in the synthesis is its high reactivity as a crosslinker [24, 25], which is necessary for the carbamate reaction-based formation of polyurethane shells at the droplet interfaces between water and the apolar continuous phase. This is based on the fact that the benzene ring in aromatic diisocyanates acts as an electron-withdrawing group resulting in delocalization of negative charge in the π ring system. This results in enhancing the positive charge of the isocyanate carbon, which promotes the nucleophilic addition reaction by the oxygen in the alcoholic group of the glycolic reactants [26]. Furthermore, the cycloaliphatic alternative IPDI underlies a steric hindrance due to three methyl groups slowing down the reaction kinetics of this crosslinker [26]. However, using TDI as a crosslinker for shell formation could also promote cytotoxicity following the photodegradative process. Cell viability experiments on HaCaT cells revealed that NCs synthesized with the crosslinker IPDI show a sufficient biocompatibility even after UVA-induced degradation of the capsules, while a drop of cell viability was observed when exposing HaCaT cells to photodegraded PU-NCs containing TDI. This phenomenon was in consistency with previous publications [27-30] since aromatic diisocyanites are known to be more cell-toxic as compared to (cyclo-)aliphatic diisocyanates. Intrafollicular persistence of 10 days is generally expected for NCs [7]. Clearance occurs automatically via sebum flow. Nevertheless, it must also be noted that NCs or their fragments can potentially enter the wound during surgical procedures and thus may be able to enter the bloodstream. There, clearance is accomplished through phagocytosis by macrophages [31] . A limitation of the study is that potential systemic toxicological effects were not evaluated in an animal model. Nevertheless, it is known that PU-NCs in the submicron size range are produced for systemic application as a carrier material for contrast agents, for example [32, 33].

On the other hand, no detrimental effects are to be expected from the UVA radiation side. Since the applied dose was below the irradiation limits for actinic damage according to the

International Commission on Non-Ionizing Radiation Protection (ICNIRP), the LED system could be applied without risking radiation-related tissue damage.

One disadvantage of the present publication is that the follicular penetration of the particles and the release of the model drug were tested only in the original vehicle cyclohexane required for particle synthesis. This is because the phase transfer of the nanoparticles to more polar phases, as usual for antiseptic agents, was difficult to implement. On the other hand, the apolar cyclohexane was found to be beneficial for tracking the release mechanisms, as the model drug SR101 was highly responsive to the polarity of the environment in terms of its fluorescence properties.
In summary, this model system represents a first approach for anatomically and temporally targeted intrafollicular drug release by UVA light.

4.1.2. Hair follicle decontamination with HES-NCs

Previous studies showed that skin decolonization can be improved by encapsulation of antiseptics into nanoparticulate drug delivery systems [34-37]. Thus, the approach presented in **publication I** had to be refined for the translation into clinical practice with application in preoperative skin antisepsis, which was pursued in **publication II** using HES-NCs.
In this publication a UVA LED radiation source (peak emission wavelength of 365 nm) developed within the project was used, which is suitable for the application in preoperative antisepsis. This LED system was applied with an increased irradiance (~ 200 mW/cm^2) of approximately factor 17 as compared to **publication I**.
In this context, the irradiation time could be reduced to 1 min, which is of considerable advantage for preoperative application. However, the dose was still below the ICNIRP limits for actinic damage and below the threshold of 50% MED that causes irreversible lipid oxygen species in the skin according to Lohan et al. [38]. After further evaluation of follicular penetration of the HES-NCs as well as intrafollicular drug release using the model drug SR101, the antiseptic performance of the system was tested on *ex vivo* porcine skin to get closer to a possible translation to a preoperative application.
The photosensitivity of this system again relied on the presence of the *o*-nitrobenzyl group NXG in the NCs shell using the crosslinker TDI. By using HES to manufacture the NCs, the biocompatibility was aimed to be increased.

In order to get one step closer to the implementation of the system in clinical applications, phase transfer studies in PBS as well as 80% ethanol were performed at the University Medicine Greifswald. A suitable stabilizer was found to be the amphoteric surfactant betaine monohydrate (0.1%), which at the same time did not impair cell viability. The same was observed for the HES-NCs in intact and photodegraded condition.
Besides the z-average, also the polydispersity index (PDI), the number mean and the mean intensity of peak 1 were used for assessing the success of phase transfer in the framework of a dynamic light scattering (DLS) analysis. Since a particle size of 600–800 nm is optimal for penetration into the hair follicle [39, 40], it represents the desired range for the physicochemical parameters z-average and number mean. Additional criteria are a comparable peak 1 mean (intensity) and a low polydispersity represented by the PDI (<0.7). Number mean and peak 1 mean for HES-NCs in PBS with 0.1% betaine monohydrate were in the desired range for follicular penetration using 0.1% betaine monohydrate while an increased z-average and PDI could be observed. On the other hand, Tween 20 (0.1%), CTMA-Cl (0.1%), and NP-40 (0.1%) led to a z-average and peak 1 mean intensity in the desired range but very low number peaks. This effect is due to the intensity of large particles superimposing the intensity of many small particles, which could be the result of particle dissolution in the polar continuous phase. In addition, the physicochemical parameters were most consistent for solutions with betaine monohydrate (0.1%) when the HES-NCs were transferred to ethanol/water, which is why this surfactant was used as a stabilizer for all further experiments.

Similar to the previously tested PU-NCs in hair follicles of *ex vivo* porcine ear skin, a strong UVA-induced release of the model drug SR101 could be demonstrated after application of the HES-NCs in cyclohexane. Thus, the evaluation of cryohistological sections by CLSM showed a mean follicular penetration depth of 499 to 541 µm, which can be compared very well to the data obtained in **publication I**. Intrafollicularly located, a release of the model drug SR101 from the HES-NC was detected as indicated by 40% loss of fluorescence intensity after 1 min irradiation with UVA (approx. 200 mW/cm^2).

Contrary to this, it was observed that the indication of an intrafollicular release of SR101 is difficult using polar continuous phases. In **publication I** it was postulated that the decrease in fluorescence intensity is associated with the release of the model drug SR101 from the polar intraparticulate environment into the apolar extraparticulate environment [41]. In **publication II** the intrafollicular fluorescence intensity of SR101 showed no differences before and after irradiation with UVA making it difficult to detect any release. Furthermore, a lower penetration depth of 344 to 383 µm was observed after the transfer to PBS. Interestingly, a significant

influence of the polarity and viscosity of the vehicle on the follicular penetration depth of NPs seems to be negligible when these parameters do not affect the stability of the formulations independently of the penetration process [42, 43]. A possible explanation could be the previously assessed increase of z-average and PDI of the HES-NCs. Particles with an average size of 600 nm are most appropriate for follicular penetration [39, 40]. After synthesis of the HES-NCs, an average diameter of 400 to 500 nm with a PDI of 0.1 to 0.2 were obtained, providing good conditions for penetration of the hair follicles. After the transport process, microaggregates of > 3 µm (z-average) with a PDI of approximately 0.8 were observed. Another factor may have been an intrainfundibular crouding leading to a congestion effect. The size specificity of penetration is based on the ratchet effect, which requires the particle size to match the space between the cuticle and the intrafollicular stratum corneum [44]. Thus, a certain proportion of the particles either were trapped in the described interstitial space or the massage-induced formation of an intrainfundibular plug could have impaired the penetration of further particles. Nevertheless, a 22% increased penetration depth in comparison to the pure SR101 solution in PBS could still be observed.

A follow-up experiment on *ex vivo* porcine skin was conducted to evaluate the antiseptic performance of the system. Here, the newly developed LED module was used to trigger the release of the encapsulated phase (ethanol). The cup scrub method was used, in which the skin surface is rubbed vigorously with a glass rod in a neutralization medium to sample not only the skin surface microbiome but also follicular localized microbiota.
In this experiment, a high concordance of the sampled microbiota communities with the human skin microbiome was observed [45]. Under aerobic and culture conditions mainly Staphylococci and *Corynebacterium* ssp. were found on porcine skin, which besides Propionibacteriaceae also make up the main part of the colonization of human skin [46, 47]. Interestingly, after treatment with HES-NCs + UVA the proportion of Staphylococci was increased as compared to the untreated and ethanol-treated areas.
These results provide a preliminary indication of an influence of the decontamination process on the composition of the skin microbiome. Nevertheless, in the context of an *in vivo* study with an increased sample size it should be evaluated whether the HES-NCs actually influence the composition. Despite a potentially agglomeration-based reduced penetration depth, HES-NCs in 80% ethanol led to a significant skin decolonization in the framework of this experiment. Nevertheless, it must be kept in mind that the ethanol control without HES-NCs showed only a minimally lower decolonization of the skin. A decontamination effect caused by irradiation with UVA light as reported in previous studies [48] could not be observed.

The results show that the choice of nanocarrier materials should always be based on the field of application and compatibility with the continuous phase. In summary, the intended field of application should be considered when synthesizing the NCs in order to avoid possible incompatibilities. Even though no improved decolonization of hair follicles could be demonstrated in this project, the approach of an externally triggered release of active substances in hair follicles remains highly interesting due to the application range of potential therapeutic fields. UV-responsive NCs in combination with UVA-LEDs are therefore interesting for approaches curing hair follicle-associated diseases (**Section 1.3.1.**). The preoperative use of alternative UVA-responsive nano-delivery systems in combination with UVA-LEDs is a conceivable approach to open paths to enhanced compatibility.
Here, for example, incorporation of photoisomeric groups into the backbone of the NCs shell [49, 50], which is based on a trans to cis photoisomerization of the azobenzene group [51-55] or spiropyran-merocyanine [51, 56, 57] is a conceivable option.
Hence, the approach of deep skin disinfection remains an interesting complement or alternative for far-UVC-based skin surface disinfection, which was evaluated in **publications III, IV and V** as a non-pharmacological approach.

4.2. Efficient and safe far-UVC-based skin surface decontamination

4.2.1. Risk assessment of 233 nm far-UVC on intact skin

Here, an innovative approach for skin antisepsis using a novel developed 233 nm far-UVC LED module was evaluated. Due to the nature of far-UVC light, this approach is suitable for the preoperative or sequential intraoperative surface decolonization of skin, and thus, it represents a complement or an alternative to the deep antisepsis presented in the first part of this thesis (**publications I and II**). Unlike longer wavelength UV light (> 240 nm), far-UVC light is strongly absorbed within the non-nucleated stratum corneum of the epidermis and thus only reaches the upper layers of the viable epidermis without interacting with DNA in the stem cells of the basal layers. Nonetheless, it is of utmost importance to perform a comprehensive risk assessment evaluating potential skin damage. Thus, in **publication III**, 233 nm radiation was applied on intact *ex vivo* skin and *in vitro* epidermal 3D models. In this context, scientists at the University Medicine Greifswald first performed blood agar tests and germ carrier tests on the methicillin-resistant *Staphylococcus aureus* (MRSA) strain DSM11822, the methicillin-sensitive *Staphylococcus aureus* (MSSA) strain DSM799, and *S. epidermidis* DSM1798 to determine the dose required for pathogen eradication. Based on this, the epidermal DNA damage (cyclobutane pyrimidine dimers (CPDs) and pyrimidine (6-4) pyrimidone photoproducts (6-

4PPs)), cell viability and free radical formation were evaluated in comparison to UVC radiation of 222 nm and 254 nm as well as UVB radiation (280–380 nm).

At the University Medicine Greifswald it was found that viable microorganisms can be reduced by a $\log_{10}$ reduction (LR) of 5 $\log_{10}$ levels applying the 233 nm LED at a dose of 40 mJ/cm^2. This effect was diminished to an LR of 1.5–3.3 if mucin and protein were used as soil loads, while a salt solution representing artificial sweat (pH 8.4) had only minor effects on the reduction.

The viability of the skin models was not reduced meaning that a significant decrease to < 80% [58, 59] was not observed directly after irradiation. Nevertheless, it has to be kept in mind that a decrease of cell viability at later time points is possible. Furthermore, no apoptosis was observed after 24 hours of irradiation.

Regarding DNA lesion formation, it could be found that the applied doses of far-UVC irradiation (222 and 233 nm) induce only a small fraction of CPDs caused by 10% of a minimal erythema dose (MED) of UVB radiation. It must be remembered that 10% of a MED UVB is almost unavoidable in everyday life, as this dose corresponds to an approximate stay of 2 minutes in the midday sun for skin type II. In addition, it should be noted that a suberythemal exposure to UV radiation is required for the endogenous synthesis of vitamin D [60] although no critical threshold for UV-related damage has been published [61, 62].
While DNA lesions caused by UVB and 254 nm irradiation were found throughout the whole epidermis with a high abundance, reaching the basal stem cells and even fibroblasts of the dermis, far-UVC irradiation only reached the upper cell layers of the viable epidermis. A closer look at the damage caused by far-UVC shows that 233 nm photons appear to have a deeper penetration depth compared to 222 nm in *ex vivo* human skin as well as 3D epidermal models.

Since it is known that UV-induced DNA lesions are reversible by enzymatic repair mechanisms [63] or can be deposited by apoptosis [64], the time-dependent abundance of DNA lesions was further evaluated using 3D epidermal models. Here, one part of the models was fixated directly after irradiation and the other part was re-incubated in cell culture medium. Interestingly, a complete repair of DNA damage was observed after 24h 233 nm irradiation with a dose of 80 mJ/cm^2 as well as 222 nm irradiation with a dose of 150 mJ/cm^2. A recent *in vivo* study on humans showed that after 24 hours of irradiation with 233 nm and 60 mJ/cm^2 still a small fraction of superficial CPDs can be detected in the epidermis [65], while high abundant DNA

damage associated with increased levels of p53 can be found 24h after irradiation with broadband UVB. Even though it has been described that photolyase-based repair of DNA lesions occurs as fast as in the femtosecond range [66], repair mechanisms in irradiated skin seem to become effective within days. Thus, previous studies using 222 nm even proposed a repair mechanism for CPD damage after 7 days in mice [67]. In a further study on mice, a gradual decrease of CPD abundance from 37 to 13% within 24 h was observed after applying 222 nm far-UVC light [68]. After *in vivo* irradiation with broadband UV light containing similarly high proportions of UVB as well as UVA, a significant reduction of CPD damage was observed 3 days after irradiation in human skin, which further reduced to zero after 10 days [62]. On the other hand, after applying UV with a high proportion of UVA, most CPDs were repaired within 2 days after irradiation with 80% MED [61].
Interestingly, the abundance of CPD^+ cells immediately found after a single irradiation with 80 mJ/cm^2 at 233 nm vanished after irradiating four times every 24 h. From this it can be concluded that the repair mechanism becomes more effective when multiple irradiations are applied. The safety of sequential application of 233 nm far-UVC light is of particular interest in scenarios requiring repetitive application, such as complex chronic wounds or extensive surgical procedures where there is a risk of skin recontamination from which SSI can potentially result. Furthermore, this result is of considerable interest with regard to regular skin exposure in public spaces or in the nosocomial environment (e.g., respiratory disease units such as COVID-19 units).

Having a look at DNA lesions in *ex vivo* human skin, a considerably higher abundance (factor 10 as compared to 3D epidermal models at 233 nm, 40 mJ/cm^2) could be observed. This may be a result of the lower activity of cellular repair mechanisms. Even though the skin was freshly irradiated, it was not kept under culture conditions. Furthermore, an increased variance of DNA lesions after irradiation with 233 nm far-UVC was noticed, which can be explained by the increased biological variability in *ex vivo* human skin. Any pre-existing DNA damage could be excluded, as shown by the non-irradiated control.

Furthermore, radical formation was evaluated in both skin models using electron paramagnetic resonance (EPR) spectroscopy. Having a look at the radical formation in 3D epidermal models, a high divergence between 233 nm (40 to 60 mJ/cm^2) and visible and near-infrared (VIS–NIR) irradiation (equivalent to 20 min solar exposure in the midday sun) was noticeable. As with DNA damage, there is uncertainty about the inflection point from physiological to deleterious radical generation. Nevertheless 20 min VIS–NIR irradiation are known to be safe since this

amount can be compensated by the antioxidant defence system. The radical formation after irradiation with far-UVC was higher in 3D epidermal models as compared to *ex vivo* human skin (233 nm: 32%, 222 nm: 98%, both 40 mJ/cm^2) based on the higher metabolic rate in 3D epidermal models. These findings are consistent with an *in vitro – in vivo* comparison conducted by Albrecht et al. using a sun simulator [69]. A further reason could be the decreased content of antioxidants in epidermal models since an external supply source is not available here.

In *ex vivo* human skin only the both far-UVC wavelengths 222 nm and 233 were evaluated for radical formation. Here, no significant difference between 233 nm irradiation and 222 nm irradiation was observed, based on a variance after irradiation of 233 nm. A possible inter-donor variability might have been the result of diverging physiological parameters such as the melanin and/or antioxidant content.

The results of **publication III** provided the basis for a further risk assessment for the use of 233 nm far-UVC light for the purpose of skin antisepsis. This study included the first comprehensive risk assessment study for the application of the newly developed 233 nm far-UVC LED forming the basis for the preoperative and intraoperative use of radiation. Furthermore, this is of immense importance for the control of nosocomial diseases, as such technology could be used in areas such as nasal cavity, throat or wounds for the eradication of MSSA or MRSA. The treatment, however, of critically or chronic wounds is associated with the development of multi-drug resistant pathogens and several treatments are known to bear a risk of resistance development, such as chlorhexidine gluconate, quaternary ammonium compounds or silver ions [2, 70]. Not only for this reason, but also because of the radical forming potential demonstrated in **publication III,** far-UVC constitutes an interesting alternative approach for the treatment of wounds. In this context, far-UVC could be used to initiate wound healing processes in chronic wounds, as also known from cold plasma [71].

4.2.2. Effects of 233 nm far-UVC on wounds

In addition, the potential repetitive use of far-UVC in prolonged surgical procedures requires a risk assessment on wounds to be able to assess the potential for damage to surgical wounds. Hence, in **publication IV** 233 nm far-UVC radiation was applied on artificially wounded *ex vivo* human skin and evaluated for DNA damage and free radicals. Furthermore, these data were compared with the simulated skin penetration depth of photons for wavelengths between 200 nm and 300 nm.

For this purpose, a disruption of normal anatomic skin structure and function [72] was induced by applying cyanoacrylate tape-stripping (CA-TS). Applying this technique, the stratum corneum was mechanically detached from the viable epidermis.
Barrier-disruption of the skin could be successfully determined by measuring an increase of transepidermal water loss (TEWL) and the stratum corneum loss could be determined morphologically by 2-photon microscopy (2-PM). In this context, a decrease of stratum corneum thickness of approximately 60% was achieved. Interestingly, these results diverged from results previously obtained by Dong et al., where the entire stratum corneum was already removed after 4 CA-TS [73]. In this study a cubic block was applied for the induction of pressure, whereas in the present study 6 CA-TS were applied with a roller. In addition to the velocity of tape-stripping [74], this might be a factor influencing the removed amount of stratum corneum [75]. As a second indicator, TEWL was used. With this parameter the barrier impairment [76] resulting from superficial wound formation can be characterized inversely correlating to the thickness [77] of the stratum corneum based on Fick's law of diffusion [78]. In this context, a 5-fold increase of the baseline value was measured, which was comparable with values obtained in a work by Döge et al. using 50 × TS for mechanical detachment of the entire stratum corneum [73, 78].

After irradiation of the skin with 233 nm far-UVC, the tissue was screened immunohistochemically for the development of CPDs and 6-4PPs as already executed in **publication III**. It was found that the abundance of DNA lesions was elevated in wound skin in comparison to intact skin after irradiation with far-UVC. In contrast, no increase in DNA lesions was detected when artificial wound exudate consisting of cell culture medium and serum was applied to the disrupted skin surface prior to irradiation.

In the first experiment, which was performed without artificial wound exudate, doses previously classified as microbiocidal in **publication III** (40 and 60 mJ/cm^2) were evaluated. UVC light of wavelength 254 nm at 40 mJ/cm^2 was used here as a positive control, since it has a high damage potential and penetrates deeply into the skin [68, 79-82].
Applying 233 nm light with doses of 40 to 60 mJ/cm^2 on wounds, a 3-fold increase of CPDs and an 4 to 8-fold increase of 6-4PPs was observed. In accordance with previous publications [79, 80] 254 nm UVC radiation induced 6 times more CPDs and around 19 times more 6-4PPs in intact skin, while in wounded skin the CPD abundance was only 3 times higher for CPDs and 4 times higher for 6-4PPs. The smaller increase in DNA damage compared to intact skin was related to the fact that 254 nm photons are less absorbed by the stratum corneum [83]

and can therefore already penetrate the intact skin. As a result, a saturation of the abundance of photo-lesions is already reached in intact skin. A more accurate method for the quantitation of DNA lesions in skin is the detection via mass spectrometry [84, 85] since here also the count of lesions per nucleus can be quantified. This possibility is not available in the immunohistological identification of DNA lesions, which represents a limitation of evaluation. Nevertheless, immunohistochemical evaluation is mandatory as it includes localization of the damage. This is of utmost importance, as a risk assessment should evaluate whether the basal localized stem cells are affected by the radiation.

Considering the epidermal depth of the DNA lesions, a pattern similar to the abundance of DNA lesions became apparent. Irradiation with 233 nm at 40 to 60 mJ/cm^2 evoked an increase of 32% to 54% in CPD depth and 43% to 53% in 6-4PP depth. In this context, a maximum depth of about 35 µm was reached indicating that the stem cells of the stratum basale were not touched by the radiation. In contrast to that, the CPD depth after irradiation of superficially wounded skin with 254 nm UVC reached around 62 µm meaning that CPDs were induced in 95% of the epidermis. These data agreed well with the results previously published by Zwicker et al. [79].

However, wounds are covered with a wound exudate depending on their state and condition [86-88]. To reconstruct a scenario closer to the clinical situation, a follow-up experiment was conducted in which artificial wound exudate was applied to the skin surface before irradiation. In this context, the influence of different amounts of artificial wound exudate on the formation of DNA lesions was assessed. After inducing superficial wounds, the amount of DNA lesions increased about 3 to 4 times. Application of 5 µl of artificial wound exudate failed to provide sufficient attenuation of the radiation, so that epidermal damage was largely maintained. Doubling the amount applied, however, led to a reduction in the damage. Thus, significant differences to an intact stratum corneum could not be observed anymore. After further doubling the applied amount of artificial wound exudate to 20 µl, similar values to intact skin were achieved. While the depth of photo-lesions was raised after detaching the stratum corneum by 17% (CPDs) and 51% (6-4PPs), already the application of 5 µl artificial wound exudate ensured a significant reduction so that absorption characteristics of a physiological stratum corneum could be reproduced.

In this experiment it could be clearly shown that artificial wound exudate [79] is able to attenuate the damage caused to barrier-damaged skin and hence resemble the physiological function of an intact stratum corneum. However, it must be considered that cellular components like erythrocytes and leukocytes or further protein components like fibrin were not contained in

the artificial wound exudate [89]. Thus, an additional scattering factor was not included, which could have led to the effect being underestimated.

In a third experiment, EPR spectroscopy was applied again to compare the radical formation in intact and superficially wounded *ex vivo* human skin after irradiation with 233 nm at 60 mJ/cm^2. This was further compared to the radical formation after irradiation with VIS–NIR light on intact skin at a dose of 120 J/cm^2 (see also: **publication III**). Interestingly, the EPR analysis showed no significant deviations in radical formation between intact skin and superficially wounded skin after irradiation with 233 nm far-UVC. Compared to VIS–NIR 120 J/cm^2 a slight reduction was observed. As already mentioned in **publication III** this dose is equivalent to a 20 min stay in the sun and is controllable by the antioxidative system [79].
It must be taken into account that the exposed skin layers (intact skin: stratum corneum, wounded skin: stratum granulosum) diverge strongly in their bio- and physico-chemical compositions. While the stratum corneum has strongly lipophilic components, the stratum granulosum, as part of the viable epidermis has a much higher water content [90]. In addition, unlike the stratum corneum, the living epidermis harbors DNA bases [91], which contribute to radical formation [92] as major UV-absorbing chromophores [93]. As a result of the direct exposure of nucleic acids to radicals in the viable epidermis, the delayed formation of so-called dark CPDs should further be considered [85, 94, 95]. Despite this fact, no quantitative differences in radical formation were found between intact and superficially wounded skin. A qualitative investigation of free radicals would therefore be a highly interesting subject for future studies. A further limitation of this study is, that unlike in the DNA experiments, radical formation in wounds was not performed with artificial wound exudate, since the technical set-up (irradiation of the skin biopsy in the EPR measuring cell) did not enable this.
Despite the slight reduction in radical formation compared with VIS–NIR exposure, the formation of free radicals could also be used as a stimulating factor for possible wound healing processes, as already known from cold plasma therapy [71]. In addition to the antiseptic effect of the radiation, this would be a further aspect in favor of the therapeutic use of far-UVC on chronic wounds making it an important subject for follow-up projects.

In the framework of a final experiment, an *in silico* study simulating the penetration depth of light between 200 and 300 nm into the skin was executed with the support of the Ferdinand Braun Institute in Berlin. Here, the observations on *ex vivo* skin damage have been compared to Monte Carlo ray tracing simulations representing the skin penetration depth of UVC radiation. This model was based on the biophysical properties of the skin (absorption, scattering)

determined in the framework of an inverse Monte Carlo simulation by Zamudio Díaz et al. [65]. To be able to assess the influence of the absorption of artificial wound exudate, absorption properties were determined by UV spectrometry. This was followed by a simulation of the ideal wound exudate layer thickness at the Ferdinand Braun Institute in Berlin. In this context an ideal layer thickness of 1 mm was simulated which, interestingly, lied exactly between the layer thicknesses for 10 µl artificial wound exudate and 20 µl artificial wound exudate (0.8 and 1.3 mm) as applied in the previous *ex vivo* experiments.
In intact skin, radiation of 233 nm penetrated approximately 20 µm into the viable epidermis (rest intensity of 10%). In contrast, UVC radiation of 254 nm penetrated approximately 45 µm of the viable epidermis. In artificially wounded skin, the penetration depth increased to approximately 30 µm at 233 nm and even > 60 µm at 254 nm covering almost the whole viable epidermis. Since a penetration depth of 30 µm does not reach the basal layer of the epidermis, the epidermal stem cells are not affected by this.
After application of artificial wound exudate with the previously simulated ideal layer thickness of 1 mm, a radiation barrier of a physiological stratum corneum could be resembled. These data were comparable very well with the results of CPD depth of the previous *ex vivo* experiments making the *in silico* model suitable as part of a predictional risk assessment for future studies. Nevertheless, the absence of cellular components contributing to scattering effects must be considered.

In this publication it was shown that an application of 233 nm far-UVC on wounds would be a conceivable approach, especially since this has already been successfully demonstrated with 222 nm far-UVC light *in vivo* on mice and patients [67, 96, 97]. In this context, not only intraoperative application on surgical wounds for the prevention of SSI is conceivable, but also the treatment of existing SSI as well as complex chronic wounds. Since the penetration depth of 233 nm far-UVC was higher in comparison to 222 nm far-UVC, a very interesting subject for future studies would be the evaluation of microbiocidal potential on wounds. In view of the complex situation of chronic wounds, this could be another advantage of 233 nm radiation. Thus, 233 nm far-UVC could conceivably be applied to wounds due to its increased penetration depth, while 222 nm far-UVC would be suitable for use in nosocomial settings or public spaces. Concluding, 233 nm LED light at a dose of 60 mJ/cm^2 could be applied safely on superficial wounds for the purpose of skin antisepsis as long as the wounds are covered with wound exudate. However, it should always be kept in mind that based on multiple factors, such as depth, localization, chronicity, inflammatory status and progression, a complexity and diversity of wounds emerges [72]. This publication provides a very important basis for assessing the

risks and potentials that may arise from the application of far-UVC radiation to wounds. However, follow-up studies are needed for a more detailed consideration.

4.2.3. Influence of the skin type on the safety of 233 nm far-UVC

After the system had been extensively tested on intact *ex vivo* human skin, on reconstructed epidermal models and on *ex vivo* barrier-damaged skin, an additional important risk assessment step was to assess the safety on different skin types. This is of particular interest because melanin, which is synthesized skin type-dependent in the epidermal melanocytes, is a potent antioxidant, UV absorber but also UV photosensitizer significantly influencing the skin UV tolerance in a complex manner [84, 94, 98-103]. The extent of skin damage in the form of CPDs and oxidative damage depends not only on the concentration but also on the melanin type (eumelanin versus pheomelanin) as well as on the distribution [94, 98, 101]. On the other hand, detrimental effects depend on the penetration depth and energy associated with the wavelength of the UV radiation [99]. Therefore, a complex interplay between both, exogenous as well as endogenous factors has to be considered in risk assessment.

Until now, no studies on far-UVC-induced DNA damage in different skin types have been published. Thus, in the framework of **publication V**, the influence of far-UVC on CPD formation in different skin types was tested in comparison to the positive control UVB. In addition, the causes of this formation were elucidated using biophysical measurement methods focusing on the characterization of melanin distribution.

After irradiating the skin with microbiocidal doses (40 mJ/cm^2) of far-UVC of the wavelengths 222 and 233 nm as well as broadband UVB (10% MED, 3 mJ/cm^2), the tissue was screened once again for CPD$^+$ cells using immunohistochemistry (see also: **publications III and IV**). Additionally, the area score of CPD$^+$ cells representative for the epidermal depth of DNA lesions was calculated using a semantic machine learning model of Wagner et al. [104]. It was found that skin type I–III showed an increased abundance of CPD$^+$ cells by a factor of two as compared to skin type IV–VI after irradiation with 10% MED UVB. A similar difference was found for 233 nm 40 mJ/cm^2, while no differences were observed for 222 nm 40 mJ/cm^2. This may be due to the fact that the penetration depth of UVB is known to be higher than that of far-UVC. Furthermore, it is known that the penetration depth of 233 nm is slightly increased compared to 222 nm [65, 79, 105].

Using two-photon excited fluorescence lifetime imaging (TPE-FLIM), the vertical melanin distribution of the epidermis was tracked based on the short fluorescence lifetime of melanin. It was found that the difference of melanin content between light and dark skin types is much higher in the stratum basale (deep epidermis) as compared to the stratum granulosum (upper epidermis) indicating a natural vertical melanin gradient. Since UVB radiation is known to penetrate the whole epidermis [106], skin types IV–VI have an increased protection, especially in the deeper fractions of the epidermis as already shown by Fajuyigbe et al. [84, 101]. Contrary to that, as already shown in **publication IV**, 222 nm penetrates the skin only superficially if the stratum corneum is intact. As already mentioned, the difference in melanin content between light and dark skin types is comparatively smaller in this area, which is why the abundance of CPD^+ cells in the skin showed no significant differences. Since the penetration depth of 233 nm far-UVC is slightly higher as compared to 222 nm (approximately one third of the viable epidermis) it is able to penetrate fractions where the difference in melanin content between light and dark skin types is still pronounced. To investigate this further, the area score was utilized in addition to the abundance of CPD^+ cells. This score correlates with the depth of the damage assuming a homogeneous horizontal distribution of damage. Here, partially intact basal layers in two of the four dark skin sections were found after irradiation with UVB while light skin showed CPD^+ cells along the entire epidermis. It must be borne in mind that the machine learning model by Wagner et al. [104] was only generated with skin sections of a comparably low melanin content, which may have caused false-positive results. Further biasing factors resulting in the necessity of an increased sample size are deviating epidermis thicknesses and a heterogeneous melanin distribution along the stratum basale. After irradiation with 233 nm, the depth of CPD^+ cells was slightly lower for dark skin. After irradiation with 222 nm no difference between skin types could be observed, which is in good agreement with the results on CPD abundance.

It can be concluded that the results of this publication demonstrate different biophysical effects of far-UVC radiation compared to UVB light with respect to different skin types. Far-UVC radiation produced less pronounced differences in DNA damage in light and dark skin types compared to UVB radiation which can be attributed to the lower penetration depth of far-UVC photons as well as the vertical distribution and concentration of melanin in the skin. Nevertheless, this subject should be further investigated in future studies with higher sample sizes also including *in vivo* investigations. With this study, far-UVC was shown to be applicable to different skin types, thus securing a further step for the translation of the system and the implementation in the clinical field.

4.3. Comparison of both approaches: advantages and disadvantages

In a conclusive comparison of both systems, NC-based and far-UVC-based skin antisepsis, certain advantages and disadvantages as well as limitations can be identified. As we have just read, with **publication III**, **IV** and **V**, a comprehensive *ex vivo* risk assessment for the implementation of an innovative non-pharmacological approach has been established. The advantage of this approach is a rapid skin surface disinfection of a non-specific nature, which can be applied consecutively. Since, from the current point of view, no resistance of microorganisms to this radiation is known, the approach is suitable for future preoperative skin antisepsis, intraoperative skin and wound antisepsis, as well as for the postoperative treatment of chronic wounds, including a possible stimulation of wound healing processes. This has the potential benefit of preventing the development of multidrug-resistant pathogens based on antibiotics or microbiostatic antiseptics. However, in contrast to the targeting of deeper skin fractions with NCs, far-UVC can only reach the skin surface microbiota. Thus, a disadvantage of the system with regard to preoperative use, especially before long operations, is that recolonization of the skin from deep areas of the hair follicles cannot be prevented. Nevertheless, the simplicity of application of far-UVC allows it to be used intraoperatively in a sequential manner to decolonize the skin during prolonged surgical procedures. First results for the possibility of sequential application without damaging the skin were presented in **publication III**.
To prevent recolonization, antiseptics with a remanent effect such as PVP-iodine or chlorhexidine provide a considerable advantage in preoperative skin antisepsis rendering a repeated application unnecessary [107, 108].
The flipside of the coin, however, is, that some antiseptics from the remanent class of active ingredients like chlorhexidine may lead to the generation of bacterial cross-resistance [70].

In order to implement an enhanced preoperative skin antisepsis for the purpose of reducing intraoperative skin recolonization, an approach for the targeted preoperative decolonization of hair follicles was covered in **publications I and II** of this dissertation in addition to a sequential intraoperative application of far-UVC light.
With this approach, many different antiseptics could potentially be used. Here, NCs serve to transport the antiseptics into the hair follicles, while the UVA light simply represents an external trigger for the release of the antiseptics from the hair follicles. Since the light is emitted by LEDs, many different preoperative lamp designs are conceivable due to the compact LED construction. In the context of this work, the parameters for a rod-shaped hand-held lamp system were determined with which a rapid intrafollicular release of active substance in a

timeframe of 3 min is possible. This allows preoperative application while complying with ICNIRP guidelines in terms of actinic skin damage. In theory, the system of antiseptic-loaded NCs in combination with the UVA-LED light source thus provides an ideal complement or alternative to the 233 nm far-UVC-LED light source. Due to the compact design of LEDs, even a combination device would be suitable, from which both wavelengths could be specifically emitted. Thus, both systems could be used, e.g., preoperatively.

A disadvantage, however, is the complexity of this system. In addition to the encapsulation of active ingredients, stability of the NCs in a polar phase must also be ensured. The average size and PDI of the NCs are of immense importance for the success of the therapy, since it is known that the different segments of the hair follicle can be reached selectively depending on the nanoparticle size. A particle size of approximately 600 nm is ideal for targeting the deeper sections of the hair follicle. If the size of the nanoparticles deviates too much upwards or downwards, the penetration depth will be reduced, which can be explained by the so-called ratchet effect presented by Radtke et al. [44]. With an ideal particle size, the particles fit into the zigzag structure of the hair surface formed by the cuticle, and a transverse movement of the hair leads to deposition of the particles in the direction of the proximal parts of the hair follicle. If the particles are too large, they are entrapped in the space between the intrafollicular stratum corneum and the cuticle surface, which prevents deposition. If the particles are too small, there is insufficient contact between them and the cuticle as well as the intrafollicular stratum corneum. Resultingly, the ratchet effect cannot take place. This means that the PDI of the particles is essential for sufficient penetration of the antiseptic agent into the hair follicles. If the PDI of the formulation is too high, not enough particles will be transported into the deep sections of the hair follicles. This could potentially lead to a lack of therapeutic success.

In the course of the work with UV-responsive PU- and HES-NCs, it became apparent that phase transfer into polar phases is of great difficulty. This led to a more or less pronounced agglomeration of the particles. This can explain the reduced penetration depth found in **publication II**, which was followed by a non-significantly increased decolonization rate compared to the vehicle ethanol.

Another parameter contributing to the complexity of the system is the requirement of a photoresponsive organic group within the NCs shell. Since in many cases this group has to be incorporated by synthesis, the choice of the particle material is reduced. The latter, however, must in turn be coordinated with regard to its compatibility with the continuous phase. Nevertheless, it should be mentioned that this nano-delivery system could potentially be used for other agents that serve to combat hair follicle-associated diseases (see also: **Section 1.1.4.**).

An alternative approach for NC-based targeting of deeper areas of the hair follicles for the purpose of skin antisepsis is discussed in the follow-up chapter (**Section 5.**).

References

[1] C. Eckmann, A. Kramer, O. Assadian, S. Flessa, C. Huebner, K. Michnacs, C. Muehlendyck, K.M. Podolski, M. Wilke, W. Heinlein, D.J. Leaper, Clinical and economic burden of surgical site infections in inpatient care in Germany: A retrospective, cross-sectional analysis from 79 hospitals, PLoS One 17(12) (2022) e0275970.

[2] A. Kramer, J. Dissemond, S. Kim, C. Willy, D. Mayer, R. Papke, F. Tuchmann, O. Assadian, Consensus on Wound Antisepsis: Update 2018, Skin Pharmacol Physiol 31(1) (2018) 28-58.

[3] B. Lange-Asschenfeldt, D. Marenbach, C. Lang, A. Patzelt, M. Ulrich, A. Maltusch, D. Terhorst, E. Stockfleth, W. Sterry, J. Lademann, Distribution of bacteria in the epidermal layers and hair follicles of the human skin, Skin Pharmacol Physiol 24(6) (2011) 305-311.

[4] S. Selwyn, H. Ellis, Skin Bacteria and Skin Disinfection Reconsidered, Br Med J 1(5793) (1972) 136-140.

[5] D. Dörfel, M. Maiwald, G. Daeschlein, G. Müller, R. Hudek, O. Assadian, G. Kampf, T. Kohlmann, J.C. Harnoss, A. Kramer, Comparison of the antimicrobial efficacy of povidone-iodine-alcohol versus chlorhexidine-alcohol for surgical skin preparation on the aerobic and anaerobic skin flora of the shoulder region, Antimicrob Resist Infect Control 10(1) (2021) 17.

[6] M. Ulmer, J. Lademann, A. Patzelt, F. Knorr, A. Kramer, T. Koburger, O. Assadian, G. Daeschlein, B. Lange-Asschenfeldt, New strategies for preoperative skin antisepsis, Skin Pharmacol Physiol 27(6) (2014) 283-292.

[7] J. Lademann, H. Richter, A. Teichmann, N. Otberg, U. Blume-Peytavi, J. Luengo, B. Weiss, U.F. Schaefer, C.M. Lehr, R. Wepf, W. Sterry, Nanoparticles--an efficient carrier for drug delivery into the hair follicles, Eur J Pharm Biopharm 66(2) (2007) 159-164.

[8] T. Dai, M.S. Vrahas, C.K. Murray, M.R. Hamblin, Ultraviolet C irradiation: an alternative antimicrobial approach to localized infections?, Expert Rev Anti Infect Ther 10(2) (2012) 185-195.

[9] H. Choi, P. Chatterjee, M. Hwang, E.M. Stock, J.S. Lukey, J.E. Zeber, C. Jinadatha, Can multidrug-resistant organisms become resistant to ultraviolet (UV) light following serial exposures? Characterization of post-UV genomic changes using whole-genome sequencing, Infect Control Hosp Epidemiol 43(1) (2022) 72-78.

[10] J. Lademann, H. Richter, F. Knorr, A. Patzelt, M.E. Darvin, E. Rühl, K.Y. Cheung, K.K. Lai, R. Renneberg, W.C. Mak, Triggered release of model drug from AuNP-doped BSA nanocarriers in hair follicles using IRA radiation, Acta Biomater 30 (2016) 388-396.

[11] P. Dong, F.F. Sahle, S.B. Lohan, S. Saeidpour, S. Albrecht, C. Teutloff, R. Bodmeier, M. Unbehauen, C. Wolff, R. Haag, J. Lademann, A. Patzelt, M. Schäfer-Korting, M.C. Meinke, pH-sensitive Eudragit(R) L 100 nanoparticles promote cutaneous penetration and drug release on the skin, J Control Release 295 (2019) 214-222.

[12] D. Kaden, L. Dähne, F. Knorr, H. Richter, J. Lademann, M.C. Meinke, A. Patzelt, M.E. Darvin, S. Jung, Determination of the pH Gradient in Hair Follicles of Human Volunteers Using pH-Sensitive Melamine Formaldehyde-Pyranine Nile Blue Microparticles, Sensors (Basel) 20(18) (2020) 5243.

[13] W.C. Mak, A. Patzelt, H. Richter, R. Renneberg, K.K. Lai, E. Rühl, W. Sterry, J. Lademann, Triggering of drug release of particles in hair follicles, J Control Release 160(3) (2012) 509-514.

[14] W.C. Mak, H. Richter, A. Patzelt, W. Sterry, K.K. Lai, R. Renneberg, J. Lademann, Drug delivery into the skin by degradable particles, Eur J Pharm Biopharm 79(1) (2011) 23-27.

[15] N. Tran, F. Knorr, W.C. Mak, K.Y. Cheung, H. Richter, M. Meinke, J. Lademann, A. Patzelt, Gradient-dependent release of the model drug TRITC-dextran from FITC-labeled BSA hydrogel nanocarriers in the hair follicles of porcine ear skin, Eur J Pharm Biopharm 116 (2017) 12-16.

[16] B. Limcharoen, P. Toprangkobsin, W. Banlunara, S. Wanichwecharungruang, H. Richter, J. Lademann, A. Patzelt, Increasing the percutaneous absorption and follicular penetration of retinal by topical application of proretinal nanoparticles, Eur J Pharm Biopharm 139 (2019) 93-100.

[17] A. Kramer, C.-D. Heidecke, Präoperative Hautantiseptik und Hautschutz, Trauma und Berufskrankheit 17(S2) (2015) 322-329.

[18] M. Ding, X. Zeng, X. He, J. Li, H. Tan, Q. Fu, Cell internalizable and intracellularly degradable cationic polyurethane micelles as a potential platform for efficient imaging and drug delivery, Biomacromolecules 15(8) (2014) 2896-2906.

[19] C. Wei, Y. Zhang, Z. Song, Y. Xia, H. Xu, M. Lang, Enhanced bioreduction-responsive biodegradable diselenide-containing poly(ester urethane) nanocarriers, Biomater Sci 5(4) (2017) 669-677.

[20] Y. Guan, Y. Su, L. Zhao, F. Meng, Q. Wang, Y. Yao, J. Luo, Biodegradable polyurethane micelles with pH and reduction responsive properties for intracellular drug delivery, Mater Sci Eng C Mater Biol Appl 75 (2017) 1221-1230.

[21] M.R. Nabid, I. Omrani, Facile preparation of pH-responsive polyurethane nanocarrier for oral delivery, Mater Sci Eng C Mater Biol Appl 69 (2016) 532-537.

[22] I. Omrani, N. Babanejad, H.K. Shendi, M.R. Nabid, Fully glutathione degradable waterborne polyurethane nanocarriers: Preparation, redox-sensitivity, and triggered intracellular drug release, Mater Sci Eng C Mater Biol Appl 70(Pt 1) (2017) 607-616.

[23] A.Y. Khosroushahi, H. Naderi-Manesh, H. Yeganeh, J. Barar, Y. Omidi, Novel water-soluble polyurethane nanomicelles for cancer chemotherapy: physicochemical characterization and cellular activities, J Nanobiotechnology 10 (2012) 2.

[24] T. Gebauer, A.T. Neffe, A. Lendlein, Influence of diisocyanate reactivity and water solubility on the formation and the mechanical properties of gelatin-based networks in water, MRS Proceedings 1569 (2013) 15-20.

[25] F.M.B. Coutinho, M.C.G. Rocha, Kinetic study of the reactions between hydroxylated polybutadiene and isocyanates in chlorobenzene—IV. Reactions with tolylene diisocyanate, 3-isocyanatomethyl-3, 5, 5-trimethylcyclohexyl isocyanate and hexamethylene diisocyanate, Eur Polym J 27(2) (1991) 213-216.

[26] N.H. Mudri, L.C. Abdullah, M.M. Aung, M.Z. Salleh, D.R. Awang Biak, M. Rayung, Comparative Study of Aromatic and Cycloaliphatic Isocyanate Effects on Physico-Chemical Properties of Bio-Based Polyurethane Acrylate Coatings, Polymers (Basel) 12(7) (2020) 1494.

[27] J.Y. Cherng, T.Y. Hou, M.F. Shih, H. Talsma, W.E. Hennink, Polyurethane-based drug delivery systems, Int J Pharm 450(1-2) (2013) 145-162.

[28] G. Morral-Ruíz, P. Melgar-Lesmes, M.L. García, C. Solans, M.J. García-Celma, Polyurethane and polyurea nanoparticles based on polyoxyethylene castor oil derivative surfactant suitable for endovascular applications, Int J Pharm 461(1-2) (2014) 1-13.

[29] M.B. Lowinger, S.E. Barrett, F. Zhang, R.O. Williams, 3rd, Sustained Release Drug Delivery Applications of Polyurethanes, Pharmaceutics 10(2) (2018) 55.

[30] A. Wang, H. Gao, Y. Sun, Y.L. Sun, Y.W. Yang, G. Wu, Y. Wang, Y. Fan, J. Ma, Temperature- and pH-responsive nanoparticles of biocompatible polyurethanes for doxorubicin delivery, Int J Pharm 441(1-2) (2013) 30-39.

[31] J.W. Yoo, E. Chambers, S. Mitragotri, Factors that control the circulation time of nanoparticles in blood: challenges, solutions and future prospects, Curr Pharm Des 16(21) (2010) 2298-2307.

[32] N. Jagielski, S. Sharma, V. Hombach, V. Mailänder, V. Rasche, K. Landfester, Nanocapsules Synthesized by Miniemulsion Technique for Application as New Contrast Agent Materials, Macromolecular Chemistry and Physics 208(19-20) (2007) 2229-2241.

[33] S. Sharma, U. Paiphansiri, V. Hombach, V. Mailander, O. Zimmermann, K. Landfester, V. Rasche, Characterization of MRI contrast agent-loaded polymeric nanocapsules as versatile vehicle for targeted imaging, Contrast Media Mol Imaging 5(2) (2010) 59-69.

[34] H. Lboutounne, J.F. Chaulet, C. Ploton, F. Falson, F. Pirot, Sustained ex vivo skin antiseptic activity of chlorhexidine in poly(ε-caprolactone) nanocapsule encapsulated form and as a digluconate, J Control Release 82(2-3) (2002) 319-334.

[35] H. Lboutounne, V. Faivre, F. Falson, F. Pirot, Characterization of transport of chlorhexidine-loaded nanocapsules through hairless and wistar rat skin, Skin Pharmacol Physiol 17(4) (2004) 176-182.

[36] D.T. Nhung, A.M. Freydiere, H. Constant, F. Falson, F. Pirot, Sustained antibacterial effect of a hand rub gel incorporating chlorhexdine-loaded nanocapsules (Nanochlorex), Int J Pharm 334(1-2) (2007) 166-172.

[37] M. Ulmer, A. Patzelt, T. Vergou, H. Richter, G. Müller, A. Kramer, W. Sterry, V. Czaika, J. Lademann, In vivo investigation of the efficiency of a nanoparticle-emulsion containing polihexanide on the human skin, Eur J Pharm Biopharm 84(2) (2013) 325-329.

[38] S.B. Lohan, D. Ivanov, N. Schuler, B. Berger, L. Zastrow, J. Lademann, M.C. Meinke, Switching from healthy to unhealthy oxidative stress - does the radical type can be used as an indicator?, Free Radic Biol Med 162 (2021) 401-411.

[39] A. Patzelt, H. Richter, F. Knorr, U. Schäfer, C.M. Lehr, L. Dähne, W. Sterry, J. Lademann, Selective follicular targeting by modification of the particle sizes, J Control Release 150(1) (2011) 45-48.

[40] L. Busch, Y. Keziban, L. Dähne, C.M. Keck, M.C. Meinke, J. Lademann, A. Patzelt, The impact of skin massage frequency on the intrafollicular transport of silica nanoparticles: Validation of the ratchet effect on an ex vivo porcine skin model, Eur J Pharm Biopharm 158 (2021) 266-272.

[41] L. Busch, Y. Avlasevich, P. Zwicker, G. Thiede, K. Landfester, C.M. Keck, M.C. Meinke, M.E. Darvin, A. Kramer, G. Müller, M. Kerscher, J. Lademann, A. Patzelt, Release of the model drug SR101 from polyurethane nanocapsules in porcine hair follicles triggered by LED-derived low dose UVA light, Int J Pharm 597 (2021) 120339.

[42] O. Pelikh, R.W. Eckert, S.R. Pinnapireddy, C.M. Keck, Hair follicle targeting with curcumin nanocrystals: Influence of the formulation properties on the penetration efficacy, J Control Release 329 (2021) 598-613.

[43] A. Patzelt, H. Richter, L. Dähne, P. Walden, K.H. Wiesmüller, U. Wank, W. Sterry, J. Lademann, Influence of the vehicle on the penetration of particles into hair follicles, Pharmaceutics 3(2) (2011) 307-314.

[44] M. Radtke, A. Patzelt, F. Knorr, J. Lademann, R.R. Netz, Ratchet effect for nanoparticle transport in hair follicles, Eur J Pharm Biopharm 116 (2017) 125-130.

[45] S. Wareham-Mathiassen, V. Pinto Glenting, L. Bay, M. Allesen-Holm, H. Bengtsson, T. Bjarnsholt, Characterization of pig skin microbiome and appraisal as an in vivo subcutaneous injection model, Lab Anim (2022) 236772221136173.

[46] A.L. Byrd, Y. Belkaid, J.A. Segre, The human skin microbiome, Nat Rev Microbiol 16(3) (2018) 143-155.

[47] A.A. Ross, A. Rodrigues Hoffmann, J.D. Neufeld, The skin microbiome of vertebrates, Microbiome 7(1) (2019) 79.

[48] A. Rezaie, G.G.S. Leite, G.Y. Melmed, R. Mathur, M.J. Villanueva-Millan, G. Parodi, J. Sin, J.F. Germano, W. Morales, S. Weitsman, S.Y. Kim, J.H. Park, S. Sakhaie, M. Pimentel, Ultraviolet A light effectively reduces bacteria and viruses including coronavirus, PLoS One 15(7) (2020) e0236199.

[49] X. Liu, Y. Yang, M.W. Urban, Stimuli-Responsive Polymeric Nanoparticles, Macromol Rapid Commun 38(13) (2017) 1700030.

[50] M.F. Bedard, B.G. De Geest, A.G. Skirtach, H. Mohwald, G.B. Sukhorukov, Polymeric microcapsules with light responsive properties for encapsulation and release, Adv Colloid Interface Sci 158(1-2) (2010) 2-14.

[51] S. Mura, J. Nicolas, P. Couvreur, Stimuli-responsive nanocarriers for drug delivery, Nat Mater 12(11) (2013) 991-1003.

[52] B. Zheng, X. Gong, H. Wang, S. Wang, H. Wang, W. Li, J. Tan, J. Chang, A NIR-remote controlled upconverting nanoparticle: an improved tool for living cell dye-labeling, Nanotechnology 26(42) (2015) 425102.

[53] C. Yao, P. Wang, X. Li, X. Hu, J. Hou, L. Wang, F. Zhang, Near-Infrared-Triggered Azobenzene-Liposome/Upconversion Nanoparticle Hybrid Vesicles for Remotely Controlled Drug Delivery to Overcome Cancer Multidrug Resistance, Adv Mater 28(42) (2016) 9341-9348.

[54] D.K. Prusty, V. Adam, R.M. Zadegan, S. Irsen, M. Famulok, Supramolecular aptamer nano-constructs for receptor-mediated targeting and light-triggered release of chemotherapeutics into cancer cells, Nat Commun 9(1) (2018) 535.

[55] Y. Zhao, Rational design of light-controllable polymer micelles, Chem Rec 7(5) (2007) 286-294.

[56] R. Tong, H.D. Hemmati, R. Langer, D.S. Kohane, Photoswitchable nanoparticles for triggered tissue penetration and drug delivery, J Am Chem Soc 134(21) (2012) 8848-8855.

[57] S. Chen, F. Jiang, Z. Cao, G. Wang, Z.M. Dang, Photo, pH, and thermo triple-responsive spiropyran-based copolymer nanoparticles for controlled release, Chem Commun (Camb) 51(63) (2015) 12633-12636.

[58] J. López-García, M. Lehocký, P. Humpolíček, P. Sáha, HaCaT Keratinocytes Response on Antimicrobial Atelocollagen Substrates: Extent of Cytotoxicity, Cell Viability and Proliferation, J Funct Biomater 5(2) (2014) 43-57.

[59] DIN EN ISO 10993-5:2009-10, Biological evaluation of medical devices - Part 5: Tests for in vitro cytotoxicity, 2009.

[60] B.A. Gilchrest, Sun exposure and vitamin D sufficiency, Am J Clin Nutr 88(2) (2008) 570S-577S.

[61] B.B. Shih, M.D. Farrar, M.S. Cooke, J. Osman, A.K. Langton, R. Kift, A.R. Webb, J.L. Berry, R.E.B. Watson, A. Vail, F.R. de Gruijl, L.E. Rhodes, Fractional Sunburn Threshold UVR Doses Generate Equivalent Vitamin D and DNA Damage in Skin Types I-VI but with Epidermal

DNA Damage Gradient Correlated to Skin Darkness, J Invest Dermatol 138(10) (2018) 2244-2252.

[62] S.K. Katiyar, M.S. Matsui, H. Mukhtar, Kinetics of UV light-induced cyclobutane pyrimidine dimers in human skin in vivo: an immunohistochemical analysis of both epidermis and dermis, Photochem Photobiol 72(6) (2000) 788-793.

[63] J.D. Mallet, M.M. Dorr, M.C. Drigeard Desgarnier, N. Bastien, S.P. Gendron, P.J. Rochette, Faster DNA Repair of Ultraviolet-Induced Cyclobutane Pyrimidine Dimers and Lower Sensitivity to Apoptosis in Human Corneal Epithelial Cells than in Epidermal Keratinocytes, PLoS One 11(9) (2016) e0162212.

[64] C.H. Lee, S.B. Wu, C.H. Hong, H.S. Yu, Y.H. Wei, Molecular Mechanisms of UV-Induced Apoptosis and Its Effects on Skin Residential Cells: The Implication in UV-Based Phototherapy, Int J Mol Sci 14(3) (2013) 6414-6435.

[65] D.F. Zamudio Díaz, A.L. Klein, M. Guttmann, P. Zwicker, L. Busch, M. Kröger, H. Klose, S. Rohn, J. Schleusener, M.C. Meinke, Skin optical properties from 200–300 nm support far-UVC skin safety in vivo, J Photochem Photobiol B 247 (2023) 112784.

[66] Z. Liu, L. Wang, D. Zhong, Dynamics and mechanisms of DNA repair by photolyase, Phys Chem Chem Phys 17(18) (2015) 11933-11949.

[67] B. Ponnaiya, M. Buonanno, D. Welch, I. Shuryak, G. Randers-Pehrson, D.J. Brenner, Far-UVC light prevents MRSA infection of superficial wounds in vivo, PLoS One 13(2) (2018) e0192053.

[68] K. Narita, K. Asano, Y. Morimoto, T. Igarashi, A. Nakane, Chronic irradiation with 222-nm UVC light induces neither DNA damage nor epidermal lesions in mouse skin, even at high doses, PLoS One 13(7) (2018) e0201259.

[69] S. Albrecht, A. Elpelt, C. Kasim, C. Reble, L. Mundhenk, H. Pischon, S. Hedtrich, C. Witzel, J. Lademann, L. Zastrow, I. Beckers, M.C. Meinke, Quantification and characterization of radical production in human, animal and 3D skin models during sun irradiation measured by EPR spectroscopy, Free Radic Biol Med 131 (2019) 299-308.

[70] G. Kampf, Acquired resistance to chlorhexidine - is it time to establish an 'antiseptic stewardship' initiative?, J Hosp Infect 94(3) (2016) 213-227.

[71] S. Mirpour, S. Fathollah, P. Mansouri, B. Larijani, M. Ghoranneviss, M. Mohajeri Tehrani, M.R. Amini, Cold atmospheric plasma as an effective method to treat diabetic foot ulcers: A randomized clinical trial, Sci Rep 10(1) (2020) 10440.

[72] G.S. Lazarus, D.M. Cooper, D.R. Knighton, R.E. Percoraro, G. Rodeheaver, M.C. Robson, Definitions and guidelines for assessment of wounds and evaluation of healing, Wound Repair Regen 2(3) (1994) 165-170.

[73] P. Dong, V. Nikolaev, M. Kroger, C. Zoschke, M.E. Darvin, C. Witzel, J. Lademann, A. Patzelt, M. Schafer-Korting, M.C. Meinke, Barrier-disrupted skin: Quantitative analysis of tape and cyanoacrylate stripping efficiency by multiphoton tomography, Int J Pharm 574 (2020) 118843.

[74] J. Lademann, U. Jacobi, C. Surber, H.J. Weigmann, J.W. Fluhr, The tape stripping procedure--evaluation of some critical parameters, Eur J Pharm Biopharm 72(2) (2009) 317-323.

[75] M. Breternitz, M. Flach, J. Prassler, P. Elsner, J.W. Fluhr, Acute barrier disruption by adhesive tapes is influenced by pressure, time and anatomical location: integrity and cohesion assessed by sequential tape stripping. A randomized, controlled study, Br J Dermatol 156(2) (2007) 231-240.

[76] M. Machado, T.M. Salgado, J. Hadgraft, M.E. Lane, The relationship between transepidermal water loss and skin permeability, Int J Pharm 384(1-2) (2010) 73-77.

[77] D.A. Schwindt, K.P. Wilhelm, H.I. Maibach, Water diffusion characteristics of human stratum corneum at different anatomical sites in vivo, J Invest Dermatol 111(3) (1998) 385-389.

[78] N. Döge, A. Avetisyan, S. Hadam, E.K.B. Pfannes, F. Rancan, U. Blume-Peytavi, A. Vogt, Assessment of skin barrier function and biochemical changes of ex vivo human skin in response to physical and chemical barrier disruption, Eur J Pharm Biopharm 116 (2017) 138-148.

[79] P. Zwicker, J. Schleusener, S.B. Lohan, L. Busch, C. Sicher, S. Einfeldt, M. Kneissl, A.A. Kuhl, C.M. Keck, C. Witzel, A. Kramer, M.C. Meinke, Application of 233 nm far-UVC LEDs for eradication of MRSA and MSSA and risk assessment on skin models, Sci Rep 12(1) (2022) 2587.

[80] J. Glaab, N. Lobo-Ploch, H.K. Cho, T. Filler, H. Gundlach, M. Guttmann, S. Hagedorn, S.B. Lohan, F. Mehnke, J. Schleusener, C. Sicher, L. Sulmoni, T. Wernicke, L. Wittenbecher, U. Woggon, P. Zwicker, A. Kramer, M.C. Meinke, M. Kneissl, M. Weyers, U. Winterwerber, S. Einfeldt, Skin tolerant inactivation of multiresistant pathogens using far-UVC LEDs, Sci Rep 11(1) (2021) 14647.

[81] M. Buonanno, B. Ponnaiya, D. Welch, M. Stanislauskas, G. Randers-Pehrson, L. Smilenov, F.D. Lowy, D.M. Owens, D.J. Brenner, Germicidal Efficacy and Mammalian Skin Safety of 222-nm UV Light, Radiat Res 187(4) (2017) 483-491.

[82] D. Welch, M. Aquino de Muro, M. Buonanno, D.J. Brenner, Wavelength-dependent DNA Photodamage in a 3-D human Skin Model over the Far-UVC and Germicidal UVC Wavelength Ranges from 215 to 255 nm, Photochem Photobiol 98(5) (2022) 1167-1171.

[83] J. Schleusener, S.B. Lohan, L. Busch, K. Ghoreschi, N.L. Ploch, S. May, S. Vogel, J. Eberle, M.C. Meinke, Treatment of the Candida subspecies Candida albicans and Candida parapsilosis with two far-UVC sources to minimise mycoses in clinical practice, Mycoses 66(1) (2023) 25-28.

[84] D. Fajuyigbe, T. Douki, A. van Dijk, R.P.E. Sarkany, A.R. Young, Dark cyclobutane pyrimidine dimers are formed in the epidermis of Fitzpatrick skin types I/II and VI in vivo after exposure to solar-simulated radiation, Pigment Cell Melanoma Res 34(3) (2021) 575-584.

[85] K.P. Lawrence, G.J. Delinasios, S. Premi, A.R. Young, M.S. Cooke, Perspectives on Cyclobutane Pyrimidine Dimers-Rise of the Dark Dimers, Photochem Photobiol 98(3) (2022) 609-616.

[86] M. Spear, Wound Exudate—The Good, the Bad, and the Ugly, Plastic Surgical Nursing 32(2) (2012) 77-79.

[87] K.F. Cutting, Wound exudate: composition and functions, Br J Community Nurs 8(9 Suppl) (2003) suppl 4-9.

[88] T. Chambers, P. Bradley, Wound Exudate, Br J Nurs 27(20) (2018) S28-S32.

[89] R.I. Litvinov, J.W. Weisel, Fibrin mechanical properties and their structural origins, Matrix Biol 60-61 (2017) 110-123.

[90] S.E. Cross, B.M. Magnusson, G. Winckle, Y. Anissimov, M.S. Roberts, Determination of the effect of lipophilicity on the in vitro permeability and tissue reservoir characteristics of topically applied solutes in human skin layers, J Invest Dermatol 120(5) (2003) 759-764.

[91] Z. Nemes, P.M. Steinert, Bricks and mortar of the epidermal barrier, Exp Mol Med 31(1) (1999) 5-19.

[92] A. Tewari, M.M. Grage, G.I. Harrison, R. Sarkany, A.R. Young, UVA1 is skin deep: molecular and clinical implications, Photochem Photobiol Sci 12(1) (2013) 95-103.

[93] S.L. Walker, A.R. Young, An action spectrum (290-320 nm) for TNFalpha protein in human skin in vivo suggests that basal-layer epidermal DNA is the chromophore, Proc Natl Acad Sci U S A 104(48) (2007) 19051-19054.

[94] D.E. Brash, UV-induced Melanin Chemiexcitation: A New Mode of Melanoma Pathogenesis, Toxicol Pathol 44(4) (2016) 552-554.

[95] S. Premi, S. Wallisch, C.M. Mano, A.B. Weiner, A. Bacchiocchi, K. Wakamatsu, E.J. Bechara, R. Halaban, T. Douki, D.E. Brash, Photochemistry. Chemiexcitation of melanin derivatives induces DNA photoproducts long after UV exposure, Science 347(6224) (2015) 842-847.

[96] J.C. Goh, D. Fisher, E.C.H. Hing, L. Hanjing, Y.Y. Lin, J. Lim, O.W. Chen, L.T. Chye, Disinfection capabilities of a 222 nm wavelength ultraviolet lighting device: a pilot study, J Wound Care 30(2) (2021) 96-104.

[97] K. Narita, K. Asano, Y. Morimoto, T. Igarashi, M.R. Hamblin, T. Dai, A. Nakane, Disinfection and healing effects of 222-nm UVC light on methicillin-resistant Staphylococcus aureus infection in mouse wounds, J Photochem Photobiol B 178 (2018) 10-18.

[98] M. Brenner, V.J. Hearing, The protective role of melanin against UV damage in human skin, Photochem Photobiol 84(3) (2008) 539-549.

[99] J. D'Orazio, S. Jarrett, A. Amaro-Ortiz, T. Scott, UV radiation and the skin, Int J Mol Sci 14(6) (2013) 12222-12248.

[100] D. Fajuyigbe, A.R. Young, The impact of skin colour on human photobiological responses, Pigment Cell Melanoma Res 29(6) (2016) 607-618.

[101] D. Fajuyigbe, S.M. Lwin, B.L. Diffey, R. Baker, D.J. Tobin, R.P.E. Sarkany, A.R. Young, Melanin distribution in human epidermis affords localized protection against DNA photodamage and concurs with skin cancer incidence difference in extreme phototypes, FASEB J 32(7) (2018) 3700-3706.

[102] S. Del Bino, J. Sok, F. Bernerd, Assessment of ultraviolet-radiation-induced DNA damage within melanocytes in skin of different constitutive pigmentation, Br J Dermatol 168(5) (2013) 1120-1123.

[103] S. Del Bino, J. Sok, E. Bessac, F. Bernerd, Relationship between skin response to ultraviolet exposure and skin color type, Pigment Cell Res 19(6) (2006) 606-614.

[104] P. Wagner, M. Springenberg, M. Kröger, R.K.C. Moritz, J. Schleusener, M.C. Meinke, J. Ma, Semantic modeling of cell damage prediction: a machine learning approach at human-level performance in dermatology, Sci Rep 13(1) (2023) 8336.

[105] L. Busch, M. Kröger, J. Schleusener, A.L. Klein, S.B. Lohan, M. Guttmann, C.M. Keck, M.C. Meinke, Evaluation of DNA lesions and radicals generated by a 233 nm far-UVC LED in superficial ex vivo skin wounds, J Photochem Photobiol B 245 (2023) 112757.

[106] M. Meinhardt, R. Krebs, A. Anders, U. Heinrich, H. Tronnier, Wavelength-dependent penetration depths of ultraviolet radiation in human skin, J Biomed Opt 13(4) (2008) 044030.

[107] A. Kramer, J.C. Harnoss, P. Walger, C.D. Heidecke, A. Schreiber, S. Maier, J. Pochhammer, Fachspezifische Maßnahmen zur Prävention von Surgical Site Infections (SSI), Zentralbl Chir 141(6) (2016) 591-596.

[108] M. Reichel, P. Heisig, T. Kohlmann, G. Kampf, Alcohols for skin antisepsis at clinically relevant skin sites, Antimicrob Agents Chemother 53(11) (2009) 4778-4782.

5. Conclusions and translational outlook

As discussed in the previous section, both approaches, nanocapsule (NC)- as well as far-ultraviolet C (UVC)-based skin antisepsis, entail certain advantages and disadvantages. They could be used in both, complementary and alternative ways for pre- and intraoperative skin antisepsis.

We have learned that the application of the NC-based system involves a high degree of complexity and that agglomeration of the NCs in polar phases can occur even if a targeting of deep hair follicle fractions with NCs and an intrafollicular UVA-triggered release is potentially possible (**publications I and II**). To avoid the disadvantage of the NC-based systems complexity, another NC-based approach for the transport of solved and suspended actives has emerged as promising in the framework of a patent that was recently released [1]: By adding inert nanoparticles to an antiseptic solution, the transport of the antiseptic into the hair follicles can be increased by an adhesional effect. In this case, the antiseptic is present only in the external phase, purely independently of the nanoparticles. The latter are to be regarded as a mere additive for increasing the penetration of the active substance in this context. First unpublished data show that nanoparticles of different materials are suitable for this mechanism and that not only the transport of small drugs but also of macromolecules is possible. This results in a significant expansion of the repertoire of applicable nanoparticles, which is advantageous in terms of compatibility with the continuous phase. In addition, the previously required step of a swift externally triggered drug release is not necessary, because no drug is encapsulated inside the nanoparticles. An interesting advantage of this system is the possibility of a co-delivery approach with a sustained release of, e.g., antioxidants from nanocrystals. Due to the simplicity of this system, it represents a potential approach for optimized preoperative skin decontamination, which must be tested for its effectiveness in future studies.

The comprehensive risk assessment study for far-UVC application on skin showed promising results for a future translation to nosocomial and surgical applications (**publications III, IV and V**).

A first step for translation of the far-UVC-based system into the clinical field has been already accomplished with a work of Zamudio Diaz et al., who performed an *in vivo* risk assessment of 233 nm far-UVC for the first time and could show that 24 h after application only minor DNA lesions were histologically detectable in the epidermis [2]. This was not associated with an increase in p53 in contrast to a minimal erythema dose (MED) of UVB. Furthermore, in a small

pilot study involving n = 6 individuals, decolonization was comparable to the application of 70% isopropanol according to a standardized protocol [2]. Due to the extremely compact design of light emitting diodes (LEDs), the technology can be used in body cavities, for example to decolonize the mucous membrane in the oral cavity or in the nasal cavity. First, not yet published results show that reconstructed 3D mucosa models have a sufficient regenerative capacity 24h after irradiation with microbiocidal doses, as it is already known from the 3D epidermal models [3]. Furthermore, successful decolonization of agar plates with candida cultures was shown for 233 nm, which would be a promising result for a potential application in public areas such as swimming pools for the purpose of prevention of interdigital mycoses [4].

Furthermore, far-UVC light is potentially suitable for indoor air and skin surface disinfection in public spaces or in the nosocomial environment to inhibit the spread of multi-drug resistant pathogens or airborne viruses like SARS-CoV-2 [5-7]. While 233 nm far-UVC light may have an advantage for the decolonization of wounds due to its deeper penetration depth into wound exudate, 222 nm may have an advantage for application in air disinfection in nosocomial settings or public spaces.

However, further steps are required for the final implementation of this system in the clinical area and its application in public and nosocomial facilities. Extensive risk assessment projects are ongoing for ocular safety of 233 nm far-UVC radiation (not published yet), which is an essential step for future application. In particular, corneal tissue exposure to far-UVC light should be investigated, which is essential not only for the patients or persons exposed in public spaces, but also for the surgeons or technical assistants working with far-UVC light. Another interesting research topic for future projects is the investigation of radical-induced stimulation of wound healing with 233 nm far-UVC radiation.

In summary, the pharmacological NC-based approach for skin decolonization as well as the non-pharmacological far-UVC light-based approach entail a very promising potential for future application. Nonetheless, considerable optimization on the pharmaceutical side or alternative approaches still need to be sought for final implementation.

The use of far-UVC LEDs for skin surface decolonization has been extensively addressed for the first time in this cumulative work. Nevertheless, further risk-assessment studies are required for the final implementation of this approach.

References

[1] J. Lademann, M.C. Meinke, A.L. Klein, L. Busch, C.M. Keck, O. Pelikh, Composition for particle-mediated transport of a dissolved active agent into hair follicles (Patent, 2023).

[2] D.F. Zamudio Díaz, A.L. Klein, M. Guttmann, P. Zwicker, L. Busch, M. Kröger, H. Klose, S. Rohn, J. Schleusener, M.C. Meinke, Skin optical properties from 200–300 nm support far-UVC skin safety in vivo, J Photochem Photobiol B 247 (2023) 112784.

[3] J. Schleusener, S.B. Lohan, L. Busch, D.F. Zamudio Díaz, N. Opitz, C. Sicher, T. Lichtenthäler, K. Danker, S. Dommerich, T. Filler, M.C. Meinke, P. Zwicker, Irradiation of human oral mucosa by 233 nm far-UVC-LEDs for the safe inactivation of nosocomial pathogens, In preparation.

[4] J. Schleusener, S.B. Lohan, L. Busch, K. Ghoreschi, N.L. Ploch, S. May, S. Vogel, J. Eberle, M.C. Meinke, Treatment of the Candida subspecies Candida albicans and Candida parapsilosis with two far-UVC sources to minimise mycoses in clinical practice, Mycoses 66(1) (2023) 25-28.

[5] M. Buonanno, D. Welch, I. Shuryak, D.J. Brenner, Far-UVC light (222 nm) efficiently and safely inactivates airborne human coronaviruses, Sci Rep 10(1) (2020) 10285.

[6] D. Welch, N.J. Kleiman, P.C. Arden, C.L. Kuryla, M. Buonanno, B. Ponnaiya, X. Wu, D.J. Brenner, No Evidence of Induced Skin Cancer or Other Skin Abnormalities after Long-Term (66 week) Chronic Exposure to 222-nm Far-UVC Radiation, Photochem Photobiol 99(1) (2023) 168-175.

[7] E. Eadie, W. Hiwar, L. Fletcher, E. Tidswell, P. O'Mahoney, M. Buonanno, D. Welch, C.S. Adamson, D.J. Brenner, C. Noakes, K. Wood, Far-UVC (222 nm) efficiently inactivates an airborne pathogen in a room-sized chamber, Sci Rep 12(1) (2022) 4373.

Danksagung

My story in the Berlin CCP started in late 2017 with an email to **Prof. Dr. Jürgen Lademann**. At this time he was at the IFSCC congress in Seoul and promised me a meeting after his return. Starting in 2018, I did my first research work at the CCP, which was still part of my master's thesis at the time. With this a great journey began.

I would like to thank you very much for this, Mr. Lademann. I would also like to thank **Priv. Doz. Dr. Alexa Patzelt**, because you laid the foundation for everything.

I would like to express my deepest gratitude to my supervisors and mentors **Prof. Dr. Cornelia Keck** and **Prof. Dr. Martina Meinke**. Thank you for the extensive scientific discussions and for the incomparable mentorship. You are the true definition of innovators.

I would further like to thank **Dr. Dr. Maxim Darvin**. Together we have managed to overcome hurdles that seemed insurmountable.

Dr. Anna Lena Klein and **Marius Kröger**, you have supported me in all the years wherever you could and I learned a lot from you. I am very grateful for that! Thank you for your friendship.

Dr. Silke Lohan and **Dr. Johannes Schleusener**, I could always count on you and your support within the VIMRE project was excellent. I would like to thank you very much for that. Even though the project was very strenuous on some days, you always made it fun.

Daniela Fernanda Zamudio Díaz, you were the best master's student I could have ever imagined. Thank you for the great time we spent together at the CCP and thank you for your friendship.

I would also like to thank all the other members and guests of the **CCP** and the **AG Keck** who have accompanied me on my journey. Together we have always formed a great team, where team work was of great value. Special thanks to **Heike Richter** and **Sabine Schanzer** for teaching me so much and supporting me at all times. Thank you, **Sabine Grenz**, for all the years of proofreading support. Many thanks to **Julia Michaelis**, who always supported me with administrative questions. Furthermore, my thanks go to **Dr. Gisela Thiede** and **Christiane Domke** for the support and good cooperation.

Thank you to all PhD and master's students. The scientific exchange and the private time I had with you was great. **Phuong Thao Tran**, **Dr. Victor Hugo Pacagnelli Infante**, **Izadora de Souza**, **Christian Raab**, **Darya "Haniye" Asadzadeh**, **Lalita Roscetti**, **Dr. Benchaphorn "Ben" Limcharoen**, **Dr. Parichat "Bee" Tavornchat**, my precious friend **Ali Jaafar** and last but not least my dear friend **Yasemin Keziban**.

A big thank you goes to all the project partners I had the pleasure to work with during my doctorate. The realization of excellent research would have been impossible without you: **Priv. Doz. Dr. Anja Kühl** and the **iPATH team of the Charité**. **Dr. Holger Klose** and his team of the **Meoclinic Berlin**. **Priv. Doz. Dr. Christian Witzel** and his team of the **Division of Plastic and Reconstructive Surgery at the Charité**. **Martin Guttmann**, **Dr. Sven Einfeldt** and the entire team of the **Ferdinand-Braun-Institut Berlin**. **Prof. Dr. Michael Kneissl** and his team at the **Institute of Solid State Physics at TU Berlin**. **Dr. Moshe Weizman**, **Dr. Peter Rotsch** and the team of **OSA Opto Light GmbH** as well as **Dr. Yuri Avlasevich**, **Prof. Dr. Katharina Landfester** and the team of the **Max Planck Institute for Polymer Research**. Last but not least, a very big thank you goes to **Dr. Paula Zwicker**, **Prof. Dr. Axel Kramer** and the staff of the **Institute of Hygiene and Environmental Medicine, University Medicine Greifswald** for the many years of excellent cooperation.

I would further like to thank the **IUVA** and **SFFR-E** for their financial support. Thanks to you, it was possible for me to make contact with the international scientific community on conference trips.

My deepest thanks go to **Cathrin Zahavi**. Thank you for all the years and our extensive talks in the kitchen.

Yashar Hajiesmaelian, **Samin Tajangi**, you are my superstars. Together we have experienced and achieved a lot, but most of all I admire what you have achieved.

Thank you from the bottom of my heart to **Virginia Ebbers** and **Dr. Jürgen Ebbers** as well as **Petra Schürmann** for always believing in me.

Thank you **Mom** and **Dad** for everything, you have been there for me since day one. I love you eternally.

Publikationen in Fachjournalen

Johannes Schleusener, Silke B. Lohan, Loris Busch, Daniela F. Zamudio Díaz, Nevin Opitz, Claudia Sicher, Tom Lichtenthäler, Kerstin Danker, Steffen Dommerich, Thomas Filler, Martina C. Meinke, Paula Zwicker: Irradiation of human oral mucosa by 233 nm far-UVC-LEDs for the safe inactivation of nosocomial pathogens. In preparation.

Daniela F. Zamudio Díaz, Loris Busch, Marius Kröger, Anna Lena Klein, Silke B. Lohan, Karsten Mewes, Lars Vierkotten, Christian Witzel, Sascha Rohn, Martina C. Meinke: Influence of epidermal melanin content and distribution on UV-induced DNA lesions and radicals in 3D epidermal models. In preparation.

Daniela F. Zamudio Díaz, Anna Lena Klein, Martin Guttmann, Paula Zwicker, Loris Busch, Marius Kröger, Holger Klose, Sascha Rohn, Johannes Schleusener, Martina C. Meinke: Skin optical properties from 200–300 nm support far-UVC skin-safety - from theory to in vivo. J Photochem Photobiol B 2023;247:112784.

Loris Busch, Marius Kröger, Daniela F. Zamudio Díaz, Johannes Schleusener, Silke B. Lohan, Christian Witzel, Cornelia M. Keck, Martina C. Meinke: Far-UVC- and UVB-induced DNA damage depending on skin type. Exp Dermatol 2023;32(9):1582-1587.

Loris Busch, Johannes Schleusener, Marius Kröger, Silke B. Lohan, Anna Lena Klein, Martin Guttmann, Holger Klose, Cornelia M. Keck, Martina C. Meinke: Evaluation of DNA lesions and radicals generated by a 233 nm far-UVC LED in ex vivo skin wounds. J Photochem Photobiol B 2023;245:112757.

Loris Busch, Anna Lena Klein, James R. Schwartz, Kathleen Pearson, Heike Richter, Sabine Schanzer, Silke B. Lohan, Fabian Schumacher, Burkhard Kleuser, Martina C. Meinke: Follicular Delivery of Caffeine from a Shampoo for Hair Retention. Cosmetics 2023;10(4):104.

Loris Busch, Anna Maria Hanuschik, Yuri Avlasevich, Katrin Darm, Elisa F. Hochheiser, Christian Kohler, Evgeny A. Idelevich, Karsten Becker, Peter Rotsch, Katharina Landfester, Maxim E. Darvin, Martina C. Meinke, Cornelia M. Keck, Axel Kramer, Paula Zwicker: Advanced skin antisepsis: application of UVA-cleavable hydroxyethyl starch nanocapsules for improved eradication of hair follicle-associated microorganisms. Pharmaceutics 2023;15(2):609.

Mohammad Alhibah, Marius Kröger, Sabine Schanzer, Loris Busch, Jürgen Lademann, Ingeborg Beckers, Martina C. Meinke, Maxim E. Darvin: Penetration depth of propylene glycol, sodium fluorescein and nile red into the skin using non-invasive two-photon excited FLIM. Pharmaceutics 2022;14(9):1790.

Johannes Schleusener, Silke B. Lohan, Loris Busch, Kamran Ghoreschi, Neysha Lobo-Ploch, Stefanie May, Simone Vogel, Jürgen Eberle, Martina C. Meinke: Treatment of the Candida subspecies C. albicans and C. parapsilosis with two far-UVC sources to minimize mycoses in clinical practice. Mycoses 2023;66(1):25-28.

Paula Zwicker, Johannes Schleusener , Silke B. Lohan, Loris Busch, Claudia Sicher, Sven Einfeldt, Michael Kneissl, Anja A. Kühl , Cornelia M. Keck, Christian Witzel, Axel Kramer, Martina C. Meinke: Application of 233 nm far-UVC LEDs for eradication of MRSA and MSSA and risk assessment on skin models. Sci Rep 2021;12:2587.

Martina C. Meinke, Loris Busch, Silke B. Lohan: Wavelength, dose, skin type and skin model related radical formation in skin. Biophys Rev 2021;13:1091-1100.

Anna Lena Klein, Markus Lubda, David Specht, Sung-Min Pyo, Loris Busch, Jürgen Lademann, Martina C. Meinke, Ingeborg Beckers, Jörg von Hagen, Cornelia M. Keck, Alexa Patzelt: Microdialysis on Ex Vivo Porcine Ear Skin Can Validly Study Dermal Penetration including the Fraction of Transfollicular Penetration-Demonstrated on Caffeine Nanocrystals. Nanomaterials (Basel) 2021;11(9):2387.

Loris Busch, Yuri Avlasevich, Paula Zwicker, Gisela Thiede, Katharina Landfester, Cornelia M. Keck, Martina C. Meinke, Maxim E. Darvin, Axel Kramer, Gerald Müller, Martina Kerscher, Jürgen Lademann, Alexa Patzelt: Release of the model drug SR101 from polyurethane nanocapsules in porcine hair follicles triggered by LED-derived low dose UVA-light. Int J Pharm 2021;597:120339.

Loris Busch, Yasemin Keziban, Lars Dähne, Cornelia M. Keck, Martina C. Meinke, Jürgen Lademann, Alexa Patzelt: The impact of skin massage frequency on the intrafollicular transport of silica nanoparticles: Validation of the ratchet effect on an *ex vivo* porcine skin model. Eur J Pharm Biopharm 2021;158:266-272.

Essentielle Kongressbeiträge

Loris Busch, Johannes Schleusener, Silke B. Lohan, Marius Kröger, Daniela F. Zamudio Díaz, Neysha Lobo-Ploch, Claudia Sicher, Nevin Opitz, Paula Zwicker, Cornelia M. Keck, Martina C. Meinke: Application of 233 nm far-UVC wavelength for skin disinfection: Safety considerations. IUVA World Congress 2023, Vortrag, Dubai, VAE., 10. – 13. September 2023.

Loris Busch, Johannes Schleusener, Marius Kröger, Silke B. Lohan, Martin Guttmann, Sven Einfeldt, Paula Zwicker, Holger Klose, Cornelia M. Keck, Martina C. Meinke: Safety assessment for the application of a novel 233 nm far-UVC LED system on skin wounds. ICULTA – 3rd International Conference on UV LED Technologies & Applications, Vortrag, Berlin, 23. – 26. April 2023.

Loris Busch, Johannes Schleusener, Daniela F. Zamudio Díaz, Marius Kröger, Silke B. Lohan, Paula Zwicker, Sven Einfeldt, Michael Kneissl, Anja A. Kühl, Christian Witzel, Holger Klose, Cornelia M. Keck, Axel Kramer, Martina C. Meinke: The influence of skin barrier disruption and melanin content on the formation of DNA lesions and radicals in *ex vivo* human skin induced by 233 nm far-UVC irradiation from LEDs. SFRR-E Redox Biology Congress, Poster, Ghent, Belgien, 24. – 26. August 2022. Free Radic Biol Med 2022;189 S1:30-31.

Loris Busch, Paula Zwicker, Anna Maria Hanuschik, Yuri Avlasevich, Katharina Landfester, Martina C. Meinke, Maxim E. Darvin, Axel Kramer, Cornelia M. Keck: Application of polyurethane and hydroxyethyl starch nanocapsules for follicular drug delivery and UVA-triggered intrafollicular drug release. Controlled Release Society Annual Meeting, Poster, Montreal, Canada, 11. – 15. Juli 2022.

Loris Busch, Johannes Schleusener, Silke B. Lohan, Paula Zwicker, Claudia Sicher, Daniela F. Zamudio Díaz, Marius Kröger, Sven Einfeldt, Michael Kneissl, Anja A. Kühl, Christian Witzel, Cornelia M. Keck, Axel Kramer, Martina C. Meinke: Skin safety assessment of 233 nm UVC light emitted by a novel LED system for skin decolonization. 9th International Conference on Oxidative Stress in Skin Biology and Medicine (Online), Vortrag, Andros, Griechenland, 10. September 2021.

Loris Busch, Yuri Avlasevich, Paula Zwicker, Maxim E. Darvin, Katharina Landfester, Martina C. Meinke, Cornelia M. Keck, Axel Kramer, Jürgen Lademann, Alexa Patzelt: Targeting hair follicles with UVA-responsive nanocapsules for optimized skin antisepsis. 13th International

Conference and Workshop on Biological Barriers (Virtual), Vortrag, Saarbrücken, 8. September 2021.

Loris Busch, Yuri Avlasevich, Paula Zwicker, Maxim E. Darvin, Katharina Landfester, Martina C. Meinke, Cornelia M. Keck, Axel Kramer, Jürgen Lademann, Alexa Patzelt: Intrafollicular UVA-induced drug release from nanocapsules – a photochemical approach for enhanced dermal drug delivery. 19th Congress of the European Society for Photobiology (Virtual), Vortrag, Salzburg, Österreich, 3. September 2021.

Loris Busch: Enhancing skin decolonization by intrafollicular UVA-triggered release of antiseptics from nanocarriers. Charité – Researchseminar of the Department of Dermatology, Venerology und Allergology, Vortrag, Berlin, 7. Juni 2021.

Loris Busch, Yuri Avlasevich, Gisela Thiede, Katharina Landfester, Axel Kramer, Gerald Müller, Paula Zwicker, Maxim E. Darvin, Martina C. Meinke, Cornelia M. Keck, Jürgen Lademann, Alexa Patzelt: Triggering the release of drugs from nanocarriers by the application of UV-LEDs. Virtual ICULTA 2021: 2nd International Conference on UV LED Technologies & Applications, Poster, Berlin, 19. – 20. April 2021.

Loris Busch, Yuri Avlasevich, Paula Zwicker, Maxim E. Darvin, Katharina Landfester, Martina C. Meinke, Cornelia M. Keck, Axel Kramer, Jürgen Lademann, Alexa Patzelt: UVA-induced drug release from nanocapsules in hair follicles. Controlled Release Society Local Chapter Meeting Germany and BeNeLux & France 2021, Kurzvortrag, Aachen, 3. März 2021.

Loris Busch, Yuri Avlasevich, Katharina Landfester, Axel Kramer, Gerald Müller, Martina Kerscher, Jürgen Lademann, Alexa Patzelt: UVA-triggered release of a model drug from polyurethane nanocarriers in hair follicles as a preclinical model for improved preoperative skin antisepsis. Gordon Research Conference on Barrier Function of Mammalian Skin, Poster, Waterville Valley, NH, USA, 11. – 16. August 2019.

Curriculum Vitae

Aus Datenschutzgründen wird der Lebenslauf in der elektronischen Version dieser Dissertation nicht veröffentlicht.

For data protection reasons, the CV is not published in the electronic version of this dissertation.